Systematic Sensitivity and Uncertainty Analysis of Sodium-Cooled Fast Reactor Systems

Friederike BOSTELMANN

Life must not be easy
if it is only rich in content.
— Lise Meitner

To my parents.

Acknowledgements

Firstly, I would like to express my sincere gratitude to my advisor Prof. Andreas Pautz for the continuous support of my doctoral research and for his valuable feedback, especially during the final phase of my work. Special thanks goes to my advisor and co-director, Dr. Winfried Zwermann (Gesellschaft für Anlagen- und Reaktorsicherheit, GRS) for sharing his great knowledge of reactor physics and uncertainty and sensitivity analysis with me, and for always asking the right questions. I am grateful that both Prof. Andreas Pautz and Dr. Winfried Zwermann continued their support despite my wish to move to the United States halfway through the thesis.

It was an honor to have Prof. Nuria García Herranz, Dr. Matthew A. Jessee, Prof. Ivan A. Kodeli, and Prof. Bruno Sudret on my thesis committee. Their interest, their time spent on reviewing my thesis, and their valuable comments are highly appreciated.

Special thanks belongs to Dr. Kiril Velkov who supported my PhD research during the time at GRS; he kept me free from most distractions. My sincere thanks goes to Dr. Bradley T. Rearden and Dr. William A. Wieselquist, who provided me with the opportunity to join their team at Oak Ridge National Laboratory (ORNL) with continuous support for my PhD research. I would also like to thank Dr. Doug G. Bowen, Dr. Kevin T. Clarno and Dr. Germina Ilas for welcoming me in their groups and providing support throughout the thesis.

Special thanks belongs to my colleagues both at GRS and ORNL who allowed stimulating discussions, helped with technical problems, and who provided a wonderful work environment. I would especially like to thank Alexander Aures for being a great office mate and a great partner for discussions around programming, the propagation of error, and R^2. Dr. Bernard Krzykacz-Hausmann and Dr. Nadine Berner offered tremendous help with questions in the area of statistics. I am very grateful for the discussions with Dr. Matthew A. Jessee about uncertainty and sensitivity analysis, and any other method-related question. For questions regarding AMPX, programming, and any other issue—technical or not—I cannot thank Dr. Dorothea Wiarda enough for her patience and support. I appreciate Dr. Nicholas R. Brown's support during

Acknowledgements

Last but not the least, I would like to thank my family and my friends. No matter which place I choose for living and which area of work I enjoy, my parents, my sister and my brother-in-law are there for me with their unconditional love and support. I truly appreciate the friendship to the "Göttinger Dänemarktrupp", the "Aachener Nukis", Estelle & Gerhard, Johanne & Christian, Timo & Stefan, and my friends from Munich and Knoxville. In spite of distances of sometimes more than 15,000 km and time differences up to 15 hours, Magdalena Kersting felt always close; her friendship has been very important during the last couple of years in this rollercoaster of life. Aşkın Güler Yiğitoğlu is my Knoxville family; her friendship means a lot while being so far away from home.

Knoxville, TN, USA, December 20, 2019   *F. B.*

Abstract

Sodium-cooled fast reactor (SFR) technologies have the potential to guarantee energy supply and to reduce the burden of nuclear waste for future generations. For an adequate simulation of these reactor systems, well-established tools that have so far been applied mainly to light water reactor (LWR) concepts need to be validated and enhanced.

For licensing purposes, there is an increasing interest in replacing conservative calculations by best-estimate calculations supplemented by uncertainty analyses. Nuclear data are a major source of uncertainties in reactor physics calculations. The propagation of nuclear data uncertainties to important system responses is important for determining appropriate safety margins in safety analyses.

A systematic approach for quantifying nuclear data–induced uncertainties for all stages of modeling is needed to assess the performance of traditional methods for uncertainty and sensitivity analysis and to unveil the major drivers of observed uncertainties in SFRs. This thesis presents a basis for such a systematic approach through the use of sub-exercises that address different levels of modeling as addition to the OECD/NEA Benchmark for Uncertainty Analysis in Modelling of SFRs.

The major analysis method applied within this thesis was the random sampling–based XSUSA method in which nuclear data is varied based on the corresponding covariance data. As a basis for analyses using several multigroup neutron transport codes from the SCALE code system, new multigroup cross section and covariance libraries were developed and optimized for the analysis of SFR systems. In order to use the time-efficient XSUSA method in combination with the SCALE 6.2 release, SCALE's random sampling sequence Sampler was extended to allow the perturbation of cross sections after the self-shielding calculation, including an optional approximation for consideration of implicit effects.

XSUSA allowed for the determination of one correlation-based sensitivity index to identify the main contributors to observed uncertainties. This sensitivity analysis was extended by a second correlation-based sensitivity index, as well as variance-based

Zusammenfassung

Natrium-gekühlte schnelle Reaktorsysteme (SFR) haben das Potential, die Energiever-sorgung der Zukunft zu sichern und die Last des radioaktiven Abfalls für zukünftige Generationen zu reduzieren. Für die adäquate Simulation dieser Systeme müssen etablierte Simulationswerkzeuge, welche bislang vor allem für die Simulation von Leichtwasserreaktoren (LWR) eingesetzt wurden, neu validiert und bei Bedarf erwei-tert werden.

Im Rahmen von Lizenzverfahren gibt es ein wachsendes Interesse, konservative Be-rechnungsmethoden durch realistische Rechnungen kombiniert mit Unsicherheits-analysen zu ersetzen. Eine der größten Ursachen für Unsicherheiten in berechneten reaktorphysikalischen Größen sind die verwendeten nuklearen Daten. Die Berück-sichtigung dieser Unsicherheiten ist von größter Bedeutung, um geeignete Sicher-heitsgrenzen in Sicherheitsanalysen zu definieren.

Um das Verhalten traditioneller Methoden für Unsicherheitsanalysen von SFR zu evaluieren und um die Hauptursachen für auftretende Unsicherheiten aufzudecken, müssen die Unsicherheiten in einem systematischen Ansatz quantifiziert werden. Als Basis für solch ein systematisches Vorgehen wurden innerhalb dieser Arbeit Spe-zifikationen für die Analyse verschiedener Modellierungsebenen als Zusatz für das bestehende OECD/NEA Benchmark für Unsicherheitsanalysen von SFRs entwickelt.

Für die Unsicherheitsanalysen innerhalb dieser Arbeit wurde primär das Stichproben-verfahren mittels der XSUSA Methode verwendet, bei welchem die nuklearen Daten basierend auf ihren Kovarianzdaten variiert werden. Für die Anwendung diverser Multigruppen-Neutronentransportcodes aus dem Programmpaket SCALE wurden Wirkungsquerschnittsbibliotheken sowie Kovarianzbibliotheken speziell für die Analy-se von SFRs entwickelt. Für die Verwendung der XSUSA Methode mit SCALE 6.2 wurde SCALEs Stichprobenverfahren erweitert, sodass die Wirkungsquerschnitte nach der Abschirmungsrechnung variiert werden können, optional mit einer Näherung für die Berücksichtigung implizierter Effekte.

Die Sensitivitätsanalyse mit XSUSA erlaubte bislang die Berechnung eines korrelati-

Acknowledgements

Contents

Contents

Contents

List of Figures

List of Tables

1 Introduction

In the early days of computational reactor safety analysis, the concept of conservative methods was introduced to account for uncertainties resulting from limited modeling capabilities and limited knowledge of physical phenomena. In this approach, any input parameter for the analysis is specified in a way that will lead to conservative results for safety parameters with respect to acceptance criteria. However, the use of a conservative methodology may mask important safety issues and might inhibit operational flexibility. Furthermore, since this concept was initially presented, the development of computer codes has greatly improved the ability to predict experimental results. (IAE, 2009)

Due to these reasons, there is an increasing interest in replacing conservative calculations with best-estimate calculations supplemented by uncertainty analyses. This is also known as *Best Estimate Plus Uncertainty (BEPU)* (D'Auria et al., 2012). In a best estimate calculation, the physical processes in nuclear power plants are realistically described. Uncertainties of output parameters are then determined based on uncertainties of the input parameters to the applied computer code (Boyack et al., 1990). Although the regulators rely mostly on the conservative approach, the BEPU approach has been introduced into some regulations. In 1989, the US Nuclear Regulatory Commission (NRC) included BEPU analysis for emergency core cooling system performance in Regulatory Guide 1.157 (Task RS 701-4) (NRC, 1989). The Reactor Safety Commission in Germany has suggested the use of BEPU analyses in loss of coolant accidents since 2005 (RSK, 2005). In 2009, the International Atomic Energy Agency (IAEA) released the Specific Safety Guide SSG-2 on Deterministic Safety Analyses for Nuclear Power Plants, designating the BEPU approach as one of four options for computational safety analysis (IAE, 2009).

Chapter 1. Introduction

The BEPU approach is becoming more relevant given the growing interest in concepts other than traditional light water reactors (LWRs). Advanced reactor concepts currently being developed throughout the industry are sodium-cooled fast reactors (SFRs), high-temperature gas-cooled reactors (HTGRs), lead-cooled fast reactors (LFRs), fluoride salt-cooled high-temperature reactors (FHRs), heat pipe reactors, and various molten salt reactor (MSR) concepts (Rearden, 2018). With anticipated license requests from the industry in the near future, research institutes, industry, and national regulators all have a growing interest in the BEPU approach for safety analysis. There are major differences between these reactor concepts and LWRs, such as the geometries, materials, and temperatures. The uncertainties in the input parameters for reactor safety analysis have to be assessed and thorough uncertainty analyses must be performed to allow for the definition of appropriate safety margins and to understand the origin of important uncertainties.

One major source of input uncertainties is the nuclear data providing the basis for every reactor physics calculation. The nuclear cross sections, fission yields, and decay data are mostly obtained through measurements and subsequent evaluations, so they are subject to uncertainties. To study the impact of nuclear data uncertainties on relevant output quantities and to promote the development of uncertainty analysis methods in best-estimate coupled multiphysics and multiscale simulations, the OECD/NEA benchmark for Uncertainty Analysis in Modeling (UAM) of LWRs (Ivanov et al., 2016) was launched several years ago. For HTGRs, which represent one of the Generation IV concepts, there is a corresponding benchmark in the form of the IAEA Coordinated Research Project on HTGR Physics, Thermal-Hydraulics, and Depletion Uncertainty Analysis (Reitsma et al., 2014; Strydom and Bostelmann, 2015). In contrast, only limited studies have been conducted for other advanced reactor systems at this writing.

The Benchmark for Uncertainty Analysis in Modeling for Design, Operation and Safety Analysis of SFRs (UAM SFR) (Buiron et al., 2019) is currently in progress. This effort was launched in 2015 to study reactivity feedback coefficients and their uncertainties with a medium-sized 1,000 MWth metallic core (MET1000) and a large 3,600 MWth oxide core (MOX3600). The UAM SFR benchmark only covers full core neutronics and coupled neutronics/thermal-hydraulics analysis. The major part of the investigation is the analysis of the impact of nuclear data uncertainties on relevant output quantities of these full core calculations. However, in addition to investigations of the full core level, analyses of several sub-exercises on the fuel pin and assembly level are also needed

to systematically assess the influence of nuclear data in fast reactor simulations. Especially when studying simple models, comparisons between computational results using different methods, models, and applied nuclear data libraries allow the cause of the observed differences and uncertainties to be identified. If these analyses would only be performed on the global level of the whole core, uncertainties might be hidden due to the compensation of various effects. In view of only little operating experience with fast reactor systems compared to LWR systems, a thorough understanding of the uncertainties in this reactor concept is important to ensure appropriate safety margins and to decide where additional efforts should be focused to reduce input uncertainties.

The goal of this work is to explore the BEPU approach for SFR systems using a systematic approach to assess traditional methods for uncertainty and sensitivity analysis of these systems and to determine the major drivers of observed uncertainties.

The following subsection provides an overview of the SFR technology (Section 1.1). The subsequent subsection summarizes the methods and tools currently used for the computational analysis of SFR systems (Section 1.2). Then the role of nuclear data uncertainties for reactor physics analysis is discussed, with focus on the particular relevance for SFR analysis (Section 1.3). Commonly used methods and tools for uncertainty and sensitivity analysis with respect to nuclear data are reviewed in Section 1.4. Finally, the objectives of this dissertation are summarized (Section 1.5), and the remaining structure of this document is outlined (Section 1.6).

1.1 Sodium-cooled fast reactors

SFR systems are a promising advanced reactor technology option for securing future energy supply (Kelly, 2014). One motivation factor for the development of SFR systems has been the improved utilization of uranium. In contrast to about 1% utilization in thermal spectrum systems such as LWRs, SFR systems utilize almost all the energy in uranium. Given the limited uranium reserves on our planet, SFR systems can extend the natural resource utilization. In the course of discussions about the difficulty to dispose spent fuel from the currently operating LWR fleet, the SFR technology became of interest because of the capability to transmute long-living actinides into fission products through absorption of high-energy neutrons. SFRs have consequently the potential to reduce the burden of nuclear waste for future generations. (Ziegler and

Allelein, 2013)

The main concept in fast reactors is to breed nuclear fuel by converting abundant fertile materials to fissile materials. For example, the fertile ^{238}U can be converted to the fissile ^{239}Pu via the following process:

$$^{238}_{92}\text{U}\,(n,\gamma)\,^{239}_{92}\text{U} \quad \xrightarrow{\beta^-} \quad ^{239}_{93}\text{Np} \quad \xrightarrow{\beta^-} \quad ^{239}_{94}\text{Pu} \tag{1.1}$$
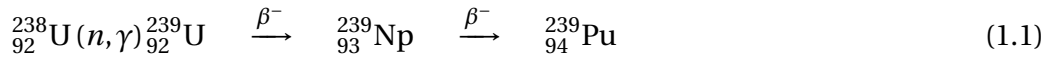
The conversion rate CR is defined as the ratio of produced and consumed fissile nuclides. If CR is greater than 1, it is called breeding ratio. To allow CR greater than 1, the number of neutrons produced by fission in fissile isotopes (η) must be substantially greater than 2 since one neutron is used for fission, one neutron is absorbed in fertile material to produce a new fissile nuclide, and a fraction of neutrons is lost due to parasitic absorption and leakage. (Yang, 2012)

As an example, η of ^{239}Pu rapidly increases with increasing energy and shows values larger than 2 for energies above 100 keV (Figure 1.1). ^{239}Pu can consequently be used for breading if the average energy of the neutrons is higher than about 100 keV. The harder the neutron spectrum, the larger is the breeding ratio. Spectrum hardening is achieved by a high fuel density and a high fuel volume fraction, realized by using a tight triangular fuel pin lattice in the fuel assemblies. (Yang, 2012)
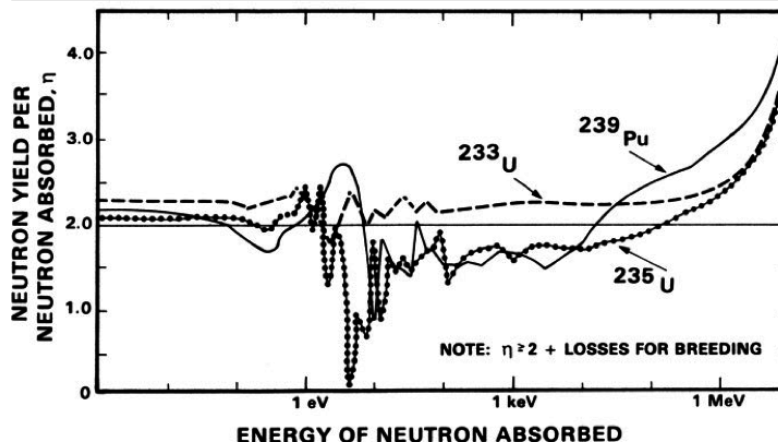
Figure 1.1 – The number of neutrons produced by fission in fissile isotopes (Waltar et al., 2012b).

To allow a compact reactor core with a high power density, efficient heat removal

needs to be guaranteed. This can be realized with liquid metals. Especially sodium is suitable as coolant because it has a large heat capacity, a large heat conductivity, and it is liquid in the temperature range between 97.8 and 882.9°C. In contrast to other metals, it does not have a corrosive effect on the materials used in the primary circuit of the reactor. A disadvantage is, however, the strong reaction in contact with air and water that is resulting in specific safety requirements of these plants. (Ziegler and Allelein, 2013)

Figure 1.2 shows a simplified schematic for a sodium-cooled reactor. In the primary loop, sodium coolant is pumped through the core and circulated through an intermediate heat exchanger. Neutron activation of the sodium in this loop requires a secondary sodium loop in which heat is transported from the intermediate heat exchanger to the steam generator. In a pool system, the intermediate heat exchanger and the primary pump are placed inside the reactor tank; in a loop system, these components are connected via pipes to the reactor vessel. (Waltar et al., 2012b)

The reactivity in the core is influenced by several nuclear physics and materials phenomena: the fuel Doppler coefficient, changes in the coolant density, the axial and radial expansion of the fuel, the radial expansion of the core, the expansion of the control rod driveline, and bowing of the fuel assembly. The sodium void coefficient is always positive, while the Doppler coefficient is always negative. The void coefficient can only be allowed as large as it can be compensated with the Doppler feedback such that the total reactivity effect remains negative. The void coefficient can be influenced by the ratio of the height and diameter of the core, leading to so-called "pancaked" cores with a height much smaller than the diameter and with dominating leakage effects. (Waltar et al., 2012b)

Two SFRs are currently in commercial operation: the BN-600 reactor (commercial start in 1981) and the BN-800 reactor (commercial start in 2016) in Russia with net powers of 560 and 820 MWe, respectively. The Prototype Fast Breeder Reactor (PFBR) reactor in India with a planned net power of 500 MWe is currently under construction with a scheduled first criticality in 2020. The China Experimental Fast Reactor (CEFR) with net power 20 MWe has achieved criticality in 2010, and the Chinese Xiapu reactor with a planned net power of 600 MWe is scheduled to start commercial operation in 2023. (NNM, 2019) Together with several research and demonstration reactors, operating experience of almost 400 reactor-years has been gained for SFRs so far (Ruggieri et al., 2017).
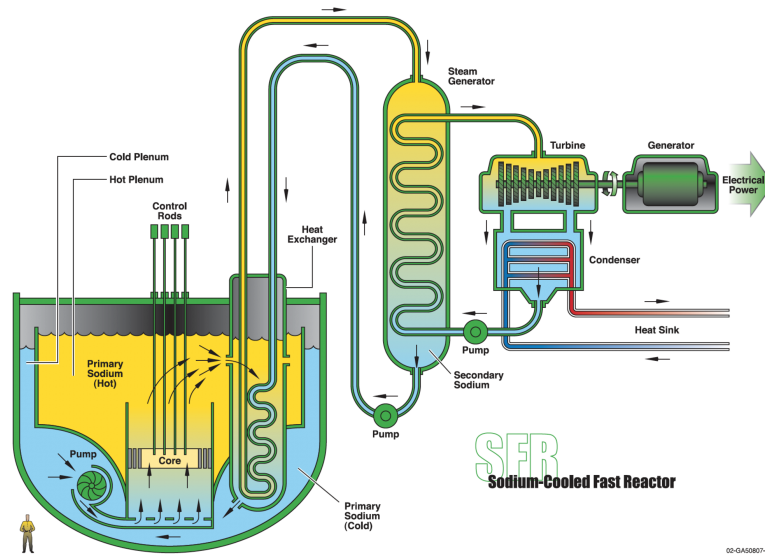
Figure 1.2 – Sodium-cooled fast reactor schematic (Com, 2002).

While only a few commercial and demonstration SFR facilities have been operated to date, the interest in this technology has recently been renewed. In addition to the countries mentioned above, the United States and Korea show interest in this technology. In the United States, TerraPower is currently developing the Traveling Wave Reactor and GE is developing the PRISM reactor. The Korean Atomic Energy Commission follows a research and development plan with completion of a prototype SFR design by 2017, specific design approval by 2020, and the construction of a prototype SFR (PGSFR) by 2028. (IAEA, 2017)

1.2 Computational analysis of SFR

There are two main challenges for the computational analysis of the neutronics of fast reactor systems. The fast neutron spectrum shows a large number of resonances in the high energy range (Figure 1.3) mainly due to the significant resonance scattering structure of intermediate weight nuclei of the coolant (^{23}Na) and the structure (e.g. ^{56}Fe). These resonances must be appropriately captured in the processing of the cross sections. The other challenge is the high axial and radial neutron leakage from the core that has a significant impact on the neutron flux spectrum. (Yang, 2012) With respect to time-dependent behavior, the simulation challenges are the above mentioned feedback effects, in particular the expansion effects that introduce significant geometry and material density changes (Waltar et al., 2012b).
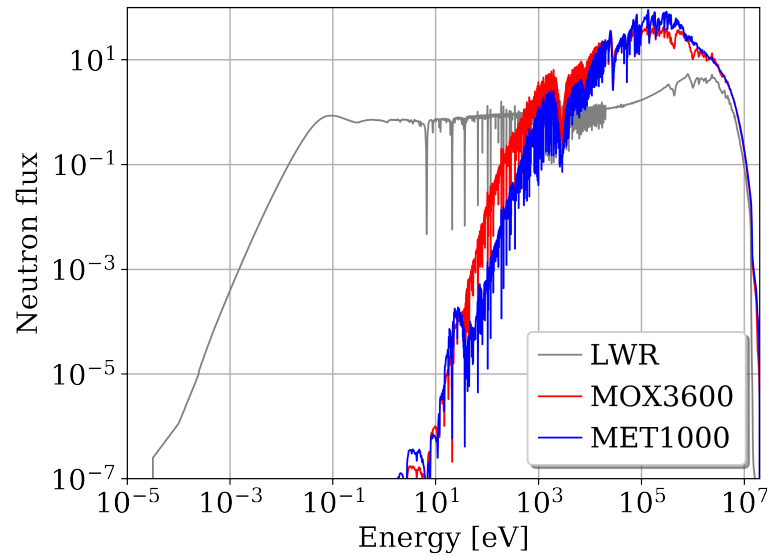
Figure 1.3 – Normalized neutron flux of two SFR assemblies with metallic fuel (MET1000) and oxide fuel (MOX3600) compared to the flux of a typical LWR pin cell.

Two of the most common code systems for reactor physics analysis of fast reactors, including many years of experience with the simulation of these reactor systems, are developed at the Argonne National Laboratory (ANL) in the United States and at Commissariat à l'énergie atomique et aux énergies alternatives (CEA) in France. At ANL, cross sections are prepared using MC^2-3 (Lee and Yang, 2017) together with the TWODANT code (Alcouffe et al., 1990). MC^2-3 prepares self-shielded cross sections for each region of the model in an ultra-fine group structure (often 2,082 groups) based on pointwise cross sections. Afterwards, TWODANT is performing a transport calculation on an approximate RZ model of the core to solve for region-wise flux solutions with very fine group cross sections (often in 1,041 groups). Finally, the ultra-fine group cross sections are collapsed to a few-group structure (often 33 groups) using the region-wise flux from TWODANT. These cross sections are used for whole core flux calculations with the DIF3D code (Destine, 1984; ANL, 2014) that applies the variational nodal transport solver VARIANT (Palmiotti, 1993).

At CEA, the ERANOS code (Rimpault, 2002) has been developed for many years. ERANOS includes the cell and lattice code ECCO, and multiple flux solvers for full reactor cores. ECCO is used to prepare self-shielded cross sections by combining a slowing-down treatment in a very fine 1,968-group structure with the sub-group method. The flux in heterogeneous geometries including fuel assemblies with hexagonal wrapper

tubes are performed using the collision probability method.

A lot of experience with the simulation of fast reactor systems is furthermore found at Paul Scherrer Institut (PSI) in Switzerland. The FAST code system (Mikityuk et al., 2005) has been developed for static and transient analysis of fast reactors. The code system consists of the just mentioned ERANOS code for static neutronic calculations, PARCS for dynamic reactor calculations, TRACE for system thermal-hydraulic modeling, and FRED for fuel behavior analysis. PARCS (Downar et al., 2010) is a code from the United States Nuclear Regulatory Commission (NRC) that is mainly developed at the University of Michigan in the United States. PARCS solves the time-dependent neutron transport equation to perform simulations of quasi-steady-state core operations and transient reactor kinetics. The NRC code TRACE is a best-estimate system code for static and transient thermal-hydraulic analyses of LWR systems that has been extended at PSI for advanced fast reactors.

In addition to ERANOS, the three-dimensional continuous-energy Monte Carlo code Serpent from VTT in Finland (Leppänen, 2007; Leppänen et al., 2014) is used by PSI for the generation of cross sections for PARCS. Serpent is also used by Helmholtz-Zentrum Dresden-Rossendorf (HZDR) in Germany to prepare cross sections for their reactor dynamics code DYN3D (Rohde et al., 2016) that is being continuously extended to innovative reactor designs, particularly to SFRs (Nikitin, 2019). Other codes for the analysis of fast reactor systems include the Russian codes TRIGEX, JAR, GEFEST and SYNTES, the Japanese SLAROM-UF code, the Korean K-CORE system (IAE, 2012), and the recently developed SARAX code (Zheng et al., 2018) at Xi'an Jiaotong University in China.

Due to the expected increasing role of fast reactor systems in the future, there is a growing interest to validate or enhance existing tools for adequate simulations of the reactor physics with fast neutron spectra. One widely known tool for criticality safety, reactor physics, shielding, sensitivity and uncertainty analysis and more is the SCALE code system (Rearden and Jessee, 2016).

SCALE has been developed at Oak Ridge National Laboratory since 1969. For neutron transport calculations, SCALE provides the one-dimensional deterministic code XSDRN, the two-dimensional deterministic code NEWT, and the three-dimensional Monte Carlo code KENO. While KENO can be applied with either continuous-energy (CE) or multigroup (MG) cross sections, XSDRN and NEWT are only used with MG cross sections. The TRITON sequence of SCALE allows the generation of homoge-

nized few-group macroscopic cross sections for use in nodal diffusion codes. TRITON furthermore enables depletion calculations in combination with the depletion/irradiation/decay solver ORIGEN. In the past, SCALE has been mainly applied to LWR analysis. Although SCALE is widely applied for the criticality safety analysis of fast spectrum systems, SCALE has only recently been applied to SFRs (Aures et al., 2015; Bostelmann et al., 2016).

When using CE data for Monte Carlo simulations, no approximations are being made so that this method can be used for both LWR and SFR systems. The cross section processing for the generation of self-shielded MG cross section in SCALE has, however, only been extensively tested for thermal systems. Furthermore SCALE's MG libraries for reactor physics analyses were optimized for LWR applications. For example, they show a fine energy group structure in the resolved resonance region, but only a coarse structure in the higher energy range such that resonances in higher energy ranges might not be appropriately captured.

To benefit from the large number of analysis tools in SCALE that apply MG data, it is of interest to generate a new MG library optimized for fast spectrum systems and to verify MG calculations with the help of corresponding CE reference calculations.

1.3 The role of nuclear data uncertainties for reactor physics analysis

In nuclear safety analyses for licensing processes, there is an ongoing tendency to take existing uncertainties of input parameters into account by performing best-estimate calculations accompanied with systematic uncertainty analyses (BEPU). The uncertain input parameters for neutronics calculations are manufacturing uncertainties, including the geometric dimensions and the material compositions, the material temperatures, and uncertainties of the nuclear data. Other relevant uncertainties are associated with methods and modeling approximations in the applied codes and user error.

One of the most important group of uncertain input parameter is the nuclear data which provides the basis for every reactor physics calculation. The nuclear cross sections, fission yields and decay data are obtained in measurements and subsequent evaluations. They are subject to systematic and statistical uncertainties. After

extensive evaluations including validation studies with criticality experiments, the result is stored as a set of data files that can be processed for use in reactor physics codes. The most common data files are the European Joint Evaluated Fission and Fusion File (JEFF) (Sublet et al., 2003), the Japanese Evaluated Nuclear Data Library (JENDL) (Shibata et al., 2012) files and the American Evaluated Nuclear Data File (ENDF/B) (Chadwick et al., 2011). The libraries are undergoing continuous modifications based on additional measurements or improved evaluations, with new revisions being released on a regular basis.
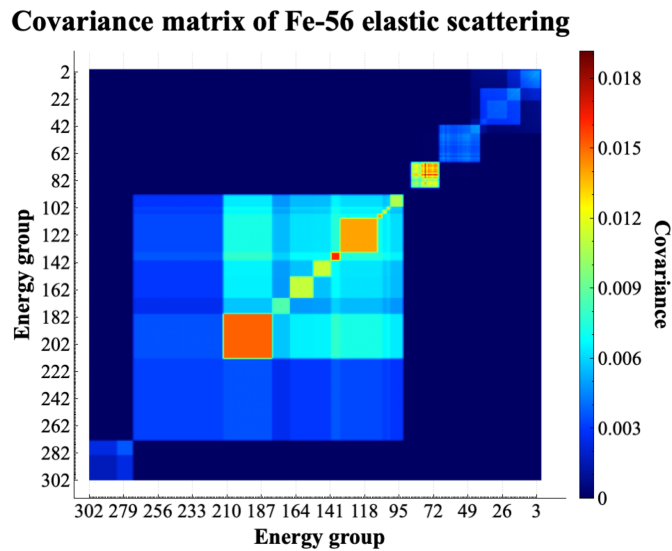
Figure 1.4 – Covariance matrix of ^{56}Fe elastic scattering in a 302-group structure.

In addition to the nominal cross section values, the nuclear data files contain information about the uncertainties in the form of so-called covariance matrices. As an example, the covariance matrix for ^{56}Fe elastic scattering is presented in Figure 1.4. The diagonal elements describe the variance of the cross sections in the individual energy groups. The square root of the variance is the standard deviation that is the uncertainty of the cross section. The value in the i-th row and j-th colum is the covariance between the scattering cross section in the i-th and j-th energy group. The covariance is a measure of the joint variability of the two cross sections.

The nuclear data libraries that are provided together with an analysis code are often just considered as one of several input parameters. However, when propagating the uncertainties of the cross sections through the calculation chain, large uncertainties of the output quantity of interest can often be observed. For LWR, eigenvalue uncertainties of about 0.5% were found for fresh fuel cases and more than 1% for mixed

oxide (MOX) fuel cases. Uncertainties of more than 5% were observed for the power in the assemblies of a fresh LWR core, while more than 10% uncertainty were observed for MOX cores (Zwermann et al., 2009; Rochman et al., 2017). In recent studies of control rod ejection transients, significant reactivity uncertainties between 6 and 9% were found (Aures et al., 2020).
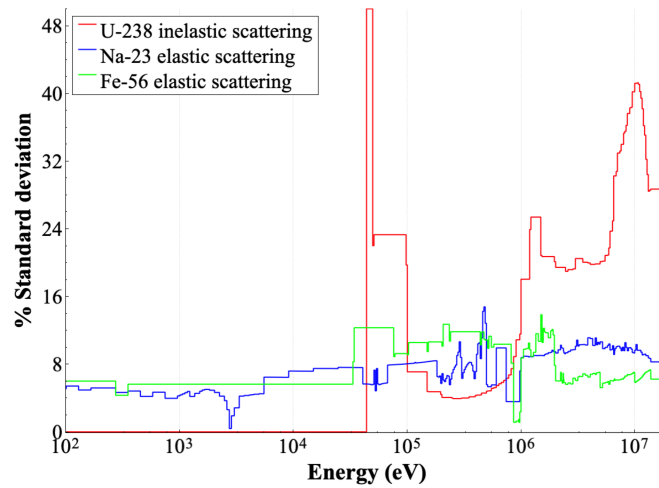
Figure 1.5 – Relative uncertainty in the high energy range; 302-group representation based on ENDF/B-VII.1 data.
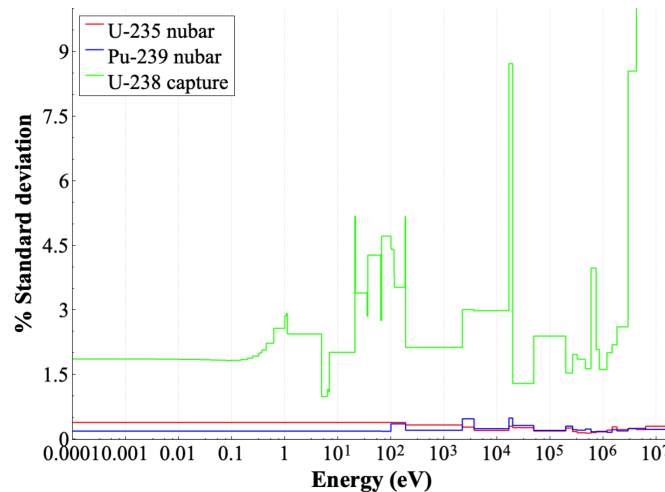
Figure 1.6 – Relative uncertainty in a 56-group representation based on ENDF/B-VII.1 data.

Nuclear data uncertainties play an especially big role for the analysis of fast reactor systems because the uncertainties of relevant cross section are often larger in the fast energy region (Figure 1.5) compared to relevant cross sections uncertainties for

thermal systems (Figure 1.6). Previous studies showed that output uncertainties in fast systems can be more than three times as large as in corresponding LWR calculations for relevant output quantities (Stauff et al., 2016).

Given the limited operating experience, the accurate simulation of reactor physics and quantification of associated uncertainties are essential for ensuring that SFRs operate within the appropriate safety margins. Main differences of this reactor type compared to common LWRs—different materials, the fast neutron spectrum, the long neutron-mean free path, and high neutron leakage—and the limited operating experience require extensive testing of traditional modeling and simulation tools and their corresponding nuclear data libraries. In addition to the quantification of important output uncertainties, sensitivity analyses can provide information about the individual cross sections that contribute the most to the output uncertainty. In this way, recommendations for measurements of particular cross sections can be expressed.

1.4 Methods for nuclear data uncertainty and sensitivity analysis

To quantify the uncertainty originating from nuclear data, it is possible to propagate input uncertainties through the calculation chain to output quantities of interest. There are currently two common methods in use: an approach based on perturbation-theory and the random sampling approach.

For the first approach, sensitivities of system responses, such as the multiplication factor, reaction rates and reactivity coefficients, due to changes in the nuclear data are determined using perturbation theory. These sensitivities are determined for the cross sections of all nuclide reactions considered in the investigated model in all energy groups. A sensitivity of a response to a cross section in a certain energy group describes by how much the response would change due to a change in this particular cross section. (Williams, 1986)

When using adjoint-based first-order perturbation theory, the calculation of the sensitivity coefficients requires the determination of the forward and adjoint energy-dependent scalar neutron fluxes as well as the moments of these fluxes, which is achieved by a forward and an adjoint flux calculation (Williams et al., 2001). Recent

developments allow the calculation of sensitivities in one forward calculation based on CE Monte Carlo neutron transport calculations (Kiedrowski and Brown, 2014; Perfetti and Rearden, 2016). The multiplication of all sensitivity coefficients with the corresponding covariance matrices results in the uncertainty of the system response. Furthermore, when multiplying only the sensitivities of one nuclide reaction with the corresponing covariance matrix, the contribution to the output uncertainty of only this individual covariance matrix can be determined. This sensitivity analysis is usually a byproduct of the analysis.

The perturbation theory–based approach is, for example, implemented in the SUSD3D code at Jožef Stefan Institute (Kodeli, 2001), in the ANL code PERSENT (Aliberti and Smith, 2015; Zhang et al., 2018), and in the TSUNAMI code (Broadhead, 2004) as part of the SCALE code system. SUSD3D is used in conjunction with several neutron transport codes such as DORT and TORT for the calculation of flux moments. PERSENT is used to calculate sensitivity coefficients based on fluxes determined by DIF3D (see Section 1.2). The MG version of TSUNAMI can be used in combination with XSDRN, NEWT and KENO (see Section 1.2). Since the release of SCALE 6.2, a CE version is available that requires only one forward flux calculation with KENO in CE mode. Similar approaches are also implemented in the Monte Carlo codes Serpent (Aufiero et al., 2015) and MCNP (Kiedrowski and Brown, 2014).

For the random sampling approach, cross sections are sampled using conditional sampling based on the covariance data. After running a set of calculations with the perturbed cross sections, a statistical analysis is performed to obtain a mean value with a corresponding standard deviation of the response of interest. If the random sampling tool is used in combination with a code for the generation of macroscopic few-group cross sections for full core analysis with a nodal code, it is possible to generate sets of perturbed few-group cross sections that can be used for full core uncertainty analysis. The coupling of the nodal code to a thermal hydraulics code allows uncertainty analyses of steady-state and transient calculations.

The random sampling approach is, for example, included in the Gesellschaft für Anlagen- und Reaktorsicherheit (GRS) code XSUSA (Zwermann et al., 2009), in the Sampler code of SCALE (Williams et al., 2013), in the PSI codes SHARK-X (Wieselquist et al., 2013) and NUSS (Zhu et al., 2015), and in the fast Total Monte Carlo (TMC) code of the Nuclear Research and Consultancy Group (NRG) (Rochman et al., 2014). XSUSA is generating cross section perturbations based on MG covariance data. These

perturbations are applied to the shielded (problem-dependent) MG cross sections for the transport calculation. Sampler is following a similar approach, but applies the perturbations to the unshielded (problem-independent) MG cross sections. In this way, Sampler considers the so-called *implicit effects*, i.e. the impact of the self-shielding calculation on the cross section perturbation. However, this approach requires a self-shielding calculation for each sample calculation, whereas XSUSA needs to run only one nominal self-shielding calculation. SHARK-X is following a similar approach as XSUSA and Sampler. With NUSS, the CE data used by MCNP is perturbed based on MG covariance data. In the TMC code, perturbations are not generated based on the covariance matrices, but based on the inputs of the nuclear reaction models (level density model, optical model, compound nucleus model etc.). It is noted that the widely used Dakota tools for uncertainty analysis (Sandia National Laboratories) has recently been extended by the sampling of nuclear data, although this extension is not yet publicly available (Swiler et al., 2018).

In addition to being a simple, straightforward approach, there are two main advantages of the random sampling over the perturbation theory–based approach: Any output of the calculation can be statistically analyzed, while the perturbation theory–based approach is limited to responses such as the eigenvalue, reactivity differences and reaction rate ratios. Furthermore, nonlinear effects are automatically considered. A disadvantage is the increased computation time due to the requirement of a certain sample size to obtain a statistically significant result. A sensitivity analysis for the identification of important nuclide reactions for the output uncertainty is not a byproduct of the analysis. It is possible to perform individual sets of calculations based on perturbed cross sections of always only one nuclide reaction. However, repeating this for all relevant nuclide reactions is computationally very expensive. Another option is the calculation of correlation-based sensitivity indices as it is done by GRS, or variance-based sensitivity indices similar to Sobol' indices which is again computationally expensive (Sobol, 1993; Krzykacz-Hausmann, 2006).

1.5 Objectives of this thesis

The objectives of this work can be summarized as follows:

1. Development of specifications for systematic analysis of uncertainties and sensitivities of SFR systems on all levels of modeling as sub-exercises of the UAM

SFR Benchmark.

2. Generation of MG libraries for SFR analysis with SCALE.

3. Implementation of the XSUSA approach in SCALE 6.2 including an approximation for implicit effects.

4. Extension of the XSUSA sensitivity analysis and implementation of corresponding sensitivity indices for comparison with perturbation theory–based results.

5. Systematic uncertainty and sensitivity analysis of the sub-exercises.

Based on the specification of the UAM SFR benchmark, specifications for sub-exercises are developed that cover the pin cell, fuel assembly and supercell level and that request more detailed full core results. The focus is the analysis of the impact of nuclear data uncertainties on important output quantities.

As basis for analyses using several MG solvers from the SCALE code system, new MG libraries are developed that are optimized for the analysis of SFR systems with respect to the group structure and the weighting function.

XSUSA has been extensively used in combination with modules of SCALE 6.1. To allow calculations with the time-efficient XSUSA method in combination with modules of the recent SCALE 6.2 release, the Sampler sequence of SCALE 6.2 is extended to allow the perturbation of cross sections after the self-shielding calculation. For the consideration of implicit effects with the XSUSA approach, an approximation based on linear perturbation theory is implemented.

The sensitivity analysis with XSUSA allowed so far the determination of one correlation-based sensitivity index. This sensitivity analysis is extended by a second correlation-based sensitivity index as well as variance-based sensitivity indices based on Sobol' indices. Furthermore, corresponding indices that use sensitivity coefficients from perturbation theory are developed to enable the possibility of comparisons between the two approaches.

Finally, systematic uncertainty and sensitivity analyses with respect to nuclear data are performed based on the developed specifications. Calculations are performed with the TSUNAMI, XSUSA, and Sampler approach in combination with modules of the SCALE code system. Full core results are added using the nodal code PARCS. The

uncertainty quantification of various important output parameters are accompanied by the identification of important nuclide reactions for the observed uncertainty by the use of sensitivity analysis. By systematically analyzing every level of modeling, it is simultaneously studied whether the main conclusions from full core analysis can already be drawn from simple models, i.e. if the analysis of simple models would, for example, be sufficient for first assessments of the impact of nuclear data uncertainties for a potential new SFR design. By comparing results based on various methods and models, these studies also contribute to the development and assessment of calculation methods and models for uncertainty analysis accompanying best-estimate reactor simulations of SFRs.

1.6   Thesis outline

Chapter 2 contains an extended version of the developed sub-exercise specifications for the UAM SFR benchmark, including pin cell, fuel assembly, supercell and full core descriptions. In Chapter 3, the generation of new MG libraries for SCALE is described and the results of extensive testing against CE reference results are presented.

The two most common methods for uncertainty analysis with respect to nuclear data are described in Chapter 4. The perturbation theory–based approach is thereby only briefly summarized. The focus is the description of the random sampling approach including the development of an approximation for the consideration of implicit effects without repeating the self-shielding calculation for each sample calculation.

Sensitivity analysis methods are covered in Chapter 5. The description of variance-based sensitivity indices similar to Sobol' indices is followed by correlation-based sensitivity indices using randomly sampled cross sections. Furthermore, an approach for the determination of comparable sensitivity indices based on the sensitivity coefficient from perturbation theory is presented.

Chapter 6 shows results for all levels of modeling as specified in Chapter 2. The uncertainties and sensitivities of the various specified output quantities are analyzed using the methods presented in the previous chapters.

The final chapter summarizes the results of this work and suggests possible areas for future developments and analyses based on this work.

2 Sub-exercise specifications for the OECD/NEA benchmark for uncertainty analysis in modeling of SFRs

In addition to the investigation of full core models within the UAM SFR benchmark, the analysis of several sub-exercises was suggested in order to systematically assess the influence of input uncertainties on important output quantities on all levels of modeling.

Uncertainty analysis shall be performed using different methods, models and nuclear data libraries. By the application of sensitivity analyses, information about the individual input parameters that contribute the most to the output uncertainty can be obtained.

The models defined in the sub-exercises are derived from the medium-sized metallic core (MET1000) and the large oxide core (MOX3600) of the UAM SFR specifications. The sub-exercises are following the lines of Phase I of the OECD/NEA UAM LWR benchmark (Ivanov et al., 2016) and the IAEA CRP on HTGR Uncertainty Analysis (Reitsma et al., 2014; Strydom and Bostelmann, 2015).

In general, the input uncertainties arise from:

- Nuclear data uncertainties (covariance data),

- Manufacturing uncertainties, such as unit cell dimensions and nuclide densities,

- Uncertainties associated with methods and modeling approximations utilized in lattice physics codes, including the selection of the multigroup structure and

the self-shielding method.

However, the focus of the exercises is the analysis of the impact of nuclear data uncertainties. Uncertainties or errors associated with method and model approximations are code dependent and beyond the scope of the benchmark. The analyses are therefore limited to the comparison of the results between different methods and models. Manufacturing uncertainties might be added at a later date when reliable values can be provided.

The following sections contain an extended version of the sub-exercise definitions as they have been provided to the UAM-SFR benchmark team (Bostelmann et al., 2018). Tables including dimensions, material compositions and temperatures are provided in Appendix A.1. In the course of time while writing this thesis, the sub-exercise specifications have been included in the full UAM-SFR benchmark specifications (Buiron et al., 2019).

2.1 Exercise I-1: Pin cell

Exercise I-1 describes simple fuel pin cells in an infinite lattice. Due to the negligence of leakage effects and the simulation of only a very simple model, the identification of the sources of differences between calculations is simplified. Differences caused by the application of different cross section and covariance data can be assessed, and differences caused by different methodologies for the transport calculation, the self-shielding of the cross sections, the selection of the multigroup structure and modeling choices can easier be identified since they are not hidden by the interference of various effects as it might occur for a complicated geometry.

The two-dimensional, hexagonal pin cells contain EOEC (End Of Equilibrium Cycle) fuel cylinders surrounded by cladding and cooled by sodium (Figure 2.1). In case of the MOX3600 pin cell, the fuel pin contains a central hole. Periodic boundary conditions are applied.

Output quantities of interest are the uncertainties of the eigenvalue, several 1-group microscopic cross sections, and 1-group homogenized macroscopic cross section of the fuel region as listed in Table 2.1.

(a) MET1000 (b) MOX3600
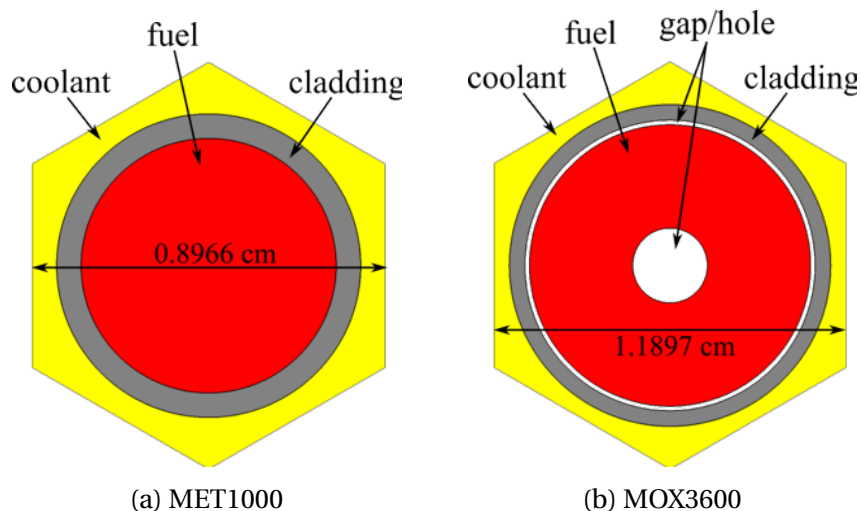
Figure 2.1 – Pin cell models.

Table 2.1 – Requested 1-group microscopic and 1-group macroscopic cross sections for Ex. I-1.

Output Identifier	Description
coolant_mic_el_23Na	coolant-only, ^{23}Na elastic scattering (mt=2)
cladding_mic_el_56Fe	cladding-only, ^{56}Fe elastic scattering (mt=2)
fuel_mic_inel_238U	fuel-only, ^{238}U inelastic scattering (mt=4)
fuel_mic_fis_238U	fuel-only, ^{238}U fission (mt=18)
fuel_mic_fis_239Pu	fuel-only, ^{239}Pu fission (mt=18)
fuel_mic_fis_240Pu	fuel-only, ^{240}Pu fission (mt=18)
fuel_mic_fis_241Pu	fuel-only, ^{241}Pu fission (mt=18)
fuel_mic_fis_242Pu	fuel-only, ^{242}Pu fission (mt=18)
fuel_mic_n_gam_238U	fuel-only, ^{238}U n,γ (mt=102)
fuel_mic_n_gam_239Pu	fuel-only, ^{239}Pu n,γ (mt=102)
fuel_mic_n_gam_240Pu	fuel-only, ^{240}Pu n,γ (mt=102)
fuel_mic_n_gam_241Pu	fuel-only, ^{241}Pu n,γ (mt=102)
fuel_mic_n_gam_242Pu	fuel-only, ^{242}Pu n,γ (mt=102)
fuel_mac_fis	fuel-only, macroscopic fission cross section
fuel_mac_abs	fuel-only, macroscopic absorption cross section

2.2   Exercise I-2: Fuel assembly

The investigation of two-dimensional fuel assemblies is especially important because they are often used for the generation of lattice physics parameters for full core simulations. It is furthermore possible to propagate the obtained lattice physics parameter uncertainties to output uncertainties of full core calculations (Exercise I-4).

The two-dimensional fuel assemblies (Figure 2.2) contain 271 fuel pin cells that are enclosed in a duct composed of structural material. Periodic boundary conditions are applied.

(a) MET1000   (b) MOX3600
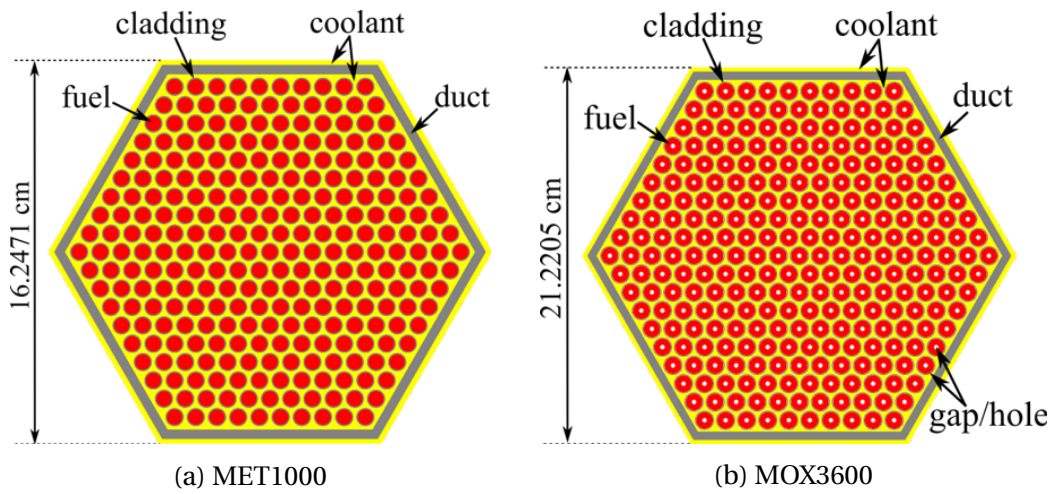
Figure 2.2 – Fuel assembly models.

Output quantities of interest are the uncertainties of the eigenvalue, the Doppler constant K_D and the sodium void coefficient $\Delta\rho_{Na}$. For the Doppler constant, the fuel temperature is doubled; for the sodium void worth, all sodium is removed from the model:

$$\text{Doppler constant:} \qquad K_D = \frac{\frac{1}{k_{nom}} - \frac{1}{k_{mod}}}{\ln\left(\frac{T_{mod}}{T_{nom}}\right)} \qquad (2.1)$$

$$\text{Na-void worth:} \qquad \Delta\rho_{Na} = \frac{1}{k_{nom}} - \frac{1}{k_{mod}} \qquad (2.2)$$

where *nom* is nominal, and *mod* is modified.

Furthermore, the uncertainties of the following homogenized macroscopic 4-group cross sections (see energy group structure in Table 2.2) are requested: total cross section Σ_{tot}, absorption cross section Σ_{abs}, nubar-fission $\bar{\nu}\Sigma_{\text{fis}}$, and total scattering cross section Σ_s (i.e. the total scattering from an individual energy group to all other groups).

Table 2.2 – The 4-group structure for Exercise I-2 and I-3.

Group	Upper energy
1	20 MeV
2	820 keV
3	110 keV
4	15 keV

2.3   Exercise I-3: Super-cell

In addition to the analysis of the fuel assemblies in Exercise I-2, uncertainties due to the nuclear data and the influence of the calculation methods are investigated for two-dimensional so-called supercells. For the generation of lattice physics parameters for non-multiplying assemblies, exemplary models are created in which the assembly of interest is surrounded by fuel assemblies which provide a representative neutron flux spectrum. Similar to Exercise I-2, it is possible to propagate the obtained lattice physics parameter uncertainties to output uncertainties of full core calculations (Exercise I-4).

The supercells consist of a two-dimensional hexagonal primary control assembly that is surrounded by fuel assemblies. There are two options to model the surrounding fuel assemblies:

- Option A: The fuel assemblies are modeled using flux-volume-homogenized cross sections based on the models described in Exercise I-2 (Figure 2.3). This simplification is considered as appropriate approximation of the fuel assemblies and might lead to a significant reduction of the computational costs.

- Option B: The fuel assemblies are modeled in detail using the specifications described in Exercise I-2 (Figure 2.4).

(a) MET1000   (b) MOX3600
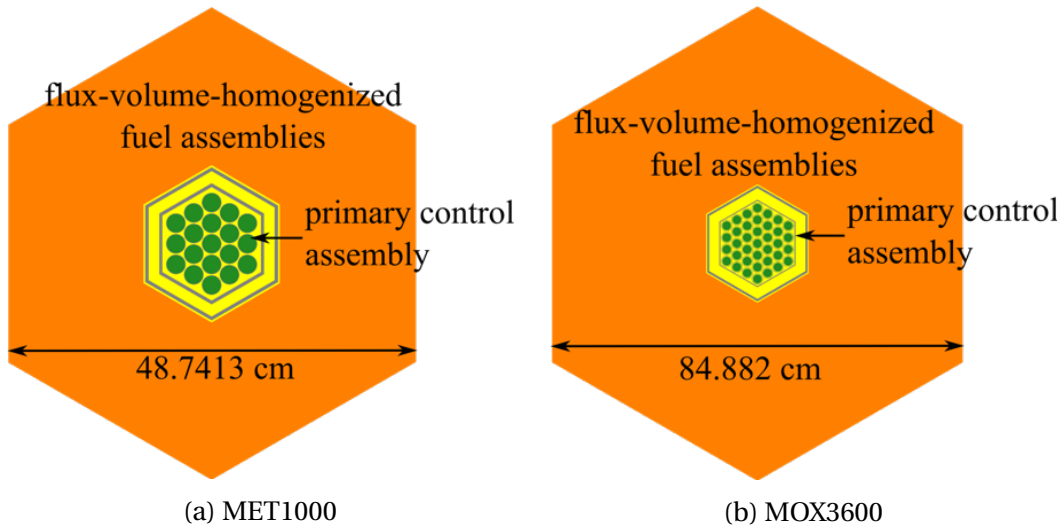
Figure 2.3 – Option A: Super-cell models—flux-volume-homogenized fuel assemblies surrounding a primary control rod assembly

(a) MET1000   (b) MOX3600
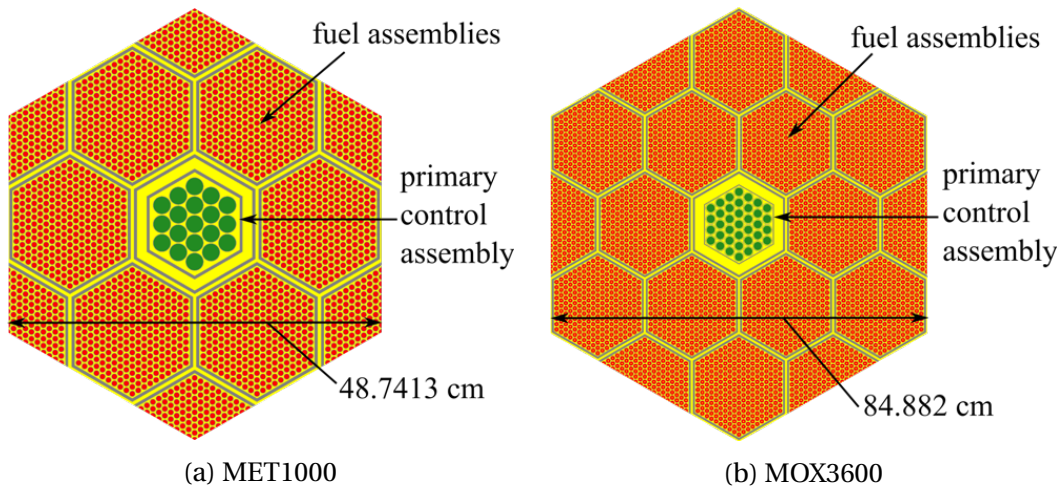
Figure 2.4 – Option B: Super-cell model—detailed fuel assemblies surrounding a primary control rod assembly.

Independent of the modeling of the fuel assemblies, the central control rod assembly is modeled with heterogeneous detail. The control assembly consists of an outer and an interior duct. The absorber rods are included in the interior duct and consist of tubes made of structural material that contain boron carbide pellets. The pitch of the hexagonal supercell is chosen with regard to the actual lattice configuration within the full core and an appropriate fuel-to-absorber ratio. Periodic boundary conditions are applied.

Output quantities of interest are the uncertainties of the eigenvalue, and the control rod worth in the form of the reactivity difference between the nominal model and a model in which the primary control assembly is removed. Furthermore, the uncertainties of the following homogenized macroscopic 4-group cross sections are requested: total cross section Σ_{tot}, absorption cross section Σ_{abs}, and total scattering cross section Σ_s (i.e. the total scattering from an individual energy group to all other groups).

2.4 Exercise I-4: Heterogeneous reactor core

The MET1000 and MOX3600 reactor cores are modeled according to the full core specifications of the UAM SFR benchmark.

The MET1000 core model is based on the reference 1000 MWth Advanced Burner Reactor (ABR) metallic core (Kim et al., 2009). The core consists of 180 drivers, 114 radial reflectors, 66 radial shields, and 19 control assemblies (Figure 2.5). It is divided into an inner and an outer core zone, composed of 78 and 102 driver assemblies, respectively. A primary control system consists of 15 control assemblies containing natural boron. A secondary system contains four control assemblies in the inner core region containing enriched boron. The assembly pitch is 16.2471 cm and the active core height is 85.82 cm.

The MOX3600 core model is a large 3600 MWth oxide core. It consists of 453 fuel, 330 radial reflector and 33 control assemblies (Figure 2.5). The core is divided into an inner and an outer core zones, composed of 225 and 228 fuel assemblies, respectively. A primary control system consists of 24 control assemblies containing natural boron. A secondary system contains 9 control assemblies located in the inner core region containing enriched boron. The assembly pitch is 21.2205 cm and the active core height is 100.56 cm.

For both core models, vacuum boundary conditions are applied. Input uncertainties can either directly be applied to full core models, or they can be propagated from fuel assembly/supercell level in terms of lattice physics parameters.

In addition to the eigenvalue and several reactivity effects as defined in the UAM SFR benchmark specifications, the axially integrated fuel assembly power (radial power distribution; Figure 2.6 and 2.9) and the axial power distribution of one specified

assembly of each of the two cores (MET1000: assembly 6; MOX3600: assembly 133; see Figure 2.7 and 2.10) are of interest.
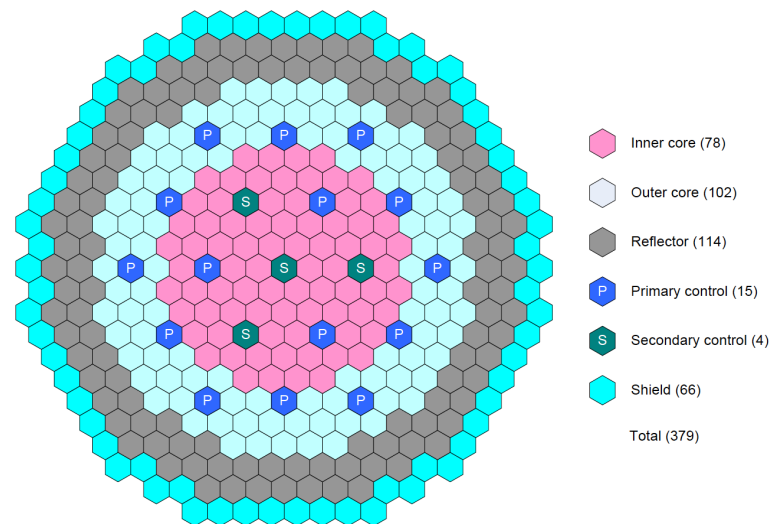
Figure 2.5 – MET1000 full core model (Buiron et al., 2019).
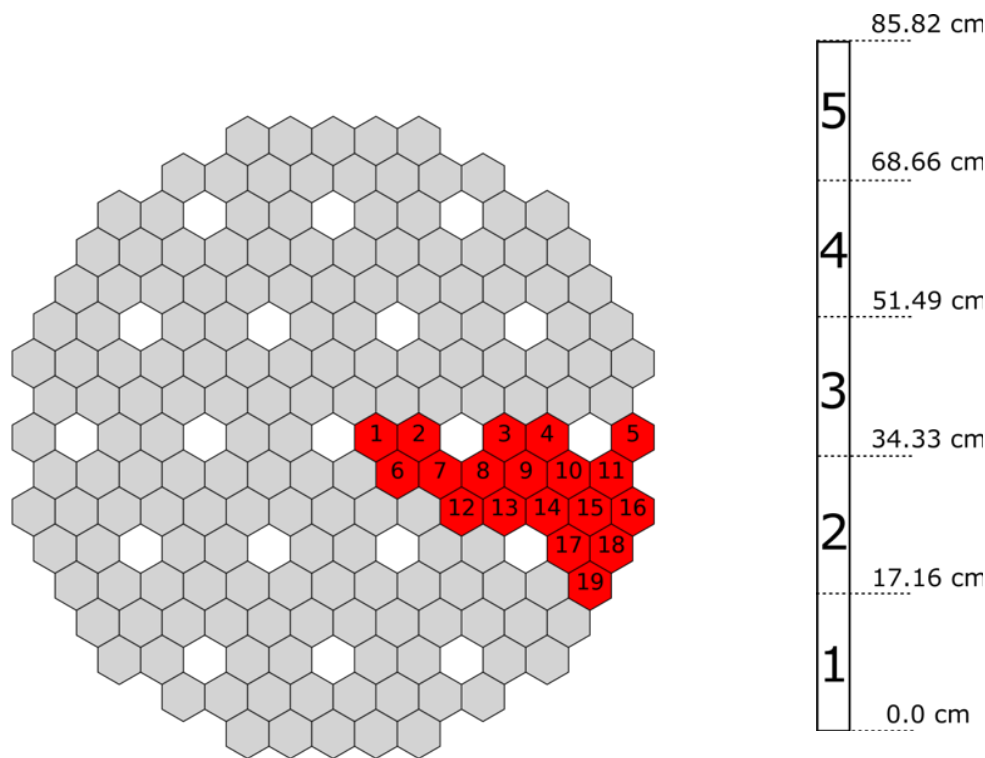
Figure 2.6 – Fuel assembly map of the MET1000 core. Requested axially integrated assembly powers indicated in red.

Figure 2.7 – Axial zones of the active fuel assembly region of the MET1000 core.
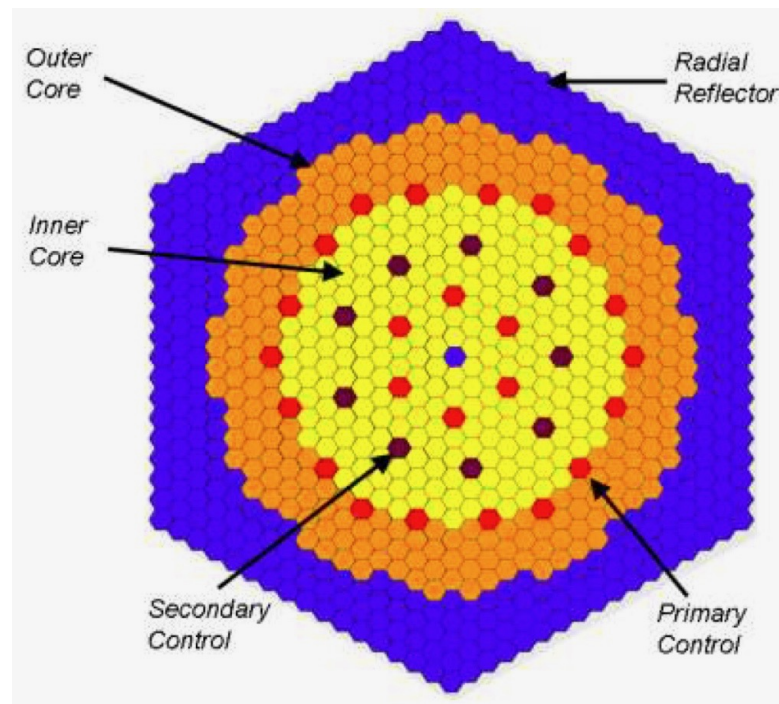
Figure 2.8 – MOX3600 full core model (Buiron et al., 2019).
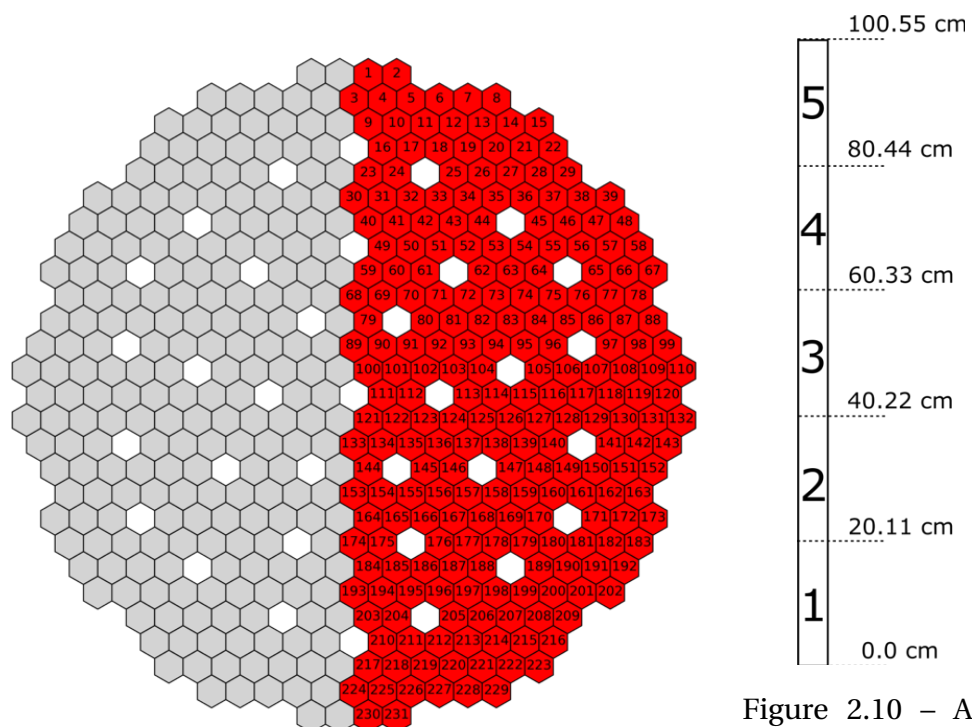
Figure 2.9 – Fuel assembly map of the MOX3600 core. Requested axially integrated assembly powers indicated in red.

Figure 2.10 – Axial zones of the active fuel assembly region of the MOX3600 core.

25

2.5 Validation Exercises

The validation experiments for the sub-exercises were chosen based on a similarity assessment between various experiments with fast neutron spectra from the International Criticality Safety Benchmark Experiment Handbook (ICSBEP handbook) (NEA, 2015a) and the MET1000 and MOX3600 fuel assemblies, respectively. First the experiments and the fuel assemblies were calculated using the TSUNAMI code of SCALE 6.2 to obtain the energy-dependent sensitivities of the eigenvalue to the cross sections. Then TSUNAMI-IP was used to determine the correlation coefficient index c_k between the systems using on SCALE 6.2 covariance data. This index describes an estimate of the correlated uncertainty between systems. Systems with the same materials and similar spectra are correlated, while systems with different materials or spectra are not correlated. (Broadhead, 2004)

Table 2.3 – Correlation factor c_k between the experiment and the MET1000 and MOX3600 fuel assemblies, respectively, determined with TSUNAMI-IP.

ICSBEP Experiment	MET1000	MOX3600
MIX-COMP-FAST-001-001[*]	0.8269	0.9117
MIX-COMP-FAST-002-001	0.8264	0.9124
MIX-COMP-FAST-003-001	0.8421	0.9197
MIX-COMP-FAST-003-002	0.8550	0.9352
MIX-COMP-FAST-004-001	0.6438	0.7346
MIX-COMP-FAST-005-001	0.8849	0.9546
MIX-COMP-FAST-006-001[†]	0.8143	0.8882

[*] IRPhEP handbook acronym: ZPR-LMFR-EXP-001 (ZPR-6 Assembly 7).

[†] IRPhEP handbook acronym: ZPPR-LMFR-EXP-011 (ZPPR-2).

The TSUNAMI-IP calculations resulted in significant correlation factors (see Table 2.3) only for the mixed (Pu,U)-oxide fuel compound systems with fast neutron spectrum (MIX-COMP-FAST). Based on this assessment and under the consideration of the expected modeling effort after studying the MIX-COMP-FAST benchmark specifications, the ZPR-6 Assembly 7 (MIX-COMP-FAST-001-001) and the ZPPR-2 experiment (MIX-COMP-FAST-006-001) were chosen as validation exercises in this benchmark. While the criticality part of these experiment is included in the ICSBEP handbook, additional

investigations for both experiments are included in the International Handbook of Evaluated Reactor Physics Benchmark Experiments (IRPhEP handbook) (NEA, 2015b).

2.5.1 ZPR-6 Assembly 7

The first validation exercise is the ZPR-6 Assembly 7, a fast reactor core with mixed (Pu,U)-oxide fuel and sodium with a thick depleted-uranium reflector. The experiment was performed at the ZPR-6 fast critical facility at Argonne National Laboratory in the 1970s.

The ZPR-6 facility was a horizontal split-table type machine consisting of a large cast-steel bed supporting two tables, one stationary and the other movable, with a width of 3.7 m and a length of 2.4 m (Figure 2.11). For operation, the movable table was driven against the stationary table; otherwise the tables were separated. Stainless steel square tubes, 1 mm thick, 55 mm on a side and 1.2 m long, were stacked horizontally on both tables to form a square 45x45 matrix. The matrix was loaded with drawers containing rectangular plates of different materials such as various uranium compositions, stainless steel, or sodium (Figure 2.12a). The matrix tubes were supported by massive cast-iron structures and cooled by a provided flow path for cooling air. Control rods could be horizontally inserted through holes in a steel back plate.

A description of this experiment including the detailed specifications is given in the IRPhEP handbook under the acronym ZPR-LMFR-EXP-001. The parameters for which the nominal value and the corresponding uncertainty caused by uncertainties of the nuclear data are analyzed are the multiplication factor and the sodium void worth for loading 46.

Specifications for a heterogeneous as-built model for the criticality calculation as well as a simplified model are available. Although the benchmark multiplication factors of the simplified and the detailed model show large differences, the impact of the simplification on the multiplication factor uncertainty caused by nuclear data is expected to be small. Therefore calculations based on the simplified model are still expected to result in qualitatively the same results as for the detailed model.

For the calculation of the sodium void worth, the experiment can be modeled in full detail or one-dimensional cell definitions can be applied for the generation of cross

sections for the individual areas in the core as specified in the IRPhEP benchmark description.

2.5.2   ZPPR-2

The second validation exercise is the ZPPR Assembly 2, an assembly with mixed (Pu,U)-oxide fuel and sodium reflected by depleted uranium, sodium, and steel. The experiment was performed at Argonne National Laboratory in the 1970s.

Similar to the ZPR-6 facility, the ZPPR-2 experiment was a horizontal split-table type machine with a matrix of 53x55 steel tubes (Figure 2.12b). The core length in each half of the matrix was 0.457 m, the axial blanket thickness 0.406 m, and the radial blanket thickness 0.356 m; the minimum reflector thickness was 0.102 m. The core area consisted of drawers (Figure 2.12a) containing Pu-U-Mo plates. The axial and radial blanket area was loaded with drawers containing depleted U_3O_8, iron oxide, sodium, and Pu-U-Mo alloy plates. The radial reflector consisted of steel blocks, and the axial reflector of steel and sodium plates.

A description of this experiment including the detailed specifications has recently been added to the IRPhEP handbook under the acronym ZPPR-LMFR-EXP-011. The multiplication factor for case 1 and the sodium void worth for case 9 is compared.

For the criticality calculation, the handbook specifications provide the description of a detailed as-built model and a simplified RZ model. However, the sodium void worth calculation has to be performed with the detailed as-built model.
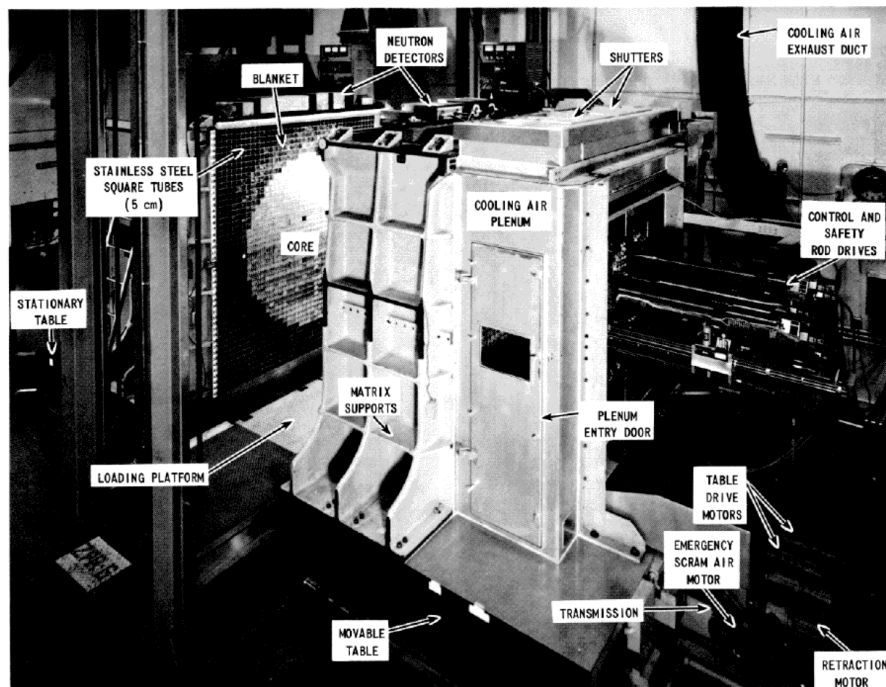
Figure 2.11 – Photo of the ZPR-6 Facility (NEA, 2015a).
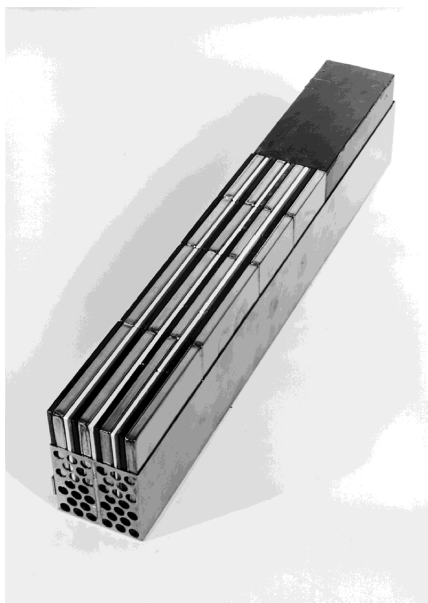
(a) Typical ZPR or ZPPR drawer (NEA, 2015b).

(b) Manual Loading of the ZPPR Matrix (NEA, 2015b).

3 SCALE/AMPX multigroup libraries for SFR systems

The systematic uncertainty and sensitivity analyses of the SFR systems shall be performed with modules of the SCALE code system. SCALE's neutron transport codes apply multigroup (MG) cross sections; only KENO can also be used with continuous-energy (CE) cross sections.

The MG libraries provided with SCALE have been optimized for thermal systems. The energy group structure in the thermal and intermediate energy range is fine, while the structure in the high energy range is rather coarse. The weighting spectrum for the available libraries is furthermore the neutron flux spectrum of a LWR pin cell. In case of fast spectrum systems, there are resonances in the high energy range caused by, for example, structural materials that need to be appropriately captured. Furthermore, an appropriate weighting spectrum is required. To allow analyses of fast systems with SCALE, the first step is the generation of new MG libraries that are optimized for fast spectrum systems.

Several SCALE MG libraries with different energy group structures and weighting spectra were generated using the AMPX code system (Wiarda et al., 2016) of SCALE 6.2.3. For the library with the best agreement when compared to reference calculations and with a reasonable runtime for criticality calculations, a covariance library for uncertainty and sensitivity analyses was created. Additionally, a covariance library with only a few energy groups was sought in order to allow the determination of sensitivity indices when performing uncertainty analyses based on the random-sampling approach.

The studies performed in this chapter have been published as journal paper (Bostelmann et al., 2019).

3.1 Multigroup cross section libraries

This sections covers an overview of the procedure of the MG library generation, a description of the models and tools for the library performance assessment, and finally the results of the criticality calculations, few-group cross section generation and full core assembly power calculations.

3.1.1 Generation of multigroup cross section libraries

The generation of a MG library was performed in several steps with multiple AMPX modules as presented in Figure 3.1. Only a brief summary is given here; a detailed description is provided in the AMPX documentation (Wiarda et al., 2016). For each available nuclide, the following steps were performed:

- POLIDENT was used to generate CE cross sections at 0 K and to process resonance parameters if available. TGEL was then used to reconstruct the total cross sections from the partial ones.

- BROADEN takes the CE data from POLIDENT and Doppler-broadens the cross sections to the user-defined temperature set. The module TGEL was used to reconstruct the total cross section from the partial reactions after broadening.

- Y12 was used to generate the two-dimensional kinematics data for neutron scattering.

- Using the generated CE data, kinematics data, and a user-defined weighting spectrum, module X10 was used to generate the neutron one-dimensional cross section data and the neutron scattering matrices.

- Y12 was then used to generate thermal scattering matrices for free gas scattering.

- Resonance treatment in the unresolved resonance region (URR) with one of two options:

    (a) Either the PURM module was used to generate probability tables for the URR, or

    (b) the PRUDE module was executed to calculate the temperature and background-dependent cross section data in the URR based on narrow resonance (NR) approximations.

- Bondarenko factors were generated with FABULOUS using the broadened one-dimensional CE cross sections and the one-dimensional MG cross sections. If probability tables were used, FABULOUS_URR was applied instead.

- The module SIMONIZE combines the processed MG data into one library. This includes recalculating all redundant cross sections and renormalizing scattering matrices as necessary.

As indicated above, cross section data for selected temperatures and background cross sections in the URR can be generated based on the resonance treatment with either PURM or PRUDE. The MG libraries released with SCALE 6.2 were generated based on probability tables from PURM. However, it should be noted that the generation of probability tables for the unresolved resonance range with AMPX has recently been updated (Kim et al., 2019). The SCALE MG and CE ENDF/B-VII.1 libraries that were shipped with SCALE 6.2 were recently updated accordingly. The new libraries will be released with SCALE 6.3 and were used for the calculations performed in this thesis.

At the beginning of this study, MG libraries were generated using PURM and FABULOUS. However, in the course of time, the MG libraries were mainly generated using probability tables and FABULOUS_URR in order to be more consistent with the CE libraries and with the official (updated) SCALE libraries. The latter libraries were generated based on the updated probability tables generated for the updated CE SCALE libraries.

After the above procedure was executed for all available nuclides, module AJAX was used to bind all individual libraries together. The final MG library was tested by running simple SCALE input files that were automatically created with AMPX to assure the accessibility of all nuclides.

The libraries generated for this study are based on ENDF/B-VII.1 data (Chadwick et al., 2011). To assess the impact of the weighting spectrum, the libraries were generated with two different weighting spectra (Figure 1.3): Either the pointwise neutron flux of the homogenized MET1000 fuel assembly or the pointwise neutron flux of the homogenized MOX3600 fuel assembly (see Chapter 2) was chosen. The pointwise neutron flux was thereby generated with the SCALE modules CENTRM and BONAMI. For the generation of the first MG libraries, energy group structures were adopted from ANL's MC^2-3 code (Lee and Yang, 2012). From MC^2-3's various libraries with group structures optimized for fast spectrum systems, the 230, 425, and 2082-group
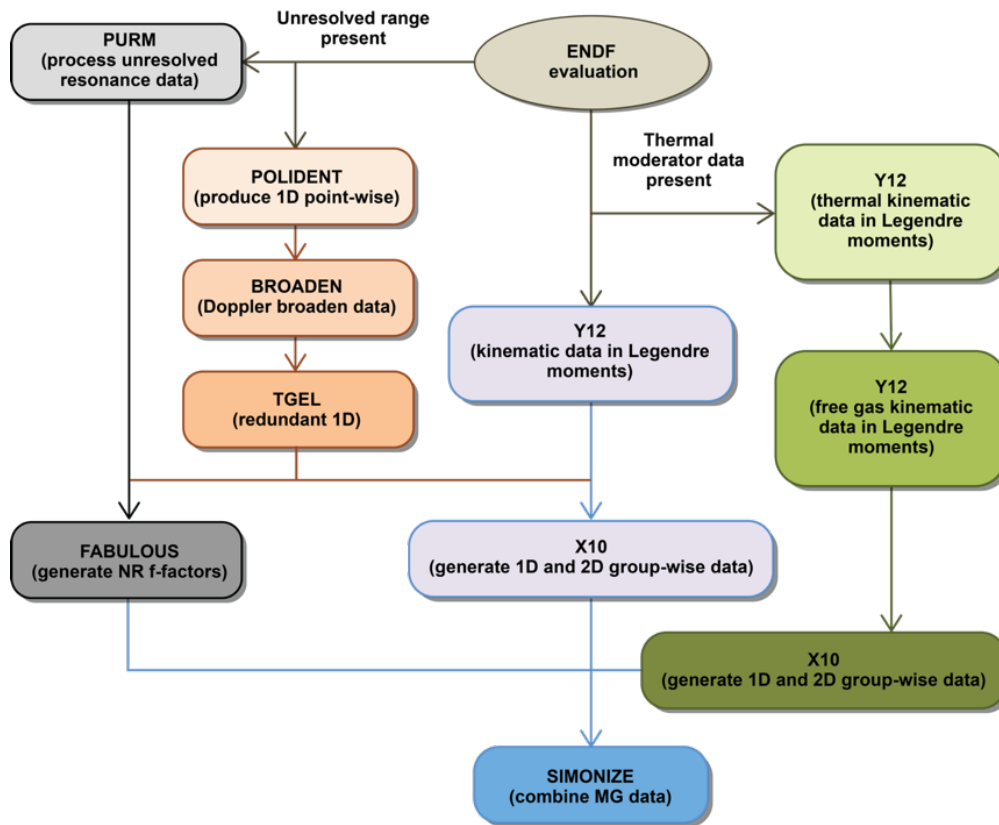
Figure 3.1 – AMPX flowchart for the generation of MG library for one nuclide (Wiarda et al., 2016).

structures were used here. The finest 2082-group structure is an equal-lethargy group structure within the energy range of 0.414 eV to 14.191 MeV. The other group structures are subsets of this structure. To find a library that provides reasonable results with a minimal number of groups to minimize computation time, combinations of MC^2-3's group structures were tested (Table 3.1). In particular, boundaries of the 425-group structure were gradually added to the 230-group structure to include a finer resolution of occurring resonances (245-, 253-, 271- and 302-group structures). For example, the 302-group structure corresponds to the 425-group structure between $1.9305 \cdot 10^4$ and $5.5023 \cdot 10^5$ eV. The choice of additional group boundaries was thereby based on neutron flux comparisons between MG and CE calculations. Figure 3.2 presents the MOX3600 weighting spectrum collapsed into the 2082-, 302- and 230-group structure, that demonstrates the finer energy group structure across the fast energy region compared to the LWR library.
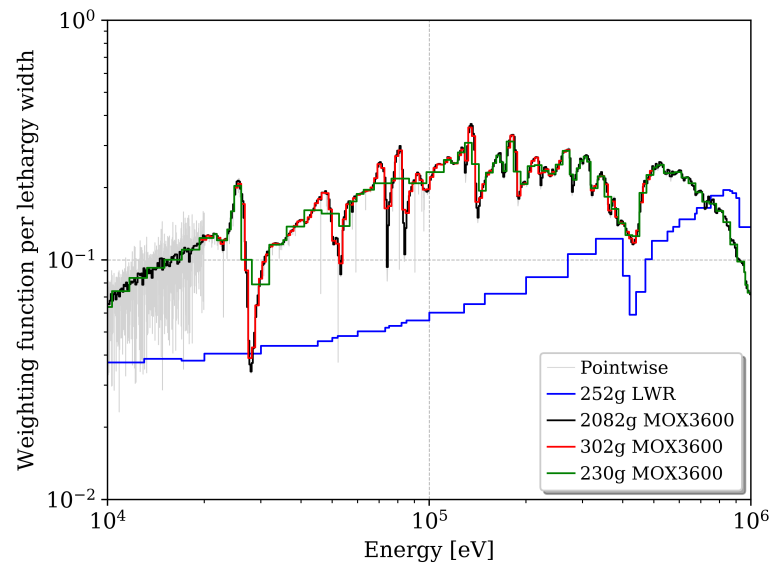
Figure 3.2 – Weighting spectra collapsed into multigroup structures; energy range in which group boundaries of the 425-group structure are added to the 230-group structure to obtain the 302-group library.

3.1.2   Models and tools for library performance assessment

The models applied in the cross section library performance assessment are the SFR pin cells, fuel assemblies, and full core models as described in Chapter 2. Additionally, volume-homogenized mixtures of both the MET1000 and MOX3600 fuel assembly were determined to allow models that only contain a single mixture, excluding any geometrical effect on the results.

The new MG libraries were tested in criticality calculations using the three-dimensional Monte Carlo code KENO-VI (KENO-MG) of SCALE 6.2.3 (Rearden and Jessee, 2016).

Table 3.1 – Overview of generated MG cross section libraries.

Number of groups	Weighting Spectrum
230	MET1000, MOX3600
245	MOX3600
253	MOX3600
271	MOX3600
302	MET1000, MOX3600
425	MET1000, MOX3600
2082	MET1000, MOX3600

Prior to their application in the transport calculation, MG cross sections must be corrected for self-shielding effects. In SCALE, the self-shielding is performed by the modules BONAMI, CENTRM and PMC. BONAMI calculates self-shielded cross sections for all energy groups and nuclides based on the Bondarenko approach. CENTRM computes pointwise neutron spectra up to an energy of 20 keV by solving the Boltzmann transport equation. For the volume-homogenized mixture model, CENTRM calculated a homogenous infinite media; for the pin cells, fuel assemblies and full cores, the pin cell model was specified for CENTRM's transport calculation. PCM then uses the pointwise flux spectrum from CENTRM to calculate the MG cross sections and scattering matrices, which then replace the previous values obtained from BONAMI up to 20 keV. SCALE's CSAS6 sequence allowed the automatic execution of the generation of problem-dependent cross sections with BONAMI, CENTRM and PCM, and their application with KENO-VI.

The analysis of the various SFR models covers the eigenvalue, the neutron flux, and several reaction rates. Reference solutions for all criticality calculations are the results obtained from KENO-VI using CE cross sections (KENO-CE). In addition to the results with the new MG libraries, results obtained with the SCALE 252g LWR library are added in some comparisons to stress the need of new MG libraries for SFR systems and to clearly show the great improvement with the new libraries.

To assess the library performance for the generation of nodal data, the two-dimensional deterministic transport code NEWT was used to generate homogenized macroscopic 24-group cross sections based on the fuel assembly models. The 24-group structure was taken from Nikitin (Nikitin, 2019). However, the individual boundaries were slightly adjusted to match the boundaries of the generated MG cross section libraries (Table A.7 in the Appendix). As reference for comparison, 24-group cross sections were obtained using the three-dimensional CE Monte Carlo code Serpent 2.1.30 (Leppänen et al., 2014). It was decided to use a 24-group structure for this study instead of the 4-group structure as specified in the UAM SFR benchmark in order to be able to compare a larger number of energy groups in the fast energy range which allows to clearly distinguish energy groups in which larger differences occur, and in order to be consistent with the energy group structure that is used for macroscopic cross section generation for full core calculations with PARCS in Chapter 6.

3.1.3 Criticality calculation results

Eigenvalue differences between criticality calculations are reported as reactivity difference $\Delta\rho$ between the MG eigenvalue k_{MG} and the CE eigenvalue k_{CE}, while the CE result is treated as reference result:

$$\Delta\rho = \frac{1}{k_{\mathrm{CE,ref}}} - \frac{1}{k_{\mathrm{MG}}} \,. \tag{3.1}$$

The results in this section are based on MG libraries that include URR data based on probability tables. Only for the homogenized fuel assemblies, an assessment of the impact of the resonance treatment in the URR during the library generation was performed.

Criticality calculations of homogenized fuel assemblies

Table 3.2 presents the differences of the multiplication factors obtained with KENO using various MG libraries and the reference KENO-CE solution for the homogenized fuel assemblies. These MG libraries thereby include URR data based on probability tables. The 252-group SCALE library shows a significant disagreement in the multiplication factor. This disagreement can also be observed when comparing the corresponding flux distribution in Figure 3.3. These results emphasize the need for an additional SCALE library optimized for fast neutron spectra.

The 230-, 302-, 425-, and 2,082-group libraries were generated with both the MET1000 and MOX3600 weighting spectra and therefore allowed for the assessment of the impact of the weighting spectrum. The finer the energy group structure, the smaller is the impact of the weighting spectrum. The largest impact of the weighting spectrum was consequentially found for the 230-group library: For the MOX3600 model, a small influence of about 40 pcm was found. For the MET1000 model, a slightly larger influence of about 100 pcm was observed. This difference decreased to about 60 pcm for the 302- and 425-group calculations.

A bias arising from geometrical approximations was excluded by using volume-homogenized models in this part of the study. KENO calculations performed with the very fine 2082-group libraries were therefore expected to result in the best agreement

Table 3.2 – KENO eigenvalues of homogenized fuel assemblies (1σ statistical errors of Monte Carlo calculations in parentheses).

	MET1000		MOX3600	
Library	k_∞	$\Delta\rho$ [pcm]	k_∞	$\Delta\rho$ [pcm]
CE	1.27539(11)	(ref)	1.14002(11)	(ref)
252g, LWR	1.27047(8)	-304(14)	1.13891(8)	-85(14)
230g, MET1000	1.27865(8)	200(14)	1.14229(8)	174(14)
230g, MOX3600	1.27694(8)	95(14)	1.14174(7)	132(13)
245g, MOX3600	1.27690(7)	93(14)	1.14132(8)	100(14)
253g, MOX3600	1.27613(8)	45(14)	1.14112(8)	84(14)
271g, MOX3600	1.27559(8)	12(14)	1.14085(8)	63(14)
302g, MET1000	1.27659(8)	74(14)	1.14118(7)	89(13)
302g, MOX3600	1.27563(8)	15(14)	1.14093(7)	70(13)
425g, MET1000	1.27654(8)	71(14)	1.14116(7)	88(13)
425g, MOX3600	1.27563(8)	15(14)	1.14086(8)	65(14)
2082g, MET1000	1.27560(8)	13(14)	1.14082(8)	62(14)
2082g, MOX3600	1.27513(8)	-16(14)	1.14061(9)	45(14)

with the corresponding CE reference solution. This was indeed the case for the metallic fuel, for which the deviation was smaller than two statistical standard deviations in the Monte Carlo results. For the oxide fuel case, a small MG bias of around 50 pcm was observed.

The 230-group results show a bias of up to 200 pcm. But when gradually adding energy groups to this library, the deviation from the reference decreased. The 302-group structure seemed to be sufficient to provide reasonable agreement with the reference results regarding the multiplication factor; the finer 425-group structure did not provide a significantly better result. Slightly better results were thereby obtained with the MOX3600 weighting spectrum.

The good agreement with the 302-group MOX3600 library was also observed for the flux spectra. For a meaningful comparison, the KENO-CE results were tallied in 302 groups to match the MG structure of the compared KENO-MG output (Figure 3.4). Figure 3.6 further compares the fission and absorption reaction rates of ^{56}Fe, ^{238}U, ^{239}Pu and ^{241}Pu from the MET1000 model in terms of the reactivity differences (Kim et al., 2019). The significant improvement of the new library compared to the 252-group results is clearly visible. The corresponding MOX3600 results show similar improvement. The peak at about 10^3 eV for ^{56}Fe absorption to 200 pcm is caused by a

sharp resonance that cannot be resolved by a comparably coarse MG library. (It also needs to be noted that the absorption of ^{56}Fe is not as important as the scattering reactions. But the reaction rate differences can at this point only be determined for fission and absorption.)

To gain a better understanding of the cumulative impact of the MG library on important reactions, KENO was used to collapse the problem-dependent cross sections to one-group cross sections. Figure 3.7 compares a selection of cross sections to the corresponding KENO-CE reference values. The significant improvement compared to the 252-group LWR library is clearly visible, in particular for the (n,γ) cross section of ^{238}U that plays an important role in the temperature feedback. The difference of the 302-group calculation to the reference is decreased from about 2.0%/0.4% to less than 0.02%/0.03% for the MET1000/MOX3600 models, respectively. In contrast, the 1-group cross section of elastic scattering on ^{56}Fe did not initially seem to be improved, but this was most likely a result of an error cancellation since the very fine resonance structure of elastic scattering in the high energy ranges cannot be adequately resolved with a comparably coarse MG library. As shown in Figure 3.5, in general the representation of ^{56}Fe elastic scattering was greatly improved with the new group structure.

To understand the impact of the resonance treatment in the URR during the library generation, an additional 302-group library was generated with URR data based on the NR approximations. NEWT calculations with this library were then compared to results with the 302-group library based on probability tables (ptab). Several output quantities as requested for Ex. I-1 in the UAM-SFR benchmark were compared for the homogenized fuel assemblies. Table 3.3 shows eigenvalue differences of about 100 and 60 pcm for the MET1000 and MOX3600 assemblies, respectively, and differences between the 1-group cross sections below 0.65%. The MET1000 ptab library result is thereby closer to the CE reference in terms of the eigenvalue than the NR library result; for the MOX3600, the opposite is the case. Although especially the eigenvalue difference is clearly visible, the differences are considered small enough to play only an insignificant role for uncertainty analyses.
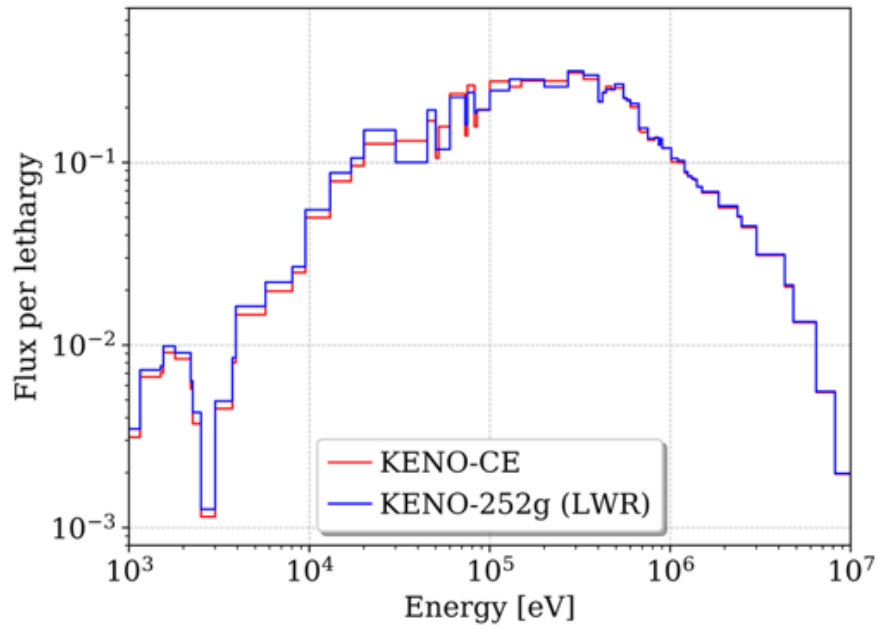
Figure 3.3 – Neutron flux distribution of the homogenized MET1000 fuel assembly in the fast energy range; the KENO-MG calculation was performed with the 252-group LWR library.
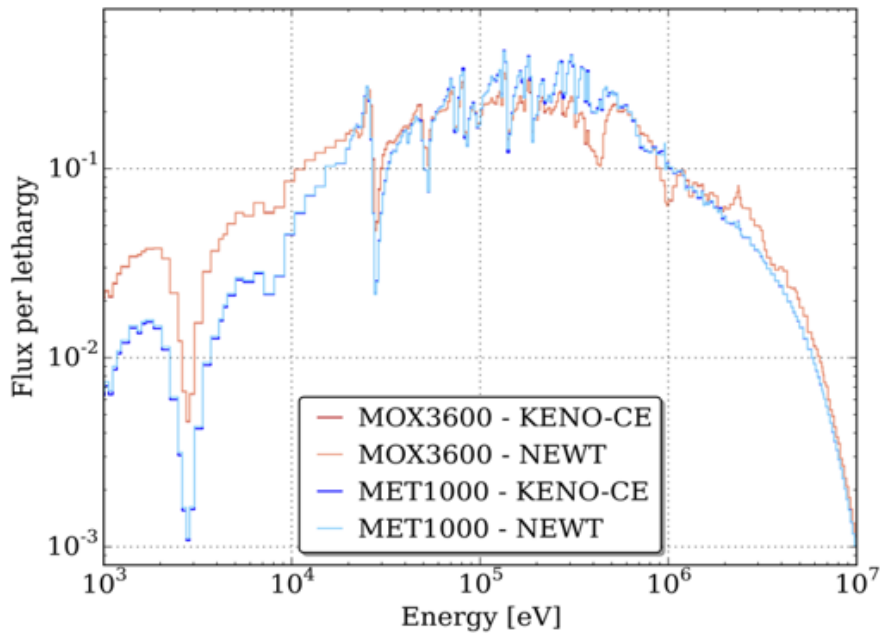
Figure 3.4 – Neutron flux distribution of the homogenized fuel assemblies in the fast energy range; the KENO-MG calculations are performed with the 302-group library using the MOX3600 weighting spectrum.

Table 3.3 – NEWT eigenvalues of homogenized fuel assemblies with the 302-group library based on either probability tables (ptab) or narrow resonance approximations (NR).

Output quantity	MET1000			MOX3600		
	xs302g - ptab	xs302g - NR	Difference	xs302g - ptab	xs302g - NR	Difference
eigenvalue	1.27561	1.27458	-103 pcm	1.14077	1.14015	-62 pcm
mic_el_23Na [b]	4.1312E+00	4.1264E+00	-0.12%	4.8554E+00	4.8519E+00	-0.07%
mic_el_56Fe [b]	3.4074E+00	3.4052E+00	-0.07%	4.0136E+00	4.0122E+00	-0.03%
mic_inel_238U[b]	1.0232E+00	1.0250E+00	0.17%	9.2057E-01	9.2164E-01	0.12%
mic_fis_238U [b]	3.1557E-02	3.1596E-02	0.12%	3.9038E-02	3.9084E-02	0.12%
mic_fis_239Pu [b]	1.6504E+00	1.6502E+00	-0.01%	1.7805E+00	1.7806E+00	0.01%
mic_fis_240Pu [b]	3.2714E-01	3.2892E-01	0.54%	3.4235E-01	3.4452E-01	0.64%
mic_fis_241Pu [b]	2.1954E+00	2.1931E+00	-0.11%	2.5498E+00	2.5490E+00	-0.03%
mic_fis_242Pu [b]	2.3393E-01	2.3422E-01	0.12%	2.4165E-01	2.4193E-01	0.11%
mic_n_gam_238U [b]	2.2781E-01	2.2896E-01	0.50%	2.9468E-01	2.9557E-01	0.30%
mic_n_gam_239Pu [b]	3.3902E-01	3.3784E-01	-0.35%	5.1557E-01	5.1479E-01	-0.15%
mic_n_gam_240Pu [b]	3.9540E-01	3.9360E-01	-0.46%	5.1689E-01	5.1529E-01	-0.31%
mic_n_gam_241Pu [b]	3.4460E-01	3.4359E-01	-0.29%	4.5693E-01	4.5638E-01	-0.12%
mic_n_gam_242Pu [b]	3.2050E-01	3.1977E-01	-0.23%	4.4567E-01	4.4626E-01	0.13%
mac_fis [1/cm]	2.0700E-03	2.0709E-03	0.04%	2.3984E-03	2.3999E-03	0.06%
mac_abs [1/cm]	4.7835E-03	4.7894E-03	0.13%	6.1734E-03	6.1806E-03	0.12%
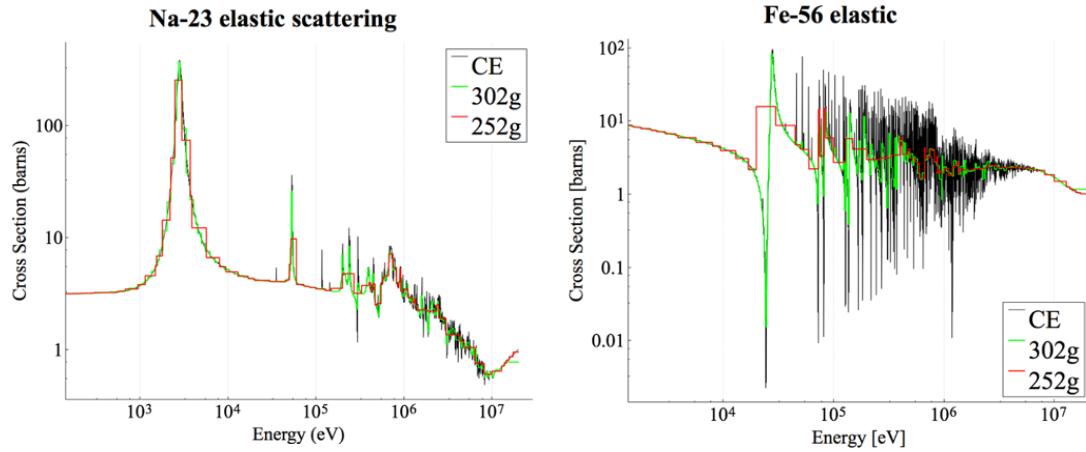
Figure 3.5 – ^{23}Na and ^{56}Fe elastic scattering cross sections compared between the CE and MG libraries.
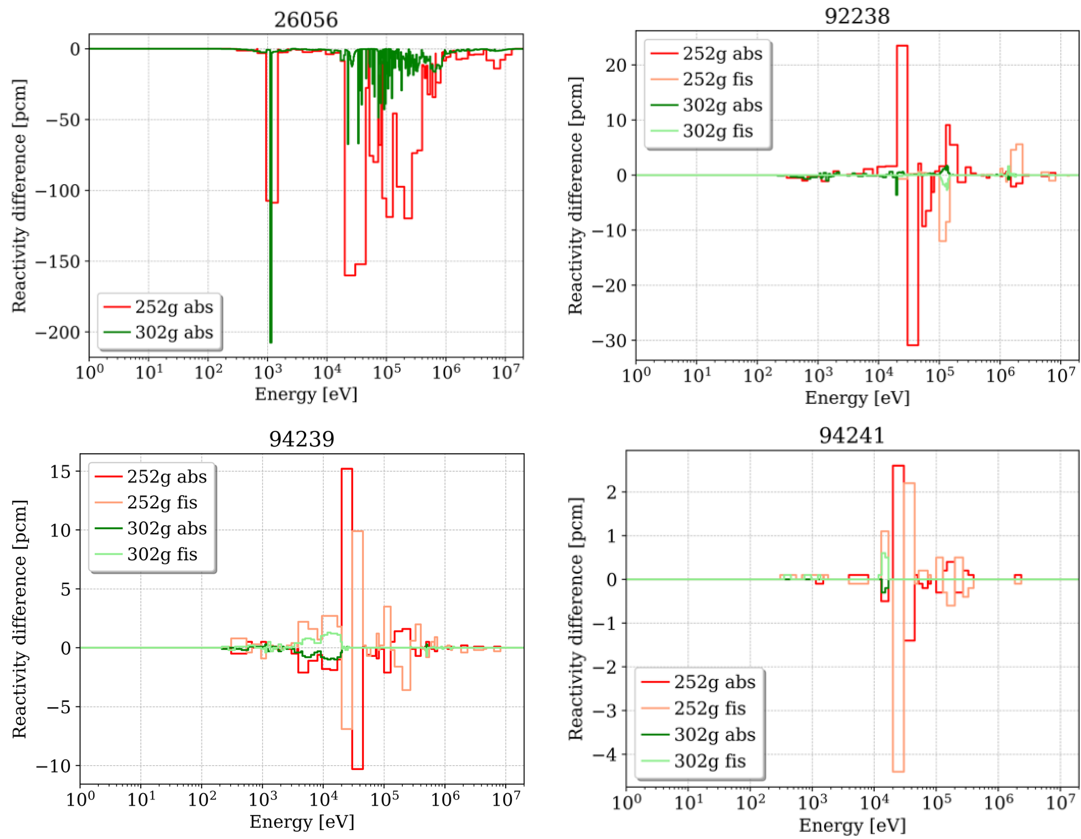
Figure 3.6 – Reaction rate differences in terms of reactivity between the MG calculations and the CE reference for fission (if applicable) and absorption of ^{56}Fe, ^{238}U, ^{239}Pu and ^{241}Pu for the homogenized MET1000 fuel assembly.
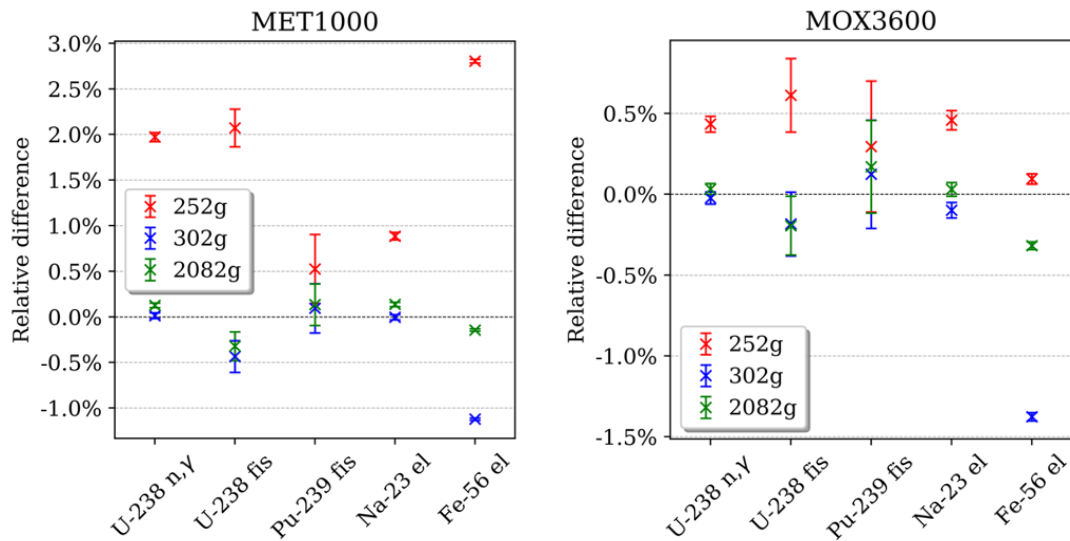
Figure 3.7 – Collapsed one-group cross sections of the homogenized fuel assemblies compared to the CE reference (Note the different y-axis scales).

Criticality calculations of heterogeneous fuel pin cells

The next comparisons were performed on fuel pin cells in an infinite triangular lattice for each of the considered assembly types. As mentioned earlier, unlike the investigation of the homogenized model, the resonance self-shielding calculation with BONAMI and CENTRM was performed on a one-dimensional fuel pin cell. In addition to the radii of the fuel, the gap and the cladding, the lattice pitch corresponding to Figure 2.1, was specified in the input block for this cell and internally converted to an outer cell radius of equal area. For the transport calculation with KENO, the fuel pins were modeled in hexagonal cells as displayed in Figure 2.1.

The multiplication factors of KENO-MG and KENO-CE are compared in Table 3.4. The 2082- and 302-group calculations agree with the CE reference within two statistical standard deviations. The 302-group library is therefore considered to be adequate for the simulation of these models.

Criticality calculations of heterogeneous fuel assemblies

The major difference between the heterogeneous fuel assembly models and the fuel pin cells is the additional duct (mostly iron and chromium) and associate assembly gap around the fuel pins. Since the traditional CENTRM self-shielding calculation in

Table 3.4 – KENO eigenvalues of heterogeneous pin cells (1σ statistical errors of Monte Carlo calculations in parentheses).

	MET1000		MOX3600	
Library	k_∞	$\Delta\rho$ [pcm]	k_∞	$\Delta\rho$ [pcm]
CE	1.35878(13)	(ref)	1.19203(11)	(ref)
252g, LWR	1.35583(8)	160(16)	1.19195(8)	-5(14)
302g, MET1000	1.35945(8)	6(16)	1.19249(8)	32(14)
302g, MOX3600	1.35861(9)	9(16)	1.19216(9)	9(14)
2082g, MET1000	1.35844(9)	18(16)	1.19239(9)	25(14)
2082g, MOX3600	1.35821(8)	31(16)	1.19214(8)	8(14)

SCALE is limited to one-dimensional models with repeating lattice structures, it was not possible to explicitly model this duct in the cell for the self-shielding. The problem-dependent cross sections were therefore determined with the one-dimensional pin cell models, as it was done for the pin cell calculations. Table 3.5 shows the KENO-MG results compared with the reference KENO-CE results.

The eigenvalue calculations using the described self-shielding cell led to a MG bias of up to 250 pcm. It was assumed that the missing influence of the duct and assembly (e.g., especially the additional neutron scattering on iron) had a significant contribution to this bias. Therefore, a second self-shielding cell for only the fuel pins adjacent to the duct was created. For a so-called multiregion cell, the hexagonal fuel pin cell was first translated into a cylindrical cell in which the area for the coolant was retained. A ring of duct material was placed around the ring of coolant. The width of this ring was determined by equally dividing the duct to the 54 adjacent fuel pins. Figure 3.8 shows the cell for the MET1000 pin cells. The shielded cross sections of the duct material were then also used for the duct in the fuel assembly. White boundary conditions were applied to this cell. With this modification, the MG bias for the MET1000 fuel assembly was reduced to 100 pcm, and the 2,082- and 302-group calculations for the MOX3600 fuel assembly were consistent with the reference considering the two sigma statistical standard deviations under consideration.

In addition to the eigenvalue, the Doppler constant K_D and the Na-void worth $\Delta\rho_{Na}$ as defined in Eq. 2.1 and 2.1, respectively, were investigated. To determine the Doppler constant, the fuel temperature of the metallic fuel was doubled. For the oxide fuel, however, the fuel temperature was only raised from 1,500 K to 2,400 K so as not to exceed the highest temperature available in the cross section libraries. To determine
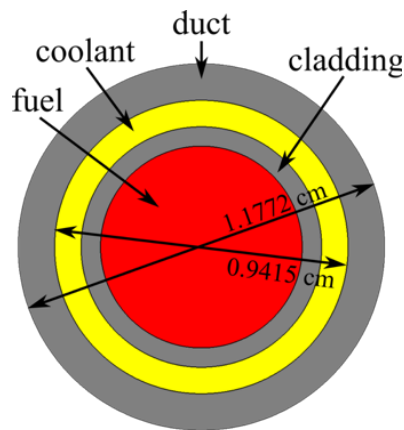
Figure 3.8 – Model for the self-shielding of cross sections in fuel pins adjacent to the duct in the MET1000 fuel assembly.

the sodium void worth, the sodium was completely removed from the models.

The calculated Doppler constants were consistent between the CE and all MG calculations (Table 3.5). For the sodium void worth, a small bias of about 50 pcm in the 2,082-group calculation was observed only for the metallic system; the 302-group calculation resulted in a slightly larger bias of about 100 pcm.

Although the agreement of the eigenvalues, Doppler, and Na-void coefficients was greatly improved by modifying the self-shielding cell, this was only one of several possibilities attempted in order to compensate for a two-dimensional self-shielding cell that accounts for the duct. Considering that the long mean free path in these SFR systems is several centimeters long, another option would be to consider duct material in the self-shielding calculation of all pins instead of only the pins adjacent to the duct. Another opportunity for possible improvement is the determination of Dancoff factors for this geometry with the SCALE module MCDancoff, as Dancoff factors can be provided to CENTRM for the self-shielding calculation using the CENTRM data block. Other CENTRM options for the self-shielding calculation can also be modified, such as the maximum energy until which CENTRM calculates the flux (default is 20 keV), the elastic matrix processing, the Legendre polynomial order of scattering, the order of the angular quadrature and more. It has, however, to be kept in mind that the cancellation of errors played a significant role; the effect of a modification of one parameter might cancel out the effect of other modifications.

Table 3.5 – KENO eigenvalues of heterogeneous fuel assemblies (1σ statistical errors of Monte Carlo calculations in parentheses).

Library	Cell: Fuel pin cell				Cell: Fuel pin cell and duct cell			
	MET1000		MOX3600		MET1000		MOX3600	
	k_∞	$\Delta\rho$ [pcm]	k_∞	$\Delta\rho$ [pcm]	k_∞	$\Delta\rho$ [pcm]	k_∞	$\Delta\rho$ [pcm]
CE	1.27982(12)	(ref)	1.14677(11)	(ref)	1.27982(12)	(ref)	1.14677(11)	(ref)
252g, LWR	1.28104(9)	74(15)	1.14981(8)	231(14)	1.27263(8)	-441(15)	1.1444(8)	-181(14)
302g, MET1000	1.28387(9)	246(15)	1.15051(8)	284(14)	1.27937(8)	-28(15)	1.14665(8)	-9(14)
302g, MOX3600	1.28296(8)	191(15)	1.15019(8)	259(14)	1.27838(8)	-88(15)	1.14641(8)	-27(14)
2082g, MET1000	1.28282(8)	183(15)	1.15010(7)	252(14)	1.27854(9)	-78(15)	1.14648(8)	-22(14)
2082g, MOX3600	1.28181(8)	122(15)	1.14901(9)	170(14)	1.27818(8)	-100(15)	1.1463(8)	-36(14)

Table 3.6 – KENO Doppler constant and Na-void worth of heterogeneous fuel assemblies (1σ statistical errors of Monte Carlo calculations in parentheses).

Library	Doppler constant K_D				Na-void worth $\Delta\rho_{Na}$			
	MET1000		MOX3600		MET1000		MOX3600	
	K_D [pcm]	ΔK_D [pcm]	K_D [pcm]	ΔK_D [pcm]	$\Delta\rho_{Na}$ [pcm]	$\Delta(\Delta\rho_{Na})$ [pcm]	$\Delta\rho_{Na}$ [pcm]	$\Delta(\Delta\rho_{Na})$ [pcm]
CE	-323(25)	(ref)	-804(34)	(ref)	5,917(17)	(ref)	2,923(16)	(ref)
252g, LWR	-348(16)	-25(30)	-776(23)	29(40)	5,687(12)	-230(21)	2,940(11)	17(20)
302g, MET1000	-339(16)	-15(30)	-765(23)	39(40)	5,800(11)	-117(20)	2,938(11)	15(19)
302g, MOX3600	-318(16)	5(29)	-800(22)	4(40)	5,823(12)	-94(21)	2,946(12)	23(20)
2082g, MET1000	-318(16)	6(29)	-785(24)	20(41)	5,865(12)	-52(20)	2,949(11)	26(19)
2082g, MOX3600	-307(17)	16(30)	-778(23)	26(41)	5,862(12)	-55(20)	2,954(12)	31(20)

Computation time

The generated library is intended to be eventually used for uncertainty and sensitivity analyses. For analyses based on random sampling, the transport calculation needs to be repeated many times with perturbed input parameters. Hence, during the generation of a new library, the computation time for an individual calculation, scaling with the number of energy groups in the library, plays a significant role.

The computation times were significantly biased by the current traffic on the computing cluster. In a rough comparison between the various fuel assembly calculations with KENO, it was observed that the 252-, 230-, and 302-group calculations all took about the same time. The 425-group calculations took only slightly more time, and the 2,082-group calculations took more time by a factor of 1.5-2. The differences were larger in NEWT calculations, with the 2,082-group calculations lasting up to 18 times longer than the 302-group calculations (Table 3.7). Furthermore the 2,082-group library uses a lot of memory which can even limit the calculation to a smaller number of used mixtures. Conducting uncertainty analyses based on random sampling with the 2082-group libraries is not considered practical.

After considering the computation time and observing sufficiently good agreement of the results for the metallic and oxide fuel assemblies, it was decided to move forward with the 302-group library with the MOX3600 neutron flux as weighting spectrum. The group structure is provided in Table A.6 in the Appendix.

Table 3.7 – Computation time of the MET1000 fuel assembly with NEWT.

MG library	Time [minutes]
252, LWR	13.4
230, MOX3600	16.4
302, MOX3600	18.6
2082, MOX3600	324.6

3.1.4 Homogenized macroscopic few-group cross sections

The applicability of the 302-group library for the generation of homogenized macroscopic few-group cross sections was tested by comparing 24-group cross sections generated with NEWT and Serpent for the heterogeneous fuel assemblies. The product of the neutron multiplicity and the fission cross section $\bar{\nu}\Sigma_{\text{fis}}$, the reduced absorption

cross section $\Sigma_{abs,red}$ (absorption cross section less the production in (n,xn) reactions), the transport cross section Σ_{tr}, and inverse velocity $1/v$, the fission spectrum χ and the scattering matrix were compared because these quantities are used in the files provided to e.g. the nodal code PARCS. To provide some information about the range of absolute values, the cross sections and the scattering matrix of the MET1000 fuel assembly are displayed in Figure 3.9 and 3.12.

Figure 3.9 – MET1000 fuel assembly: Macroscopic 24-group cross sections generated with NEWT using the 302g library.
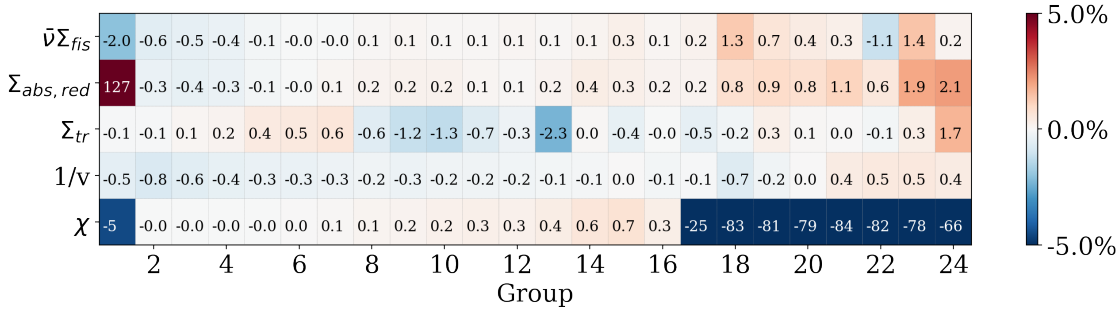
Figure 3.10 – MET1000 fuel assembly: Relative difference of the macroscopic 24-group cross sections between NEWT using the 302g library and Serpent.
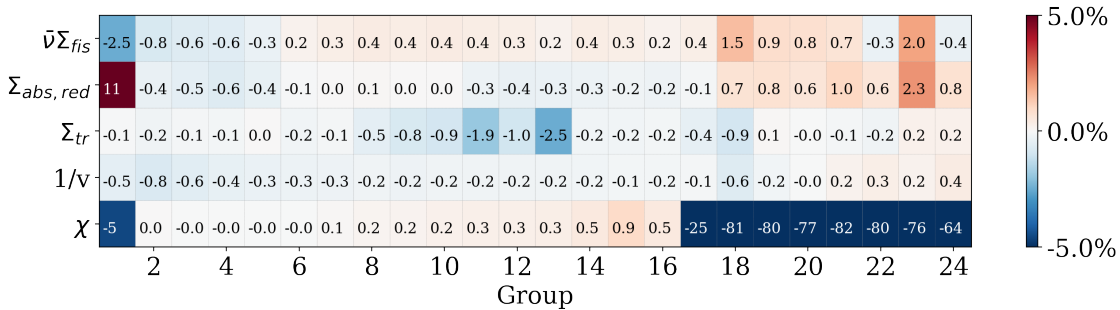
Figure 3.11 – MOX3600 fuel assembly: Relative difference of the macroscopic 24-group cross sections between NEWT using the 302g library and Serpent.

Serpent was run using 10^6 neutrons per generation in 3,500 active and 200 inactive generations to allow sufficient convergence of the macroscopic cross sections. For both assembly types, the relative 1σ statistical errors of $\bar{\nu}\Sigma_{\text{fis}}$, $\Sigma_{\text{abs,red}}$, Σ_{tr} and $1/v$ were less than 0.06% in all energy groups except for the fastest group and the most thermal group, for which errors up to 2.5% were obtained. Because of very small values for χ in the fastest group and in groups 17-24, the statistical error in these groups is large with up to 70% compared to less than 0.1% in the other groups. The statistical errors of the individual records in the scattering matrix were less than 0.07% for the diagonal elements except for the most thermal group for which slightly larger errors were obtained. The statistical error of the off-diagonal elements is increasing with their distance to the diagonal axis. For the most thermal sink groups, large statistical errors of up to 70% were obtained because of only few neutrons in these groups.
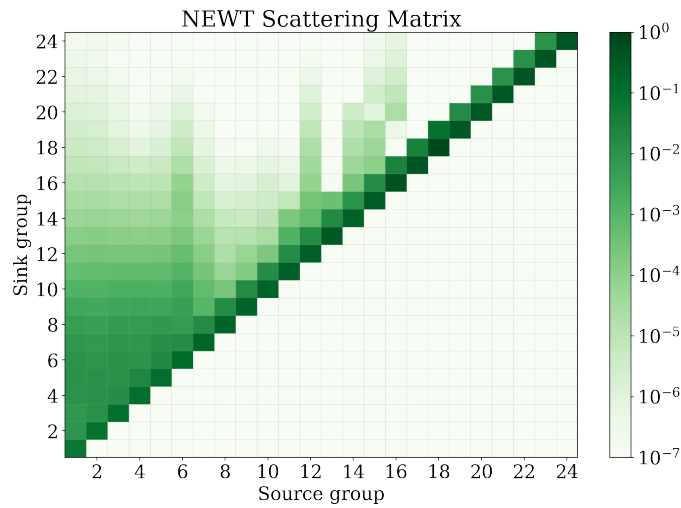
Figure 3.12 – MET1000 fuel assembly: 24-group scattering matrix generated with NEWT using the 302g library.

For completeness, it is mentioned that the eigenvalues of the KENO-CE and Serpent calculations were consistent for the MOX3600 fuel assembly. For the MET1000 fuel assembly, a small difference of about 60 pcm was observed. The NEWT 302-group calculations agree within 70 pcm with the corresponding KENO-VI calculations listed in Table 3.5; this is considered very good agreement considering the spatial discretization and convergence settings in NEWT.

In contrast to the results of the criticality calculations, the comparisons of the 24-group cross sections do not seem to be sensitive with respect to the MG library. The calculations with the 252-group SCALE library and the new 302-group library led

to similar differences with the Serpent results. Therefore, only the comparisons based on the 302-group calculations are presented in Figures 3.10, 3.11 and 3.13. Cross section differences of less than 2.5% were obtained in the groups that are well converged with Serpent. Also the scattering matrices show good agreement between Serpent and SCALE with less than 2.2% for all diagonal elements. For cross sections and scattering groups with larger statistical error in Serpent, corresponding larger differences between Serpent and SCALE were obtained.

(a) MET1000

(b) MOX3600
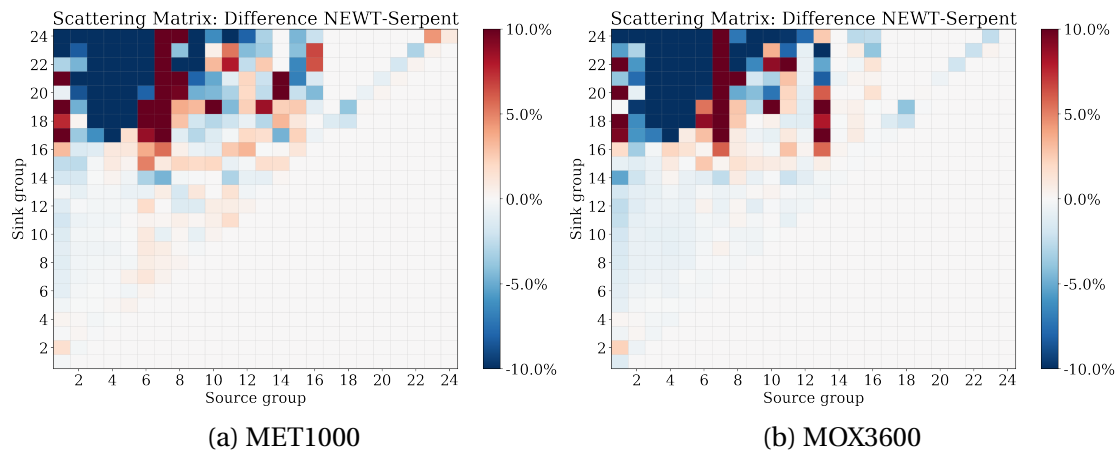
Figure 3.13 – Relative difference of the 24-group scattering matrix of fuel assemblies between NEWT using the 302g library and Serpent.

3.1.5 Full core assembly power distribution

KENO calculations of the full cores were compared to investigate the performance of the 302-group library on a large model with vacuum boundary conditions, i.e. with neutron leakage in axial and radial directions.

The full reactor cores were modeled in full detail as specified in the benchmark. In case of the MET1000 core, only a sixth of the core with appropriate boundary condition was modeled to benefit from the symmetry of the core. In case of the MOX3600 core, half of the core was modeled with appropriate boundary conditions to represent the full core. For the self-shielding calculation of the fuel assemblies, the same self-shielding cells as for the single fuel assembly calculations were used, i.e. the assembly duct was considered by artificially adding duct material to the self-shielding cell of the outermost pins in an assembly. Since both reactor cores consist of an inner and an outer fuel zone, and the fuel is axially divided into five layers, self-shielding cells

for in total ten fuel areas were specified for each core. The power in the individual assemblies was determined by tallying fission reaction rates of all fissionable nuclides and multiplying them accordingly with the energy release per fission event. All fuel assemblies had to be modeled as individual units in order to allow assembly-wise fission rate tallying.

Table 3.8 – KENO eigenvalues of full cores (1σ statistical errors of Monte Carlo calculations in parentheses).

	MET1000		MOX3600	
Library	k_∞	$\Delta\rho$ [pcm]	k_∞	$\Delta\rho$ [pcm]
CE	1.01649(1)	(ref)	1.01134(1)	(ref)
302g, MOX3600	1.01979(1)	318(1)	1.01518(2)	375(2)

10^6 neutrons per generation were simulated in all KENO calculations. For the KENO-MG calculations, 1,000/8,000 active generations were used for the MET1000/MOX3600 core. Due to the significantly increased computation time for the CE calculations, a reduced number of 600/1,000 active generations was used for the MET1000/MOX36000 core. 200 generations were skipped to assure sufficient convergence of the fission source distributions. Despite the large number of simulated neutron histories, it was noticed that the radial power distribution often shows a significant tilt over the whole core, i.e. one side of the reactor showed larger assembly powers than the other side although the assembly powers should be similar range given the core symmetry. To improve the convergence of the radial power distribution and to minimize the tilt, the full core results were determined by averaging the results of a set of ten Monte Carlo calculations with different random seeds.

The eigenvalues of the full reactor cores showed an MG bias between 300–400 pcm (Table 3.8), which is considered reasonable for full core results given the neglected leakage effects in the self-shielding calculation of the fuel pins and the MG approximations.

The obtained assembly powers were normalized to the nominal reactor power of the cores: 1,000 MW for the metallic core, and 3,600 MW for the oxide core. The assembly power distributions showed that the KENO-MG calculations slightly underestimated the power in the central fuel assemblies by about 0.5%/1.2% in the MET1000/MOX3600 core, respectively. Due to the normalization, the assembly power was overestimated correspondingly in the outermost fuel assemblies (Figure 3.14

to 3.17). This means that the MG results led to a slight power tilt in the assembly power distribution. A slight power tilt is also observed when looking at the axial power distribution of one of the central fuel assemblies (Figure 3.18 and 3.19). The general good agreement indicates, however, that full core CE calculations were reasonably represented by MG calculations, providing a reasonable basis for uncertainty analyses.
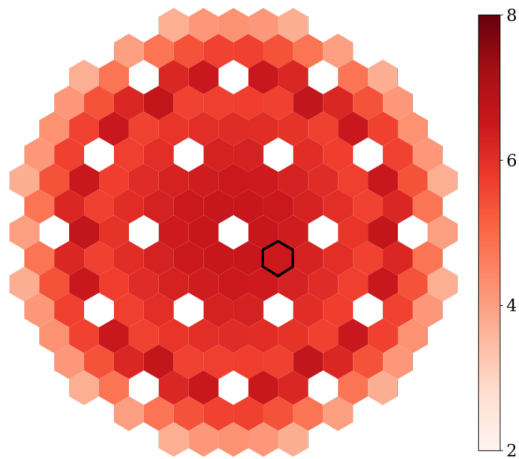
Figure 3.14 – KENO-CE assembly power distribution of the MET1000 core (powers in MW). Min/Max/Average: 3.73/6.69/5.56 MW.
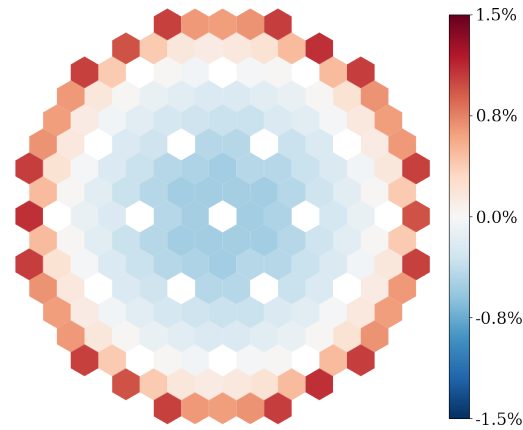
Figure 3.15 – Difference (in %) between the KENO 302g and CE assembly power distribution of the MET1000 core. RMS/Max. diff: 0.469%/1.10%.
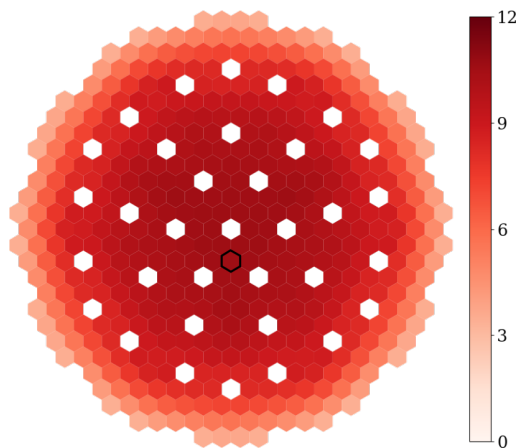
Figure 3.16 – KENO-CE assembly power distribution of the MOX3600 core (powers in MW). Min/Max/Average: 3.46/10.64/7.95 MW.
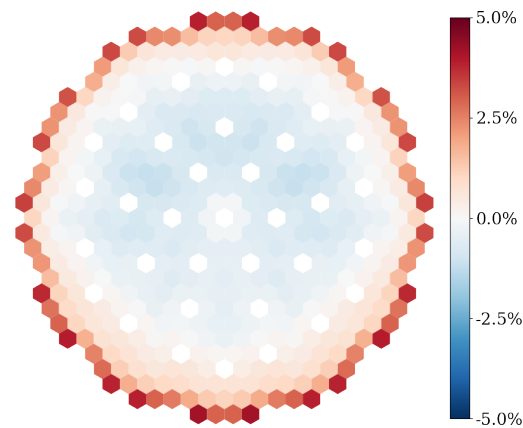
Figure 3.17 – Difference (in %) between the KENO 302g and CE assembly power distribution of the MOX3600 core. RMS/Max. diff: 1.25%/4.19%.

MET1000, Assembly 6
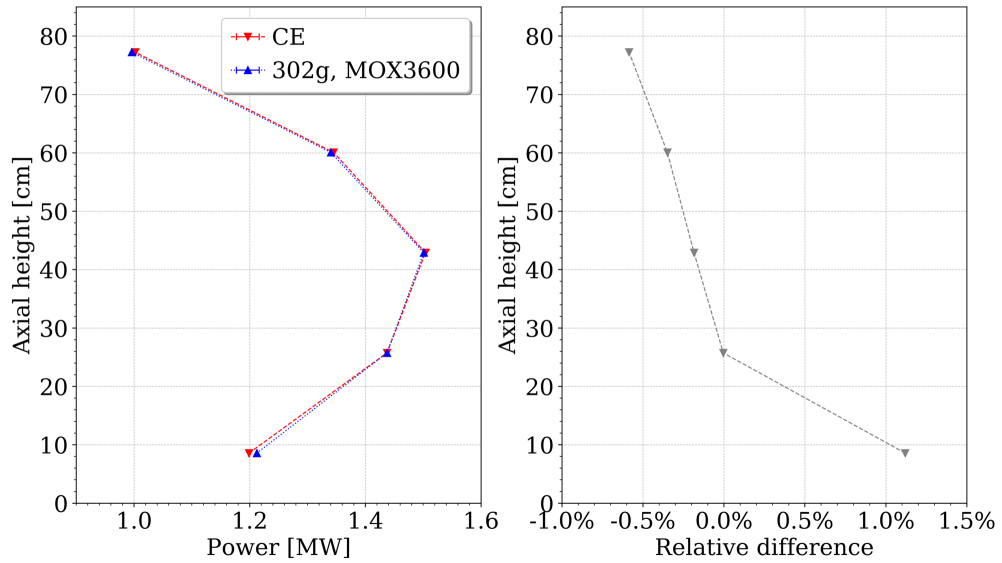
Figure 3.18 – Normalized axial power distribution of a central assembly (indicated in Figure 3.14) of the MET100 core compared between KENO 302g and CE.

MOX3600, Assembly 133
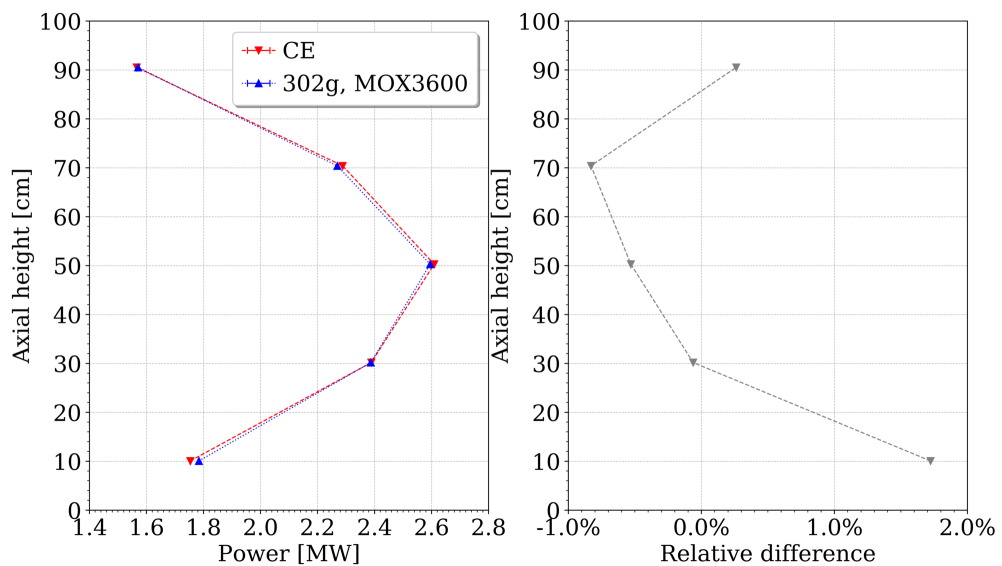
Figure 3.19 – Axial power distribution of a central assembly (indicated in Figure 3.16) of the MOX3600 core compared between KENO 302g and CE.

3.2   Multigroup covariance libraries

A new covariance library with 302 groups was generated to allow for consistent uncertainty analyses. Additionally, a covariance library with only a few energy groups was generated that allows for sensitivity analyses accompanying uncertainty analyses based on the random sampling approach.

This section covers the discussion of the relevance of the number of energy groups of the covariance library for sensitivity analyses, uncertainty analysis results based on a new 302-group covariance library, and the development of a covariance library with a reduced number of energy groups.

3.2.1   Relevance of the covariance library group structure for random sampling based sensitivity analysis

In case of random sampling based uncertainty analyses, the main contributing nuclide reactions to the output uncertainty of interest are found by calculating the sensitivity indices R^2 and SPC^2 for each relevant nuclide reaction. R^2 and SPC^2 are values between 0 and 1 with a certain interpretation with respect to the importance of the nuclide reaction to the output uncertainty (see Chapter 5).

R^2 is accompanied by a confidence interval and significance bound to express the uncertainty due to the sampling with a limited sample size. While the confidence interval depends primarily on the sample size N, the significance bound is significantly influenced by the number of independently sampled cross sections K for the nuclide reaction under consideration. K is in turn dependent on the number of energy groups in the applied covariance library. With a reduced number of K, the significance bound is strongly decreased such that a larger number of statistically significant sensitivity indices R^2 can be obtained. Figure 3.20 displays the significance bound as a function of the number independently sampled cross section for different sample sizes. Considering that the values for R^2 are between 0 and 1, a significance level of almost 0.34 when using a 302-group covariance library shows that significant R^2 will most likely be determined only for very few nuclide reactors when using a sample size of 1,000. A very large sample size would be necessary to obtain a certain number of significant values.

The sensitivity index SPC^2 is determined by subtracting the complementary R^2 (R^2

determined for all nuclide reactions except for the nuclide reaction under investigation) from the total R^2 (R^2 determined for all relevant nuclide reactions of the system of interest). The determination of this index requires a sample size that is larger than the total number of sampled input cross sections, i.e. the cross sections of all nuclides that are included in the material definition of the model under investigation. Already for a simple model, this number can be as high as several thousand. For example, the sensitivity analysis of an SFR assembly in terms of SPC^2 based on the 302-group covariance library requires a sample size larger than 32,093. As Table 3.9 shows, with a reduced number of energy groups, the number of independently sampled cross sections and consequently the required sample size for the determination of SPC^2 is significantly decreased.

All in all, a simplification of the energy group structure of the covariance library can lead to a larger number of significant sensitivity indices R^2 and allows a decreased sample size for the determination of SPC^2. A simplification is justified by the consideration that detailed uncertainty information is often given in energy ranges that are inessential for SFR systems, i.e. for energy ranges in which the sensitivity of the output response to the corresponding cross section is small. When studying the ENDF/B files, it is furthermore apparent that the covariance data in the high-energy range is often only given in a coarse energy structure. The validity of this assumption is demonstrated in the following.

Table 3.9 – Total number of independently sampled input cross sections in an uncertainty analysis of an SFR assembly (relevant for the determination of SPC^2).

Number of groups in the covariance library	Total number of independently sampled input cross sections
8	2,342
11	3,268
17	4,591
24	5,877
98	17,575
302	32,093

3.2.2 Generation of multigroup covariance libraries

Within the effort to find a covariance library with a reduced number of energy groups, covariance libraries with 2082, 302, 24, and 8 groups were initially generated with the
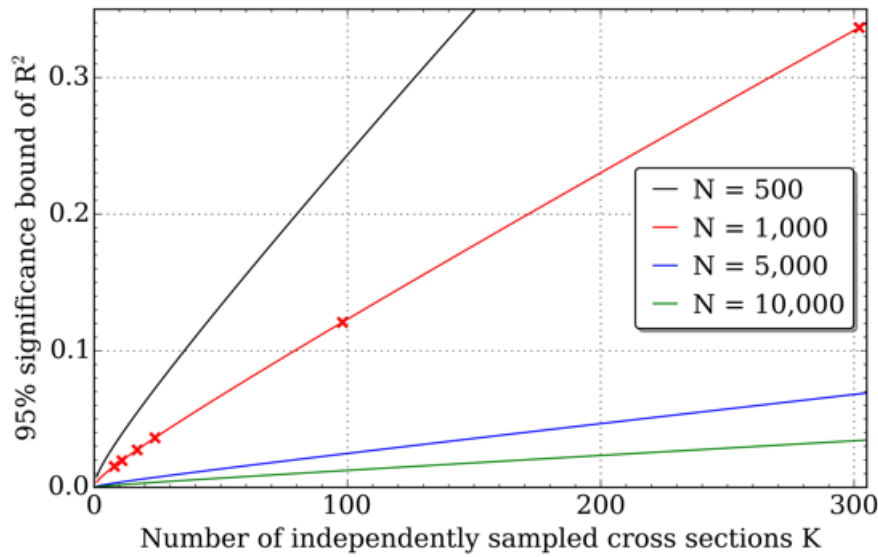
Figure 3.20 – 95% significance bound of R^2 as a function of the number of independently sampled cross sections of an individual nuclide reaction K for selected sample sizes N. Markers are set for N = 1,000 at K = [8, 11, 17, 24, 98, 302].

PUFF module of AMPX. The 24-group structure (Nikitin, 2019) is based on the 33-group structure in ERANOS (Ruggieri et al., 2006), and an 8-group structure that was suggested by Waltar for SFR analysis (Waltar et al., 2012a). Both structures have already been used for the generation of few-group cross sections for full core calculations of SFRs (Nikitin, 2019; Bousquet et al., 2017). The group boundaries were slightly adjusted in order to match boundaries of the 302-group cross section library.

In uncertainty and sensitivity analyses of SFR fuel assemblies, the covariance matrices that contribute the most to the total uncertainty of the quantities of interest were identified. The energy-dependent sensitivity profiles of these nuclide reactions and the corresponding energy-dependent uncertainty were then examined to identify possible energy ranges for simplification or for refinement. A simplification was considered adequate in energy ranges of small sensitivities or constant uncertainties, whereas a refinement was necessary in ranges with large sensitivities or in ranges with quickly changing sensitivities or uncertainties.

All generated libraries are based on the same data sources as the SCALE 6.2 56- and 252-group covariance libraries. They are mainly based on ENDF/B-VII.1 data (Chadwick et al., 2011), and some missing fission spectrum uncertainties were taken from JENDL 4.0 data. Approximate uncertainties from collaboration of Brookhaven Na-

tional Laboratory, Los Alamos National Laboratory, and Oak Ridge National Laboratory were also considered, along with approximate covariance data from WPEC Subgroup-26 (Little et al., 2008). The pointwise neutron flux of the homogenized MOX3600 fuel assembly was used as weighting spectra for all libraries.

3.2.3   Models and tools for uncertainty and sensitivity analysis

Uncertainty and sensitivity analyses of the MET1000 and MOX3600 fuel assemblies were performed with TSUNAMI (Broadhead, 2004) and Sampler (Williams et al., 2013) of SCALE 6.2. TSUNAMI uses linear perturbation theory to calculate sensitivity coefficients that describe the changes in the eigenvalue due to changes in the energy-dependent cross sections. The data-induced uncertainty in the eigenvalue is then estimated by multiplying the sensitivity coefficients with the corresponding covariance matrices. The sensitivities of system responses other than the eigenvalue, such as reaction rates and energy-integrated cross sections, were calculated using generalized perturbation theory (GPT). Sensitivities of reactivity differences such as the Doppler feedback were calculated using SCALE's TSAR module (Williams, 2007). In addition to the total output uncertainty, TSUNAMI and TSAR also provide the contributions of individual covariance matrices to the total output uncertainty.

For this study, TSUNAMI was used in combination with the two-dimensional deterministic solver NEWT as neutron transport code (i.e. TSUNAMI-2D) in combination with the new MG library. In addition to the forward calculation, the calculation of sensitivity coefficients requires an adjoint transport calculation for each requested output response. In addition to the TSUNAMI-2D calculations, TSUNAMI-3D calculations were performed using KENO-VI as the transport code in combination with the new MG library. As reference for comparison, the CE TSUNAMI-3D code was used that requires only one forward calculation with KENO-VI in combination with CE data. The contributon-linked eigenvalue sensitivity/uncertainty estimation via track length importance characterization (CLUTCH) method (Perfetti and Rearden, 2016) was used in CE TSUNAMI-3D to determine the sensitivities. The weighting function for the determination of the adjoint neutron flux (a measure of the "importance" of the neutrons) was set to 1 in the entire model because a constant weighting function was found in fuel assembly calculations that used a spatial grid. (This behavior can be explained by the small model size compared to the long mean free path of the neutrons in the system and the periodic boundary conditions in all directions.)

For random sampling–based uncertainty analyses, cross section perturbations were generated based on the new MG covariance library. Based on these perturbations, the Sampler code was used to perturb the MG cross sections used in transport calculations with NEWT. The average and standard deviation of the output quantities of interest was determined based on 350 perturbed calculations which is sufficient to determine the output uncertainties with an appropriate statistical confidence. For details on this approach, it is referred to Chapter 4.

The output responses of interest for the uncertainty analysis were the eigenvalue, the Doppler constant, and the sodium void coefficient.

At first, the general applicability of the 302-group cross section library in combination with the 302-group covariance library was demonstrated. Afterwards, the performance of the coarse group covariance libraries compared to fine group covariance libraries was assessed.

3.2.4   Application of the fine-group covariance library

Table 3.10 compares the results of TSUNAMI and Sampler using the 302-group cross section and covariance library with reference CE TSUNAMI results. The fuel assembly eigenvalues, Doppler constants, and Na-void worths show consistent nominal values and uncertainties due to the consistent source of the nuclear data between all applied codes. The same agreement was observed between the TSUNAMI calculations for the top contributing covariance matrices to the output uncertainties.

It can be concluded that the 302-group structure was sufficient for the determination of sensitivity coefficients with TSUNAMI in this group structure, as the TSUNAMI MG results provide the same outcome as the CE TSUNAMI results that are using sensitivity coefficients obtained from CE data. Furthermore, it was shown that consistent results were obtained between perturbation theory and random sampling calculations.

3.2.5   Coarse group covariance library performance assessment

Comparisons of the coarse-group with the fine-group covariance library results are performed by multiplying the covariance matrices with always the same sensitivity coefficients obtained in a CE TSUNAMI calculation. The results obtained with a 2082-group covariance library serve as reference solution for the comparisons because this

Table 3.10 – Nominal values and uncertainties due to nuclear data of eigenvalue k_∞, Doppler constant K_D, and Na-void reactivity ρ_{Na} of the fuel assemblies based on the 302-group covariance library (1σ statistical errors of TSUNAMI-3D calculations and the 95% confidence interval of Sampler calculations given in parentheses).

		k_∞	$\Delta k/k$	K_D [pcm]	$\Delta K_D/K_D$	ρ_{Na} [pcm]	$\Delta \rho_{Na}/\rho_{Na}$
MET1000	TSUNAMI-2D-MG	1.2787	1.402%	-316	6.5%	5,789	5.45%
	TSUNAMI-3D-MG	1.2783(1)	1.405(1)%	-305(9)	6.7(8)%	5,827(7)	5.47(1)%
	TSUNAMI-3D-CE	1.2800(1)	1.413(1)%	-338(12)	6.3(5)%	5,895(9)	5.47(1)%
	Sampler/NEWT	1.2801(19)	1.38(6)%	-314(3)	6.8(3)%	5,807(32)	5.1(2)%
MOX3600	TSUNAMI-2D-MG	1.1453	1.502%	-781	5.0%	2,980	5.50%
	TSUNAMI-3D-MG	1.1463(1)	1.506(1)%	-785(21)	5.4(1)%	2,949(10)	5.50(1)%
	TSUNAMI-3D-CE	1.1467(1)	1.515(1)%	-781(21)	5.2(3)%	2,945(10)	5.57(1)%
	Sampler/NEWT	1.1478(18)	1.46(5)%	-779(5)	5.1(2)%	2,986(16)	5.1(2)%

library contains the finest energy group structure and is therefore considered as most precise among the calculations. The models under investigation are again the SFR fuel assemblies.

After providing some comments on the determination of the energy group structures of the new covariance libraries, the results of the uncertainty and sensitivity analyses are presented. It shall be noted here that the provided statistical errors are propagated from the sensitivity coefficients. Although each individual output uncertainty and contribution is subject to the given statistical error, the presented relative differences are meaningful despite the provided statistical errors because the different covariance libraries are always applied to exactly the same sensitivity coefficients.

Determination of the coarse-group structures

The optimization of the group structures for fast systems, i.e. the reduction of the number of energy groups, was approached as described in the following. At first, the 302-group, 24-group and 8-group covariance libraries have been generated as described above and uncertainty calculations have been performed. The covariance matrices of the following nuclide reactions were found to play a major role for the total uncertainty of the eigenvalue, Doppler reactivity and Na-void coefficient: inelastic scattering of ^{238}U, ^{239}Pu and ^{23}Na; elastic scattering of ^{23}Na, ^{56}Fe and ^{16}O; the (n,γ) reaction of ^{238}U and ^{239}Pu; fission of ^{239}Pu. The sensitivity profiles of mainly these nuclide reactions and the corresponding uncertainties were examined to simplify

the 302-group structure to a 98-group structure while avoiding a loss of too much information, and to add energy group boundaries to the 8-group structure to improve the agreement with the reference calculations (see 11 and 17-group structures).

For example, Figure 3.21 shows the uncertainty of ^{238}U and ^{23}Na elastic scattering as a function of energy for four different energy group structures, and Figure 3.22 shows the corresponding eigenvalue sensitivity profiles. Apparently, the uncertainty of ^{238}U inelastic scattering is constant over a large energy range between 10^5 and 10^6 eV in which the eigenvalue sensitivity is relevant. A small resolution of this uncertainty is not necessary in this energy range. Furthermore, the peak between 4 and $5 \cdot 10^4$ eV is not necessary to resolve because the sensitivity in this range is small. In contrast, the eigenvalue sensitivity of ^{23}Na elastic scattering is significant between 10^4 and 10^6 eV, and the uncertainty shows significant changes of altitude. A simplification of the energy structure in this region might therefore have significant impact on the output uncertainty and the individual contributions.

An overview of the group structures of the generated covariance libraries is given in Table 3.11, and selected group structures are presented in Table A.7 in the Appendix.

Table 3.11 – Overview of the generated multigroup covariance libraries.

Number of groups	Comment
8	Based on (Waltar et al., 2012a)
11	Based on 8g
17	Based on 8g
24	Based on (Nikitin, 2019)
98	Simplification of 302g
302	Combination of MC^2-3 230g and 425g (Lee and Yang, 2012)
2082	MC^2-3 structure (Lee and Yang, 2012)

Comparison of total output uncertainties

The reference output uncertainties obtained with the 2082-group covariance library and the relative deviations of the calculations using the libraries with a reduced number of energy groups to the reference results are presented in Table 3.12 and 3.13.

The uncertainties obtained with the 302-group covariance library show good agreement with the corresponding reference. This indicates that a very fine energy group structure of the covariance library is not required despite the jagged profile of some
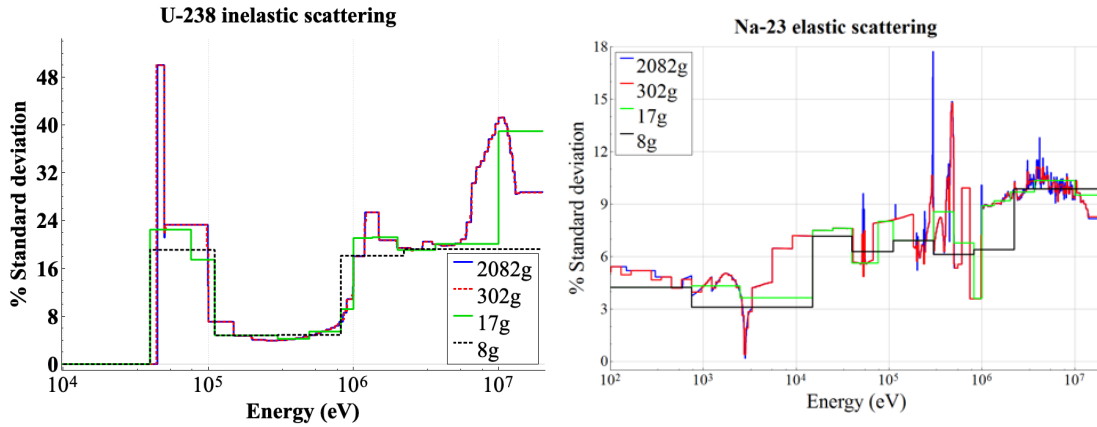
Figure 3.21 – Uncertainty of ^{238}U inelastic scattering and ^{23}Na elastic scattering in various energy group structures. Significantly increased or decreased values within energy groups of the coarse structures compared to the fine energy structures are caused by the weighting spectrum.
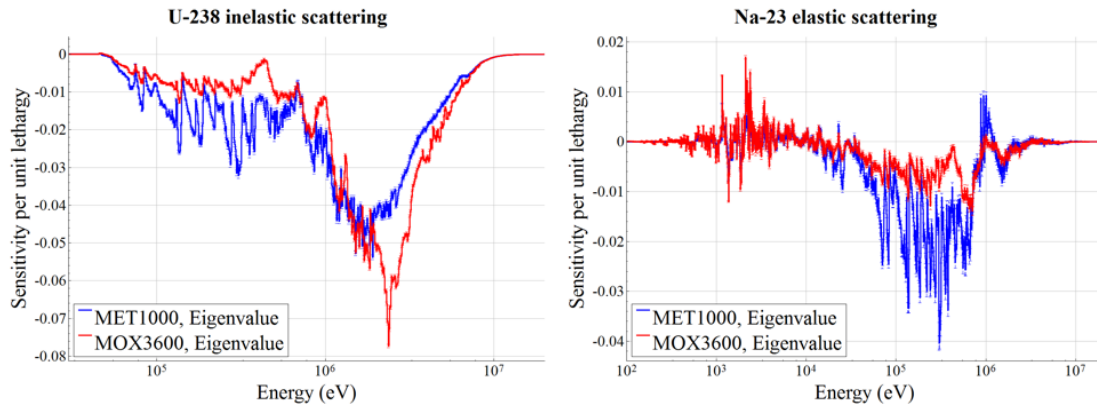
Figure 3.22 – Eigenvalue sensitivity of ^{238}U inelastic scattering and ^{23}Na elastic scattering.

uncertainties and sensitivities in the fast energy range. The results with the 98-group library show negligible differences to the corresponding references of less than a percent. The 8-group to 24-group results show relative differences of less than 4.6%. For some output quantities, the differences of the 24-group result are larger than the results with covariance libraries using fewer energy groups (see e.g. the Na-void results). Although the 24-group library has more group boundaries, the group structures of the other libraries have been optimized for the system under consideration: Groups have been added to the 8-group structure at energies concluded by the examination of the sensitivities and uncertainties.

It shall be noted here that in a side study, the 302-group and 24-group library have also

been generated using the flux spectrum of the MET1000 fuel assembly to investigate the influence of the weighting spectrum on the output uncertainty. Relative differences of less than 0.5% between the results of the covariance libraries with different weighting spectra indicate that the influence of the weighting spectrum is negligible.

In general, it can be concluded that the number of energy groups can be dramatically reduced without significantly changing the output uncertainty. It has, however, to be mentioned that the simplification of the energy group structure consistently led to a slight reduction of the output uncertainty, which is a non-conservative change of the uncertainties.

Table 3.12 – MET1000 fuel assembly: Uncertainties of the eigenvalue k_∞, the Doppler K_D and the Na-void reactivity ρ_{Na} due to uncertainties of the nuclear data. The statistical errors are given in parentheses.

Cov lib	k_∞		K_D		ρ_{Na}	
	$\%\Delta k/k$	Δ_{rel} to ref	$\%\Delta K_D/K_D$	Δ_{rel} to ref	$\%\Delta\rho_{Na}/\rho_{Na}$	Δ_{rel} to ref
2082g	1.438(1)	(ref)	8.4(2)	(ref)	5.40(1)	(ref)
302g	1.438(1)	0.00%	8.3(2)	-0.03%	5.39(1)	-0.11%
98g	1.437(1)	-0.07%	8.3(3)	-0.87%	5.38(1)	-0.31%
24g	1.435(1)	-0.21%	8.2(3)	-1.84%	5.27(1)	-2.32%
17g	1.434(1)	-0.28%	8.0(4)	-3.63%	5.33(1)	-1.30%
11g	1.434(1)	-0.28%	8.0(4)	-4.17%	5.25(1)	-2.71%
8g	1.420(1)	-1.25%	8.0(4)	-4.58%	5.21(1)	-3.46%

Table 3.13 – MOX3600 fuel assembly: Uncertainties of the eigenvalue k_∞, the Doppler K_D and the Na-void reactivity ρ_{Na} due to uncertainties of the nuclear data. The statistical errors are given in parentheses.

Cov lib	k_∞		K_D		ρ_{Na}	
	$\%\Delta k/k$	Δ_{rel} to ref	$\%\Delta K_D/K_D$	Δ_{rel} to ref	$\%\Delta\rho_{Na}/\rho_{Na}$	Δ_{rel} to ref
2082g	1.581(1)	(ref)	4.9(1)	(ref)	5.43(1)	(ref)
302g	1.581(1)	0.00%	4.9(1)	-0.45%	5.42(1)	-0.09%
98g	1.580(1)	-0.06%	4.8(1)	-0.80%	5.41(1)	-0.44%
24g	1.565(1)	-1.01%	4.8(2)	-2.13%	5.30(1)	-2.34%
17g	1.576(1)	-0.32%	4.8(2)	-2.11%	5.38(1)	-0.94%
11g	1.576(1)	-0.32%	4.8(2)	-0.90%	5.33(1)	-1.77%
8g	1.529(1)	-3.29%	4.7(2)	-3.37%	5.34(2)	-1.68%

Comparison of individual contributions to the output uncertainties

The nuclide reactions for which the corresponding covariance matrices contribute the most to the total output uncertainties of the eigenvalue, the Doppler reactivity and the sodium void reactivity for the MET1000 and MOX3600 fuel assemblies are presented in Table 3.14 and 3.15, respectively. The reference contributions of the covariance matrices are presented as well as the relative difference of the results obtained with the other covariance libraries to the reference results.

The comparison of the individual contributions was especially helpful for the identification of nuclide reactions for which the sensitivities and uncertainties should be examined for the determination of additional group boundaries to the 8-group structure. For example, an additional group boundary was added to the 8-group structure based on the examination of ^{56}Fe inelastic scattering (top sixth contributor to the MET1000 eigenvalue uncertainty) that lead to a reduction from 20% relative difference to the reference to about 3% with the 11-group library. Furthermore, an additional boundary was added based on inelastic scattering of ^{238}U such that, for example, the agreement of the contribution to the MET1000 Na-void reactivity could be improved (Table 3.14). However, it was often observed that improved agreement was caused by the effect of error cancellation. The addition of group boundaries sometimes even led to an increased difference to the reference. For example, the contribution of ^{238}U inelastic scattering to the MOX3600 Na-void uncertainty (Table 3.15) shows a better agreement with the 8-group covariance library than with the 11- or 17-group library. Especially the sensitivities to important scattering reactions often show a strongly varying structure such that only a fine energy structure can appropriately represent the uncertainty profile. The agreement of the contribution of the covariance matrix between elastic and inelastic scattering of ^{238}U for the MOX3600 Doppler uncertainty could, for example, not be improved by the addition of a few energy groups.

Table 3.14 – MET1000 fuel assembly: Top contributing covariance matrices to the uncertainty of the eigenvalue k_∞, the Doppler reactivity K_D and the Na-void reactivity ρ_{Na}. The statistical errors are given in parentheses.

	Covariance matrix		$\%\Delta k/k$ 2082g	Relative difference to 2082g reference					
				302g	98g	24g	17g	11g	8g
k_∞	^{238}U n,n'	^{238}U n,n'	1.211(1)	0.00%	-0.03%	-0.51%	0.43%	0.72%	-0.81%
	^{23}Na el.	^{23}Na el.	0.332(1)	-0.12%	-0.36%	-1.58%	-1.73%	-3.90%	-3.66%
	^{238}U n,γ	^{238}U n,γ	0.266(1)	-0.08%	-0.08%	1.71%	0.81%	0.96%	0.95%
K_D	^{238}U n,n'	^{238}U n,n'	4.90(5)	-0.06%	-0.10%	-2.20%	-0.19%	-1.70%	-4.13%
	^{23}Na el.	^{23}Na el.	4.63(3)	0.78%	0.20%	0.32%	-8.02%	-11.16%	-11.49%
	^{56}Fe el.	^{56}Fe el.	4.33(9)	-0.41%	-2.93%	-4.87%	-4.17%	-2.69%	-2.58%
ρ_{Na}	^{23}Na el.	^{23}Na el.	4.464(1)	-0.12%	-0.35%	-1.58%	-1.73%	-3.90%	-3.67%
	^{23}Na n,n'	^{23}Na n,n'	2.171(1)	0.01%	0.02%	-1.33%	0.94%	1.41%	0.38%
	^{238}U n,n'	^{238}U n,n'	1.336(1)	0.01%	-0.07%	-7.64%	-1.29%	-2.04%	-11.65%

Table 3.15 – MOX3600 fuel assembly: Top contributing covariance matrices to the uncertainty of the eigenvalue k_∞, the Doppler reactivity K_D and the Na-void reactivity ρ_{Na}. The statistical errors are given in parentheses.

	Covariance matrix		$\%\Delta k/k$ 2082g	Relative difference to 2082g reference					
				302g	98g	24g	17g	11g	8g
k_∞	^{238}U n,n'	^{238}U n,n'	1.410(1)	0.00%	-0.03%	-0.90%	0.28%	0.36%	-2.49%
	^{238}U n,γ	^{238}U n,γ	0.348(1)	-0.06%	-0.11%	-0.28%	0.59%	0.41%	0.41%
	^{239}Pu n,γ	^{239}Pu n,γ	0.244(1)	0.00%	-0.05%	-0.30%	-0.30%	0.93%	0.93%
K_D	^{238}U n,n'	^{238}U n,n'	3.90(3)	-0.17%	-0.02%	-1.62%	-0.39%	-0.72%	-3.28%
	^{16}O el.	^{16}O el.	1.33(1)	-0.03%	-0.01%	0.46%	0.29%	0.51%	0.57%
	^{238}U n,n'	^{238}U el.	1.16(3)	-2.03%	-3.48%	-12.55%	-11.75%	-12.62%	-13.45%
ρ_{Na}	^{23}Na el.	^{23}Na el.	3.656(1)	-0.06%	-0.27%	-1.91%	-0.09%	-1.01%	-0.81%
	^{23}Na n,n'	^{23}Na n,n'	3.079(1)	0.01%	0.00%	-0.42%	0.63%	0.92%	1.28%
	^{238}U n,n'	^{238}U n,n'	1.654(1)	-0.08%	-0.19%	-1.08%	-1.01%	-2.59%	-0.15%

Conclusions

Although the comparison of the individual contributions of the most important covariance matrices revealed significant deviations for some nuclide reactions, in particular for some scattering reactions because of their very jagged sensitivity profiles, the top contributing matrices could be identified and most of the contributions showed satisfying results. When considering that the uncertainties provided in the covariance matrices are subject to uncertainty, and when considering the sometimes large differences between various library releases, the obtained uncertainties are in very good agreement. A comparably coarse energy group structure of the covariance data with, for example, only 17 energy groups seems to be adequate for a reasonable assessment of the uncertainties of important quantities in the analysis of the fast systems under consideration.

3.3 Validation

To expand the performance assessment of the new cross section and covariance libraries from theoretical models to experimental measurements, several fast spectrum experiments of the International Handbook of Evaluated Criticality Safety Benchmark Experiments (ICSBEP Handbook) (NEA, 2015a) were calculated. Most of the input files were taken from the Verified, Archived Library of Inputs and Data (VALID), that contains more than 600 reviewed KENO input files of the ICSBEP Handbook and that is used for the SCALE library validation for criticality safety (Saylor et al., 2018).

The ICSBEP Handbook uses the characteristics of the experiments to form their abbreviations (only relevant ones are shown):

- Physical form of fissile material

    – metallic—**MET**, or

    – compound—**COMP**

- Fissile material

    – plutonium—**PU**,

    – mixed uranium and plutonium—**MIX**,

    – highly enriched uranium—**HEU** (enrichment at least 60 wt%), or

- intermediate or mixed enrichment uranium—**IEU** (10–60 wt% enrichment)

- Neutron spectrum, fast: at least 50% of fissions occur at energies above 100 keV—**FAST**

The nomenclature in the following figures combines always the first letter of (1) the physical form, (2) the fissile material, and (3) the spectrum. For example,"HMF" stands for "HEU-MET-FAST". The studied systems are HMF, IMF, MCF, MMF and PMF: The HMF systems are spheres or cylinders of HEU surrounded by various reflector materials; the IMF systems are assemblies of ^{235}U, either bare or reflected; the MCF systems are reflected cylindrical assemblies of mixed (Pu,U) fuel and sodium; the MMF system is a Pu sphere surrounded by HEU; and the PMF systems are Pu spheres, either bare or reflected. Table 3.16 lists the titles of the experiments that reveal slightly more information.

Figure 3.23 presents the calculated eigenvalue divided by the benchmark value (C/E) for the mentioned ICSBEP experiments with a fast neutron spectrum. The experimental uncertainty and the uncertainty of calculations resulting from uncertainties in the nuclear data are displayed. With the exception of one 252-group result, the calculated results were consistent with the corresponding measurements when considering nuclear data uncertainties.

In the computational analysis of these benchmarks, it is desired to obtain results close to the experiment. However, due to uncertainties in the nuclear data and additionally due to inaccuracies or simplifications in the benchmark specifications, even the CE results show some differences to the experimental values. The MG library assessment was therefore extended by a comparison of the 302-group and 252-group calculations to their corresponding CE reference. Figure 3.24 shows that the 302-group calculations were either as close as the 252-group calculations to the CE result, or they showed improved agreement with the CE result. The improvement of the results with the new group structure seems to be dependent on the group of experiments, especially the materials.

All in all, it is concluded that the selected experiments are adequately calculated with the new 302-group library.
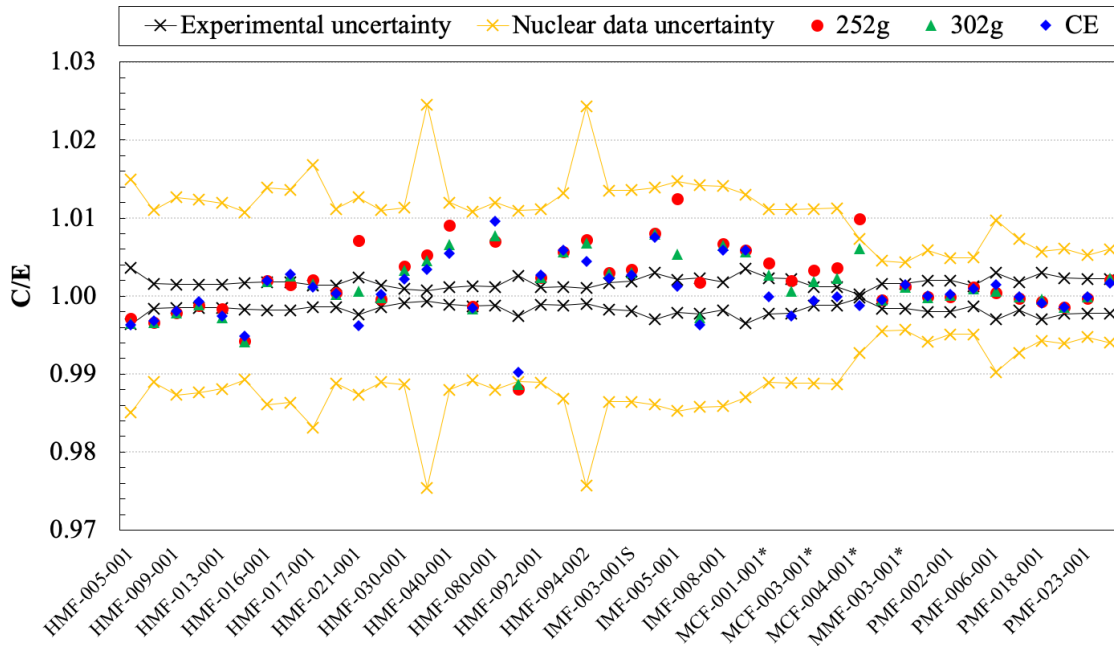
Figure 3.23 – Eigenvalue comparison of calculations (C) with selected fast spectrum experiments (E) from the ICSBEP handbook. The KENO input files are taken from the SCALE validation (VALID) suite, except if marked by an asterisk.
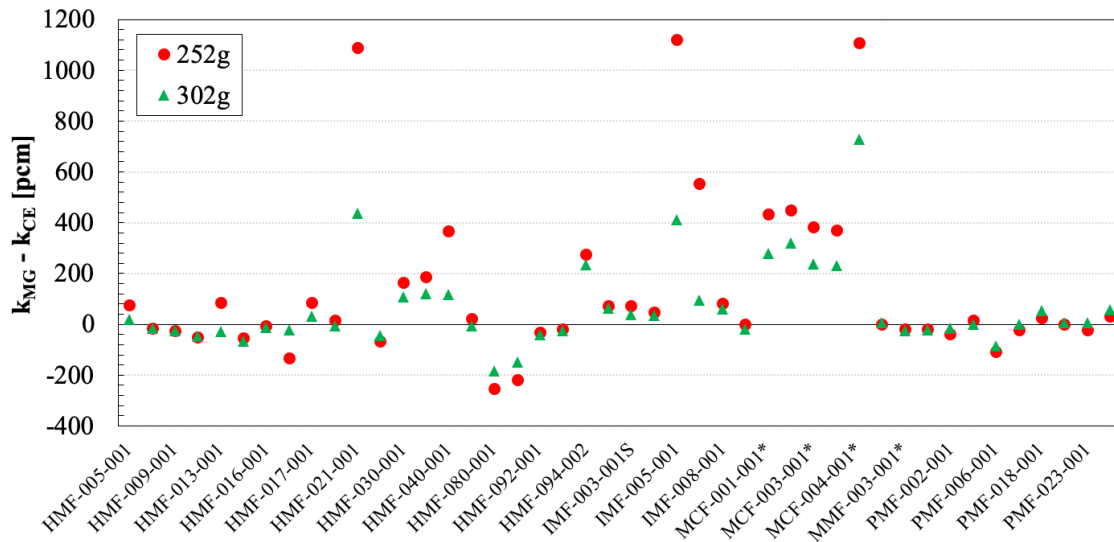
Figure 3.24 – Eigenvalue difference between the CE and MG calculations of selected fast spectrum experiments from the ICSBEP handbook. The KENO input files are taken from the SCALE validation (VALID) suite, except if marked by an asterisk.

Table 3.16 – Titles of the considered ICSBEP handbook experiments.

HMF-5	Beryllium- and Molybdenum-Reflected Cylinders of HEU
HMF-9	Spheres of HEU Reflected by Beryllium
HMF-13	Sphere of HEU Reflected by Steel
HMF-16	Beryllium-Reflected and Beryllium Oxide-Reflected Cylinders of HEU
HMF-17	Beryllium-Moderated and Reflected Cylinder of HEU
HMF-21	Steel-Reflected Spherical Assembly of ^{235}U
HMF-30	Heterogeneous Cylinder of HEU with Beryllium Moderator and Depleted-Uranium Reflector
HMF-40	Heterogeneous Vanadium-Diluted HEU Cylinder
HMF-80	Bare, HEU Fast Burst Reactor Caliban
HMF-92	Four Molybdenum-Reflected HEU Cylinders
HMF-94	Two Heterogeneous Cylinders of HEU Beryllium, Beryllium Oxide, and Molybdenum Reflected by Depleted Uranium
IMF-3	Bare Spherical Assembly of ^{235}U
IMF-5	Steel-Reflected Spherical Assembly of ^{235}U
IMF-8	Depleted-Uranium-Reflected Spherical Assembly of ^{235}U
MCF-1	ZPR-6 Assembly 7: A Cylindrical Assembly with Mixed (Pu,U)-Oxide Fuel and Sodium with a Thick Depleted-Uranium Reflector
MCF-3	ZPR-3 Assemblies 48 and 48B: Cylindrical Assemblies of Mixed (PU,U), Graphite and Sodium with a Depleted Uranium Blanket
MCF-4	ZPR-3 Assembly 56B: A Cylindrical Assembly of Mixed (PU,U), Oxide and Sodium with a Nickel-Sodium Reflector
MMF-3	Sphere of Plutonium Surrounded by HEU
PMF-2	Bare Sphere of ^{239}Pu Metal (^{240}Pu Jezebel)
PMF-6	Plutonium Sphere Reflected by Normal Uranium Using Flattop
PMF-18	Benchmark Critical Experiment of a Delta-Phase Plutonium Sphere Reflected by Beryllium
PMF-23	Graphite-Reflected Spherical Assembly of ^{239}Pu

4 Uncertainty analysis methods

This chapter describes the two most common approaches for the propagation of nuclear data uncertainties to output uncertainties in reactor physics calculations. First-order perturbation theory is only briefly presented. For the random sampling approach, the application with and without the consideration of implicit effects in multigroup calculations is described. Implicit effects are not considered with the random sampling approach when the problem-dependent (shielded) cross sections are perturbed instead of the problem-independent (unshielded) cross sections. To benefit from reduced computation time when perturbing shielded cross sections while also considering implicit effects, an approximation for implicit effects is presented that is derived from a perturbation theory–based sensitivity analysis. The chapter concludes with a demonstration of the various approaches using the MET1000 pin cell model.

4.1 First-order perturbation theory

In first-order perturbation theory, the derivatives of the output quantity Y with respect to the input parameters—in this case, cross sections Σ—are obtained for all nuclides i of the model of interest with all reactions x in all energy groups g:

$$S_{Y,\Sigma_{x,g}^i} = \left(\frac{\Sigma_i}{Y} \frac{\mathrm{d}Y}{\mathrm{d}\Sigma_{x,g}^i} \right). \tag{4.1}$$

$S_{Y,\Sigma^i_{x,g}}$ are often called sensitivity coefficients. (Note: It is important not to confuse these *sensitivity coefficients* with the *sensitivity indices* discussed in the following chapter.) These sensitivity coefficients are obtained using first-order perturbation theory that is described in detail by M. Williams (Williams, 1986; Williams et al., 2001). $S_{Y,\Sigma^i_{x,g}}$ describes the impact of a perturbation of cross section x of nuclide i in energy group g on the output quantity Y.

The nuclear data uncertainties are given in energy-dependent covariance matrices for each nuclide reaction and for correlations between different nuclide reactions (see Section 1.3). Using these covariance matrices and the sensitivity coefficients, the application of first-order uncertainty propagation (the so-called *sandwich formula*) leads to the total output variance:

$$\sigma_Y^2 = \mathbf{S}_{Y,\Sigma}^T \, \mathbf{C} \, \mathbf{S}_{Y,\Sigma} \,. \tag{4.2}$$

Vector $\mathbf{S}_{Y,\Sigma}$ includes the sensitivities of all the input cross sections to the output quantity, and the covariance matrix $\mathbf{C}$ includes the covariance matrices of all the input cross sections.

Since this approach is based on first-order (i.e. linear) perturbation theory, only linear effects are considered. In addition to the eigenvalue uncertainty, the uncertainty of reactivity differences can be determined from two sets of perturbation theory calculations (Williams, 2007). For the calculation of uncertainties of collapsed cross sections, for example, and reaction rate ratios, the implementation of Generalized Perturbation Theory (GPT) is required (Williams, 1986).

4.2   Random sampling approach

The random sampling approach can be divided into (1) preprocessing, (2) application, and (3) analysis segments.

4.2.1   Preprocessing

For the random sampling approach, cross sections are randomly sampled from a normal distribution under consideration of the covariance matrices. The output of the random sampling are perturbation factors for all cross sections in all energy groups that are generated considering the dependencies between the cross sections. The multiplication of the nominal cross sections by the corresponding perturbation factor leads to the perturbed cross sections. This conditional sampling is a standard procedure described in more detail in Appendix A.3 for application with nuclear data.

4.2.2   Application

In the application segment, the same calculation is performed a number of times with perturbed cross sections. To apply the random sampling approach in multigroup neutron transport calculations, there are two common procedures:

1. The perturbation factors can be applied to the unshielded cross sections as provided by the multigroup cross section library. The neutron transport sequence is then executed as usual, including the preparation of problem-dependent cross sections in the so-called self-shielding calculation and the subsequent neutron transport calculation. This approach is followed by the SCALE/Sampler sequence (see Figure 4.1).

2. The perturbation factors can also be applied directly to the shielded cross sections. In this case, the self-shielding calculation is performed only once for the nominal unperturbed case as part of the preprocessing. The calculation is then limited to the neutron transport calculation. This approach is followed to reduce the total computation time by omitting the self-shielding calculations for the perturbed calculations. However, this means that changes in the shielded cross sections caused by changes in the unshielded cross sections—the so-called *implicit effects*—are not taken into account; the variations of the shielded cross sections are assumed to be identical to those of the unshielded cross sections. This approach is followed by the XSUSA approach that was implemented in SCALE within the Gemino sequence (see Figure 4.2).

Initially, the first approach seems to be a better, more precise approach. However, in this approach, multigroup perturbation factors are applied to continuous-energy

data for use in the self-shielding calculation. Within an energy group, the continuous-energy cross sections are evenly increased or decreased, which comes with its own assumptions. An approximation for considering implicit effects in the second approach is described in Section 4.3.
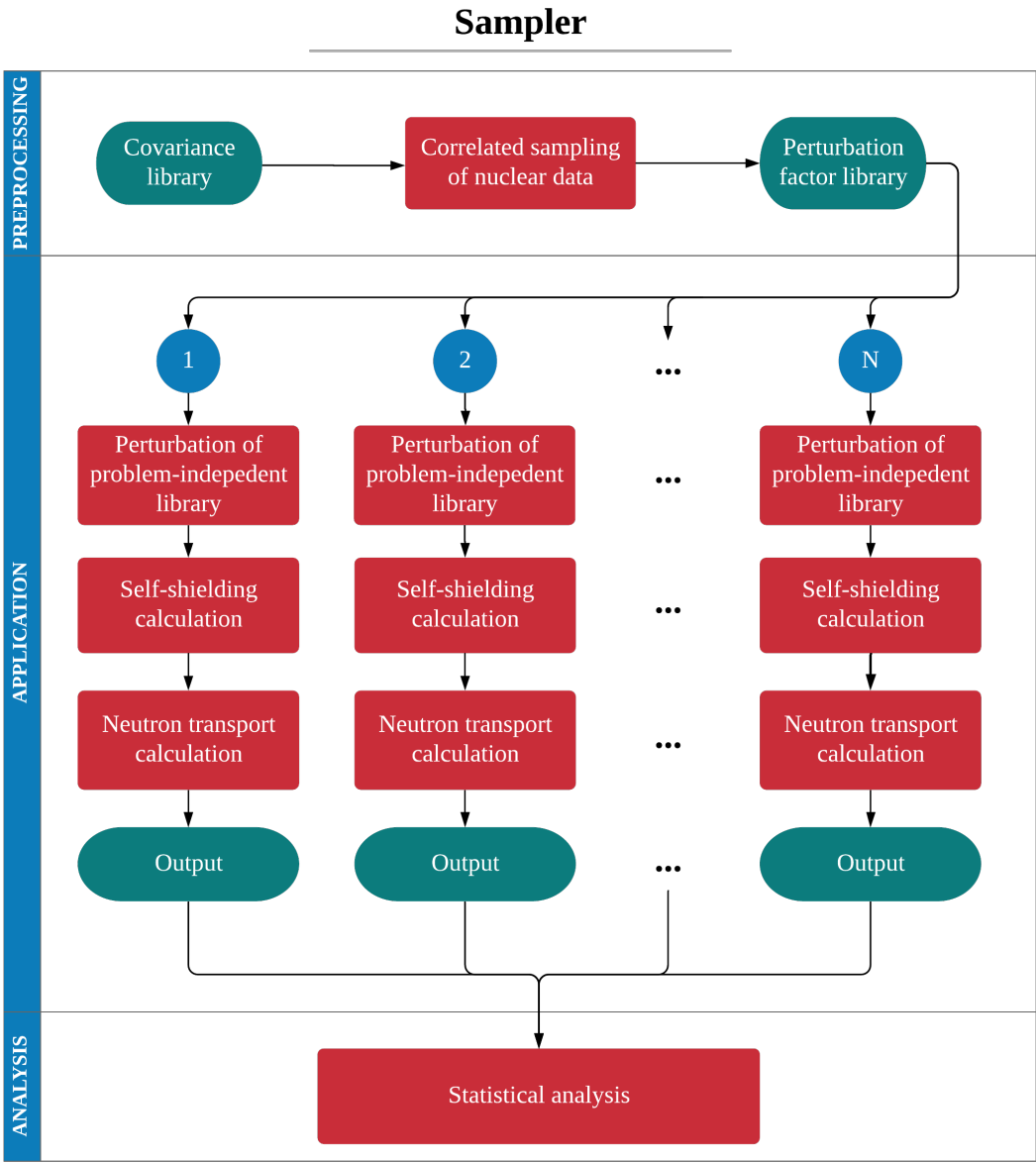
Figure 4.1 – Sampler sequence.
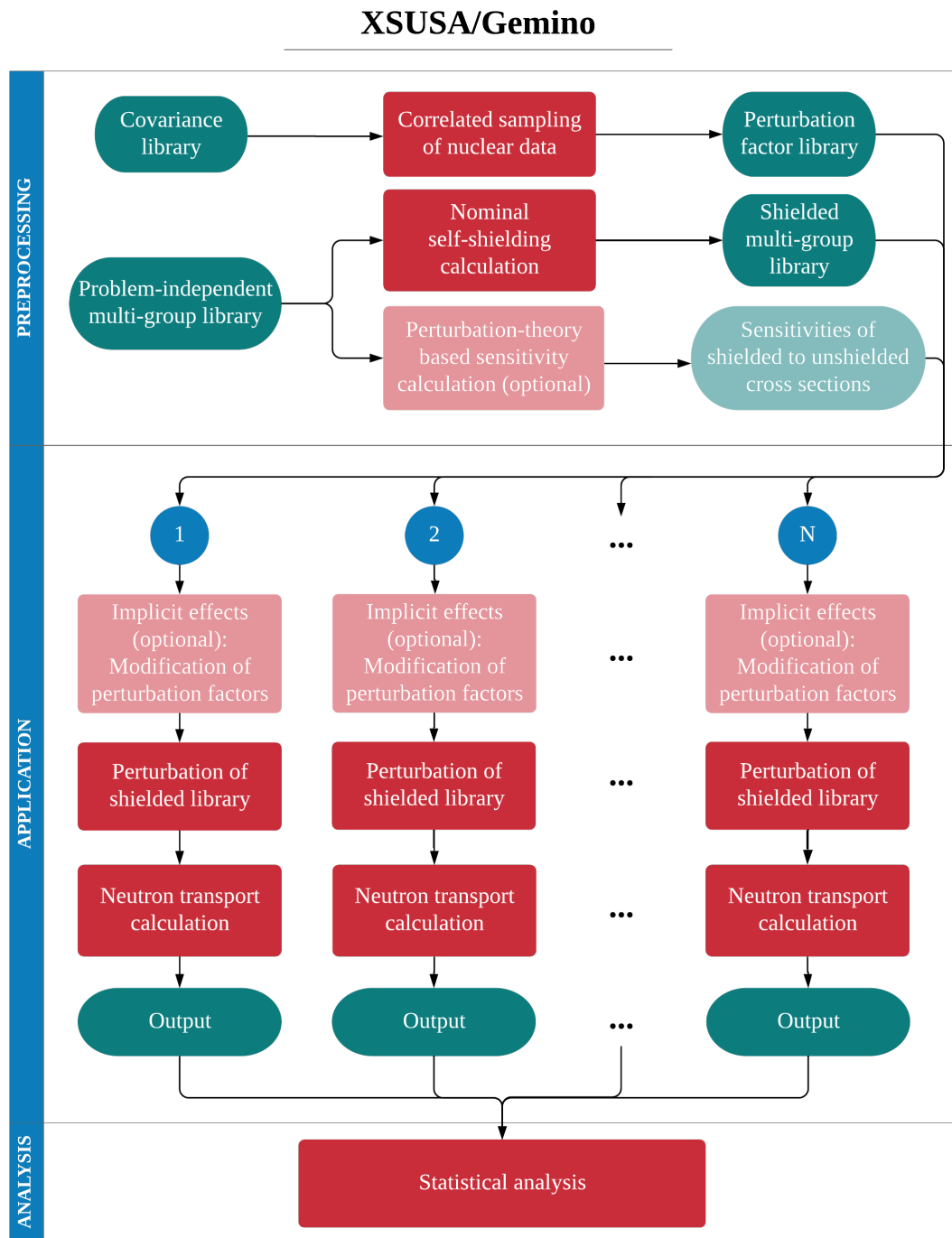
XSUSA/Gemino

Figure 4.2 – XSUSA approach as followed by the Gemino sequence.

4.2.3 Statistical analysis

With a statistical analysis of the output, the resulting mean value and the uncertainty in terms of the standard deviation can be calculated for any output quantity of interest.

For a sample size N, the sample mean $\bar{Y}$ and the standard deviation σ of the output values $Y_1, ..., Y_N$ are calculated as follows:

$$\bar{Y} = \frac{1}{N}\sum_{i=1}^{N} Y_i, \qquad \sigma = \sqrt{\frac{1}{N-1}\sum_{i=1}^{N}\left(Y_i - \bar{Y}\right)^2}. \tag{4.3}$$

Since these values are determined based on a finite sample size, they are subject to a statistical uncertainty: with a different set of sampled input parameters, the sample mean and standard deviation will be slightly different (see Figure A.2 in the Appendix). To indicate the statistical nature of these values, a confidence interval is provided—usually at a 95% confidence level.

With the assumption that the output values Y_i are normally distributed, the confidence interval of the population mean value is calculated as follows:

$$\left[\bar{Y} + \frac{t_{N-1,\frac{\alpha}{2}}\,\sigma}{\sqrt{N}}, \bar{Y} + \frac{t_{N-1,1-\frac{\alpha}{2}}\,\sigma}{\sqrt{N}}\right], \tag{4.4}$$

with t being Student's t-distribution. For reasons of symmetry, $t_{N-1,\frac{\alpha}{2}} = -t_{N-1,1-\frac{\alpha}{2}}$ applies. For example, for a 95% confidence interval and a sample size $N > 120$, the value of the two-sided t-distribution is $t_{N-1,1-\frac{\alpha}{2}} = 1.96$ (Bronstein et al., 2008).

Using the same assumption, the confidence interval for the standard deviation is calculated as follows:

$$\left[\sigma \cdot \sqrt{\frac{N-1}{\chi^2_{\left(\frac{\alpha}{2},N-1\right)}}}, \sigma \cdot \sqrt{\frac{N-1}{\chi^2_{\left(1-\frac{\alpha}{2},N-1\right)}}}\right]. \tag{4.5}$$

The standard deviation is typically the major quantity of interest. For a desired confidence level α, Eq. 4.5 shows that the confidence interval is only dependent on the sample size. A plot of the confidence interval as a function of the sample size, along with the description of the correct interpretation, is provided in Appendix A.3. Table 4.1 presents the confidence intervals for a few common sample sizes.

Table 4.1 – 95% confidence intervals of the sample standard deviation σ for various sample sizes based on the assumption of normally distributed output values.

Sample size	95% confidence interval
100	$[(1-12.20\%)\cdot\sigma,\ (1+16.17\%)\cdot\sigma]$
250	$[(1-8.07\%)\cdot\sigma,\ (1+9.63\%)\cdot\sigma]$
500	$[(1-5.84\%)\cdot\sigma,\ (1+6.62\%)\cdot\sigma]$
1,000	$[(1-4.20\%)\cdot\sigma,\ (1+4.59\%)\cdot\sigma]$
10,000	$[(1-1.37\%)\cdot\sigma,\ (1+1.41\%)\cdot\sigma]$

If the output values Y_i are not normally distributed, then the confidence intervals for the mean value and standard deviation can be obtained using the Bootstrap method, which is independent of the distribution type (Engel, 2010). For this approach, it is useful to consider the results $Y_1, ..., Y_N$ as a vector of length N with sample mean $\bar{Y}$ and sample variance σ^2. From this vector, a number of results (the number can be N, but this is not required) is randomly selected with replacement, and the corresponding mean value and variance are calculated. By repeating this procedure N times, a Bootstrap vector of mean values $\bar{Y}_i^*$ and a Bootstrap vector of variances $\sigma_i^{2,*}$ of length N are generated. The individual values of these vectors are sorted according to size. Depending on the desired confidence α, the values at particular indices of these sorted vectors are used to determine the upper and lower confidence intervals. The indices for the lower and upper boundaries are as follows:

$$i_{low} = \left\lfloor N\cdot\frac{1-\alpha}{2}\right\rfloor \quad \text{and} \quad i_{up} = \left\lceil N\cdot\left(1-\frac{1-\alpha}{2}\right)\right\rceil . \tag{4.6}$$

For example, with a sample size of $N = 1,000$, the indices for a 95% confidence interval are $i_{low} = 25$ and $i_{up} = 975$.

The Bootstrap confidence intervals for the sample mean value and sample standard deviation, respectively, are then determined as follows:

$$\left[2\bar{Y} - \bar{Y}_{i_{up}}^*, 2\bar{Y} - \bar{Y}_{i_{low}}^*\right] \quad \text{and} \quad \left[\sqrt{2\sigma^2 - \sigma_{i_{up}}^{2,*}}, \sqrt{2\sigma^2 - \sigma_{i_{low}}^{2,*}}\right] . \tag{4.7}$$

Another option for investigating the influence of uncertain input parameters on output parameters is to analyze Wilks tolerance limits instead of standard deviations. These tolerance limits show the impact of the characterized uncertainties within the determined limits—with a certain confidence. (Wilks, 1941, 1962) However, as the

output quantities under investigation in this work mostly follow a normal distribution, only standard deviations are considered here.

4.3 Approximation of implicit effects in the random sampling approach

In many comparisons with models of a broad variety of spectral conditions, it appears that the negligence of implicit effects only has a small influence on the investigated output uncertainties (Bostelmann et al., 2015a). Although the so far investigated impact of implicit effects on integrated values and their uncertainties is small, there are systems which show larger implicit effects in uncertainty analyses, and there may be a stronger influence in the accompanying sensitivity analyses.

This section presents an approach for considering implicit effects in uncertainty and sensitivity calculations using the random sampling approach. The perturbation factors that should technically be applied to unshielded cross sections are adjusted in order to consider implicit effects when they are applied to unshielded cross sections. This adjustment is based on the results of one first-order perturbation theory calculation. It is emphasized that perturbation theory is only applied to obtain corrections for the varied shielded cross sections arising from implicit effects. The main contributions to the output uncertainties arising from the explicit part are still captured through random sampling without constraints regarding the order of effects.

4.3.1 Perturbation factors for random sampling

The modification of cross section Σ to the corresponding perturbed cross section Σ^* of nuclide j with reaction y in energy group g is obtained as follows:

$$\Sigma_{y,g}^{j,*} = \Sigma_{y,g}^{j} + \Delta\Sigma_{y,g}^{j} = \left(1 + \frac{\Delta\Sigma_{y,g}^{j}}{\Sigma_{y,g}^{j}}\right) \cdot \Sigma_{y,g}^{j} = p_{y,g}^{j} \cdot \Sigma_{y,g}^{j}. \tag{4.8}$$

The perturbation factors $p_{y,g}^{j}$ are derived from the random sampling using covariance data (see Appendix A.3). Since the covariance data refers to the unshielded cross sections, a perturbation factor would normally need to be applied to the unshielded cross section $\Sigma_{y,g}^{j}$. However, with the XSUSA approach, the perturbation is applied

on shielded cross sections $\bar{\Sigma}_{y,g}^{j}$. Instead of simply applying the perturbation factor to the shielded cross sections, a shielded perturbation factor $\bar{p}_{y,g}^{j}$ is being sought that considers the impact of the self-shielding.

4.3.2 Derivation with first-order perturbation theory

In first-order perturbation theory, the relative change of a response R to a perturbation of an input parameter α can be written as (Williams, 1986):

$$\frac{\Delta R}{R} = S_{R,\alpha} \frac{\Delta \alpha}{\alpha}, \tag{4.9}$$

with $S_{R,\alpha}$ being the relative sensitivity coefficient of R with respect to α. For sufficiently small α, R depends linearly on α, and the relative sensitivity coefficient of R with respect to α becomes:

$$S_{R,\alpha} = \frac{\alpha}{R} \frac{\mathrm{d} R}{\mathrm{d} \alpha}. \tag{4.10}$$

Because of the assumption that the perturbation of the response is linearly related to the perturbation in α, the relative change of the response due to changes in different input parameters α_i is the sum of the individual perturbations:

$$\frac{\Delta R}{R} = \sum_{i} \left(S_{R,\alpha_i} \frac{\Delta \alpha_i}{\alpha_i} \right). \tag{4.11}$$

Since we are interested in the influence of the unshielded cross section (individual perturbations) to the shielded cross section (response), we obtain the following relation for the relative change of the shielded cross section due to a relative change in the unshielded cross section:

$$\frac{\Delta \bar{\Sigma}_{y,g}^{j}}{\bar{\Sigma}_{y,g}^{j}} = \sum_{i,x} \left[S_{\bar{\Sigma}_{y,g}^{j},\Sigma_{x,g}^{i}} \frac{\Delta \Sigma_{x,g}^{i}}{\Sigma_{x,g}^{i}} \right], \tag{4.12}$$

with i denoting all possible nuclides, including nuclide j, and x denoting all possible reactions, including reaction y. The sensitivity of the shielded to the unshielded cross

section is thereby expressed as follows:

$$S_{\bar{\Sigma}_{y,g}^j, \Sigma_{x,g}^i} = \frac{\Sigma_{x,g}^i}{\bar{\Sigma}_{y,g}^j} \frac{d\bar{\Sigma}_{y,g}^j}{d\Sigma_{x,g}^i} .$$

(4.13)

The perturbed shielded cross section is approximated by adding (1) the perturbation of the unshielded cross section and (2) the change due to the consideration of the self-shielding calculation to the nominal shielded cross section. The perturbation factor for the shielded cross section is then determined as follows:

$$\bar{p}_{y,g}^j = p_{y,g}^j + \frac{\Delta\bar{\Sigma}_{y,g}^j}{\bar{\Sigma}_{y,g}^j} ,$$

(4.14)

$$\stackrel{(4.12)}{=} p_{y,g}^j + \sum_{x,i} \left[S_{\bar{\Sigma}_{y,g}^j, \Sigma_{x,g}^i} \frac{\Delta\Sigma_{x,g}^i}{\Sigma_{x,g}^i} \right] ,$$

(4.15)

$$\stackrel{(4.8)}{=} p_{y,g}^j + \sum_{x,i} \left[S_{\bar{\Sigma}_{y,g}^j, \Sigma_{x,g}^i} \left(p_{x,g}^i - 1 \right) \right] .$$

(4.16)

The approximation of the perturbation factor for the application on the shielded cross section is a function of the original perturbation factors for the unshielded cross sections and the sensitivities of the shielded to the unshielded cross sections. This equation shows that even if nuclide j of reaction y is not initially perturbed due to its covariance data (i.e. $p_{y,g}^j = 1$), it might still be perturbed due to the influence of other nuclide reaction perturbations (i.e. $p_{x,g}^i \neq 1$) during the self-shielding calculation.

4.3.3   Application with SCALE

For the calculation of the perturbation factors $\bar{p}_{y,g}^j$ with Eq. 4.16, the sensitivities of the shielded cross sections with respect to the unshielded cross sections (Eq. 4.13) must be determined. By applying the chain rule for derivatives, an expression can be derived that includes terms that are evaluated by the self-shielding part of the first-order perturbation theory-based TSUNAMI-1D code (Rearden et al., 2011):

$$\frac{\Sigma_{x,g}^{i}}{\bar{\Sigma}_{y,g}^{j}}\frac{\mathrm{d}\bar{\Sigma}_{y,g}^{j}}{\mathrm{d}\Sigma_{x,g}^{i}} = \left(\underbrace{\frac{\Sigma_{T,g}^{i}}{\bar{\Sigma}_{y,g}^{j}}\frac{\partial\bar{\Sigma}_{y,g}^{j}}{\partial\Sigma_{T,g}^{i}}}_{(1)} + \sum_{m}\left[\underbrace{\frac{C_m}{\bar{\Sigma}_{y,g}^{j}}\frac{\partial\bar{\Sigma}_{y,g}^{j}}{\partial C_m}}_{(2)}\cdot\underbrace{\frac{\Sigma_{T,g}^{i}}{C_m}\frac{\partial C_m}{\partial\Sigma_{T,g}^{i}}}_{(3)}\right]\right)\cdot\underbrace{\frac{\Sigma_{x,g}^{i}}{\Sigma_{T,g}^{i}}\frac{\partial\Sigma_{T,g}^{i}}{\partial\Sigma_{x,g}^{i}}}_{(4)}, \qquad (4.17)$$

with the unshielded total cross section $\Sigma_{T,g}^{i}$ and the Dancoff factors C_m for each material zone m. The individual terms are available from several SCALE modules that are called by the TSUNAMI sequence, as described below.

The output from the BONAMIST code, that determines implicit effects of the resonance self-shielding calculations, can be used to obtain term (1). In the implementation of BONAMIST, the sensitivity of a response to the total macroscopic cross section is assumed to be equivalent to the sensitivity of this response to the material nuclide density (Rearden et al., 2011). The calculation of term (1) as written in Eq. 4.17 is therefore replaced in BONAMIST by the calculation of the sensitivity of the shielded cross sections to the corresponding material nuclide density, and the result is used here for term (1). Term (2), the sensitivity with respect to the Dancoff factors C_m, is also output from the BONAMIST code. Term (3) in the sum over the materials, the sensitivity of the Dancoff factors with respect to the total cross section, is provided by the SENLIB module, which is the sensitivity version of the SCALE material information processor.

To determine the sensitivities of the unshielded total cross sections to reactions other than total, term (4), the following relation for the implicit multiplication factor sensitivities can be used (Rearden et al., 2011):

$$\left(S_{k,\Sigma_{x,g}^{i}}\right)_{implicit} = \left(S_{k,\Sigma_{T,g}^{i}}\right)_{implicit}\cdot\frac{\Sigma_{x,g}^{i}}{\Sigma_{T,g}^{i}}\frac{\partial\Sigma_{T,g}^{i}}{\partial\Sigma_{x,g}^{i}}, \qquad (4.18)$$

$$\Longleftrightarrow \quad \frac{\Sigma_{x,g}^{i}}{\Sigma_{T,g}^{i}}\frac{\partial\Sigma_{T,g}^{i}}{\partial\Sigma_{x,g}^{i}} = \frac{\left(S_{k,\Sigma_{x,g}^{i}}\right)_{implicit}}{\left(S_{k,\Sigma_{T,g}^{i}}\right)_{implicit}}. \qquad (4.19)$$

The implicit multiplication factor sensitivities can be expressed as the difference of

total and explicit sensitivities:

$$\frac{\Sigma_{x,g}^i}{\Sigma_{T,g}^i}\frac{\partial \Sigma_{T,g}^i}{\partial \Sigma_{x,g}^i} = \frac{\left(S_{k,\Sigma_{x,g}^i}\right)_{total} - \left(S_{k,\Sigma_{x,g}^i}\right)_{explicit}}{\left(S_{k,\Sigma_{T,g}^i}\right)_{total} - \left(S_{k,\Sigma_{T,g}^i}\right)_{explicit}}. \tag{4.20}$$

The energy-wise explicit and total sensitivities for each nuclide-reaction-pair (including the total cross section) are calculated by the Sensitivity Analysis Module (SAMS) of SCALE. If implicit effects are neglected in a TSUNAMI calculation, then SAMS calculates the explicit sensitivities; otherwise the total sensitivities are calculated.

With the help of various TSUNAMI output files, the unshielded perturbation factors can be modified in order to obtain shielded perturbation factors. As usual, these perturbation factors can be applied to cross sections in direct perturbation or random sampling calculations.

4.4 Demonstration

As an application example, uncertainty calculations of the MET1000 pin cell (see Chapter 2.1) were performed using perturbation theory and the random sampling approach. For the random sampling approach, the Sampler approach, the XSUSA approach, and the XSUSA approach including the approximation for implicit effects are demonstrated in this section (the XSUSA approach as followed by the Gemino sequence in SCALE). The general approach for random sampling analysis is presented in Section 4.4.2, and the approximation of implicit effects is demonstrated in Section 4.4.3. The applied neutron transport code is the two-dimensional deterministic code NEWT of SCALE 6.2. All calculations are performed using the 302-group cross section library and the 17-group covariance library from Chapter 3.

4.4.1 Perturbation theory

Results are obtained with TSUNAMI-2D of SCALE 6.2. For demonstration purposes, only the eigenvalue k_{eff} and the 1-group macroscopic fission and absorption cross sections in the fuel, Σ_{fis} and Σ_{abs}, respectively, are considered here as output quantities of interest. Table 4.2 shows results based on explicit sensitivities, as well as total (i.e., explicit and implicit effects) sensitivities. The resulting uncertainties show almost no

impact of implicit effects on these uncertainty results.

Table 4.2 – Perturbation theory results of the MET1000 pin cell: eigenvalue k_{eff} and the 1-group macroscopic fission and absorption cross section of the fuel, Σ_{fis} and Σ_{abs}, respectively.

	k_{eff}	Σ_{fis}	Σ_{abs}
nominal value	1.35845	5.310E-03	1.127E-02
explicit uncertainty	1.5247%	1.5421%	0.9831%
total uncertainty	1.5243%	1.5418%	0.9845%

4.4.2   Random sampling

XSUSA has been used extensively in combination with modules of SCALE 6.1. To allow calculations with the time-efficient XSUSA approach in combination with modules of the recent SCALE 6.2 release, the Sampler sequence of SCALE 6.2 was extended to allow the perturbation of cross sections after the self-shielding calculation. For a simplified application, a child sequence of Sampler, Gemino, was directly implemented in SCALE 6.2. In this way, all required input files are automatically generated and, if desired, they are executed in the appropriate order.

Tables 4.3 and 4.4 present results for the k_{eff}, Σ_{fis} and Σ_{abs} for Gemino and Sampler. The Gemino and Sampler results are in very good agreement with respect to the mean values and the uncertainties. However, a significant k_{eff} difference of 100 pcm is observed between the mean values compared to the corresponding nominal values. Figure 4.3 shows the development of k_{eff} and the corresponding uncertainty as a function of the sample size, also indicating this disagreement.

Since nonlinear effects are considered in the random sampling approach, this could indicate a significant contribution of nonlinear effects. Another indicator of nonlinear effects can be found in the distribution of the output values—if the output values are not normally distributed. Figure 4.4 shows a histogram of the k_{eff} Gemino and Sampler results. The slightly transparent colors of the histograms (blue and red) cause a purple overlap and allow a clear distinction between the Sampler and Gemino results. Gaussian normal probability distribution functions (PDFs) using the respective mean values and standard deviations have also been included in this plot. Since the histograms and the normal distributions show quite a disagreement, the skewness of the output distribution was calculated as a measure of the asymmetry. A plot of

the skewed normal distribution using the obtained positive factor for the skewness shows a longer tail on the right side and an improved agreement with the histogram. The maximum value of the skewed distribution is at an eigenvalue of about 1.35400, a value more than 500 pcm smaller than the Gemino and Sampler mean values. Finally, the Shapiro-Wilk test and the Anderson-Darling test for normality have been performed for the k_{eff} values, resulting in a rejection of the null hypothesis that the values are normally distributed. The analysis of Σ_{fis} reached the same qualitative results. All these observations indicate that the k_{eff} and Σ_{fis} results are significantly influenced by nonlinear effects. A possible explanation could be the large uncertainty of inelastic scattering of ^{238}U (Figure 1.5) that is significantly influencing this result. This is further investigated in the following chapter.

Table 4.3 – Random sampling results of the MET1000 pin cell: nominal, mean values and confidence intervals (CI) of k_{eff}, Σ_{fis} and Σ_{abs}.

		Nominal	Mean	CI normal	CI Bootstrap
k_{eff}	Gemino expl.	1.35845	1.35921	[-130, +130][*]	[-131, +141][*]
	Sampler		1.35968	[-129, +130][*]	[-129, +137][*]
Σ_{fis}	Gemino expl.	5.310E-03	5.314E-03	[-0.10%, +0.10%][†]	[-0.10%, +0.10%][†]
	Sampler		5.315E-03	[-0.10%, +0.10%][†]	[-0.10%, +0.10%][†]
Σ_{abs}	Gemino expl.	1.127E-02	1.127E-02	[-0.05%, +0.05%][†]	[-0.04%, +0.06%][†]
	Sampler		1.127E-02	[-0.062%, +0.062%][†]	[-0.06%, +0.06%][†]

[*] Eigenvalue interval given as difference to mean value in pcm.

[†] Interval given as relative difference to mean value.

Table 4.4 – Random sampling results of the MET1000 pin cell: uncertainties with corresponding confidence intervals (CI) of k_{eff}, Σ_{fis} and Σ_{abs}.

		Uncertainty	CI normal	CI Bootstrap
k_{eff}	Gemino expl.	1.543%	[1.478%, 1.614%]	[1.476%, 1.613%]
	Sampler	1.538%	[1.474%, 1.609%]	[1.469%, 1.608%]
Σ_{fis}	Gemino expl.	1.573%	[1.5074%, 1.6456%]	[1.491%, 1.643%]
	Sampler	1.569%	[1.503%, 1.641%]	[1.488%, 1.639%]
Σ_{abs}	Gemino expl.	0.931%	[0.892%, 0.974%]	[0.895%, 0.967%]
	Sampler	0.930%	[0.891%, 0.972%]	[0.888%, 0.971%]
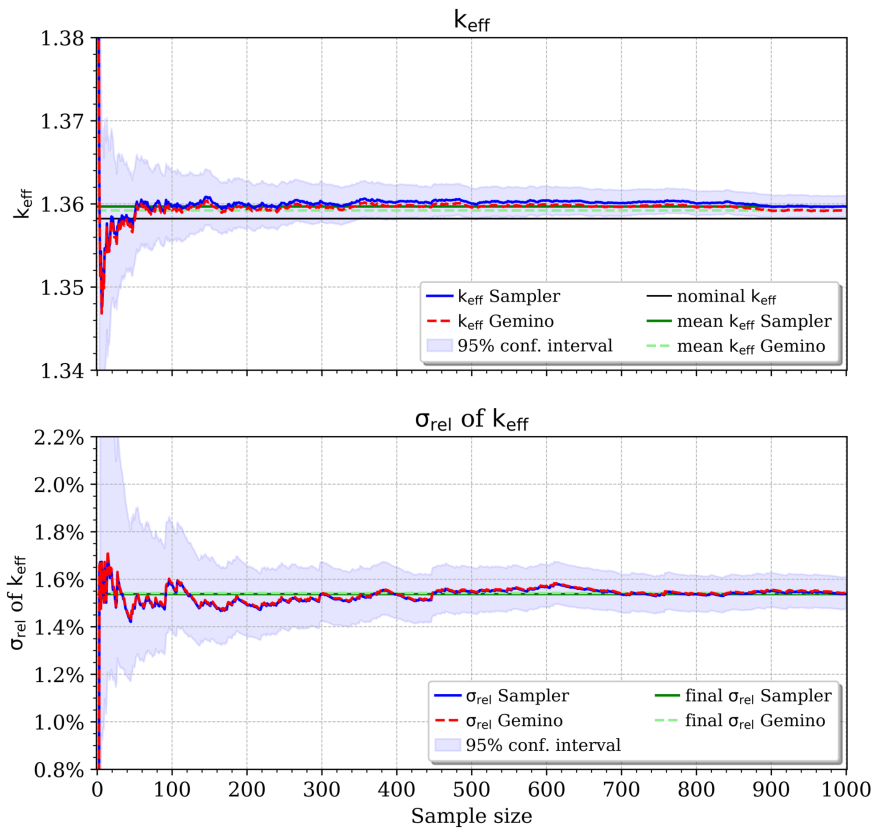
Figure 4.3 – k_{eff} and corresponding uncertainty as a function of the sample size for Gemino (explicit) and Sampler.
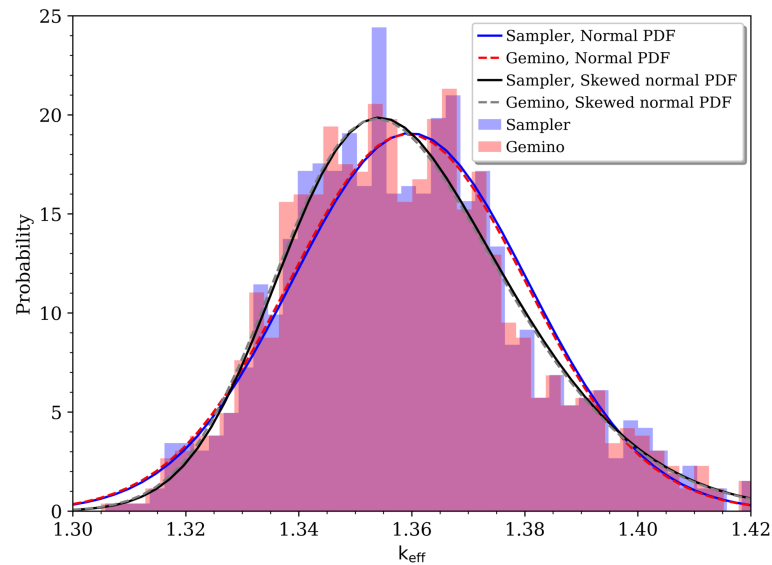
Figure 4.4 – Gemino (explicit) and Sampler k_{eff} results: histogram, approximated normal probability distribution functions (PDFs), and skewed normal PDFs.
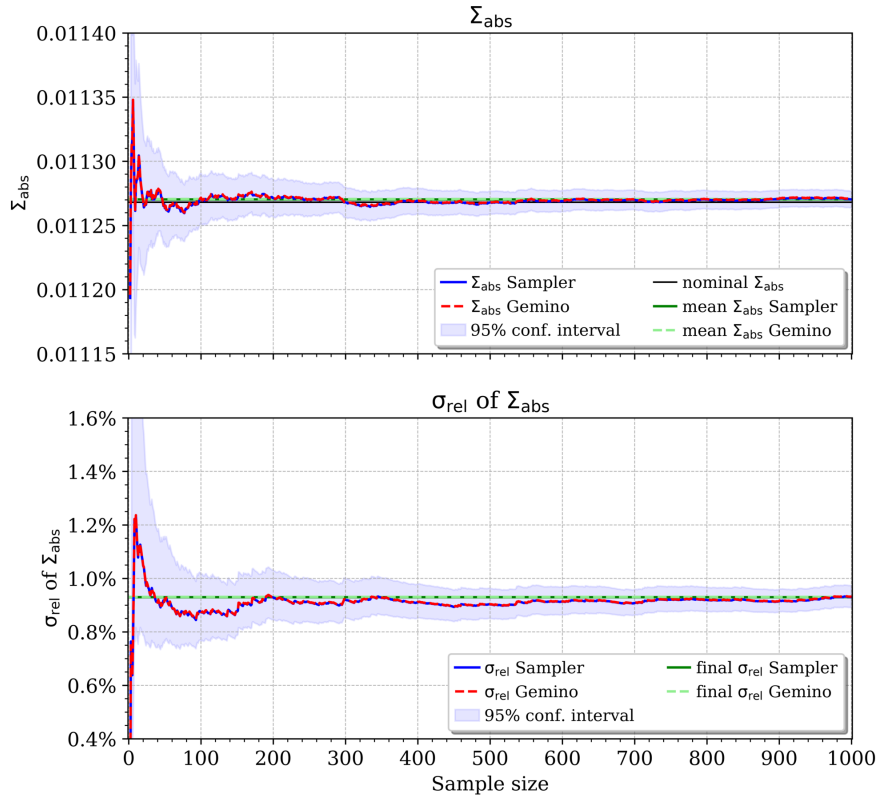
Figure 4.5 – Σ_{abs} and corresponding uncertainty as a function of the sample size for Gemino (explicit) and Sampler.
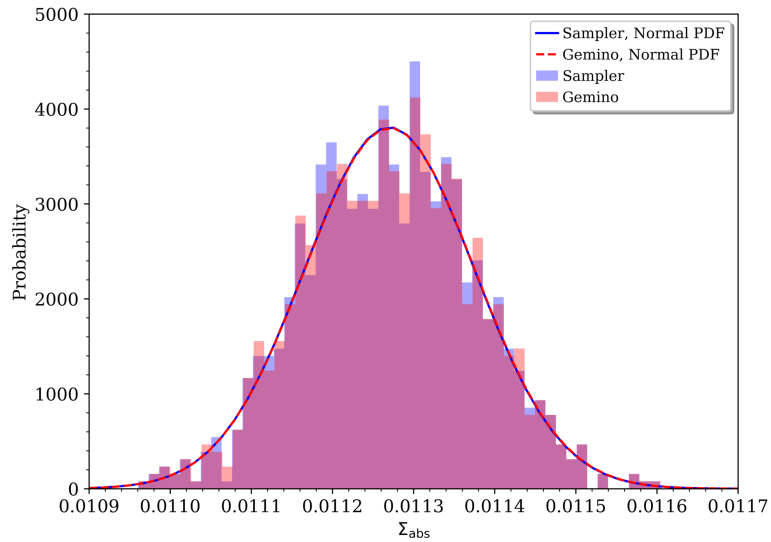
Figure 4.6 – Gemino (explicit) and Sampler Σ_{abs} results: histogram, approximated normal probability distribution functions (PDFs), and skewed normal PDFs.

As a counter example, the Σ_{abs} results are presented in Figure 4.5 and 4.6. The Gemino and Sampler mean values show very good agreement with the nominal values. Furthermore, the skewness of the Σ_{abs} histogram is so small that no visible difference between the Gaussian normal distribution and a skewed distribution is found. The Shapiro-Wilk test and the Anderson-Darling test also indicate that the output values follow a normal distribution. Nonlinear effects do not seem to play a significant role in this output quantity.

For a comparison with the results obtained from perturbation-theory, the statistical confidence intervals must be obtained. For Σ_{abs}, the confidence interval can be obtained based on the assumption of a normal distribution. For k_{eff} and Σ_{fis}, the Bootstrap method must be applied, as for both results, the tests for normal distribution have resulted in the rejection of the null hypothesis of a normal distribution. Tables 4.3 and 4.4 show confidence intervals based on both the assumption of a normal distribution and Bootstrap confidence intervals. The confidence intervals are in fact very similar. The results show excellent agreement with TSUNAMI results when considering the confidence intervals of the Sampler and Gemino results.

Finally, the computation times on a Linux cluster with 2.4 GHz AMD processors are compared for Sampler and Gemino in Table 4.5. A Sampler calculation of the MET1000 pin cell with a sample size of 1,000 takes almost 77 CPU hours to complete. The computation time with Gemino (explicit) is about 16 CPU hours, which is almost 80% shorter than for Sampler. The reduction of runtime is caused not only by performing only one self-shielding calculation with Gemino, but also by the strongly reduced runtime of Clarolplus, the module that applies the perturbations to the cross section library. In the case of Sampler, Clarolplus applies the perturbation factors on the entire multigroup cross section library, that is, on all nuclides and reactions contained in the library. In case of Gemino, the perturbations are applied to the shielded cross section library that only contains data of nuclides relevant in the model.

It should be noted that the reduction in runtime with Gemino compared to Sampler is strongly dependent on the analyzed problem. It is more apparent for investigations in which the computation time of the self-shielding calculation is a significant portion of the total runtime. The runtime advantage is also increasing with a decreasing number of nuclides in the model due to the runtime improvement of Clarolplus.

Table 4.5 – Runtime comparison between Sampler and Gemino for the MET1000 pin cell with a sample size of 1,000.

Method	Runtime [minutes]		
	Preprocessing	Neutron transport	Total
Sampler	-	-	4602.65
Gemino explicit	5.50	959.33	964.83
Gemino total	9.65	1039.43	1049.08

4.4.3   Implicit effects

To allow for consideration of implicit effects with Gemino, the Gemino sequence was extended by additional calls to TSUNAMI-1D and two new modules, Deprimo and Ferula. As part of the preprocessing, a TSUNAMI-1D calculation is performed for each specified self-shielding cell in the model under investigation. Deprimo uses the TSUNAMI-1D output to calculate the mixture-dependent sensitivities of the shielded to the unshielded cross sections (Eq. 4.13).

To reduce the runtime of Ferula, the Deprimo sensitivity output is limited to sensitivities above a certain significance level that can be provided as a user input to Deprimo: if the sensitivity values do not exceed the provided level in a single energy group, then the sensitivity of this nuclide reaction combination is not considered. The level can be controlled by an input parameter. For the Gemino calculation in this chapter, the level was set to 10^{-5}. Another option is to provide a list of nuclides for which relevant implicit effects are expected. In this way, Deprimo only considers the sensitivities of this limited number of nuclides.

Furthermore, there is a special case to be considered: if the total cross section of a nuclide is almost only dominated by one reaction x, then the differences of the total and explicit sensitivities for reaction x and the total cross section in Eq. 4.20 become almost equal in size. On the one hand, the ratio of the implicit sensitivities becomes significantly biased by the limited precision of the sensitivities as provided by the TSUNAMI output files, especially in the case of small implicit effects. On the other hand, the ratio becomes close to 1, so the sensitivity of the shielded to the unshielded reaction is almost equal to the sensitivity of the shielded cross section to the total unshielded reaction, term (1) in Eq. 4.17, leading to an over-adjustment of the perturbation factor. This is overcome by comparing the implicit sensitivities of reaction x with the total implicit sensitivities. If the difference of the corresponding

integrated values is too small, then the term is not considered. The minimum allowed differences can be controlled by an input parameter. A reasonable value for this minimum was found as 10^{-5}.

The Deprimo sensitivities are read by Ferula to modify the perturbation factors prior to their use in Clarolplus (Fig. 4.2). To allow different perturbation factors modifications that are dependent on the mixture, Ferula reads the mixture-independent original perturbation factors, modifies them, and adds them to the library as new mixture-dependent perturbation factors. Clarolplus was modified so that cross sections in a particular mixture are perturbed by perturbation factors belonging to the same mixture number. If perturbation factors are not available for this mixture, then the original perturbation factors are used.

The sensitivity of the shielded to the unshielded cross sections is determined in Deprimo for all nuclides of the MET1000 pin cell model. It is interesting to examine which shielded cross section has the largest sensitivity to which unshielded cross section. Table 4.6 provides the ten sensitivities with the largest absolute energy-integrated values. However, it must be noted that sensitivities in individual energy groups of other reactions might also be significant.

Sensitivities of various cross sections to elastic scattering cross sections are showing the largest integrated values. As an example of the energy-distribution, Figures 4.7 and 4.8 show sensitivities of ^{238}U as a function of energy. Additionally Figure 4.7 shows the top 5 integrated implicit sensitivities for the eigenvalue and the collapsed 1-group (n,γ) reaction of ^{238}U that was determined by taking the difference of the total and the explicit TSUNAMI sensitivities. For both output quantities, the sensitivity to elastic scattering of ^{238}U shows the largest implicit effect.

Direct perturbation calculation

For the first demonstration case, Gemino is applied in the direct perturbation mode. That is, instead of perturbing all cross sections at the same time based on their covariance matrices, the cross sections of a nuclide reaction are group-wise perturbed by a constant value.

The sensitivity of an output response R to a perturbation in a cross section $\Sigma_{y,g}^{j}$ of reaction y of nuclide j in energy group g in direct perturbation mode is determined based on three calculations using:

Table 4.6 – Top 10 integrated sensitivities of shielded to unshielded cross sections.

Shielded		Unshielded		Sensitivity
Nuclide	Reaction	Nuclide	Reaction	
^{56}Fe	n,γ	^{56}Fe	elastic	-7.5002
^{238}U	n,γ	^{238}U	elastic	-5.9451
^{56}Fe	elastic	^{56}Fe	elastic	-4.2922
^{240}Pu	n,γ	^{240}Pu	elastic	-3.0689
^{240}Pu	fission	^{240}Pu	elastic	-2.8636
^{238}U	elastic	^{238}U	elastic	-2.8302
^{238}U	fission	^{238}U	elastic	-2.2149
^{240}Pu	elastic	^{240}Pu	elastic	-1.7169
^{90}Zr	n,γ	^{90}Zr	elastic	-1.5948
^{94}Zr	n,γ	^{238}U	elastic	1.3883

Table 4.7 – Top 5 integrated implicit sensitivities for the eigenvalue and the collapsed 1-group cross section of ^{238}U (n,γ).

Eigenvalue			^{238}U n,γ		
^{238}U	elastic	2.398E-3	^{238}U	elastic	-1.296E-2
^{238}U	n,γ	1.419E-4	^{238}U	n,γ	-6.689E-4
^{23}Na	elastic	-6.485E-4	^{56}Fe	elastic	4.446E-3
^{239}Pu	elastic	-5.602E-4	^{23}Na	elastic	1.844E-3
^{239}Pu	fission	-1.292E-4	^{239}Pu	elastic	1.216E-3

1. the nominal input cross section $\Sigma_{y,g}^{j}$ resulting in R,

2. the cross section increased by a certain percentage, $\Sigma_{y,g}^{j,+}$, resulting in R_{+}, and

3. the cross section decreased by the same percentage, $\Sigma_{y,g}^{j,-}$, resulting in R_{-}.

The direct perturbation sensitivity coefficient of response R to $\Sigma_{y,g}^{j}$ is then computed as follows:

$$S_{R,\Sigma_{y,g}^{j}} = \frac{\Sigma_{y,g}^{j}}{R} \frac{R_{+} - R_{-}}{\Sigma_{y,g}^{j,+} - \Sigma_{y,g}^{j,-}} \tag{4.21}$$

The calculation of group-wise sensitivities with this approach leads to sensitivity profiles that can be compared with corresponding TSUNAMI calculations.

The variations must be large enough to allow for the identification of effects; but at
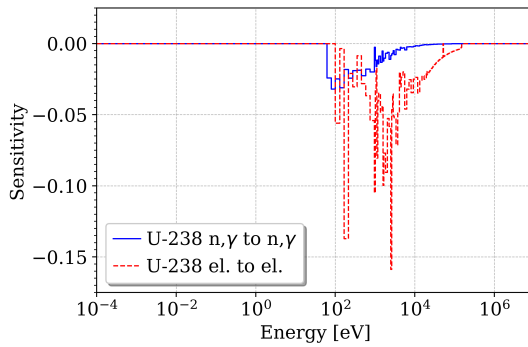
Figure 4.7 – MET1000 pin cell: Sensitivity of the shielded to the unshielded cross section for ^{238}U (n,γ) and elastic scattering.
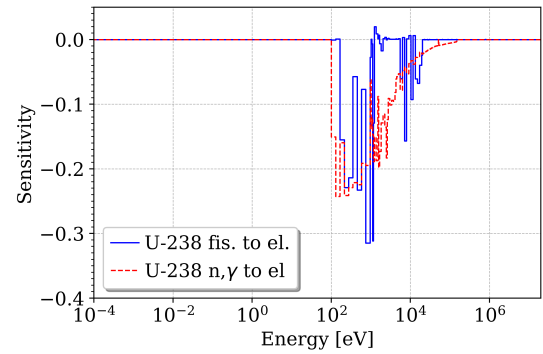
Figure 4.8 – MET1000 pin cell: Sensitivity of the shielded fission to the unshielded elastic scattering cross section and the shielded (n,γ) to the unshielded elastic scattering cross section of ^{238}U.

the same time they have to be small enough to avoid higher order effects. For the current application case of the MET1000 pin cell, these requirements are found to be met with variations of ±5%. The considered cross section is elastic scattering of ^{238}U based on the large sensitivities to this reaction found in Tables 4.6 and 4.7.

Since the 302-group cross section library is used, in addition to the nominal calculation, a total of 604 calculations are performed in which the ^{238}U elastic scattering cross sections are energy group-wise increased and decreased. The obtained sensitivity profiles are compared with profiles obtained with TSUNAMI-2D.

Figures 4.9 to 4.16 show sensitivity profiles for the multiplication factor and a collapsed 1-group cross section of ^{238}U in fuel. The first two figures compare the explicit sensitivity profiles of Gemino and TSUNAMI to show the general excellent agreement between the two approaches. The following Figures 4.11 and 4.12 compare the explicit and total sensitivity profiles obtained with Gemino. Implicit effects are clearly visible in the energy range between 10^3 and 10^5 eV, as the total sensitivities show larger absolute values in this energy range. Figures 4.13 and 4.14 show excellent agreement between the total sensitivities of Gemino and TSUNAMI, demonstrating that the approximation for implicit effects in Gemino is adequate. For reasons of completeness, Figure 4.15 and 4.16 compare the total sensitivity profiles between Sampler and Gemino, also showing excellent agreement between Sampler with its automatic consideration of implicit effects and Gemino with its linear approximation of implicit effects.
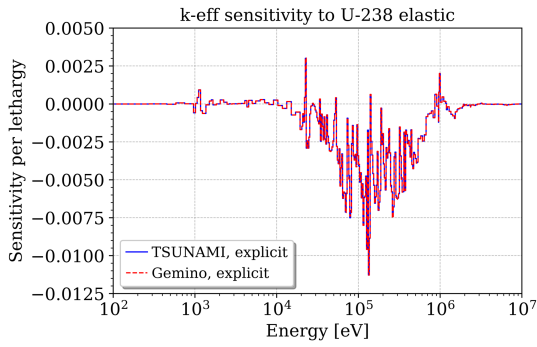
Figure 4.9 – MET1000 pin cell: explicit k_{eff} sensitivity to ^{238}U elastic scattering compared between TSUNAMI and Gemino.
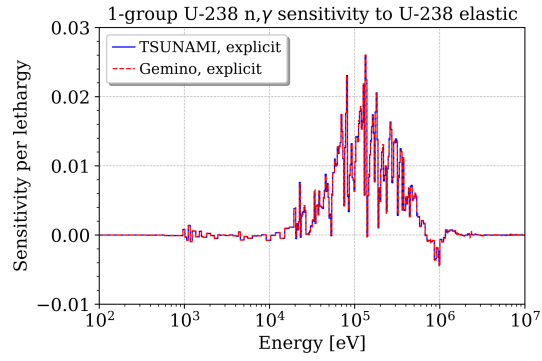
Figure 4.10 – MET1000 pin cell: explicit sensitivity of the 1-group ^{238}U (n,γ) cross section to ^{238}U elastic scattering compared between TSUNAMI and Gemino.
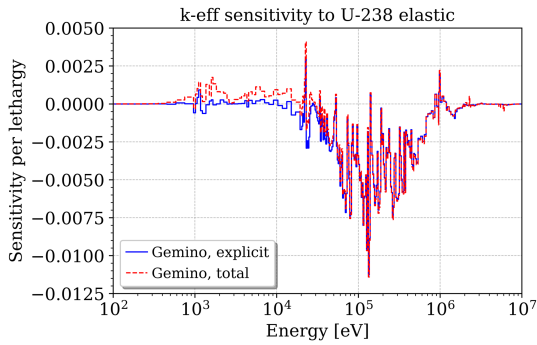
Figure 4.11 – MET1000 pin cell: k_{eff} sensitivity (explicit and total) to ^{238}U elastic scattering obtained with Gemino.
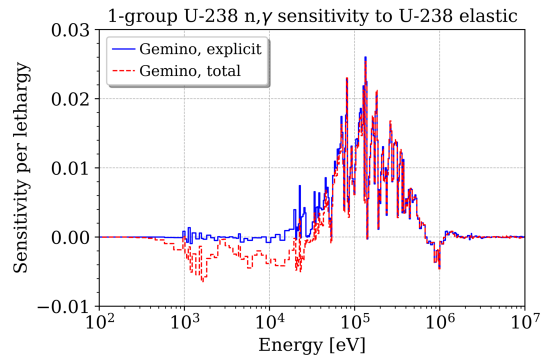
Figure 4.12 – MET1000 pin cell: sensitivity (explicit and total) of the 1-group ^{238}U (n,γ) cross section to ^{238}U elastic scattering obtained with Gemino.
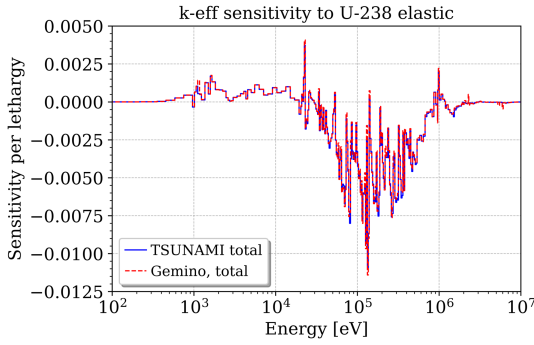
Figure 4.13 – MET1000 pin cell: total k_{eff} sensitivity to ^{238}U elastic scattering compared between TSUNAMI and Gemino.
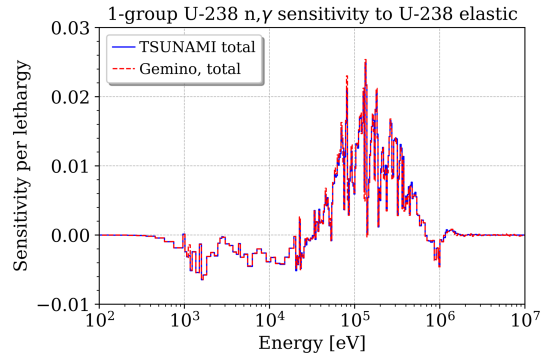
Figure 4.14 – MET1000 pin cell: total sensitivity of the 1-group ^{238}U (n,γ) cross section to ^{238}U elastic scattering compared between TSUNAMI and Gemino.
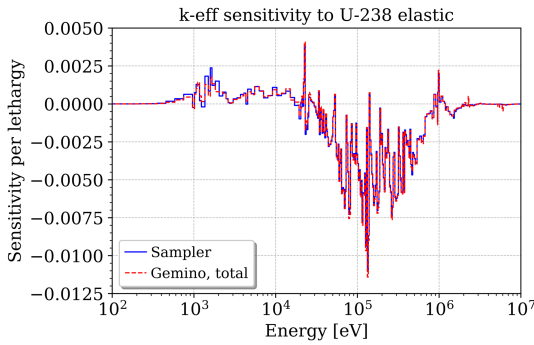
Figure 4.15 – MET1000 pin cell: Total k_{eff} sensitivity to ^{238}U elastic scattering compared between Sampler and Gemino.
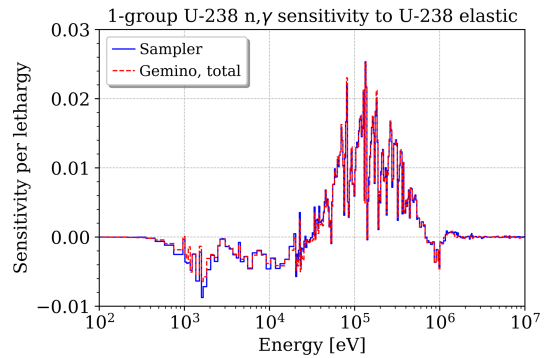
Figure 4.16 – MET1000 pin cell: total sensitivity of the 1-group ^{238}U (n,γ) cross section to ^{238}U elastic scattering compared between Sampler and Gemino.

Random sampling calculation

For the second demonstration case, Gemino is applied in the usual random sampling mode. Calculations of the MET1000 pin cell were performed for a sample size of 1,000 with Gemino with only explicit effects, with Gemino using the approximation for implicit effects, and with Sampler. Corresponding TSUNAMI calculations with and without consideration of implicit effects were also added. The uncertainties of all output quantities as requested in the UAM SFR benchmark are compared in Table 4.8.

For all output quantities except for elastic scattering of ^{56}Fe, the relative difference between the observed uncertainties is less than 0.4% (maximum absolute difference between the relative uncertainties is 0.03%); implicit effects are negligible. For elastic scattering of ^{56}Fe, slightly larger relative differences of more than 2.5% are observed between the TSUNAMI results with and without implicit effects. This difference is also visible when comparing the Gemino explicit result with the Sampler result. In contrast, the approximation of implicit effects in Gemino only shows a small effect. The sensitivity of ^{56}Fe elastic scattering is almost equal to the total sensitivity, which causes small differences in Eq. 4.20 of the approximation. For this reaction, the approximation of implicit effects is consequently limited.

The additional computation time for the consideration of implicit effects with Gemino is negligible. The preprocessing takes about 4 minutes longer due to the additional calls to TSUNAMI-1D and Deprimo, and each neutron transport calculation takes only a few seconds longer due to the application of the modifications to the perturbation factors (Table 4.5). The runtime advantage of this approach over Sampler is still significant.

Table 4.8 – MET1000 pin cell: comparison of uncertainties obtained with Sampler and Gemino.

Output quantity	TSUNAMI (explicit)	TSUNAMI (total)	Gemino (explicit)	Gemino (total)	Sampler
eigenvalue	1.520%	1.520%	1.543%	1.542%	1.538%
coolant_mic_el_23Na	5.728%	5.721%	5.789%	5.787%	5.788%
cladding_mic_el_56Fe	6.537%	6.348%	6.390%	6.370%	6.218%
fuel_mic_inel_238U	5.588%	5.588%	5.658%	5.656%	5.660%
fuel_mic_fis_238U	7.691%	7.691%	7.856%	7.859%	7.829%
fuel_mic_fis_239Pu	0.509%	0.508%	0.511%	0.510%	0.511%
fuel_mic_fis_240Pu	4.181%	4.181%	4.274%	4.283%	4.264%
fuel_mic_fis_241Pu	1.037%	1.034%	1.008%	1.007%	1.006%
fuel_mic_fis_242Pu	5.532%	5.532%	5.616%	5.617%	5.604%
fuel_mic_n_gam_238U	1.813%	1.819%	1.819%	1.808%	1.816%
fuel_mic_n_gam_239Pu	6.713%	6.709%	6.552%	6.543%	6.548%
fuel_mic_n_gam_240Pu	4.272%	4.270%	3.955%	3.942%	3.951%
fuel_mic_n_gam_241Pu	18.228%	18.227%	16.398%	16.382%	16.401%
fuel_mic_n_gam_242Pu	4.419%	4.414%	4.427%	4.422%	4.421%
fuel_mac_fis	1.542%	1.541%	1.573%	1.574%	1.569%
fuel_mac_abs	0.965%	0.967%	0.931%	0.930%	0.930%

5 Sensitivity analysis methods

While the identification of the top contributing nuclide reactions to the output uncertainty is a side product when using perturbation theory, a similar study is challenging for the random sampling approach because the reliability of sensitivity results depends on the large number of uncertain input parameters and the sample size. Since the analysis using linear perturbation theory is limited to a certain number of output responses, it is nevertheless desirable with the random sampling approach to identify important nuclide reactions contributing to the uncertainty of additional safety-relevant output quantities such as peak power or various reactivity coefficients.

One method for determining the contribution of individual cross sections to the output uncertainty in random sampling calculations involves one at a time calculations: If the cross sections of one nuclide reaction are perturbed and calculations are performed based on only these perturbations, then the statistical analysis results in the output uncertainty are caused only by this nuclide reaction. However, this approach requires one additional set of calculations for each nuclide reaction, and it also does not consider correlations between different nuclide reactions. Ideally, the calculation of importance indicators should consider correlations and should be computationally inexpensive.

With XSUSA, the sensitivity analysis has so far involved the analysis of the squared multiple correlation coefficient R^2 (Bostelmann et al., 2015b). Within this work, the analysis is extended by determining an additional sensitivity index: the semi-partial multiple squared correlation coefficient SPC^2. So far, this index has only been investigated in sampling-based uncertainty analyses with input parameters other than nuclear data (Glaeser, 2008, 2012). R^2 and SPC^2 provide two complementary ways

of determining the uncertainties' contribution of a nuclide reaction to the output uncertainty.

To compare R^2 and SPC^2 with results from linear perturbation theory, variance-based sensitivity indices were developed that correspond to R^2 and SPC^2 and that can be calculated using the standard output when using perturbation theory.

This chapter provides the mathematical description and the interpretation of sensitivity indices as importance indicators to identify the most significant nuclide reactions for output uncertainties. The first part describes the variance-based sensitivity indices, the so-called Sobol' main effect and total effect sensitivity indices. Afterwards, the sensitivity indices R^2 and SPC^2 for the random sampling approach and the perturbation theory are introduced. The chapter concludes with a demonstration of the various approaches using volume-homogenized mixtures of the MET1000 fuel assembly model.

The following descriptions are generally valid for any set of input parameters and for any output quantity of any code for which the determination of sensitivity indices is desired as part of the output analysis. For nuclear data uncertainties, the following denotation is valid: input parameters are the nuclear cross sections of nuclide reactions in a particular energy-group structure. That is, each cross section of a particular energy group is an individual parameter. A parameter group includes all the cross sections of an individual nuclide reaction. The cross sections relevant in a model are usually divided into two groups: group A includes the group of cross sections of interest (Σ_A), usually all the cross sections of a particular nuclide reaction; and group B includes all other cross sections of the model (Σ_B). The output quantity of interest is indicated by Y.

5.1 Variance-based sensitivity indices

Variance-based sensitivity analysis, sometimes referred to as Sobol' method in the case of independent parameters, is used to determine the influence of individual input parameters or groups of parameters on the variance of the model output (Sobol, 1993; Saltelli et al., 2008, 2010). Given the model $Y=f(\Sigma_A, \Sigma_B)$, with Y the scalar output quantity of interest, A, the group of input parameters under consideration, and B, the complementary (residual) group, then the reductive effect variance-based sensitivity index (first-order sensitivity index, or **S**obol's **M**ain effect sensitivity index in case of

independent parameters), is defined as follows:

$$SM_A = \frac{Var\ (\mathrm{E}[Y|\Sigma_A])}{Var\,(Y)} = \frac{Var\,(Y) - \mathrm{E}\,[Var\,(Y|\Sigma_A)]}{Var\,(Y)} = 1 - \frac{\mathrm{E}\,[Var\,(Y|\Sigma_A)]}{Var\,(Y)}\,.$$

(5.1)

SM_A is the relative variance of the conditional expectation of Y given A, i.e. the best approximation of Y in the parameters of group A. It also reveals the variance reduction of Y that is expected if the true values of parameter group A were to become known. This factor consequently indicates for which group of input parameters, the reduction of uncertainties would lead to a significant reduction of the total output uncertainty. In the case of nuclear data uncertainties, SM_A can point out the nuclide reaction for which reduced cross section uncertainties due to more accurate measurements would result in significantly improved the results.

The incremental sensitivity index (**S**obol's **T**otal effect sensitivity index in case of independent parameters) can be expressed as follows:

$$ST_A = \frac{\mathrm{E}\,[Var\,(Y|\Sigma_B)]}{Var\,(Y)} \overset{(Eq.\ 5.1)}{=} 1 - SM_B\,.$$

(5.2)

ST_A reveals the remaining variance that is expected if the true values of the complementary group B were to become known.

Krzykacz-Hausmann (Krzykacz-Hausmann, 2006) showed that the expression for SM_A in Eq. 5.1 is equal to the sample Pearson correlation coefficient r between the output Y and the conditional expectation $\mathrm{E}[Y|\Sigma_A]$:

$$SM_A = \frac{Var\ (\mathrm{E}[Y|\Sigma_A])}{Var\,(Y)} = r\,(Y, \mathrm{E}\,[Y|\Sigma_A])\,.$$

(5.3)

For the practical application, this means that the correlation between the output of two sets of calculations is calculated as follows:

1. The first reference set of calculations is based on the standard randomly sampled input parameters, generated as described in Appendix A.3.

2. The second set of calculations is based on input parameters generated using conditional sampling: the sampled parameters of group A are identical with the reference set, and a new set of new randomly sampled parameters is generated only for group B based on the known perturbations of groups A. This conditional sampling is described in more detail in Appendix A.3.2.

Accordingly, the incremental sensitivity index is calculated based on the correlation of the reference set of calculations and a second set using newly generated perturbations for group A while keeping the perturbations of group B from the reference set:

$$ST_A = 1 - SM_B = 1 - r\left(Y, \mathrm{E}\left[Y | \Sigma_B\right]\right). \tag{5.4}$$

With a sample size N, the sample correlation coefficient between two quantities a and b is determined from their covariance and the standard deviations σ:

$$r\left(A, B\right) = \frac{Cov(A, B)}{\sigma_A \sigma_B} = \frac{\sum\limits_{i=1}^{N} (a_i - \bar{a})\left(b_i - \bar{b}\right)}{\sqrt{\sum\limits_{i=1}^{N} (a_i - \bar{a})^2} \sqrt{\sum\limits_{i=1}^{N} \left(b_i - \bar{b}\right)^2}}, \tag{5.5}$$

with $\bar{a}$ and $\bar{b}$ being the mean values of a and b, respectively.

The confidence intervals of SM_A and ST_A are determined by using the standard approach to calculate the confidence interval of the sample correlation coefficient r via Fisher's z transformation (Draper and Smith, 1998):

$$z = \frac{1}{2} \ln\left(\frac{1+r}{1-r}\right). \tag{5.6}$$

If Y and $Y|\Sigma_B$ are normally distributed with correlation ρ, for which r is an estimate, then z is approximately normally distributed,

$$z \sim N\left(\mu_z, \sigma_z^2\right), \tag{5.7}$$

with expected value

$$\mu_z = \frac{1}{2} \ln\left(\frac{1+\rho}{1-\rho}\right) \qquad (5.8)$$

and variance

$$\sigma_z^2 = \frac{1}{N-3} . \qquad (5.9)$$

The lower and upper bounds of the corresponding confidence interval of z are given by

$$z_L = \mu_z - \frac{q_{\alpha/2}}{\sqrt{N-3}}, \qquad z_U = \mu_z + \frac{q_{\alpha/2}}{\sqrt{N-3}}, \qquad (5.10)$$

with $q_{\alpha/2}$ being the quantile of the normal distribution (1.96 for a confidence level of 95%). The back transformations of these bounds result in the confidence interval of the correlation coefficient:

$$\left[\frac{e^{2z_L}-1}{e^{2z_L}+1}, \frac{e^{2z_U}-1}{e^{2z_U}+1}\right] = [\tanh(z_L), \tanh(z_U)] . \qquad (5.11)$$

For two sample sizes, the development of the relative 95% confidence interval as a function of the sample correlation coefficient is presented in Figure 5.1. Due to the symmetry of the confidence interval, the interval is only presented for positive correlations. It is interesting to note that the confidence interval is increasing rapidly for correlation coefficients below about 0.3.

While the determination of SM_A and ST_A seems to be a straightforward calculation, it requires a large computational effort because additional sampling calculations are required for each parameter group of interest. For example, when using a sample size of 1,000 and when considering an average of about six reactions per nuclide, a problem with only 10 nuclides requires 61,000 individual calculations to determine either SM_A or ST_A for all nuclide reactions. For the purpose of a simple determination of a sensitivity index based on only a single set of sampling calculations, it is more practical to use linearized versions of SM_A and SM_B, respectively, as explained in the following section.
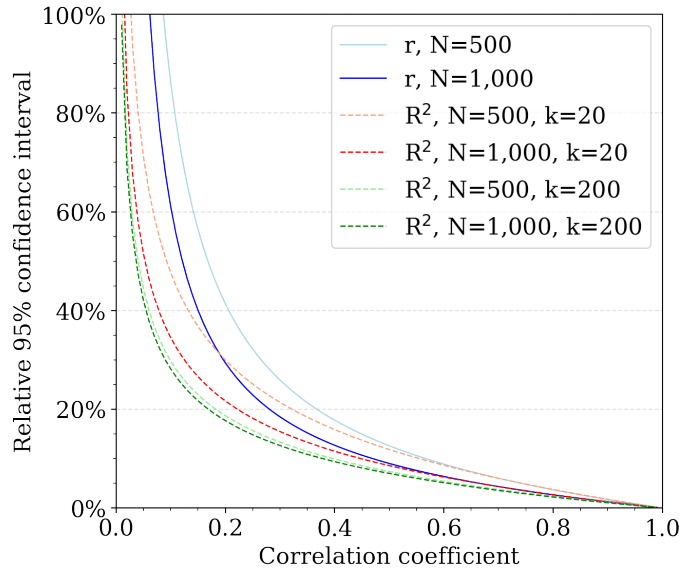
Figure 5.1 – Relative 95% confidence interval of the sample correlation coefficient r and the squared multiple correlation coefficient R^2 for a sample size of 1,000.

5.2   Correlation-based sensitivity indices using randomly sampled input parameters

This section includes the explanation of linearized versions of the variance-based sensitivity indices SM_A and SM_B.

5.2.1 R^2 - squared multiple correlation coefficient

By the application of a linear regression model, it is shown in (Kshirsagar, 1972) that a linearized version of the reductive effect sensitivity index SM_A is found in the *squared multiple correlation coefficient* R^2. This coefficient is determined from correlations of the calculated output quantity Y with the sampled input parameters Σ_A of group A while accounting for correlations between the input parameters (Glaeser, 2008, 2012):

$$R^2_{Y,A} = \ \boldsymbol{r}_{Y,A} \, \mathbf{C}^{-1}_{AA} \, \boldsymbol{r}^{t}_{Y,A}, \tag{5.12}$$

with vector $\boldsymbol{r}_{Y,A}$ of size k containing the sample correlation coefficients between the output Y and the input parameters of group A:

$$\boldsymbol{r}_{Y,A} = \ (r\,(Y,\Sigma_1)\,,...,r\,(Y,\Sigma_k))\,, \tag{5.13}$$

and matrix $\mathbf{C}_{AA}$ of size $(k \times k)$ containing the sample correlation coefficients between the input parameters:

$$\mathbf{C}_{AA} = \begin{pmatrix} r\,(\Sigma_1, \Sigma_1) & r\,(\Sigma_1, \Sigma_2) & \cdots & r\,(\Sigma_1, \Sigma_k) \\ r\,(\Sigma_2, \Sigma_1) & r\,(\Sigma_2, \Sigma_2) & \cdots & r\,(\Sigma_2, \Sigma_k) \\ \vdots & \vdots & \ddots & \vdots \\ r\,(\Sigma_k, \Sigma_1) & r\,(\Sigma_k, \Sigma_2) & \cdots & r\,(\Sigma_k, \Sigma_k) \end{pmatrix}. \tag{5.14}$$

It is important to stress that here the correlation matrix is not the population correlation matrix that was initially used for the random sampling. Rather, it is the matrix containing the sample correlation coefficients between the sampled input parameters. If the sample size approaches infinity, then the sample correlation matrix converges toward the correlation matrix that is used for sampling.

R^2 is a measure of the linear dependency between the output Y and the input parameter group. Analogous to the interpretation of SM_A, R^2 can be interpreted as the expected amount by which the total output variance would be reduced if the true values of the input parameter group A become known (Glaeser, 2008). In other words, R^2 captures the contribution to the output variance caused by the uncertainties of parameter group A, including the fraction of uncertainties that it has in common with other parameter groups due to dependencies (Glaeser, 2012). Given the definition of R^2 above, these statements only hold with respect to linear effects.

R^2 has the following characteristics:

- $0 < R^2_{Y,A} < 1$, with the above given interpretation,

- $R^2_{Y,A} = 0$ if Y does not have a linear dependence on A (i.e., Y is not linearly correlated to any of the sampled input parameters in group A),

- $R^2_{Y,A} = 1$ if Y is a linear function of only the sampled input parameters in group A, and

- $R^2_{Y,A} = r^2_{Y,A}$ if the parameter group A only consists of a single parameter (i.e., R^2 corresponds in this case to the squared sample correlation coefficient).

R^2 can be determined from the results of a single set of calculations for any group of parameters. The only condition for determining this coefficient is that the sample

size N must be larger than the number of parameters k in the group of interest; if the sample size is smaller than k, matrix $\mathbf{C}_{AA}$ is not positive definite, and consequently, it cannot be inverted. For the same reason, input parameters within a group must not have a total linear correlation. This problem is avoided by only considering the independently sampled input parameters in the analysis (see Appendix A.3).

Total $\mathbf{R}^2$

If the parameter group A includes all the input parameters of the model under investigation, then the total correlation coefficient R^2 can be determined. If nonlinear effects are insignificant, then we have:

$$Var\ (Lin\,[Y|\Sigma]) = Var\,(Y) \quad \Rightarrow \quad R^2 = R_{Y,A+B}^2 = R_{\text{tot}}^2 = 1\,. \tag{5.15}$$

Conversely, the calculation of R_{tot}^2 allows for the assessment to determine whether nonlinear effects are negligible: if R_{tot}^2 shows a significant deviation from 1 when all input parameters are considered, then it can be concluded that the output uncertainty is significantly influenced by nonlinear effects.

Adjusted $\mathbf{R}^2$

It is important to note that R_{tot}^2 approaches 1 if the sample size N is close to the number of sampled input parameters k in the model. This can be explained by the fact that R_{tot}^2 corresponds to the coefficient of determination for regression analysis that is dependent on the difference between N and k, the degrees of freedom in a problem. If $N - k$ is getting smaller, then R_{tot}^2 converges to 1 because, in this case, it is fitted to all or almost all the degrees of freedom in this regression analysis.

To consider the dependence on the degrees of freedom, the coefficient of determination can be adjusted (Golberg and Cho, 2004):

$$\overline{R}^2 = 1 - \left(1 - R^2\right) \frac{N-1}{N-k-1}\,. \tag{5.16}$$

Since $\frac{N-1}{N-k-1} > 1$, it can be shown that $\overline{R}^2 < R^2$. This means that R^2 is overestimated,

and the adjustment leads to a slight reduction.

Figure 5.2 presents the bias $R^2 - \overline{R}^2$ as a function of R^2 for various sample sizes. The sample sizes are chosen as multiples of k ($N = x \cdot k$) to demonstrate the magnitude of adjustment depending on the degrees of freedom. When considering all relevant parameters in the determination of R^2_{tot} such that R^2_{tot} is close to 1, the bias is significant when N is only slightly larger than k. The closer the sample size is to k, the larger the overestimation of R^2, or the closer R^2 is to its upper limit of 1. Since all curves decrease with increasing R^2 and end at a zero bias for $R^2 = 1$, a slight increase of the sample size to, for example, $1.5\,k$ or $2\,k$ leads to a much smaller bias. Furthermore, it can be observed that the bias is close to negligible if the sample size is larger than k by a factor of 10 or more. When applying the adjustment to the group-wise R^2 of Section 5.2.1 in a calculation based on the 17-group covariance with a sample size of 1,000, N is almost 59 times larger than k, so the largest bias is small at less than 0.017.
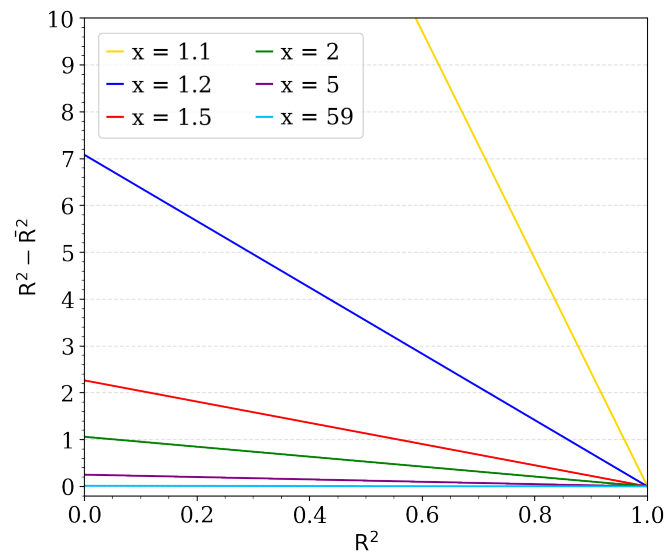
Figure 5.2 – Difference between R^2 and the corresponding adjusted value $\overline{R}^2$ as a function of R^2 for sample sizes $N = x \cdot k$, with $k = 17$.

Confidence interval

To express uncertainty due to sampling with a limited sample size, a confidence interval for R^2 can be determined as follows (Cohen, 2003; Müller, 1980):

$$\left[R^2 - q_{\alpha/2} \cdot \sigma, R^2 + q_{\alpha/2} \cdot \sigma \right],$$ (5.17)

with the standard deviation:

$$\sigma = \sqrt{\frac{4R^2(1-R^2)^2(N-k-1)^2}{(N^2-1)(N+3)}}.$$ (5.18)

For 95% confidence, $q_{\alpha/2} = 1.96$ is the corresponding quantile of the normal distribution. The development of the relative 95% confidence interval as a function of R^2 is presented in Figure 5.1. Due to the symmetry of the confidence interval, only the upper confidence level is presented. Like the confidence interval for the Pearson sample correlation coefficient r, the confidence interval for R^2 is increasing rapidly for correlation coefficients below about 0.3. It is thereby smaller than the corresponding interval for r. For k= 20, the R^2 interval matches the corresponding r interval for correlation coefficients above 0.5. It is interesting to note that the R^2 confidence interval for k=20 is smaller than the corresponding interval for k=200. This is counterintuitive since the degrees of freedom are reduced for larger k.

Significance bound

The significance bound of R^2 is determined using the assumption that the multiple correlation is zero if the parameter group of interest is insignificant for the system under consideration, or if the output is independent of the sampled input parameters. In this case, R^2 follows the beta distribution with $p = k$ and $q = N - k - 1$ (Müller, 1980). The 95% significance bound (α=0.95), which is the level at which the hypothesis that R^2 is independent of the perturbed input parameters is rejected, is therefore calculated using the inverse cumulative beta distribution function:

$$R^2_{sign} = BetaCDF^{-1}\left(\alpha; p, q\right) = BetaCDF^{-1}\left(0.95; \frac{k}{2}, \frac{N-k-1}{2}\right).$$ (5.19)

This is valid if the input parameters are normally distributed. Each calculated R^2 value should be tested for significance.

5.2.2 SPC^2 - squared semi-partial multiple correlation coefficient

As in the incremental sensitivity index ST_A, an additional importance indicator with a different interpretation can be determined basically as a linearized version of ST_A. The so-called *squared semi-partial multiple correlation coefficient* SPC_A^2 for a parameter group A is defined as follows (Glaeser, 2008, 2012):

$$SPC_{Y,A}^2 = R_{Y,A+B}^2 - R_{Y,B}^2. \tag{5.20}$$

$R_{Y,A+B}^2$ is the total squared multiple correlation coefficient between the output Y and all parameters A and B, and $R_{Y,B}^2$ is the squared multiple correlation coefficient between the output Y and the complementary group B. Due to the subtraction of these two coefficients, $SPC_{Y,A}^2$ is sometimes also called *incremental R^2*. It is a measure of the linear dependency between the output Y and the input parameter group A after excluding linear influences of the complementary group B on group A. Influences of the complementary parameter group on the output still remain (Glaeser, 2012). Analogous to the interpretation of ST_A, $SPC_{Y,A}^2$ describes the variance of the output quantity which is expected to remain when the true values of the complementary parameter group B become known (Glaeser, 2008). In other words, $SPC_{Y,A}^2$ is the fraction of the variance that group A adds to the variance caused by group B (Glaeser, 2012). Given the definition of R^2 above, these statements only apply with respect to linear effects.

As with R^2, SPC^2 can also be determined from the results of a single set of calculations for any group of parameters. However, the sample size must be larger than the number of parameters considered for the determination of $R_{Y,A+B}^2$ and $R_{Y,B}^2$. Since $R_{Y,A+B}^2$ is the *total* multiple correlation coefficient, the sample size must be significantly larger than the *total* number of sampled parameters that are relevant for the system under consideration. Already for a simple problem with only a few nuclides, the required sample size can be very large (see discussion in Section 3.2.1).

Confidence interval

With the sample size N and the quantile of the normal distribution $q_{\alpha/2}$, the confidence interval of SPC^2 is as follows (Algina, 2008):

$$\left[SPC^2_{Y,A} - q_{\alpha/2} \cdot \sigma, SPC^2_{Y,A} + q_{\alpha/2} \cdot \sigma \right] \tag{5.21}$$

with

$$\sigma = \sqrt{\phi_f + \phi_r - 2 * \phi_{fr}}, \qquad r_{ab} = \sqrt{\frac{R^2_{Y,B}}{R^2_{Y,A+B}}},$$

$$\phi_f = \frac{4}{N} \, R^2_{Y,A+B} \left(1 - R^2_{Y,A+B}\right)^2, \qquad \phi_r = \frac{4}{N} \, R^2_{Y,B} \left(1 - R^2_{Y,B}\right)^2,$$

$$\phi_{fr} = \frac{4}{N} \sqrt{R^2_{Y,A+B} R^2_{Y,B}} \left[\frac{1}{2} \left(2 r_{ab} - \sqrt{R^2_{Y,A+B} R^2_{Y,B}}\right) \left(1 - R^2_{Y,A+B} - R^2_{Y,B} - r^2_{ab}\right) \right] + r^3_{ab}.$$

Adjusted SPC^2

When considering the adjustment of R^2 using Eq. 5.16, it is possible to derive an adjusted SPC^2 based on Eq. 5.20 to consider the limited degrees of freedom:

$$\overline{SPC}^2_{Y,A} = \overline{R}^2_{Y,A+B} - \overline{R}^2_{Y,B}. \tag{5.22}$$

For a large total number of independent parameters k in the calculation, is it reasonable to assume that the number of independent parameters considered in the calculations of $\overline{R}^2_{Y,A+B}$ and $\overline{R}^2_{Y,B}$ is approximately identical because the maximum difference is the number of energy groups in the covariance library. With this assumption, it is possible to simplify the calculation of the adjusted SPC^2 as follows:

$$\overline{SPC}^2_{Y,A} \approx \left(R^2_{Y,A+B} - R^2_{Y,B} \right) \left(\frac{N-1}{N-k-1} \right). \tag{5.23}$$

5.3 Variance-based sensitivity indices using sensitivity coefficients from linear perturbation theory

In case of linear perturbation theory, the sensitivity coefficients $S_{Y,\Sigma^i_{x,g}}$ of the output quantity Y with respect to the input parameters $\Sigma^i_{x,g}$ are obtained for each input parameter (nuclide i, reaction x, energy group g). The application of first-order uncertainty propagation in which the vector of all sensitivity coefficients is multiplied with the total covariance matrix leads to the total output variance (see Section 4.1).

If the total covariance matrix $\mathbf{C}$ is divided into submatrices according to parameter group A and the complementary group B:

$$\mathbf{C} = \begin{pmatrix} \mathbf{C}_{AA} & \mathbf{C}_{AB} \\ \mathbf{C}_{BA} & \mathbf{C}_{BB} \end{pmatrix}, \tag{5.24}$$

then the expected conditional variances $Var(Y|\Sigma_A)$ and $E[Var(Y|\Sigma_B)]$ of Y, given parameter group A and B, respectively, can be expressed by applying the conditional covariance matrices $\mathbf{C}_{B|A}$ or $\mathbf{C}_{A|B}$, respectively, as follows:

$$E[Var(Y|\Sigma_A)] = \mathbf{S}^t_{Y,B}\,\mathbf{C}_{B|A}\,\mathbf{S}_{Y,B} = \mathbf{S}^t_{Y,B}\left(\mathbf{C}_{BB} - \mathbf{C}_{BA}\,\mathbf{C}^{-1}_{AA}\,\mathbf{C}_{AB}\right)\mathbf{S}_{Y,B}, \tag{5.25}$$

$$E[Var(Y|\Sigma_B)] = \mathbf{S}^t_{Y,A}\,\mathbf{C}_{A|B}\,\mathbf{S}_{Y,A} = \mathbf{S}^t_{Y,A}\left(\mathbf{C}_{AA} - \mathbf{C}_{AB}\,\mathbf{C}^{-1}_{BB}\,\mathbf{C}_{BA}\right)\mathbf{S}_{Y,A}. \tag{5.26}$$

Vectors $\mathbf{S}_{Y,A}$ and $\mathbf{S}_{Y,B}$ thereby contain all sensitivity coefficients for group A and B, respectively.

Sensitivity indices corresponding to R^2 and SPC^2 can be obtained by using these expressions in the formulation of reductive effect sensitivity index SM_A and the incremental sensitivity index ST_A, as defined in Section 5.1:

$$R^2_{Y,A} = \frac{\mathbf{S}^t_{Y,A+B}\,\mathbf{C}\,\mathbf{S}_{Y,A+B} - \mathbf{S}^t_{Y,B}\left(\mathbf{C}_{BB} - \mathbf{C}_{BA}\,\mathbf{C}^{-1}_{AA}\,\mathbf{C}_{AB}\right)\mathbf{S}_{Y,B}}{\mathbf{S}^t_{Y,A+B}\,\mathbf{C}\,\mathbf{S}_{Y,A+B}}, \tag{5.27}$$

$$SPC^2_{Y,A} = \frac{\mathbf{S}^t_{Y,A}\left(\mathbf{C}_{AA} - \mathbf{C}_{AB}\,\mathbf{C}^{-1}_{BB}\,\mathbf{C}_{BA}\right)\mathbf{S}_{Y,A}}{\mathbf{S}^t_{Y,A+B}\,\mathbf{C}\,\mathbf{S}_{Y,A+B}}. \tag{5.28}$$

The matrices $\mathbf{C}_{BB}$ and $\mathbf{C}_{BB}$ often contain rows/columns with only zero records. To allow the inversion of the matrices, those rows/columns must removed, along with the corresponding rows/columns in matrices $\mathbf{C}_{AB}$ and $\mathbf{C}_{BA}$. If the matrices are not positive definite after this modification, then their off-diagonal elements must be adjusted slightly, as it is done during pre-processing for the random sampling of nuclear data (see Appendix A.3).

It is important to note that in a perturbation theory–based uncertainty analysis, a list of individual contributions of the covariance matrices to the output uncertainty is usually provided. These contributions are determined from first-order uncertainty propagation applied to individual covariance matrices for parameter group A. However, the output of this expression only corresponds to the total contribution of parameter group A to the output uncertainty if this parameter group is independent of all other parameter groups, or if there is no correlation of the investigated nuclide reaction to other nuclide reactions. As soon as there are correlations between parameter groups (i.e., between nuclide reactions), this expression is not suitable for describing the total contribution of a nuclide reaction to the output uncertainty. The contribution of the correlation between two nuclide reactions is listed as a separate record in the list of contributions. Since the individual contributions cannot be combined to obtain total contributions of nuclide reactions in practice, it is not possible to assess the total contribution of a nuclide reaction with an appropriate consideration or interpretation of correlations to other nuclide reactions. This gap is closed by the determination of R^2 and SPC^2, as presented above.

5.4 Demonstration

For demonstration purposes, the sensitivity indices R^2 and SPC^2 were determined with all presented approaches:

1. Sobol's main and total sensitivity indices were determined using a nominal set of random sampling calculations with a sample size of 1,000 and additional sets of Gemino calculations for each nuclide reaction of interest with a sample size of always 1,000,

2. correlation-based indices were obtained by post-processing random sampling calculations with Gemino using various sample sizes, and

3. variance-based sensitivity indices were calculated based on sensitivity coefficients from TSUNAMI sensitivity files.

To understand the influence of the number of independently sampled cross sections in the model, three different homogeneous mixtures were chosen to demonstrate the application of R^2, R^2_{tot} and SPC^2. Table 5.1 lists the nuclides in the three mixtures; the nuclide densities are thereby taken from the volume-homogenization of the MET1000 fuel assembly (see Section 3.1). The nuclides in these mixtures were chosen based on the analysis of R^2 of a model containing all nuclides of the volume-homogenized MET1000 fuel assembly: mixture 1 contains five nuclides that contribute most to the eigenvalue uncertainty, and for mixtures 2 and 3, nuclides were added accordingly.

Table 5.1 – Mixture compositions and number of independently sampled cross sections k for the analysis of SPC^2.

Mix	#Nuc	Composition	k
1	5	^{238}U ^{239}Pu ^{240}Pu ^{23}Na ^{56}Fe	371
2	20	Mixture 1 + ^{242}Pu ^{241}Am ^{243}Am ^{244}Cm ^{52}Cr ^{53}Cr ^{54}Fe ^{90}Zr ^{91}Zr ^{92}Zr ^{94}Zr ^{92}Mo ^{96}Mo ^{98}Mo ^{55}Mn	1161
3	35	Mixture 2 + ^{50}Cr ^{54}Cr ^{57}Fe ^{58}Fe ^{58}Ni ^{60}Ni ^{96}Zr ^{94}Mo ^{95}Mo ^{97}Mo ^{100}Mo ^{235}U ^{237}Np ^{238}Pu ^{241}Pu	1993

In all cases, the 302-group cross section library and cross section perturbations based on the 17-group covariance library were used. The output quantities of interest are

requested quantities within the UAM-SFR benchmark: the eigenvalue k_{eff} and the 1-group macroscopic absorption cross section Σ_{abs}. The consistency between TSUNAMI and Gemino with regard to output uncertainties was already shown in Section 4.4. The following demonstration is therefore limited to the sensitivity analysis.

5.4.1 Squared multiple correlation coefficient R^2

The maximum number of independently sampled cross sections considered in the R^2 calculation with Gemino is 17 for the 17-group covariance library. Therefore, it is expected that a number of top contributors to the eigenvalue can be obtained with a reasonably small sample size in the range of a few hundred.

The most important nuclide reactions for the output uncertainties in terms of R^2 are displayed in Figure 5.3 for the three investigated mixtures. The Gemino R^2 values were not adjusted since the sample size is almost 59 times larger than the number of independently sampled parameters in the calculation of R^2, and the impact of an adjustment is therefore negligible (see Figure 5.2).

Both the Sobol and the Gemino values are shown with their corresponding 95% confidence intervals displayed as error bars. For Σ_{abs}, the Sobol confidence intervals are larger than the corresponding Gemino confidence intervals for a sample size of 1,000 because the sample correlation coefficient used to determine Sobol's indices has a larger 95% confidence interval than Gemino's R^2 if the correlation coefficient is smaller than about 0.5 (see Figure 5.1).

The Gemino results are also accompanied with their significance bound. For example, elastic scattering of ^{238}U shows an R^2 value for the eigenvalue that is larger than 0.7 for a sample size of 250 (light green column). The darker shaded column above, reaching up to about 0.1, represents the 95% significance bound: since the R^2 value is largely above this bound, this R^2 value can be considered statistically relevant. Values for R^2 are displayed only if they are larger than their significance bound. This explains why some columns are missing for some reactions. Results for various sample sizes were compared to determine whether a reduced sample size is sufficient when determining the most important nuclide reactions with Gemino.

The most important nuclide reactions for the uncertainties of k_{eff} of all mixtures were identified as elastic and inelastic scattering of ^{238}U. The contributions of all

other reactions are negligible: the TSUNAMI values are very small, the Gemino values are only barely above the corresponding significance bound, and Sobol's indices are negative (not displayed), or they show overlapping error bars with 0.0. The obtained values with all approaches are thereby in excellent agreement when considering the provided error bars.

While it is observed in Section 3.2 that large uncertainties in the high energy range of the inelastic scattering cross section of ^{238}U cause large output uncertainties in SFR systems, the contribution of elastic scattering of ^{238}U was initially unexpected. However, this can be explained by the fact that R^2 captures the impact of correlations between nuclide reactions. Elastic and inelastic scattering of ^{238}U are strongly correlated, so the importance of elastic scattering is increased (see one at a time perturbations in Section 5.4.4 below).

Due to the dominance of the ^{238}U scattering reactions, a strongly reduced sample size is sufficient for identifying R^2 for k_{eff}. With a sample size of 250, the top contributors are still clearly visible.

The scattering reactions of ^{238}U are also among the most important nuclide reactions for the uncertainty of Σ_{abs}. Other important reactions are the elastic scattering of ^{23}Na, ^{56}Fe, and the (n,γ) reaction of ^{23}Na. The TSUNAMI, Sobol, and Gemino results are again in excellent agreement.

Since the contributions to the uncertainty are spread out through a larger number of nuclides, and the R^2 values are consequently smaller, the sample size plays a greater role for Σ_{abs} than for the eigenvalue. Figure 5.3 shows five identified nuclide reactions for three different sample sizes: 1,000, 500, and 250. For a sample size of 250, it can be seen that the significance bound for some reactions is half the size of the actual sensitivity value, and the confidence interval covers a comparably broad range. For a sample size of 1,000, 13 relevant nuclide reactions can clearly be identified, while the number is decreased to 9 for a sample size of 250.

When comparing the R^2 results between the three mixtures, it is observed that the results are consistent. Since mixture 1 contains all nuclides that are the most important contributors to the output uncertainties, the addition of nuclides in mixtures 2 and 3 does not change the ranking of top contributing nuclide reactions to k_{eff} or Σ_{abs}. The R^2 values are almost identical between the mixtures, i.e. R^2 is not biased by the additional noise. This result stresses the capability of R^2 to identify the top
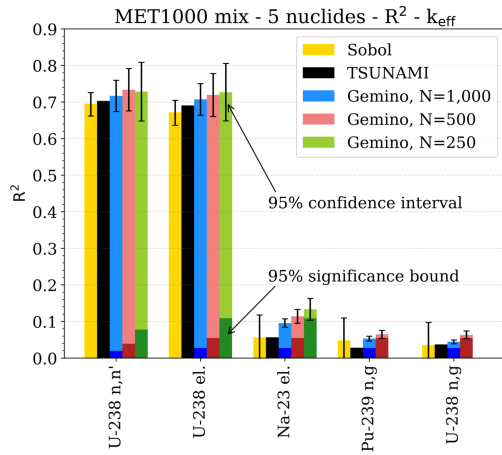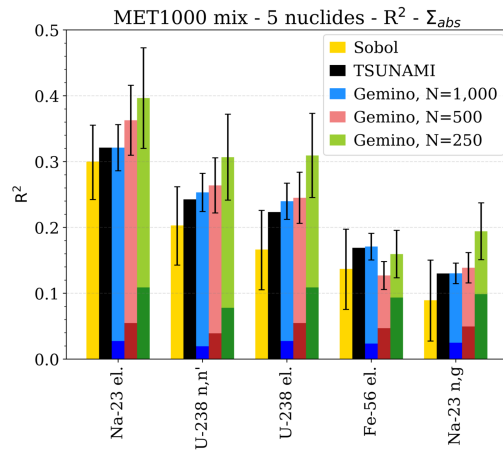
(a) Mixture 1, k_{eff}

(b) Mixture 1, Σ_{abs}
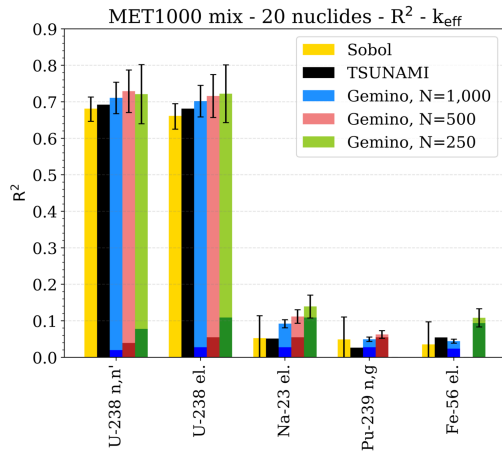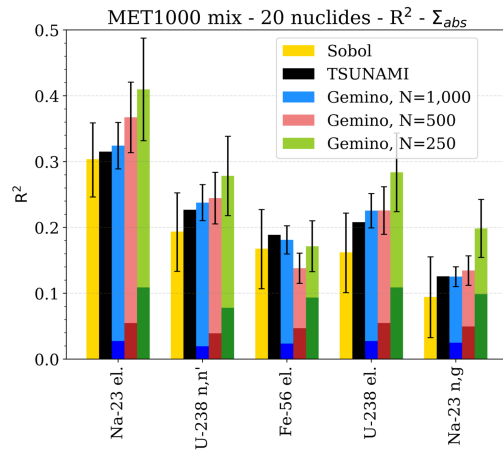
(c) Mixture 2, k_{eff}

(d) Mixture 2, Σ_{abs}
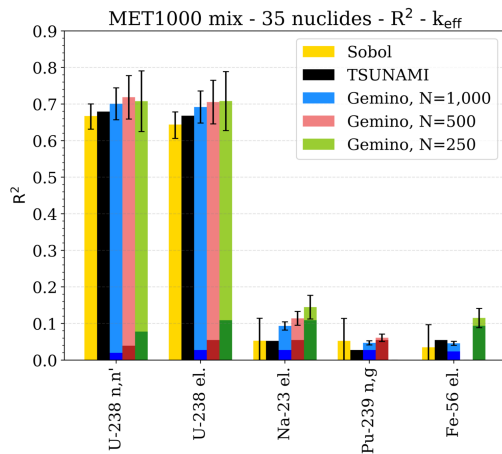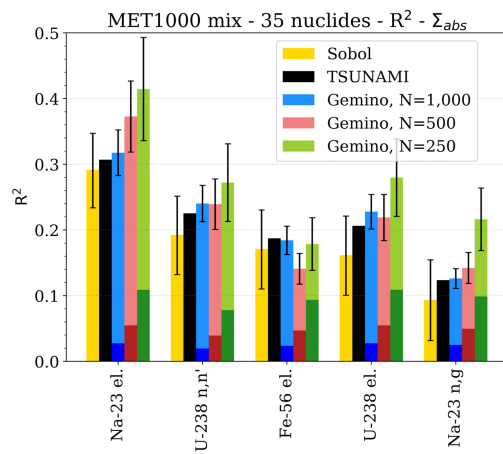
(e) Mixture 3, k_{eff}

(f) Mixture 3, Σ_{abs}

Figure 5.3 – Top contributors to k_{eff} and Σ_{abs} uncertainty in terms of R^2 for three homogeneous mixtures.

contributing nuclide reactions independently of the total number of parameters in the model.

The Gemino calculations were repeated with Sampler in order to assess the impact of implicit effects on the sensitivity analysis with R^2. The relative difference between the Gemino and Sampler R^2 results were less than 0.5% and are therefore considered negligible. Only for ^{56}Fe elastic scattering, a slightly larger relative difference of about 1.5% was found in the R^2 result for Σ_{abs}. This small implicit effect is consistent with the finding for the ^{56}Fe elastic scattering uncertainty in Section 4.4.3. However, since this difference is also small, it is concluded that implicit effects do not have a significant impact on the analysis of the output quantities presented here.

5.4.2   Total squared multiple correlation coefficient R^2_{tot}

When using the 17-group covariance library, the Gemino calculation considers 371, 1,161, and 1,993 independently sampled cross sections for the three mixtures, respectively (see Table 5.1). A sample size that is significantly larger than this number needed to be chosen to obtain statistically relevant results.

Table 5.2 – R^2_{tot} of three homogenized mixtures: Gemino results based on the 17-group covariance library and a sample size of 10,000. The 95% confidence intervals are given in parentheses.

| | k_{eff} | | Σ_{abs} | |
	unadjusted	adjusted	unadjusted	adjusted
mix 1	0.9902(8)	0.9898(8)	0.9993(1)	0.9993(1)
mix 2	0.9932(5)	0.9923(5)	0.9996(1)	0.9996(1)
mix 3	0.9944(4)	0.9930(4)	0.9997(1)	0.9996(1)

Using a sample size of 10,000, R^2_{tot} values were obtained by always considering all nuclides of the model. The results for k_{eff} and Σ_{abs} in Table 5.2 show R^2_{tot} values very close to 1. The impact of the adjustment for consideration of the limited degrees of freedom has a negligible influence, with differences below 0.0014. There is no strict criterion for a lower limit for total R^2 to determine the negligence of nonlinear effects. While all values show only small deviations from 1.0, R^2_{tot} for Σ_{abs} is significantly closer to 1.0 than for k_{eff}. This is consistent with the observation from Section 4.4, in which

the failed tests for normality suggested a non-negligible influence of nonlinear effects for k_{eff}. In contrast, the test for normality was positive for Σ_{abs}, suggesting that the nonlinear effects are negligible.

It should be noted that it is possible that nonlinear effects are significant for individual nuclide reactions; they may be overshadowed by linear contributions of more significant nuclide reactions, or they may not appear due to the effect of error cancellation.

5.4.3   Semi-partial squared multiple correlation coefficient SPC^2

The calculation of SPC^2 with Gemino requires the calculation of R^2_{tot}. Therefore, a sample size that is significantly larger than 371, 1,161, and 1,993 for the three mixtures is again needed to obtain statistically relevant results. Three sample sizes were considered: 10,000, 5,000, and 2,500.

SPC^2 results for all mixtures are presented in Figure 5.4. Gemino's SPC^2 values are not adjusted in this Figure to demonstrate the dependence on the degrees of freedom. The majority of the SPC^2 results for the individual nuclide reactions are in good agreement across the different approaches. Exceptions and observations depending on the sample size and number of considered nuclides are discussed below.

A general observation is the absence of elastic scattering of ^{238}U in the list of contributors. Furthermore, the contribution of ^{238}U inelastic scattering is no longer dominating; the contribution is rather small or even insignificant as, for example, in case of Gemino's results for Σ_{abs}. This result can be explained using the interpretation of SPC^2: SPC^2 indicates the contribution to the output variance by an individual nuclide reaction that is added when contributions of all other nuclide reactions (the complementary group) are already considered. Due to strong correlations between elastic and inelastic scattering of ^{238}U, the additional contribution of one of these reactions is negligible. For example, when investigating the additional contribution of ^{238}U inelastic scattering to the output variance, the contribution of this reaction is already considered by ^{238}U elastic scattering in the complementary group due to correlations. The additional effect is consequently small.

The absence of the main contributor to the uncertainty in the ranking of SPC^2 stresses that SPC^2 does not reveal the top contributors to the output uncertainty. It can only be used in addition to the analysis with R^2. For example, relevant correlations

between reactions can be identified by their absence in the SPC^2 ranking. (Correlations often exists between reactions of a nuclide or between reactions of different nuclides. Without this analysis, it is, however, not necessarily clear which correlation between reactions is significant for the observed output uncertainties.)

As for R^2, the sensitivity analysis with SPC^2 was repeated for Sampler results. The difference between the SPC^2 results with Gemino and Sampler were found negligible except for a slightly larger effect for ^{56}Fe elastic scattering. It is concluded again that implicit effects do not have an impact on the analysis of the output quantities presented here.

Comparisons between the approaches

The TSUNAMI results for the contribution of ^{238}U inelastic scattering to the uncertainty of k_{eff} and Σ_{abs} are inconsistent with the Sobol and Gemino results. They show SPC^2 values that are many times higher than the corresponding Sobol and Gemino values. The Sobol and Gemino results are significantly closer to each other, but they still show a noticeable difference. In the case of k_{eff}, Sobol's indices are about 2 to 3 times as large as the corresponding Gemino indices; in the case of Σ_{abs}, Sobol's indices show an SPC^2 value of about 0.05, while the corresponding Gemino values are close to zero. Similar but less extreme trends are observed for the SPC^2 values of ^{239}Pu (n,γ) and ^{56}Fe elastic scattering.

The observed discrepancies could be caused by (1) differences in the consideration of nonlinear effects and (2) the inversion of large matrices.

Differences between Gemino's/TSUNAMI's SPC^2 values and Sobol's SPC^2 values might be influenced by differences in the consideration of nonlinear effects. In the case of TSUNAMI, the sensitivity coefficients used for the calculation of SPC^2 are determined with first-order perturbation theory; nonlinear effects are not considered. In the case of Gemino, nonlinear effects are considered in the random sampling calculations. However, they are not considered in the calculation of Gemino's SPC^2. Sobol's indices consider nonlinear effects in SPC^2.

The uncertainties of ^{238}U inelastic scattering, a major contributor to the output uncertainty as identified with R^2, are so large in the fast energy range that their impact to the output uncertainty could be nonlinear. Figure 5.5 shows the uncertainties of the important reactions, and Figure 5.6 shows the TSUNAMI sensitivity coefficients as a

(a) Mixture 1, k_{eff}

(b) Mixture 1, Σ_{abs}

(c) Mixture 2, k_{eff}

(d) Mixture 2, Σ_{abs}

(e) Mixture 3, k_{eff}

(f) Mixture 3, Σ_{abs}
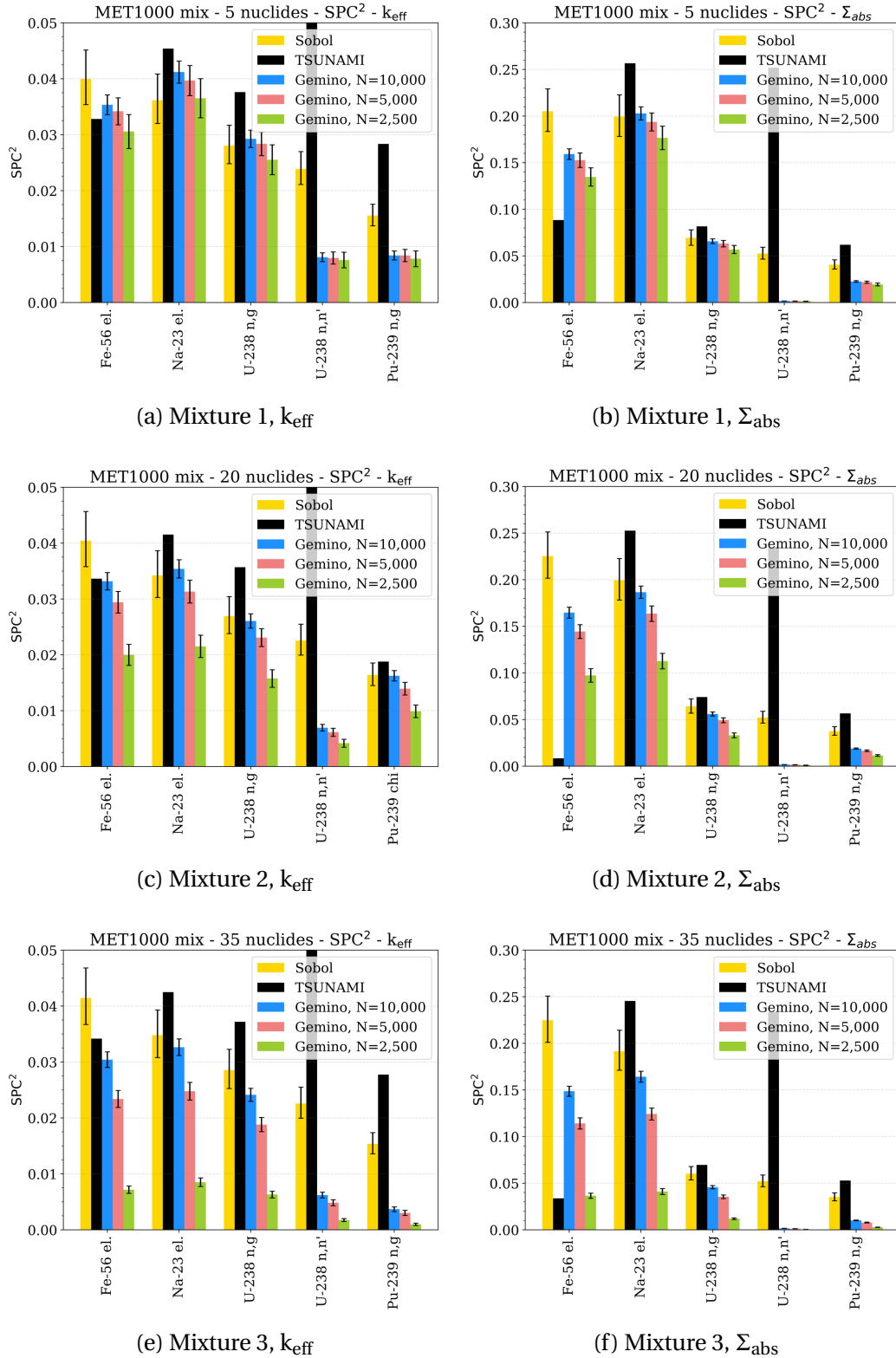
Figure 5.4 – Top contributors to k_{eff} and Σ_{abs} uncertainty in terms of SPC^2 for three homogeneous mixtures.

function of energy to stress in which energy range k_{eff} and Σ_{abs} are especially sensitive towards changes of these cross sections. For example, the absolute eigenvalue sensitivity of ^{238}U inelastic scattering is especially large between 10^6 and 10^7 eV, while the corresponding uncertainty is between 20 and 30% in this energy range.
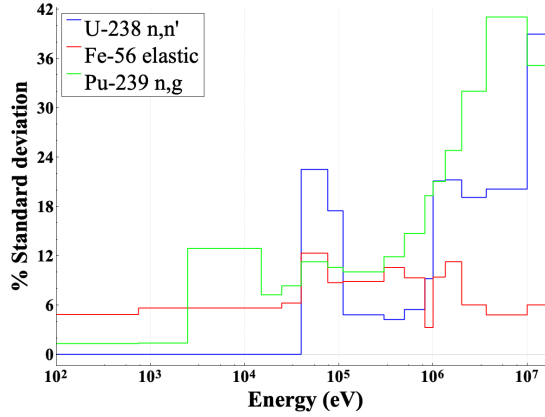
Figure 5.5 – Uncertainties of selected nuclide reactions (17-group covariance library).

(a) Mixture 1, k_{eff}

(b) Mixture 1, Σ_{abs}
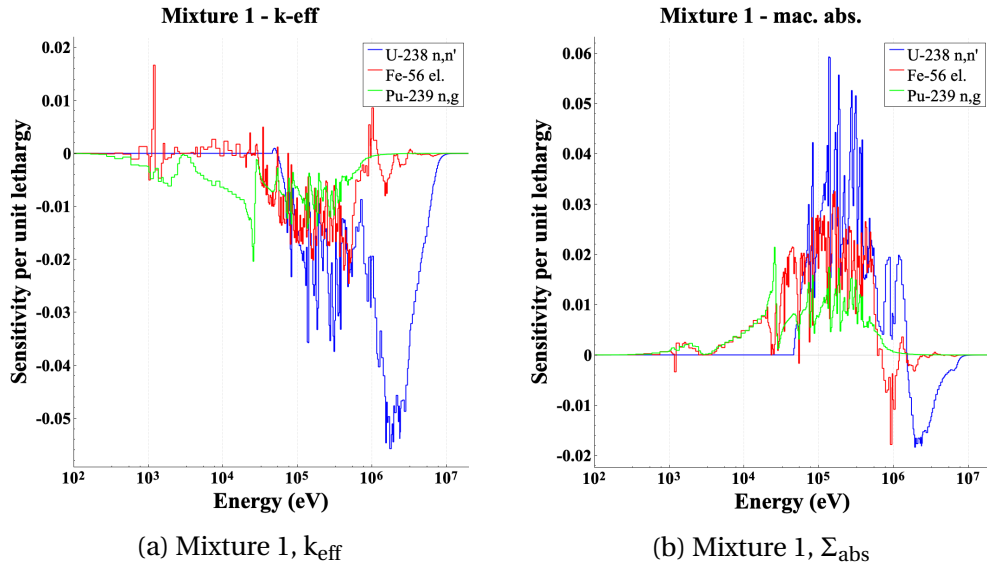
Figure 5.6 – TSUNAMI sensitivity coefficients as a function of energy for selected nuclide reactions of mixture 1.

The calculation of TSUNAMI's SPC^2 requires the inversion of large covariance matrices composed of the covariance matrices of all nuclide reactions of interest except for the nuclide reaction currently under investigation (Eq. 5.28). To invert such a large matrix, rows/colums with zero variances are removed in the first step. The remaining matrix

is often not positive definite, as negative matrix eigenvalues exist. In fact, the matrices often show a smallest negative eigenvalues with significant absolute values, indicating that stronger matrix modifications are necessary to make the matrix positive definite. For example, in the SPC^2 calculation of inelastic scattering of ^{238}U for the eigenvalue of mixture 1, the smallest eigenvalue is -1.65786. Depending on how much the matrices are modified, this matrix modification can introduce a bias.

The random sampling based on conditional distributions for the determination of Sobol's SPC^2 (described in Section A.3.2) also requires the inversion of a large correlation matrix that includes the correlation matrices of the complementary group of nuclide reactions. In fact, those are similar matrices as for the TSUNAMI SPC^2 calculation mentioned above. Modifications can also be required here to make this large matrix positive definite.

The calculation of SPC^2 with Gemino also requires the inversion of large correlation matrices. In contrast to the matrix inversion for TSUNAMI's and Sobol's SPC^2, the matrices do not require modifications to be positive definite (with the exception of the removal of completely dependent and zero variance rows/columns) because they consist of sample correlation coefficients based on perturbation factors that were generated from positive definite matrices. A bias might of course be introduced during the matrix modifications in random sampling procedure that is propagated through the calculations.

In order to investigate which of the described effects is more dominant, an analysis of mixture 1 based on perturbations of only elastic and inelastic scattering of ^{238}U was performed. The matrices to be inverted have consequently a maximum size of 17 × 17 such that the influence of a possible matrix modification is decreased. In this simplified case, all approaches resulted in consistent SPC^2 indices for ^{238}U inelastic scattering when considering their statistical uncertainty. It is therefore concluded that the described matrix modifications are the main cause of differences between the approaches. Although one of two reactions in this study has a very large uncertainty, consistent results between linear and nonlinear approaches was observed; nonlinear effects are not significant for the studied cases.

In conclusion, the large discrepancies of TSUNAMI's SPC^2 suggest a significant, unpredictable bias, therefore, this approach is not recommended as a stand-alone method for analysis. Sobol's and Gemino's SPC^2 are in better agreement, but can also include an unknown bias due to modifications of large matrices during the random sampling

procedure.

Dependence on the sample size and number of nuclides

With the above mentioned exceptions, the Sobol and TSUNAMI results are consistent between the mixtures. The consideration of additional nuclides does not change the contributions of the nuclide reactions to k_{eff} or Σ_{abs}.

In contrast, the Gemino results show increasing values with an increasing sample size for all mixtures. With increasing sample size, the confidence intervals are decreasing with about $1/\sqrt{N}$. Figure 5.4 shows that the difference between results of an individual nuclide reaction decreases with increasing sample sizes: the SPC^2 values seem to converge. Furthermore, the differences between the results using different sample sizes are increasing with an increasing number of nuclides in the mixture. At the same time, the SPC^2 values become smaller when the sample size remains constant.

These observations are caused by the limited degree of freedom (difference between the sample size N and the number of independently sampled cross sections k) considered in the Gemino SPC^2 calculation. Following Eq. 5.23, adjusted SPC^2 values are determined that consider the impact of the degrees of freedom. As an example, Figure 5.7 shows the adjusted SPC^2 values next to the unadjusted SPC^2 values for Σ_{abs} of all mixtures. If the degree of freedom is decreased either by decreasing the sample size or by adding nuclides to the mixture, then the adjustment becomes more noticeable. With the adjustment, the SPC^2 results between the different mixtures and sample sizes are consistent.

Although the adjustment to the limited degree of freedom is small for R^2 and R^2_{tot}, the findings presented in this section support the recommendation to determine the adjusted SPC^2 instead of the unadjusted SPC^2 because the influence is increased for this sensitivity index. The ranking is of reactions is identical between the unadjusted and adjusted values, but the interpretation of SPC^2 only holds for the converged results.

(a) Mixture 1, Σ_{abs}

(b) Mixture 2, Σ_{abs}

(c) Mixture 3, Σ_{abs}
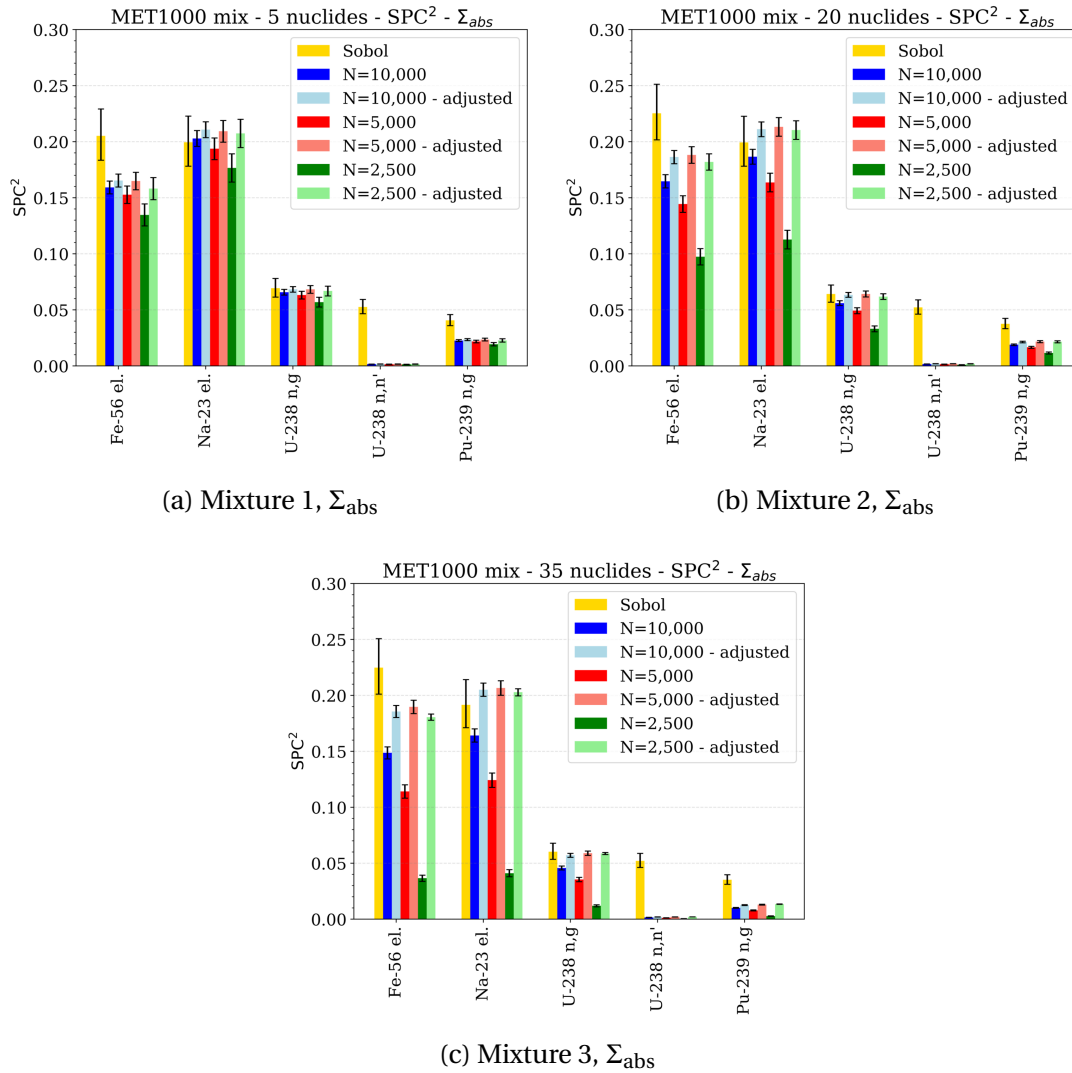
Figure 5.7 – Comparison of Gemino SPC^2 with the corresponding adjusted SPC^2 for Σ_{abs} of three homogeneous mixtures. The Sobol SPC^2 results are additionally displayed.

5.4.4 One at a time perturbations

The analysis of R^2 allowed the identification of the top contributors to the output uncertainty and the analysis of SPC^2 helped identifying relevant correlations between reactions. It was, however, not possible with these sensitivity indices to identify which one of the strongly correlated nuclide reaction causes significant uncertainties and which one only appears due to correlations.

To overcome this deficiency, it is possible to perform one at a time perturbations of

individual or a limited number of nuclide reactions. For this purpose, the random sampling is only performed with the covariance matrices of interest. The corresponding uncertainty calculations reveal the uncertainty caused by only the nuclide reaction(s) of interest. In case of perturbations of one nuclide reaction, the output uncertainty caused by this reaction is obtained without the consideration of correlations to other reactions.

Table 5.3 presents the obtained uncertainties from one at a time perturbations of relevant nuclide reactions for mixture 1. The comparison of the individual contributions of elastic scattering and the (n,γ) reaction of ^{23}Na as well their joint contribution reveals that elastic scattering causes a significant uncertainty, while the (n,γ) reaction only appeared in the R^2 ranking due to correlations to elastic scattering. In case of ^{238}U, it can be concluded that the contribution of the joint scattering reactions is almost exclusively caused by uncertainties of inelastic scattering.

Table 5.3 – Uncertainties based on one at a time perturbations of individual or multiple nuclide reactions with Gemino for mixture 1 using sample size 1,000.

Perturbed nuclide reactions	k_{eff}	Σ_{abs}
all	1.7103%	1.1735%
Fe-56 elastic	0.3272%	0.5015%
Na-23 elastic	0.4178%	0.6725%
Na-23 n,γ	0.0088%	0.0094%
Na-23 elastic and n,γ	0.4126%	0.6628%
U-238 elastic	0.0277%	0.0484%
U-238 n,n'	1.4529%	0.6167%
U-238 elastic and n,n'	1.4535%	0.6081%

6 Systematic uncertainty and sensitivity analysis of SFR systems

This chapter presents the results of the uncertainty and sensitivity analyses for the exercises specified in Chapter 2. The nominal values and uncertainties of the requested output quantities are presented. For some output quantities, the top contributing nuclide reactions to the observed uncertainties are identified.

Results are obtained using the 302-group cross section library (xs302g) and the 17-group covariance library (cov17g) described in Chapter 3. Both the XSUSA and the Sampler approach are exercised; the XSUSA approach is followed by using the new Gemino sequence in SCALE (see Chapter 4). Where possible, TSUNAMI results are added. The sensitivity analysis is limited to the determination of the squared multiple correlation coefficient R^2 because the semi-partial squared multiple correlation coefficient SPC^2 and Sobol' indices require a large computational burden (see Chapter 5).

During the preparation of this work, results for the UAM SFR benchmark were first generated using a 425-group cross section library (xs425g) and a 19-group covariance library (cov19g). In contrast to the 302-group library, the URR data of the 425-group cross section library was generated based on NR approximations, but not under the consideration of probability tables. However, the impact of this difference in the library generation on the nominal results is small (see Chapter 3.1.3), so it can be assumed that the impact on the uncertainty analysis results is negligible. Furthermore, Section 3.2 shows that the group structure of the covariance library has a negligible impact on the output uncertainties. Therefore, the results remain valid, and are also included in the comparisons. Some of the nominal output values show small differences that are not necessarily caused by the applied libraries but are instead the

result of updates in the models implemented during the course of these studies. The updates include changes in the self-shielding cell (one cell for all pins that considers wrapper material), the mesh for the deterministic transport, convergence criteria, and other neutron transport settings.

The neutron transport calculations of the pin cell, fuel assembly, and supercell exercises were performed using the two-dimensional deterministic neutron transport code NEWT. The full core exercises were calculated with the three-dimensional Monte Carlo code KENO-VI and the nodal diffusion code PARCS, for which cross sections were generated with NEWT.

Comparisons of uncertainties in this section are mostly presented in figures. Corresponding tables with detailed results are given in Appendix A.5. If a column is missing in plots of the sensitivity index R^2, then the calculation did not result in an R^2 value above the respective significance bound.

6.1 Pin cell

6.1.1 Nominal results

The nominal values of the pin cell calculations presented in Table 6.2 are consistent between the 302-group and 425-group results. Only the 1-group elastic scattering cross section of ^{56}Fe shows a difference higher than 2%, most likely due to better representation of the resonances at very high energies.

6.1.2 Uncertainty and sensitivity analysis results

The 1-group cross section uncertainties are basically collapsed cross section uncertainties that are weighted by the neutron flux of the pin cells. Large cross section uncertainties in the fast energy range propagate to large output uncertainties. Although some 1-group uncertainties are significant at over 5%, cancellation effects lead to smaller uncertainties of integrated quantities such as the eigenvalue and the macroscopic cross sections (Figures 6.1 and 6.3). The macroscopic fission cross section uncertainties are about 1.5%, while the macroscopic absorption cross section uncertainties are less than 1%. The eigenvalue uncertainty is about 1.5% in the case of the MET1000 fuel pin, and it is about 1.7% in case of the MOX3600 fuel pin. These

uncertainties are almost three times larger than the corresponding uncertainties for light water reactor pin cells.

The TSUNAMI, Sampler, Gemino, and XSUSA results are in very good agreement, considering the statistical confidence interval of the random sampling calculations (Figures 6.2 and 6.4). Exceptions are the (n,γ) cross section of the Pu isotopes, for which slightly larger uncertainties were obtained with TSUNAMI compared to the random sampling results. To understand the origin of these discrepancies, a sensitivity analysis for the Pu (n,γ) reactions was performed.

Figure 6.6 shows the top three contributors to the Pu (n,γ) uncertainties in the MET1000 pin cell in terms of R^2 for TSUNAMI and Gemino. It is observed that the reaction itself is almost exclusively responsible for the uncertainty. This makes sense given that the output quantity is a collapsed 1-group cross section. The total R^2 values for the Gemino results were above 0.998 for all Pu (n,γ) uncertainties, suggesting that nonlinear effects are insignificant. It can therefore be concluded that the differences between TSUNAMI and the random sampling results are not caused by differences in the consideration of nonlinear effects.

The uncertainties of the (n,γ) reactions of all Pu isotopes are very high in the fast energy range (Figure 6.5). It is possible that the large variance is underestimated with the random sampling approach due to the procedure for the random sampling: to only allow positive cross sections, the normal distribution from which it is sampled is truncated. The truncated distribution has a smaller variance and can therefore lead to an underestimation of the uncertainty (see Appendix A.3.3). For example, Figure 6.5 shows ^{241}Pu (n,γ) uncertainties of 30%, 50% and 80% in the energy groups between 10^5 and 10^6 eV. During the random sampling procedure of the cross section in these energy groups, the truncation of the standard normal distribution with originally $\sigma = 1$ leads to "truncated" standard deviations of 1.000, 0.999, and 0.763, respectively. While the impact of the truncation is small for 30% and 50% uncertainty, the standard deviation of the sampling distribution in other energy groups with larger uncertainty is significantly underestimated.

To estimate the impact of the truncation, a "sample" covariance library was calculated based on the perturbation factors for Sampler and Gemino. By calculating the sample correlation factors between the perturbation factors of the individual cross sections, sample correlation matrices were calculated. Using the restriction to sample only positive cross sections as described in Appendix A.3.3, truncated standard deviations

were determined and appropriately multiplied with the correlation matrices to obtain covariance matrices. In this way, a sample covariance library was generated that was then used to re-determine uncertainties with TSUNAMI. Table 6.1 shows the TSUNAMI results of the collapsed 1-group Pu capture cross sections using the original covariance library and the sample covariance library, respectively. Smaller differences to the Sampler results when using the sample covariance library confirm the relevance of the truncation for these reactions. For reasons of completeness, it shall be mentioned that the truncation did not have an influence on any other output quantity investigated for the pin cells.

Table 6.1 – MET1000 pin cell: Uncertainties of collapsed 1-group Pu capture cross sections based on original and truncated standard deviations (xn302g-cov17g).

	^{239}Pu	^{240}Pu	^{241}Pu
	TSUNAMI original	6.709%	4.270%	18.227%
Uncertainty	TSUNAMI truncated	6.540%	4.110%	17.537%
	Sampler truncated	6.548%	3.951%	16.401%
Rel. difference	Sampler vs. TSUNAMI original	2.46%	8.07%	11.13%
	Sampler vs. TSUNAMI truncated	-0.13%	4.03%	6.93%

As requested in the specifications, for the eigenvalue of the pin cells, a sensitivity analysis was performed to identify the top contributors to the observed uncertainties. For both designs, the inelastic scattering cross section of ^{238}U is the most important contributor, with R^2 values on the order of 0.8. The R^2 value of elastic scattering of ^{238}U is in the same range because of the strong correlations with inelastic scattering, as noted in Section 5. All reported results are thereby consistent (Figure 6.7).
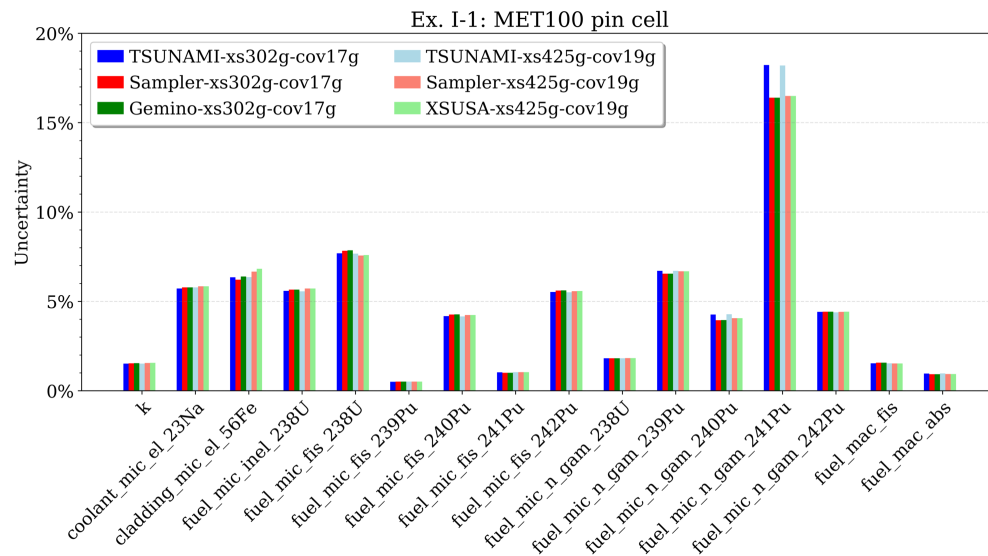
Figure 6.1 – Ex. I-1: MET1000 pin cell results—uncertainties.
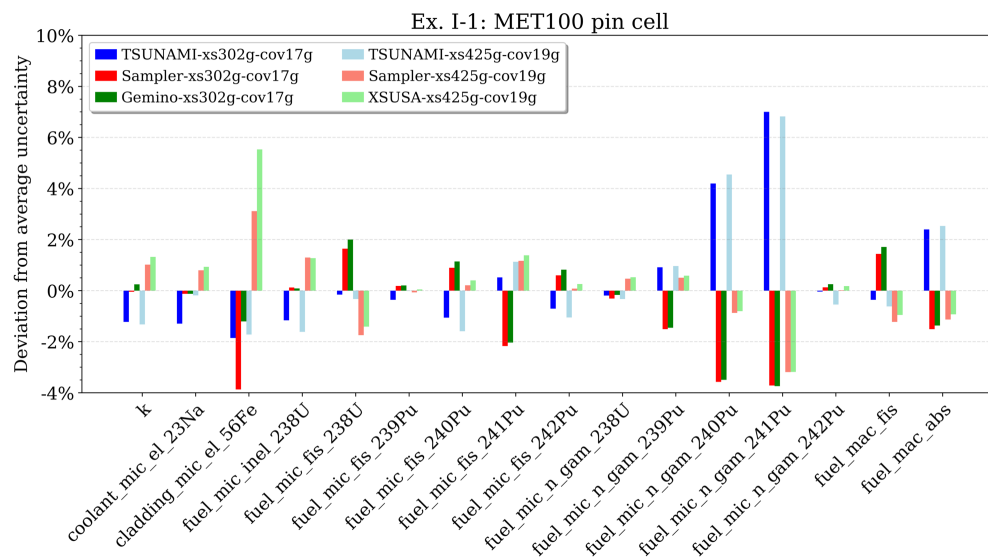
Figure 6.2 – Ex. I-1: MET1000 pin cell results—difference to average uncertainty.
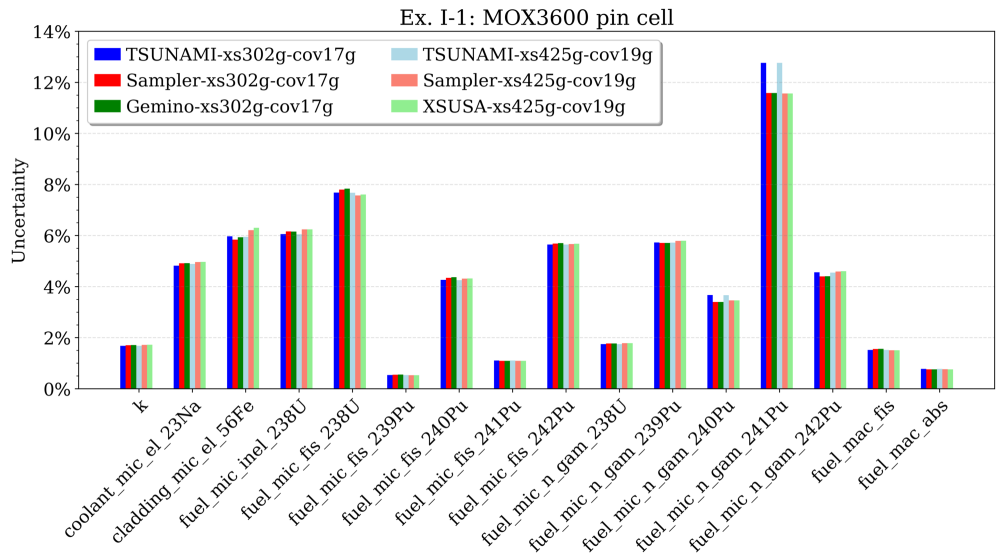
Figure 6.3 – Ex. I-1: MOX3600 pin cell results—uncertainties.
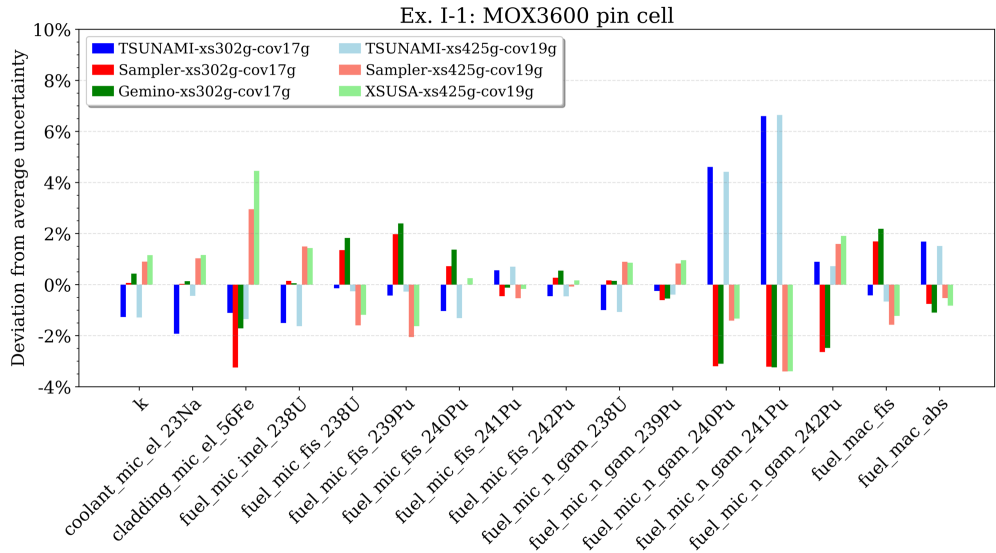
Figure 6.4 – Ex. I-1: MOX3600 pin cell results—difference to average uncertainty.
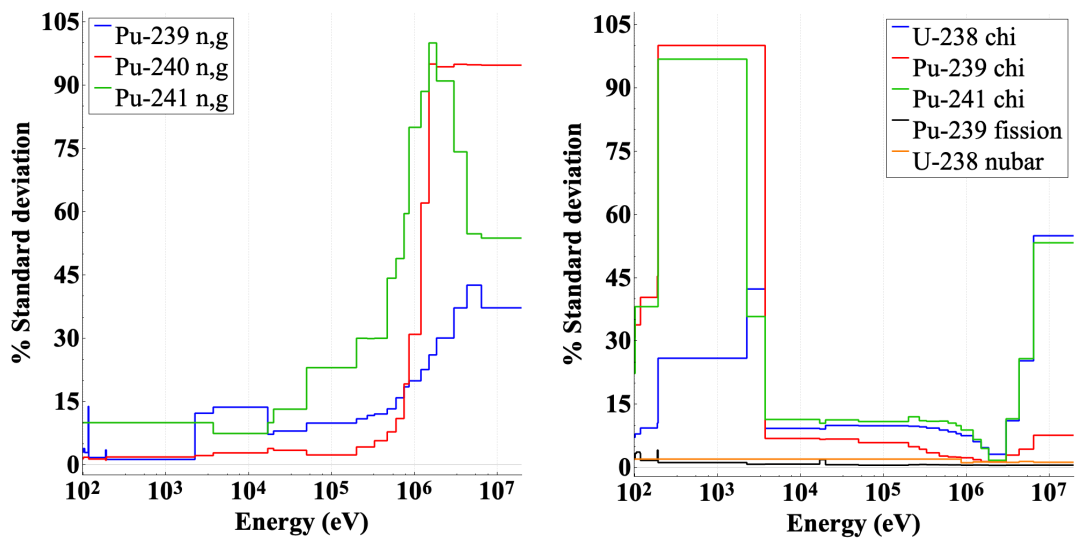
Figure 6.5 – Uncertainties of several relevant reactions as a function of the incident neutron energy.
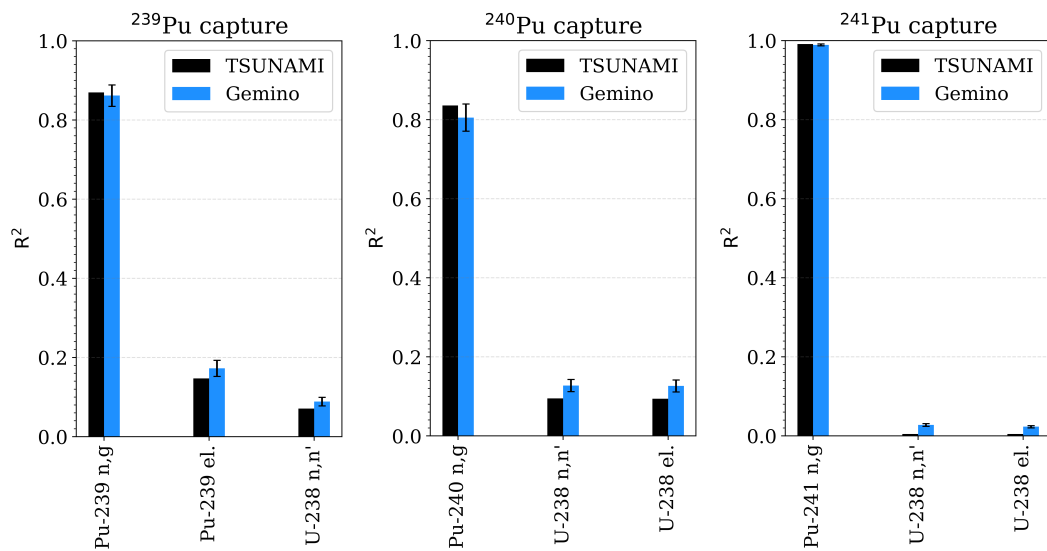
Figure 6.6 – Ex. I-1: MET1000 pin cell results (xs302g-cov17g)—top contributors to the 1-group Pu (n,γ) cross section in terms of R^2.
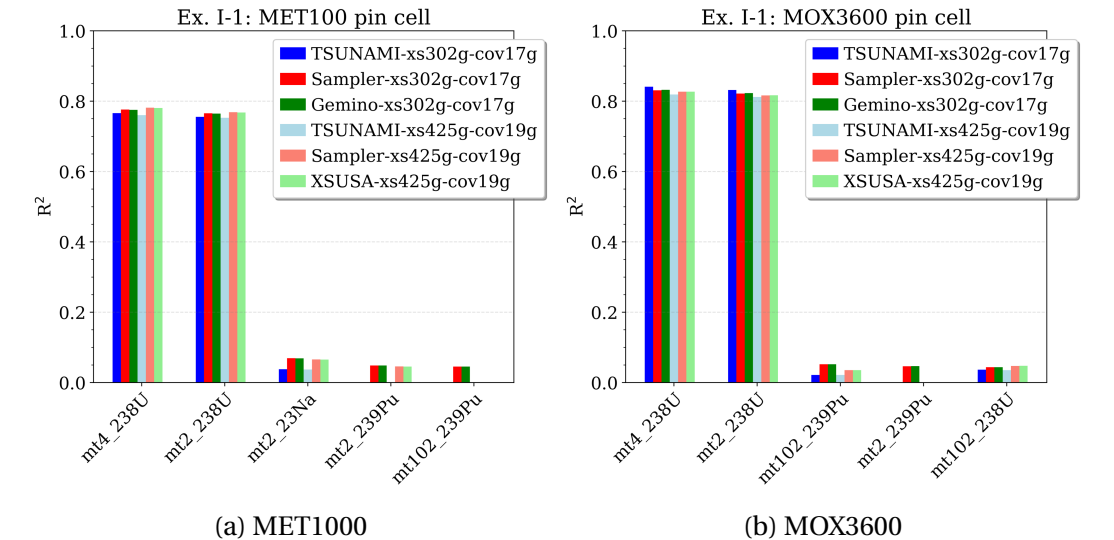
(a) MET1000   (b) MOX3600

Figure 6.7 – Ex. I-1: Pin cell results—top contributors to the eigenvalue uncertainty in terms of R^2.

Table 6.2 – Ex. I-1: Nominal pin cell results.

Output quantity	MET1000			MOX3600		
	xs302g	xs425g	Difference	xs302g	xs425g	Difference
eigenvalue	1.3584E+00	1.3576E+00	-83 pcm	1.1922E+00	1.1924E+00	4 pcm
coolant_mic_el_23Na [b]	4.0152E+00	4.0200E+00	0.12%	4.8003E+00	4.8088E+00	0.18%
cladding_mic_el_56Fe [b]	3.4640E+00	3.5695E+00	3.06%	4.1648E+00	4.2651E+00	2.42%
fuel_mic_inel_238U[b]	1.0721E+00	1.0710E+00	-0.10%	9.4262E-01	9.4220E-01	-0.05%
fuel_mic_fis_238U [b]	3.4181E-02	3.4180E-02	0.01%	4.2107E-02	4.2110E-02	-0.02%
fuel_mic_fis_239Pu [b]	1.6249E+00	1.6254E+00	0.03%	1.7500E+00	1.7514E+00	0.06%
fuel_mic_fis_240Pu [b]	3.4162E-01	3.4267E-01	0.31%	3.5323E-01	3.5430E-01	0.29%
fuel_mic_fis_241Pu [b]	2.1061E+00	2.1070E+00	0.04%	2.4768E+00	2.4786E+00	0.05%
fuel_mic_fis_242Pu [b]	2.4729E-01	2.4756E-01	0.12%	2.5099E-01	2.5106E-01	0.01%
fuel_mic_n_gam_238U [b]	2.0994E-01	2.0956E-01	-0.17%	2.8054E-01	2.8015E-01	-0.11%
fuel_mic_n_gam_239Pu [b]	2.9521E-01	2.9583E-01	0.21%	4.7752E-01	4.7911E-01	0.32%
fuel_mic_n_gam_240Pu [b]	3.6297E-01	3.6300E-01	0.00%	4.9120E-01	4.9138E-01	0.00%
fuel_mic_n_gam_241Pu [b]	3.1482E-01	3.1526E-01	0.14%	4.3406E-01	4.3459E-01	0.09%
fuel_mic_n_gam_242Pu [b]	2.8813E-01	2.8818E-01	0.02%	4.2279E-01	4.2206E-01	-0.19%
fuel_mac_fis [1/cm]	5.3096E-03	5.3124E-03	0.05%	5.2488E-03	5.2530E-03	0.06%
fuel_mac_abs [1/cm]	1.1269E-02	1.1264E-02	-0.04%	1.2734E-02	1.2734E-02	0.00%

6.2   Fuel assembly

6.2.1   Nominal results

The MOX3600 fuel assembly includes pin cells which have a central hole and a gap between the fuel and the cladding. To allow cross section homogenization with NEWT over the entire fuel assembly, the central hole was volume-homogenized with the surrounding fuel, and the gap was homogenized with the cladding. In this way, any possible problem with void areas in the model during the homogenization is avoided. Instead of modeling a hexagonal array with fuel pins as shown in Section 2.2, a corresponding rectangular cell was created in which fuel pins were included as holes in the model (see Figure 6.24(a) and 6.25(a)). Due to reflective boundary conditions, the rectangular models correspond exactly with the hexagonal model while avoiding convergence issues with NEWT and reducing and computation time.

The nominal values of the fuel assembly calculations presented in Table 6.3 are consistent between the 302-group and 425-group results. The eigenvalues differ by 73 pcm and 192 pcm for the MET1000 and MOX3600 assemblies, respectively, due to differences in the library generation, modeling choices, and settings for the transport solver.

6.2.2   Uncertainty and sensitivity analysis results

The eigenvalue uncertainties of the fuel assemblies are only slightly smaller than the corresponding pin cell uncertainties. The uncertainties of the macroscopic 4-group cross sections are all below 2.3%. The Doppler and Na-void uncertainties are about 5% and above, stressing the importance of nuclear data uncertainties for safety relevant reactivity parameters (Figures 6.8 and 6.10).

The TSUNAMI, Sampler, Gemino, and XSUSA results for the fuel assemblies are generally in good agreement considering the statistical confidence interval of the random sampling calculations (Figures 6.9 and 6.11). The only exception for both assemblies is the Doppler uncertainties determined with Sampler using the 425-group cross section library and the 19-group covariance library. While all other results are in good agreement, this Sampler result shows a comparably large discrepancy that could not be resolved within the scope of this thesis.

Other significant differences are observed for the fastest energy group of the macroscopic absorption cross section (Σ_{abs}): the random sampling–based uncertainties are clearly smaller than the corresponding TSUNAMI uncertainties for both fuel assemblies. Within the efforts to understand these discrepancies, sensitivity analyses in terms of R^2 was performed for the MOX3600 fuel assembly using the 302-group cross section and 17-group covariance library. Figure 6.13 shows the Gemino results for both the fastest group (group 1) and the most thermal group (group 4). The results for group 1 show significant contributions from the neutron energy distribution from fission (fission spectrum, chi, χ) of several isotopes and the ^{238}U scattering reactions.
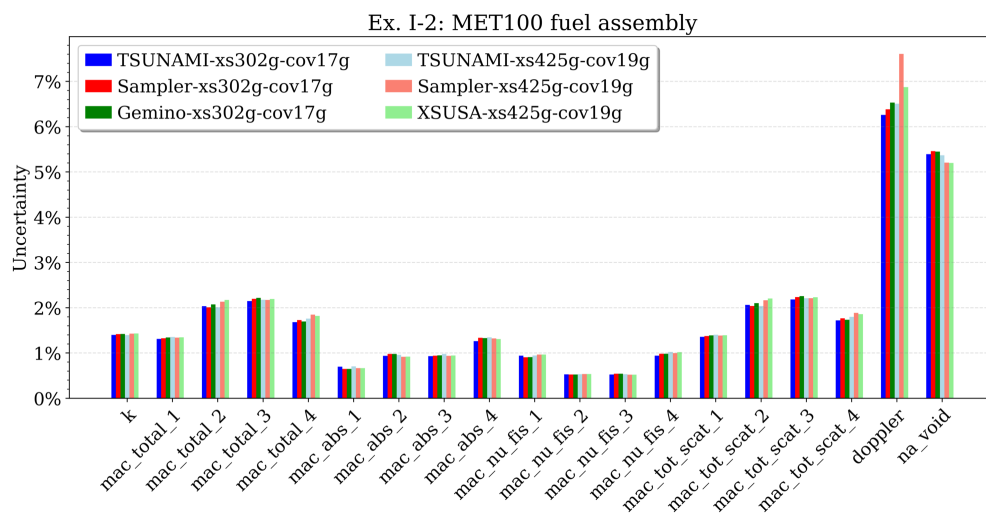
Figure 6.8 – Ex. I-2: MET1000 fuel assembly results—uncertainties.
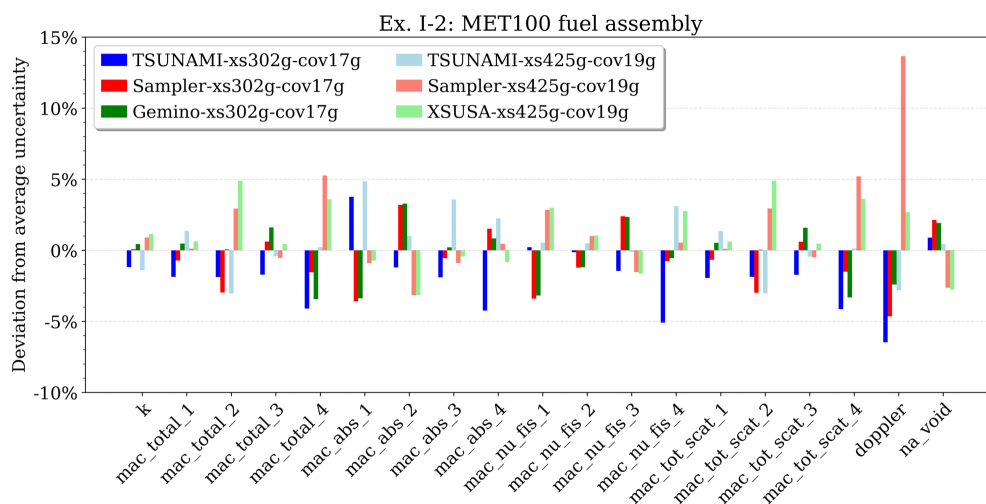
Figure 6.9 – Ex. I-2: MET1000 fuel assembly results—difference to average uncertainty.

Since the χ uncertainties are below 15% in the fast energy range (Figure 6.5), it is unlikely that the discrepancy is caused by a truncation of the corresponding variances in the random sampling procedure as for the ^{239}Pu (n,γ) of the pin cell discussed above. The ^{238}U inelastic scattering reaction shows larger uncertainties in the fast energy range. However, this reaction was identified as top contributor for several other output quantities for which consistent results between the various approaches was obtained. Since an effect of the truncation was not observed for other output quantities, it is concluded that it is negligible also here. Within the scope of this thesis, the cause of this observed discrepancy could not be resolved.
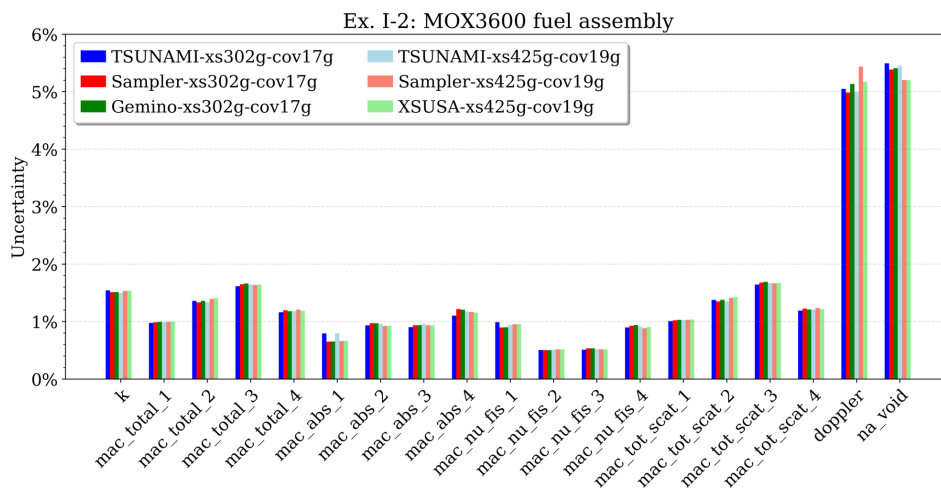
Figure 6.10 – Ex. I-2: MOX3600 fuel assembly results—uncertainties.
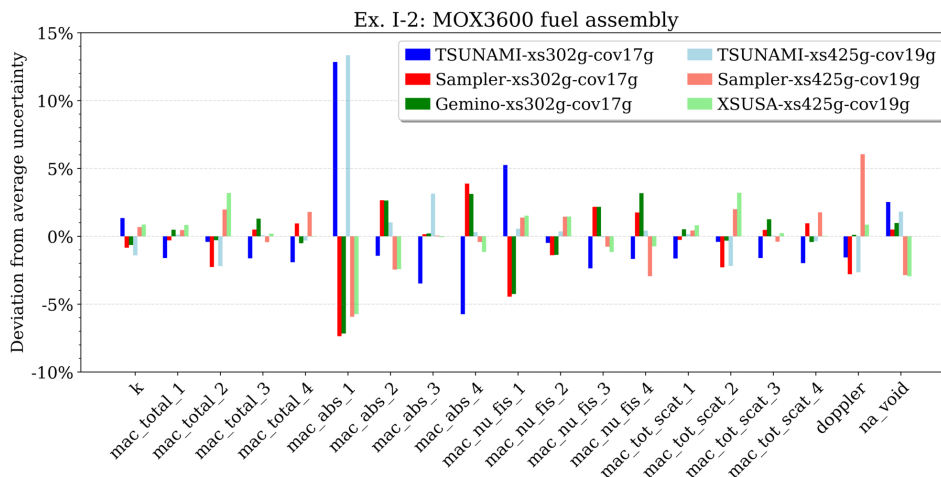
Figure 6.11 – Ex. I-2: MOX3600 fuel assembly results—difference to average uncertainty.

136

It shall be noted that the initial Gemino and Sampler results for the fastest energy group of the number of neutrons emitted per fission event times the macroscopic fission cross section (nu-fission, $\nu\Sigma_{fis}$) underestimated the corresponding TSUNAMI result. A sensitivity analysis revealed the average number of neutrons emitted per fission event (nubar, $\bar{\nu}$) of ^{238}U as top contributor to this uncertainty (Figure 6.12). The cause of this underestimation was found in the difference regarding the consideration of the $\bar{\nu}$ uncertainty. The AMPX covariance library contains data for the delayed and prompt $\bar{\nu}$ as well as the total $\bar{\nu}$ for ^{238}U. Since TSUNAMI only calculates sensitivity coefficients for the total $\bar{\nu}$, only the total $\bar{\nu}$ uncertainty is considered in the uncertainty analysis. In case of Gemino and Sampler, the three $\bar{\nu}$s are sampled together. Instead of using the perturbations of the total $\bar{\nu}$, the perturbation factors for the prompt and delayed $\bar{\nu}$ are separately applied to the corresponding nominal values and then added together.

The observed differences are a result of the generation of the covariance library with AMPX: If only two of the three data sets for $\bar{\nu}$ are given, the corresponding third one is calculated. In case of ^{238}U, ENDF/B provides nominal values for all three $\bar{\nu}$s. The delayed $\bar{\nu}$ values are small such that the total $\bar{\nu}$ is dominated by the prompt $\bar{\nu}$. Identical uncertainties are given for the prompt and total $\bar{\nu}$; uncertainty information for the delayed $\bar{\nu}$ is not available. In fact, the evaluation of delayed neutron data is an area of current research (Foligno, 2019). As a result of small nominal delayed $\bar{\nu}$ values and the limited available uncertainty information, AMPX results in delayed $\bar{\nu}$ uncertainties of 100% in all energy groups. It further provides negative correlations between the prompt and delayed $\bar{\nu}$, such that the resulting perturbation is smaller compared to the perturbation of only the total $\bar{\nu}$ (visible in the $\nu\Sigma_{fis}$ uncertainty and the corresponding sensitivity analysis). To be consistent between the approaches, the Gemino and Sampler results were repeated based on perturbations of only the total $\bar{\nu}$. In this way, the results are consistent with TSUNAMI (Figures 6.9 and 6.11).

As requested in the specifications, a sensitivity analysis was performed to find the top contributors to the observed uncertainties of the eigenvalue, the Doppler constant, and the Na-void worth. The sensitivity index R^2 was determined for all sets of results (Figures 6.14 and 6.15). For both designs, the inelastic and elastic scattering cross sections of ^{238}U clearly dominate the ranking for the eigenvalue and the Doppler constant. The uncertainty of the Na-void worth is naturally driven by the scattering reaction and the (n,γ) reaction of ^{23}Na.

(a) Σ_{abs}, group 1

(b) Σ_{abs}, group 4
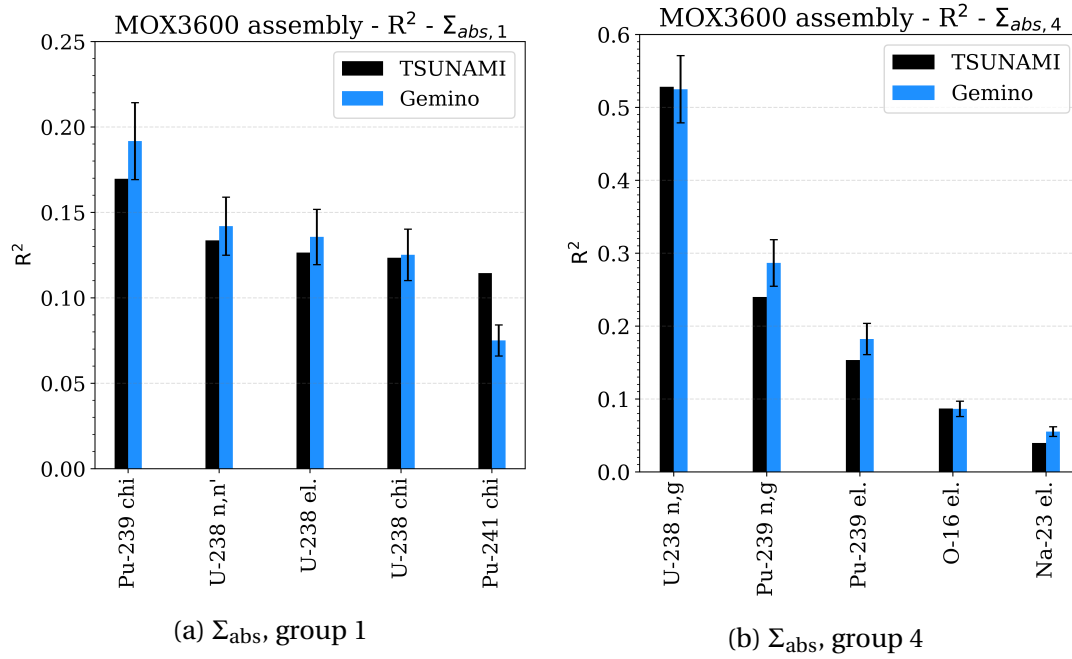
Figure 6.12 – Ex. I-2: MOX3600 fuel assembly (xs302g-cov17g)—top contributors to the uncertainty of the macroscopic fission cross sections in terms of R^2.

(a) $\nu\Sigma_{\text{fis}}$, group 1

(b) $\nu\Sigma_{\text{fis}}$, group 4
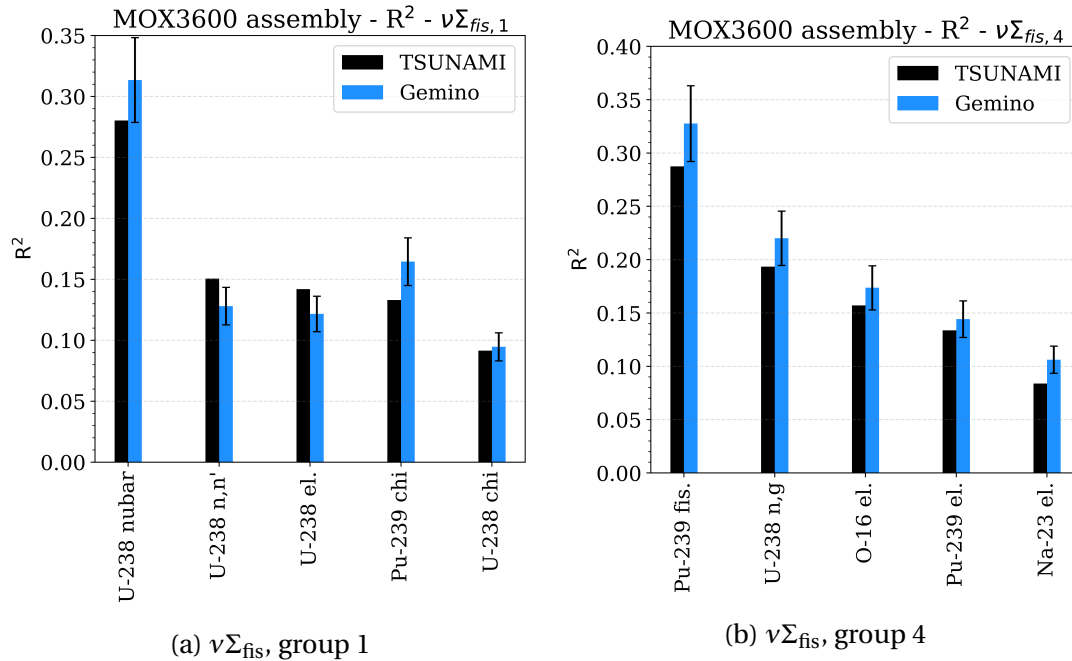
Figure 6.13 – Ex. I-2: MOX3600 fuel assembly (xs302g-cov17g)—top contributors to the uncertainty of the macroscopic absorption cross sections in terms of R^2.
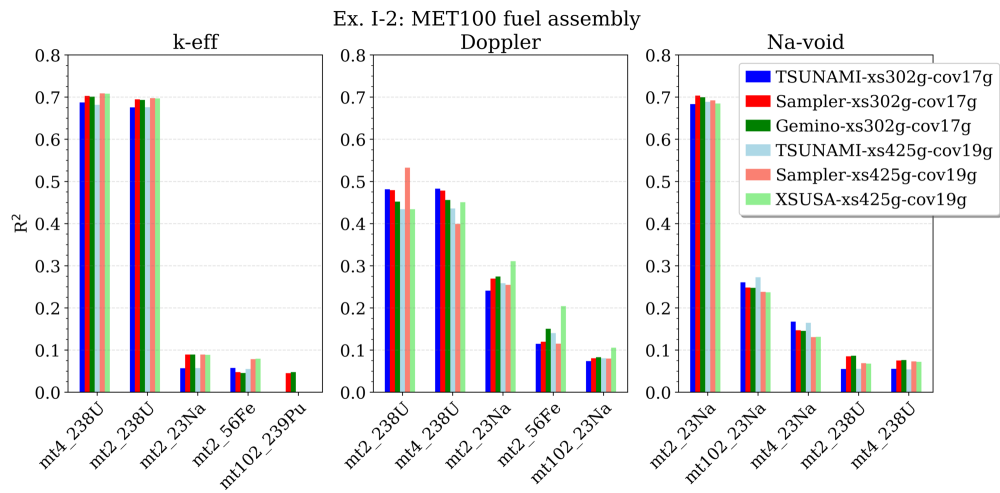
Figure 6.14 – Ex. I-2: MET1000 fuel assembly results—top contributors to the uncertainties in terms of R^2.
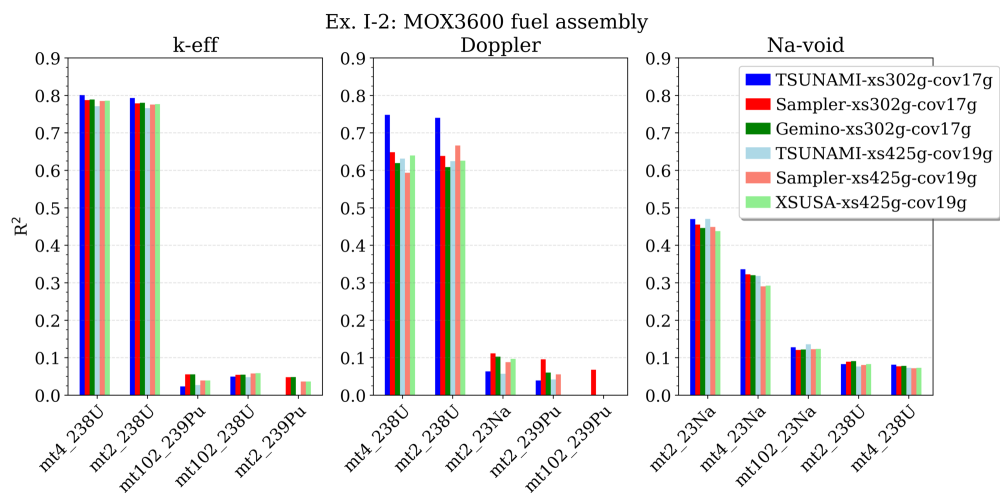
Figure 6.15 – Ex. I-2: MOX3600 fuel assembly results—top contributors to the uncertainties in terms of R^2.

Table 6.3 – Ex. I-2: Nominal fuel assembly results.

Output quantity	MET1000			MOX3600		
	xs302g	xs425g	Difference	xs302g	xs425g	Difference
eigenvalue	1.2787E+00	1.2794E+00	73 pcm	1.1452E+00	1.1471E+00	192 pcm
mac_total_1 [1/cm]	1.7266E-01	1.7220E-01	-0.27%	1.9908E-01	1.9960E-01	0.26%
mac_total_2 [1/cm]	2.1816E-01	2.1882E-01	0.30%	2.6889E-01	2.7018E-01	0.48%
mac_total_3 [1/cm]	2.8621E-01	2.8795E-01	0.61%	3.2833E-01	3.3309E-01	1.45%
mac_total_4 [1/cm]	4.0908E-01	4.1012E-01	0.25%	4.4847E-01	4.5141E-01	0.66%
mac_abs_1 [1/cm]	5.8199E-03	5.8139E-03	-0.10%	6.4173E-03	6.4624E-03	0.70%
mac_abs_2 [1/cm]	3.1264E-03	3.1234E-03	-0.10%	3.2585E-03	3.2775E-03	0.58%
mac_abs_3 [1/cm]	5.3812E-03	5.3771E-03	-0.08%	5.7719E-03	5.8052E-03	0.58%
mac_abs_4 [1/cm]	1.2254E-02	1.2305E-02	0.41%	1.4627E-02	1.4767E-02	0.95%
mac_nu_fis_1 [1/cm]	1.4948E-02	1.4927E-02	-0.14%	1.6438E-02	1.6554E-02	0.71%
mac_nu_fis_2 [1/cm]	4.8029E-03	4.8039E-03	0.02%	5.0632E-03	5.1025E-03	0.78%
mac_nu_fis_3 [1/cm]	4.6897E-03	4.6956E-03	0.12%	4.9669E-03	5.0098E-03	0.86%
mac_nu_fis_4 [1/cm]	7.7842E-03	7.7934E-03	0.12%	9.3154E-03	9.3850E-03	0.75%
mac_tot_scat_1 [1/cm]	1.6694E-01	1.6648E-01	-0.28%	1.9278E-01	1.9326E-01	0.25%
mac_tot_scat_2 [1/cm]	2.1504E-01	2.1570E-01	0.31%	2.6563E-01	2.6691E-01	0.48%
mac_tot_scat_3 [1/cm]	2.8083E-01	2.8257E-01	0.62%	3.2255E-01	3.2728E-01	1.47%
mac_tot_scat_4 [1/cm]	3.9683E-01	3.9781E-01	0.25%	4.3385E-01	4.3665E-01	0.65%
doppler	-315 pcm	-303 pcm	12 pcm	-780 pcm	-765 pcm	15 pcm
na_void	5797 pcm	5839 pcm	42 pcm	2994 pcm	2952 pcm	-42 pcm

6.3   Supercell

6.3.1   Nominal results

Just as for the fuel assembly, the NEWT supercell models were created by placing fuel and absorber pins explicitly as holes into a representative rectangular cell. As a reminder, with option B, the fuel assemblies were modeled explicitly, while for option A, flux-volume homogenized cross sections of a fuel assembly were used in the fuel assembly area of the supercell. The calculations for the 302-group library were limited to option B, while the 425-group calculations were performed with options A and B to assess the modeling simplification in option A.

The nominal values of the two different 425-group calculations are consistent with a maximum difference of 0.6% (Table 6.4). The 302-group results are mostly consistent with the 425-group results. The eigenvalues differ by about 300 pcm due to differences in the library generation, modeling choices, and settings for the transport solver. The NEWT supercell models are comparably large and contain a lot of detail due to the explicit modeling of multiple fuel assemblies. It was challenging to find settings that allowed for successful completion of the calculation.

6.3.2   Uncertainty and sensitivity analysis results

The uncertainties of the eigenvalue and the macroscopic cross sections of the super-cells are similar to those observed for the fuel assemblies. The uncertainty of the control rod worth is about 2.8% for the MET1000 supercell and about 2.4% for the MOX3600 supercell (Figure 6.16 and 6.16). As in the Doppler and Na-void reactivity of the fuel assemblies, these large uncertainties stress the relevance of nuclear data uncertainties for safety-related reactivity parameters.

The random sampling and perturbation theory calculations are consistent within the set of calculations that have the same data libraries and NEWT models. Small relative differences of up to 7% can be observed between the two sets of results, most likely caused by different modeling choices in NEWT and different group structures. A sensitivity analysis of the macroscopic cross section reveals only scattering reactions of several iron, sodium, and boron isotopes, as well as inelastic scattering of ^{238}U as most important contributors to the uncertainties. The scattering reactions have a very fine resonance structure in the very high energy range that might be better

represented by the 425-group structure.

For the eigenvalue and the control rod worth of the supercells, a sensitivity analysis was performed to determine the top contributors to the observed uncertainties (Figures 6.20 and 6.21). For both designs, the inelastic and elastic scattering cross sections of ^{238}U clearly dominate the ranking for both output quantities. The various calculations thereby show consistent results.
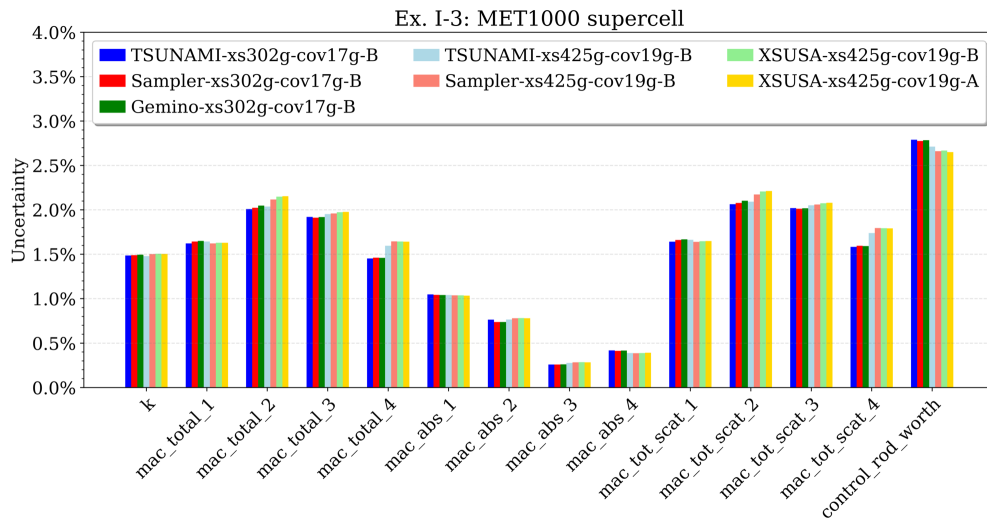

Figure 6.16 – Ex. I-3: MET1000 supercell results—uncertainties.
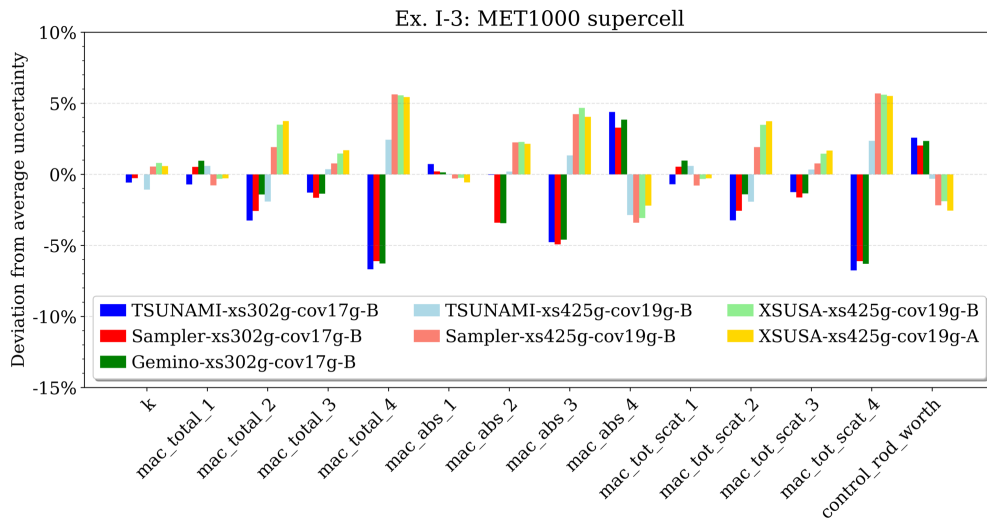
Figure 6.17 – Ex. I-3: MET1000 supercell results—difference to average uncertainty.
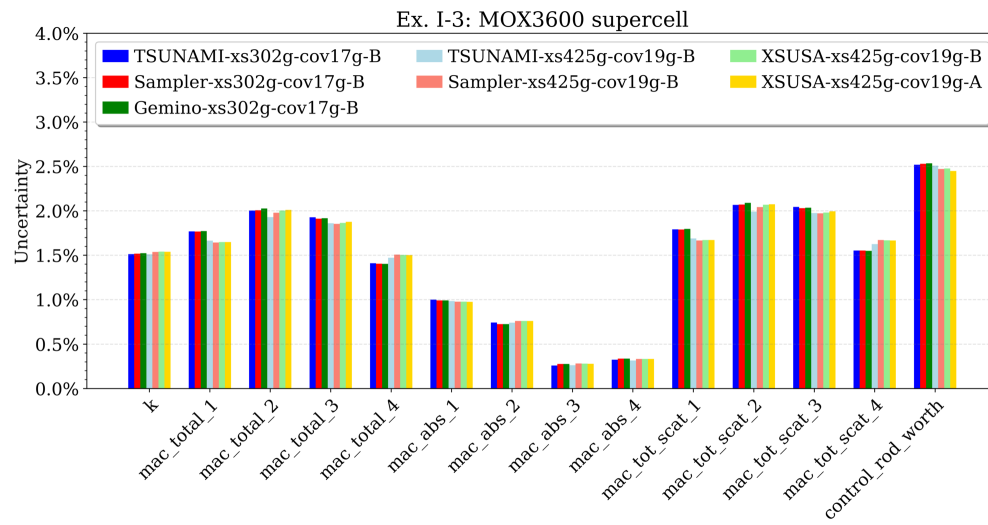
Figure 6.18 – Ex. I-3: MOX3600 supercell results—uncertainties.
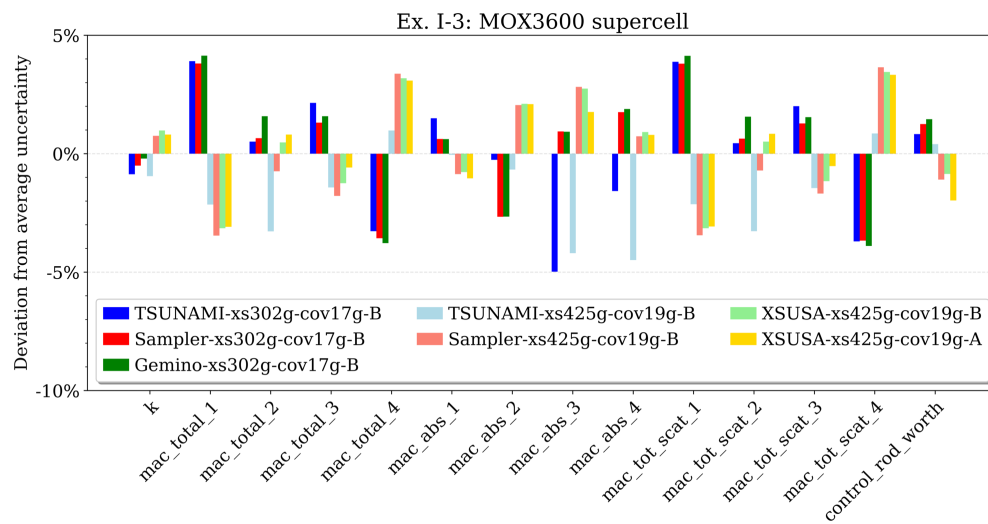
Figure 6.19 – Ex. I-3: MOX3600 supercell results—difference to average uncertainty.
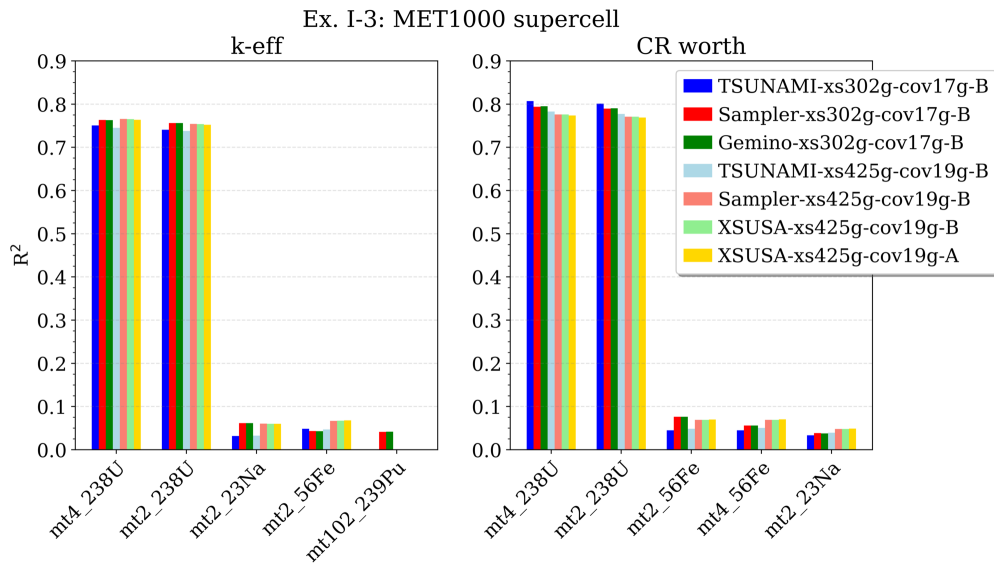
Figure 6.20 – Ex. I-3: MET1000 supercell results—top contributors to the uncertainties in terms of R^2.
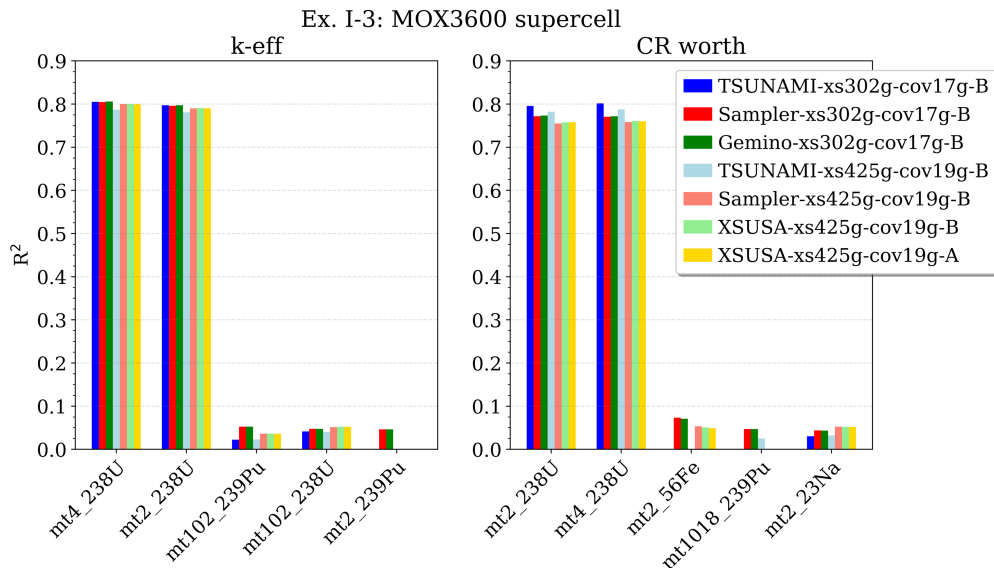
Figure 6.21 – Ex. I-3: MOX3600 supercell results—top contributors to the uncertainties in terms of R^2.

Table 6.4 – Ex. I-3: Nominal supercell assembly results.

Output quantity	MET1000			MOX3600		
	xs302g-B	xs425g-B	xs425g-A	xs302g-B	xs425g-B	xs425g-A
eigenvalue	1.0804E+00	1.0837E+00	1.0833E+00	1.0740E+00	1.0770E+00	1.0769E+00
mac_total_1 [1/cm]	1.4550E-01	1.4630E-01	1.4626E-01	1.4846E-01	1.4436E-01	1.4429E-01
mac_total_2 [1/cm]	1.9967E-01	2.0082E-01	2.0108E-01	2.0556E-01	2.0110E-01	2.0158E-01
mac_total_3 [1/cm]	2.7030E-01	2.7264E-01	2.7314E-01	2.7344E-01	2.6870E-01	2.7015E-01
mac_total_4 [1/cm]	4.1190E-01	4.1155E-01	4.1119E-01	4.0976E-01	3.9905E-01	4.0005E-01
mac_abs_1 [1/cm]	1.5578E-03	1.5580E-03	1.5598E-03	1.8927E-03	1.8994E-03	1.9030E-03
mac_abs_2 [1/cm]	5.0513E-03	5.0507E-03	5.0491E-03	5.8235E-03	5.8398E-03	5.8404E-03
mac_abs_3 [1/cm]	1.3135E-02	1.3145E-02	1.3151E-02	1.5062E-02	1.5119E-02	1.5109E-02
mac_abs_4 [1/cm]	3.4981E-02	3.4981E-02	3.5016E-02	3.7475E-02	3.7444E-02	3.7391E-02
mac_tot_scat_1 [1/cm]	1.4394E-01	1.4475E-01	1.4470E-01	1.4656E-01	1.4246E-01	1.4239E-01
mac_tot_scat_2 [1/cm]	1.9462E-01	1.9577E-01	1.9603E-01	1.9974E-01	1.9526E-01	1.9574E-01
mac_tot_scat_3 [1/cm]	2.5716E-01	2.5949E-01	2.5998E-01	2.5838E-01	2.5358E-01	2.5504E-01
mac_tot_scat_4 [1/cm]	3.7692E-01	3.7657E-01	3.7618E-01	3.7228E-01	3.6160E-01	3.6266E-01
control_rod_worth	12087 pcm	12266 pcm	12272 pcm	5020 pcm	5050 pcm	5041 pcm

145

6.4 Full core

Full core calculations were performed with the Monte Carlo codes KENO and Serpent. Furthermore, the nodal diffusion code PARCS was applied in combination with few-group cross sections generated by NEWT and Serpent, respectively. Uncertainty and sensitivity analyses based on these models were performed with Gemino, Sampler, and TSUNAMI.

6.4.1 Full core Monte Carlo results

Nominal full core results obtained with KENO using CE and MG cross section data and the settings for the simulations are presented in Section 3.1.5. Since Serpent was additionally used for cross section generation for PARCS, Serpent full core calculations were compared to KENO-CE reference results for reasons of completeness. Since Serpent does not allow different boundary conditions in positive and negative directions, the full core models were used for the calculations instead of taking advantage of core symmetries. The average of 20 calculations with different random seeds was determined for each core to reduce the power tilt over the reactor core (cf. discussion of power tilt in Section 3.1.5). Using $2 \cdot 10^6$ neutrons per generation, 200/400 active generations were calculated for the MET1000/MOX3600 core with 50 inactive generations in both cases.

Table 6.5 shows the excellent agreement of the Serpent CE and KENO-CE full core eigenvalues, and Figure 6.22 shows the excellent agreement of the radial power distributions. The MET1000 power distribution shows differences of less than 0.1%. In the case of the MOX3600 core, slightly larger differences of up to 0.64% are visible due to a slight tilt in the power distribution, despite the large number of simulated neutron histories. Due mainly to the large size of MOX3600 (about 1.5 times the size of the MET1000 core), a very large number of neutrons would be necessary to improve the convergence of the MOX3600 power distribution.

6.4.2 Generation of few-group cross sections for PARCS

To calculate the eigenvalue and the power distributions with the nodal diffusion code PARCS, macroscopic cross sections were generated with NEWT for all fuel zones and

(a) MET1000,
RMS/max. diff. = ± 0.03/0.10%

(b) MOX3600,
RMS/max. diff. = ± 0.34/0.64%
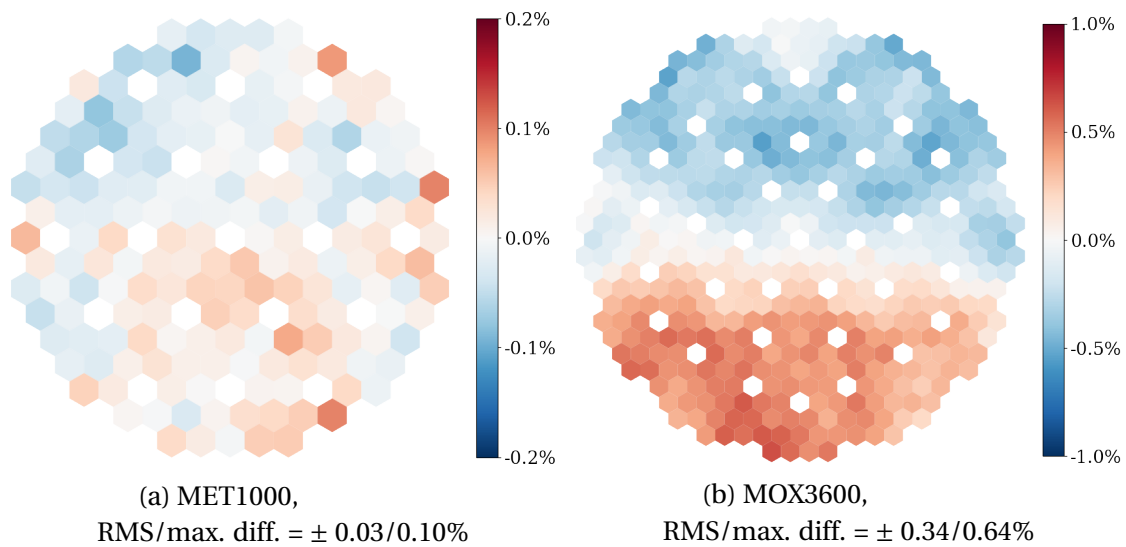
Figure 6.22 – Relative difference of the axially integrated assembly power between Serpent CE and the reference KENO-CE calculation. Note the small range of the color bar.

Table 6.5 – Ex. I-4: Nominal full core results.

Output quantity	MET1000		MOX3600	
	k_{eff}	Δk [pcm]	k_{eff}	Δk [pcm]
KENO-CE	1.01649(4)	(ref)	1.01134(2)	(ref)
Serpent CE	1.01660(1)	11	1.01163(1)	28
PARCS/NEWT	1.00541	-1108	1.00583	-551
PARCS/Serpent	1.01320	-329	1.01027	-107

all non-multiplying assemblies. Using the approach for cross section generation as presented by Nikitin (Nikitin, 2019), various supercells were used for the generation of cross sections for non-multiplying assemblies. As in Ex. I-3, supercell models with the non-multiplying assembly surrounded by fuel assemblies were created for each type of a non-multiplying assembly. To simplify the calculation with NEWT, flux-volume homogenized cross sections for the fuel assemblies were applied instead of modeling the fuel assemblies explicitly (see option B in Ex. I-3). Furthermore, the supercells were modeled as rectangular cells with reflective boundary conditions instead of modeling cells with hexagonal outer boundaries (Figure 6.23). Instead of reflecting the ratio of a particular non-multiplying assembly to fuel assemblies in the whole core with the supercell, the non-multiplying assemblies were surrounded by only three fuel assemblies to provide a characteristic neutron spectrum. These modeling

147

choices, especially the decreased model size compared to that of Ex. I-3, improved the computation time and resolved some convergence problems that were occurring with NEWT. Figures 6.24 and 6.25 show the supercell models used for the MET1000 and the MOX3600 cores, respectively.

The cross sections for the fuel assemblies were generated for a total of ten fuel zones (five axial zones for the inner core region, and five for the outer core region) using rectangular fuel assembly models as shown in Figures 6.24(a) and 6.25(a). In contrast to Nikitin's work, the fuel assemblies were modeled in two dimensions due to the limitation to use NEWT for the cross section generation.

To allow for an assessment of the impact of the applied code in general, and in particular, to allow for assessment of the MG approximations (MG cross sections, self-shielding treatment, spatial discretization etc.) for the generation of these few-group cross sections, the Monte Carlo code Serpent was also used to generate few-group cross sections based on the same models. Although Serpent allows three-dimensional models for cross section generation, the same two-dimensional models used for NEWT were used here to allow for a fair comparison.
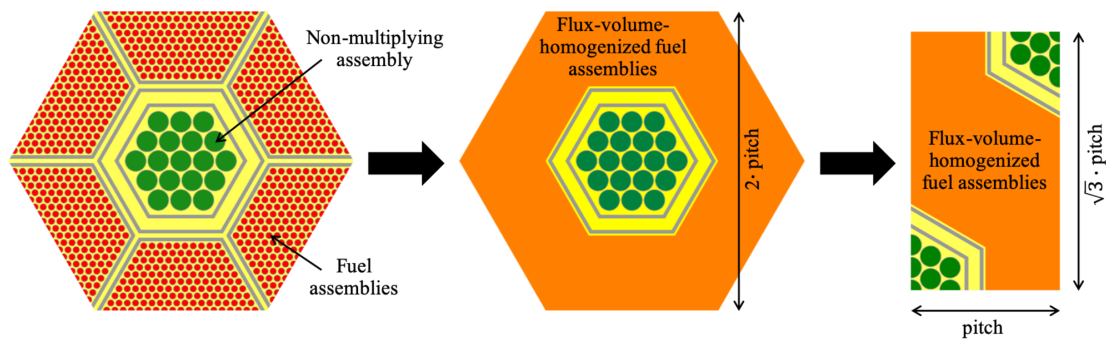
Figure 6.23 – Cross section generation for non-multiplying assemblies with supercells.

(a) Fuel assembly   (b) Bond sodium   (c) Helium

(d) Lower reflector   (e) Control rod   (f) Empty assembly

(g) Lower structure   (h) Outer reflector   (i) Outer shield
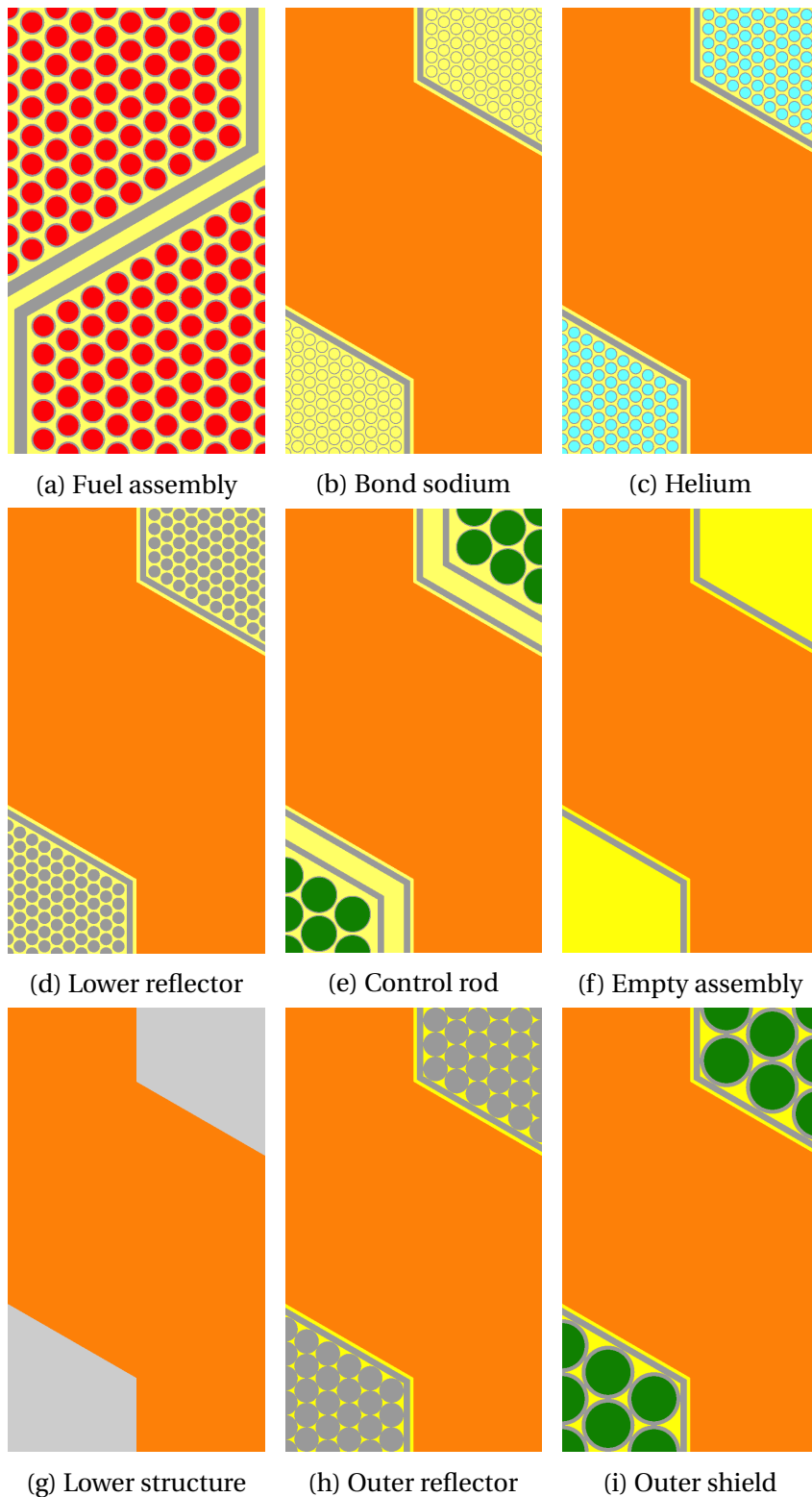
Figure 6.24 – NEWT models for the generation of macroscopic cross sections for the MET1000 full core calculations with PARCS.

(a) Fuel assembly   (b) Empty assembly   (c) Helium   (d) Reflector assembly

(e) Primary control rod   (f) Secondary control rod   (g) Outer reflector
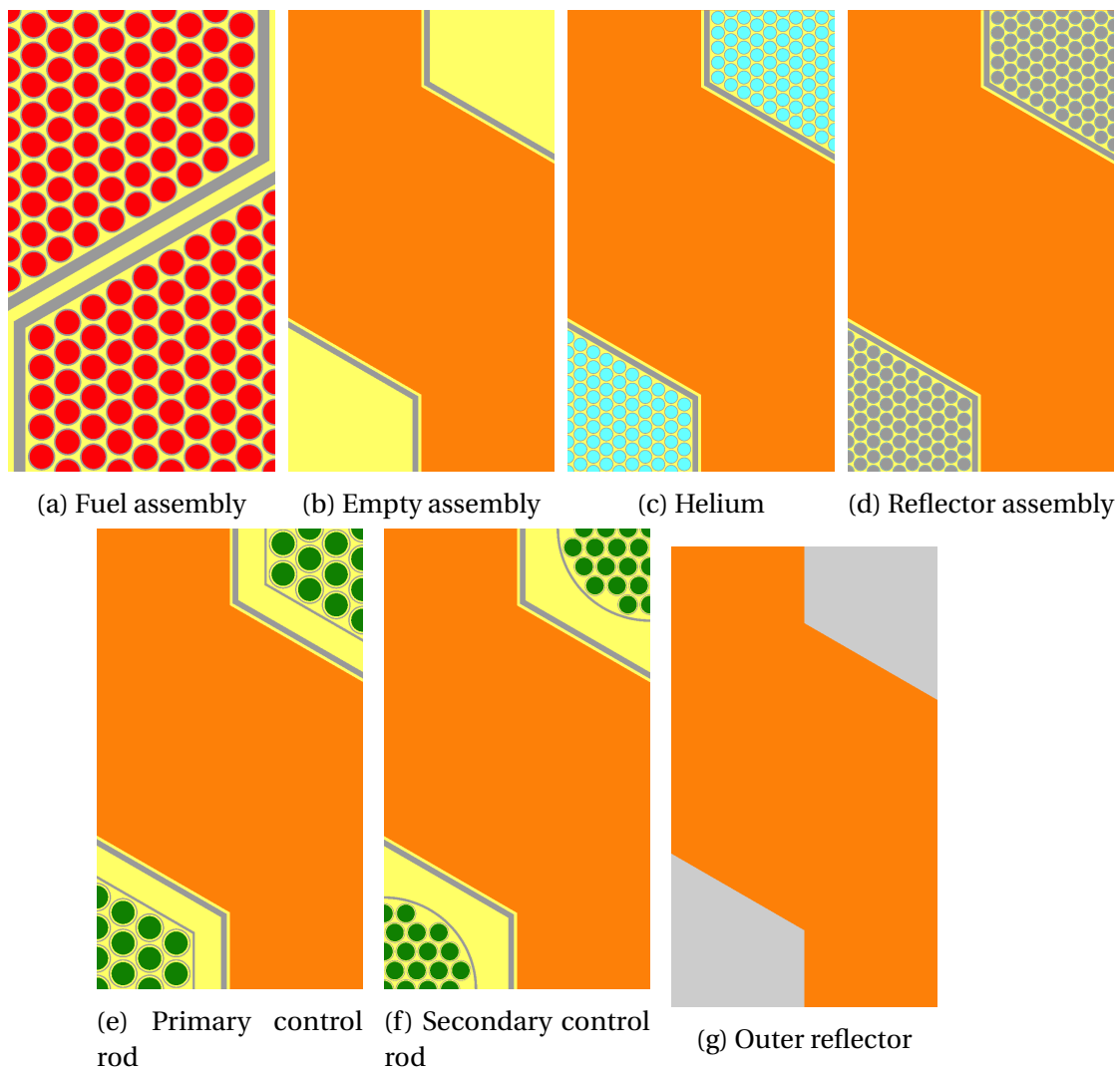
Figure 6.25 – NEWT models for the generation of macroscopic cross sections for the MOX3600 full core calculations with PARCS.

6.4.3 Nominal PARCS results

The PARCS results based on cross sections generated by Serpent are referred to as *PARCS/Serpent*, and the calculations based on cross sections generated by NEWT are referred to as *PARCS/NEWT*.

Table 6.5 compares the calculated eigenvalues of both cores. The PARCS/NEWT results show large differences of more than 1,000 pcm for the MET1000 core and differences of about 430 pcm for the MOX3600 core. Since the PARCS/Serpent results show a significantly improved agreement with the reference, a significant fraction of the PARCS/NEWT discrepancies can be explained by (1) using MG approximations with NEWT (including the previously discussed difficulties in finding appropriate self-shielding cells) instead of using CE data, and (2) by using different approaches to calculate the transport cross section with NEWT and Serpent, for example. In the case of the MOX3600 core, the observed differences between PARCS/Serpent and KENO-CE are consistent with the findings of Nikitin (Nikitin, 2019). The large difference between PARCS/NEWT and KENO-CE is consistent with findings of Bousquet (Bousquet et al., 2017) for lead-cooled fast spectrum systems. Furthermore, the result of the MOX3600 core is consistent with Rachamin's findings (Rachamin et al., 2013), who found good agreement between calculations with the nodal code DYN3D using cross sections generated with Serpent and a corresponding Serpent CE reference calculation for an oxide fuel core model that is very similar to the MOX3600 core. In contrast, they found a disagreement of more than 800 pcm when using a deterministic code with MG cross sections for the few-group cross section generation.

Some of the differences between PARCS/Serpent and KENO-CE calculations are the result of inadequate cross sections generated for the control rod assemblies. Nikitin et al. improved those cross sections by applying the Superhomogenization (SPH) method (Nikitin et al., 2015). However, this method could not be applied in this study because of the necessity to create models with hexagonal outer boundaries with the nodal transport code, which is currently not possible with PARCS (hexagonal assemblies are permitted, but a lattice of assemblies cannot be truncated in order to result in a hexagonal supercell as shown in Figure 2.4a). It was also decided not to follow the SPH method with corresponding square models, as the iterative scheme of this approach was considered to be impractical for executing a large number of PARCS calculations for uncertainty analyses.

Figures 6.26 and 6.27 present the relative difference of the axially integrated assembly power between PARCS and the reference KENO-CE calculation for the MET1000 and MOX3600 core, respectively. In addition to the absolute maximum difference between the two calculations, the root mean square is provided. As expected, the PARCS/Serpent results show excellent agreement with the KENO-CE calculation. The shape of the radial power distribution is slightly overestimated in the inner core, while it is slightly underestimated in the outer core. Maximum differences of less than 2% were achieved for both cores. The root mean square for the PARCS/NEWT calculation compared to KENO-CE are about 2%, while the maximum differences are 3% for the MET1000 core and about 3.8% for the MOX3600 core. A more pronounced overestimation of power in the central core area and a corresponding underestimation of the power in the outer core area compared to PARCS/Serpent is visible, indicating an underestimation of the transport cross section with NEWT that reduces the travel of the neutrons to the core's outer areas.

For one assembly of each core, the axial power distribution is compared in Figure 6.28. PARCS/NEWT and KENO-CE show excellent agreement, with a maximum relative difference of 2.1%.

Despite the significant disagreement regarding the eigenvalue, the PARCS/NEWT calculation leads to reasonable agreement with KENO-CE in terms of power distribution. This agreement was considered sufficient as a basis for the uncertainty analysis presented in the following.

(a) PARCS/Serpent vs. KENO-CE,
RMS/max. diff. = ± 0.91/1.21%

(b) PARCS/NEWT vs. KENO-CE,
RMS/max. diff. = ± 2.03/3.01%
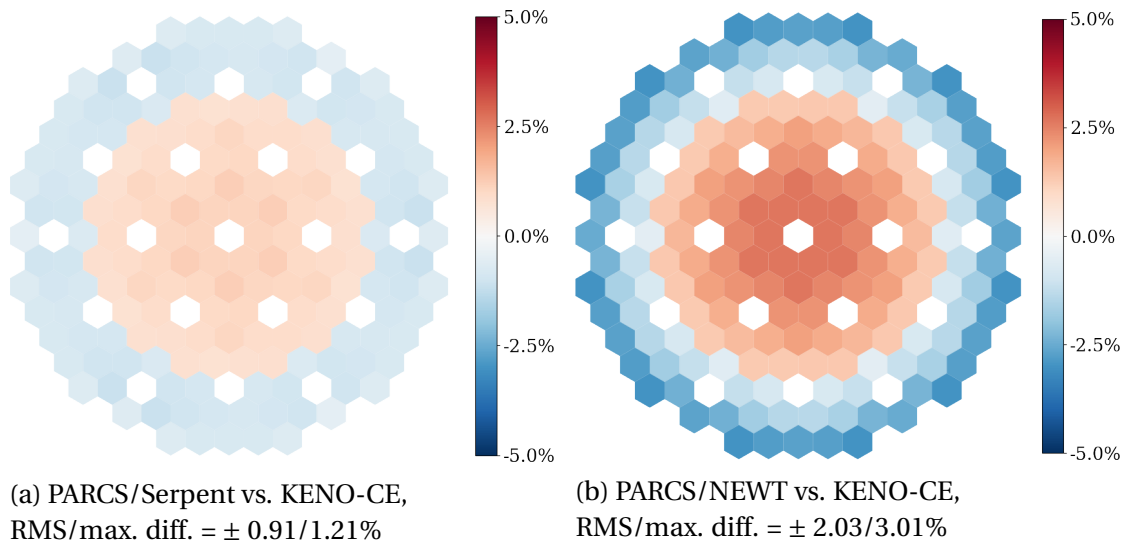
Figure 6.26 – MET1000 core: Relative difference of the axially integrated assembly power between PARCS and the reference KENO-CE calculation.

(a) PARCS/Serpent vs. KENO-CE,
RMS/max. diff. = ± 0.92/1.89%

(b) PARCS/NEWT vs. KENO-CE,
RMS/max. diff. = ± 1.89/3.77%
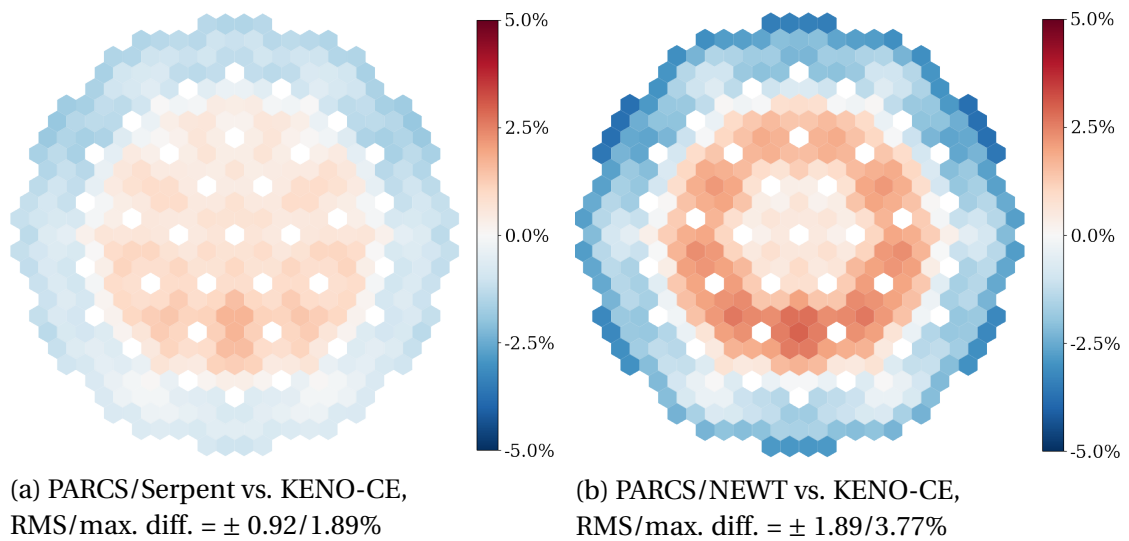
Figure 6.27 – MOX3600 core: Relative difference of the axially integrated assembly power between PARCS and the reference KENO-CE calculation.
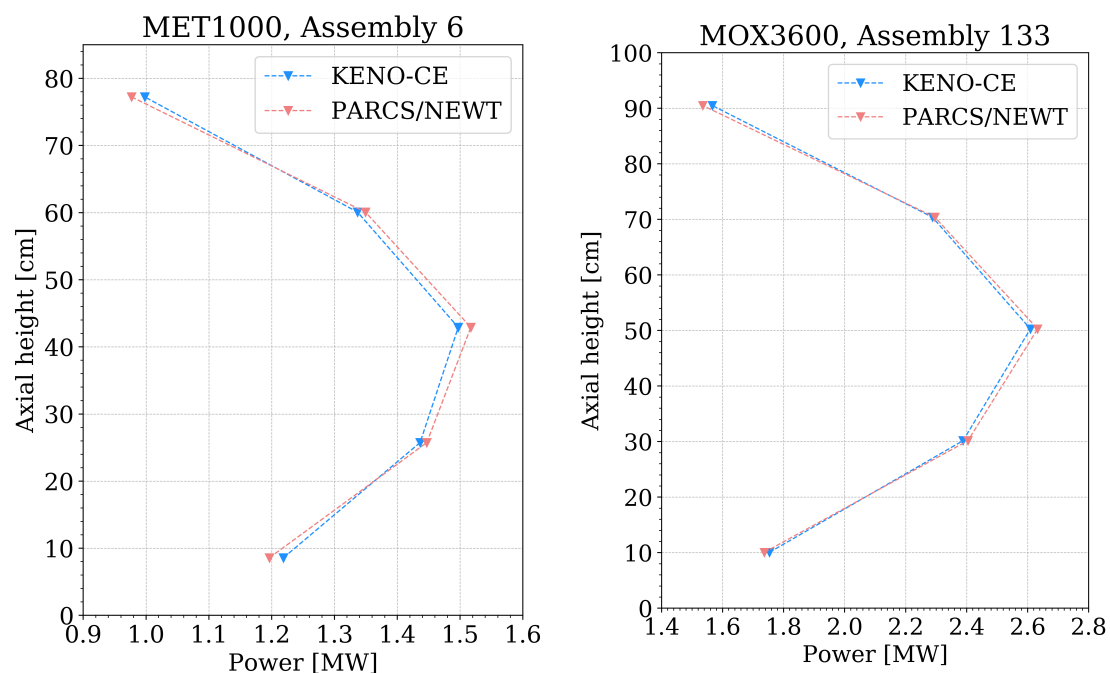
Figure 6.28 – Axial assembly power compared between PARCS/NEWT and the reference KENO-CE calculation (cf. Figures 2.6 and 2.9 for the position of the assemblies in the core).

6.4.4 Uncertainty and sensitivity analysis results

Four different approaches were followed for the full core uncertainty and sensitivity analyses:

1. TSUNAMI-MG: TSUNAMI full core calculations using KENO-MG as transport solver (only eigenvalue analysis),

2. Sampler/KENO-MG: Sampler calculations based on full core KENO-MG models,

3. Gemino/KENO-MG: Gemino calculations based on full core KENO-MG models,

4. Sampler/PARCS/NEWT: Generation of varied few-group cross section generation with Sampler/NEWT; PARCS calculations based on the varied cross sections.

The Sampler/PARCS/NEWT calculations were performed in five steps:

1. Generation of perturbed macroscopic 24-group cross sections with NEWT for all fuel assemblies with Sampler,

2. Generation of perturbed macroscopic 302-group cross sections for one fuel assembly (inner core, middle layer) with Sampler,

3. Generation of perturbed macroscopic 24-group cross sections with NEWT for all non-multiplying assemblies using the fuel assembly cross sections from step 2 with Sampler,

4. PARCS full core calculations based on the sets of varied 24-group cross sections from steps 1–3,

5. Statistical analysis of the PARCS results.

A sample size of 1,000 was used for the Sampler/PARCS/NEWT calculations. In the case of the Sampler/Gemino calculations, which were based on the KENO-MG full core calculations, a reduced sample size of 200 was used to limit the computational burden. While a single PARCS calculation takes only a few minutes, each KENO-MG full core calculation took several days when using 32 MPI tasks on a Linux computing cluster. The Sampler/KENO-MG calculations were performed for the MET1000 core,

and the Gemino/KENO-MG calculations were performed for the MOX3600 core. Due to the order of completed development steps within this work, the MET1000 calculations were performed based on the 302-group covariance library, while all other full core uncertainty analyses were based on the 17-group covariance library. However, as demonstrated in Section 3.2, the difference in the group structure of the covariance libraries does not have an impact on the results.

Table 6.6 – Ex. I-4: Full core eigenvalue uncertainty results. Values in parentheses indicate the 1σ statistical error in the case of TSUNAMI and the 95% confidence interval in the case of Sampler/Gemino.

| | $\Delta k_{eff}/k_{eff}$ | |
	MET1000	MOX3600
TSUNAMI-MG	1.1888(4)%	1.3751(3)%
Sampler/KENO-MG (N=200)	1.13(11)%	—
Gemino/KENO-MG (N=200)	—	1.25(14)
Sampler/PARCS/NEWT (N=1,000)	1.13(6)%	1.34(7)%

Table 6.6 shows eigenvalue uncertainties of about 1.2% and 1.4% for the MET1000 and MOX3600 full core models, respectively. The results with the different approaches are consistent when considering their corresponding statistical uncertainty (TSUNAMI: due to the Monte Carlo neutron transport calculation; Sampler/Gemino: due to the limited sample size). The top contributors to the eigenvalue uncertainties are inelastic and elastic scattering of ^{238}U, as displayed in Figure 6.34. The observed eigenvalue uncertainties are consequently in the same range as the corresponding pin cell, fuel assembly and supercell uncertainties and show the same top contributing nuclide reactions.

Figures 6.29 to 6.32 present the uncertainties of the axially integrated assembly power distributions from the Sampler and Gemino calculations. An average uncertainty of about 0.4% was determined for the MET1000 core, while the MOX3600 core shows an average of about 0.6%. In both cores, the central and the outermost fuel assemblies of the core show the largest uncertainties. This is caused by the normalization of the core power to always the nominal power: The total reactor power in each sample calculation is assumed identical; only the shape of the power changes. The differences in the radial power distribution are consequently most visible in areas of the lowest and highest power in the core.

The calculations based on Sampler/PARCS/NEWT and Sampler/KENO-MG show

reasonable agreement, especially when considering the limited sample sizes. A sample size of 1,000 results in relative 95% confidence intervals of about 5% for the Sampler/PARCS/NEWT results, whereas the sample size of 200 results in an interval of about 11%. The Sampler/KENO-MG calculations also show larger uncertainties because of the addition of the Monte Carlo uncertainties to the nuclear data uncertainties. In particular in the case of the outer assemblies, larger uncertainties due to higher Monte Carlo uncertainties are visible.

Figure 6.33 shows the axial power distribution of one assembly per core, along with its associated uncertainty. Due to the normalization of the assembly power for these uncertainty calculations, the uppermost and lowermost fuel zones show the largest uncertainties. Additionally, the top contributors to the uncertainty of the axially integrated power in these assemblies was investigated based on the Sampler/PARCS/NEWT results. Figure 6.35 shows that scattering reactions of ^{238}U and ^{56}Fe are the major contributors; other relevant contributors are the (n,γ) reaction of ^{238}U, elastic scattering of ^{23}Na, as well as the fission reaction, the (n,γ) reaction, and the fission spectrum of ^{239}Pu.

In general it was observed that the assembly power uncertainties are lower than those in corresponding LWR uncertainty analyses. While the study showed uncertainties below 1%, Zwermann et al. reported larger uncertainties of up to 5% for the central fuel assemblies in an LWR core (Zwermann et al., 2009). As mentioned above, the assembly power uncertainties represent differences in the radial power distribution due to nuclear data uncertainties. It is assumed that the long mean free path of the neutrons in the SFR cores led to an increased compensation of effects from nuclear data perturbations as compared to an LWR core.
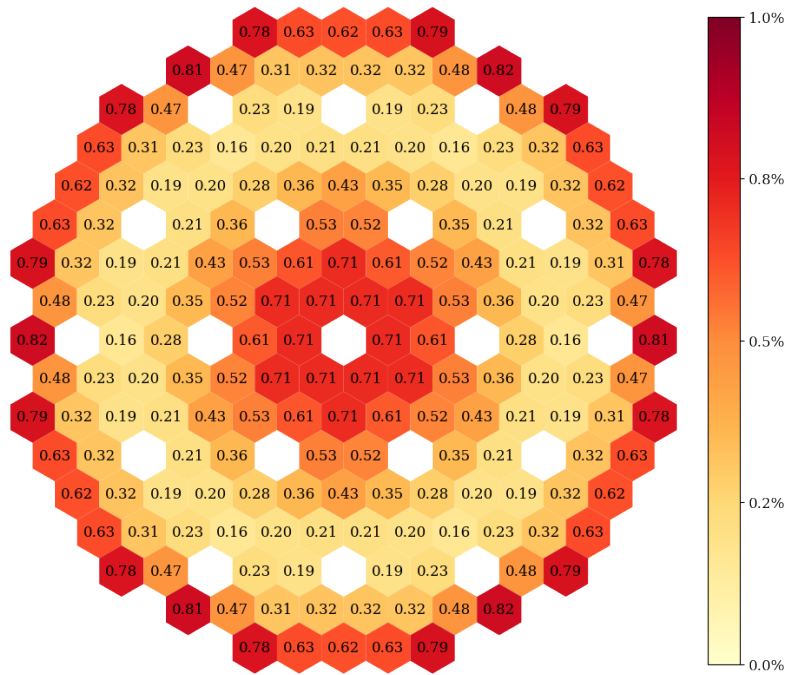
Figure 6.29 – MET1000 core: Sampler/KENO-MG uncertainty of the axially integrated assembly power. RMS/max.: 0.47/0.82%.
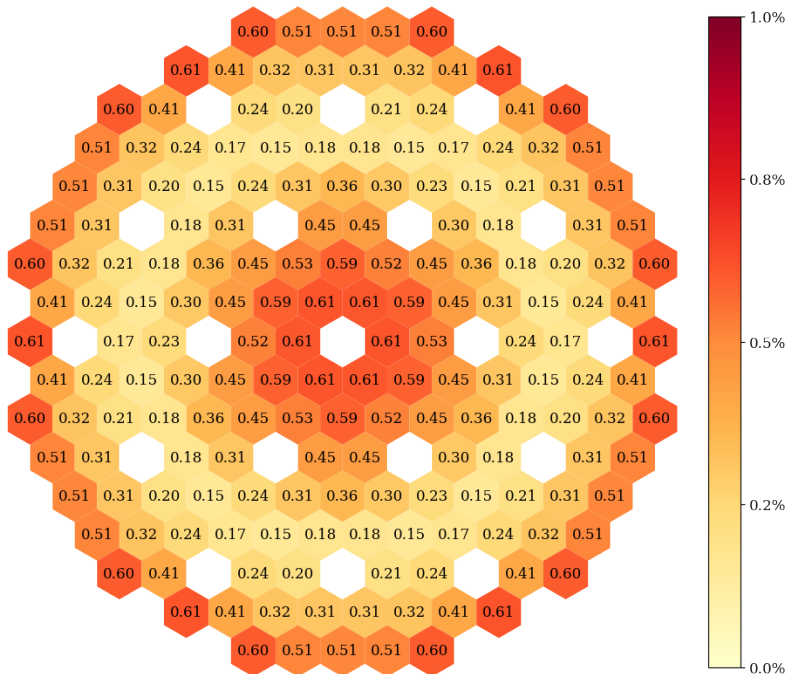
Figure 6.30 – MET1000 core: Sampler/PARCS/NEWT uncertainty of the axially integrated assembly power. RMS/max.: 0.40/0.61%.
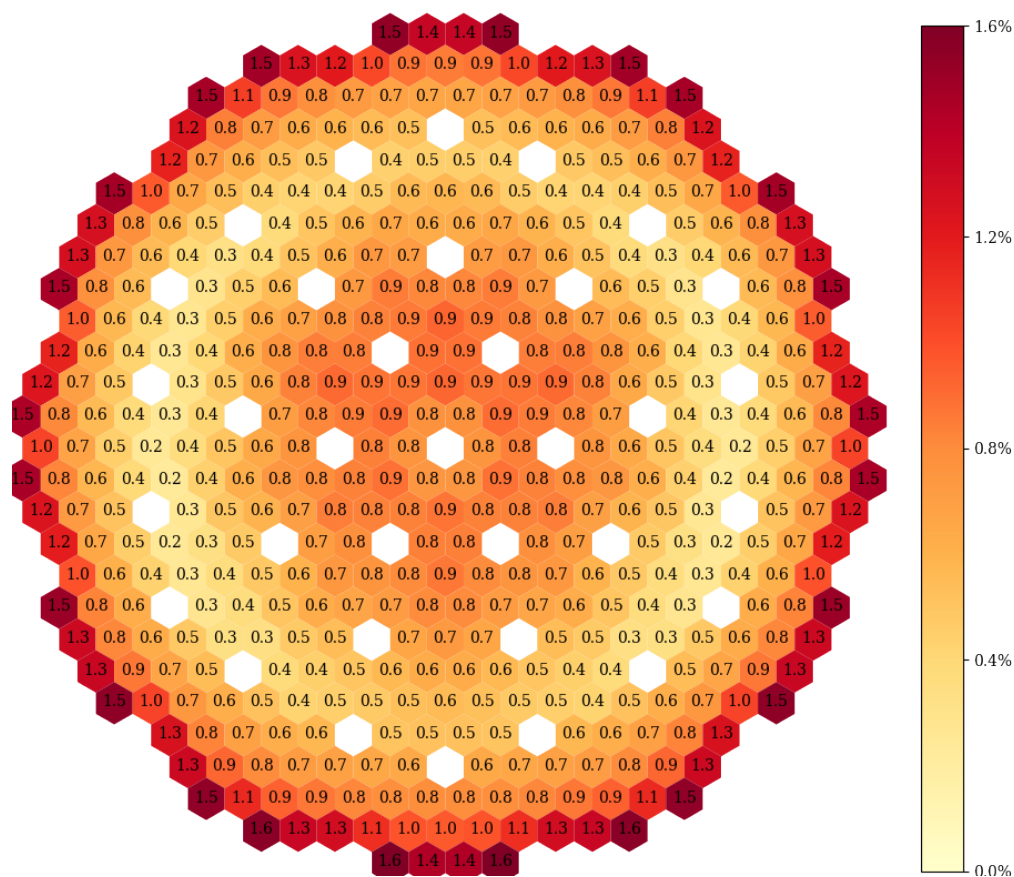
Figure 6.31 – MOX3600 core: Gemino/KENO-MG uncertainty of the axially integrated assembly power. RMS/max.: 0.00/0.00%.
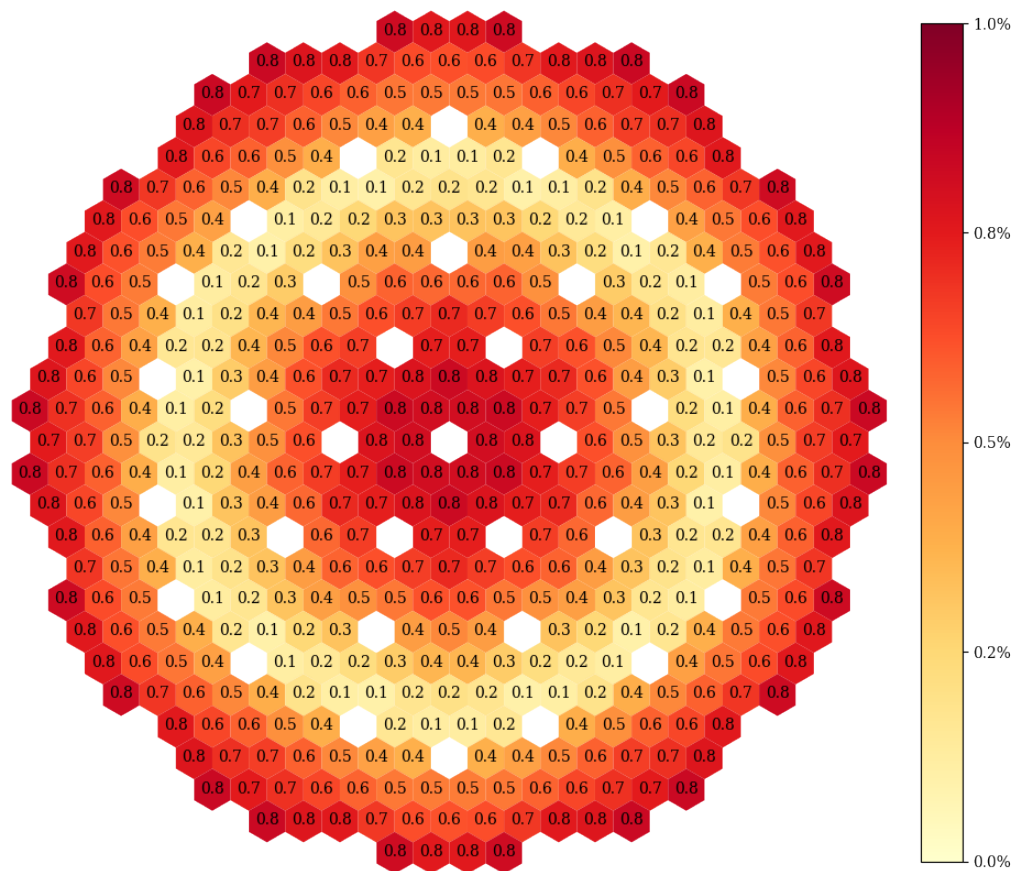
Figure 6.32 – MOX3600 core: Sampler/PARCS/NEWT uncertainty of the axially integrated assembly power. RMS/max.: 0.56/0.83%.
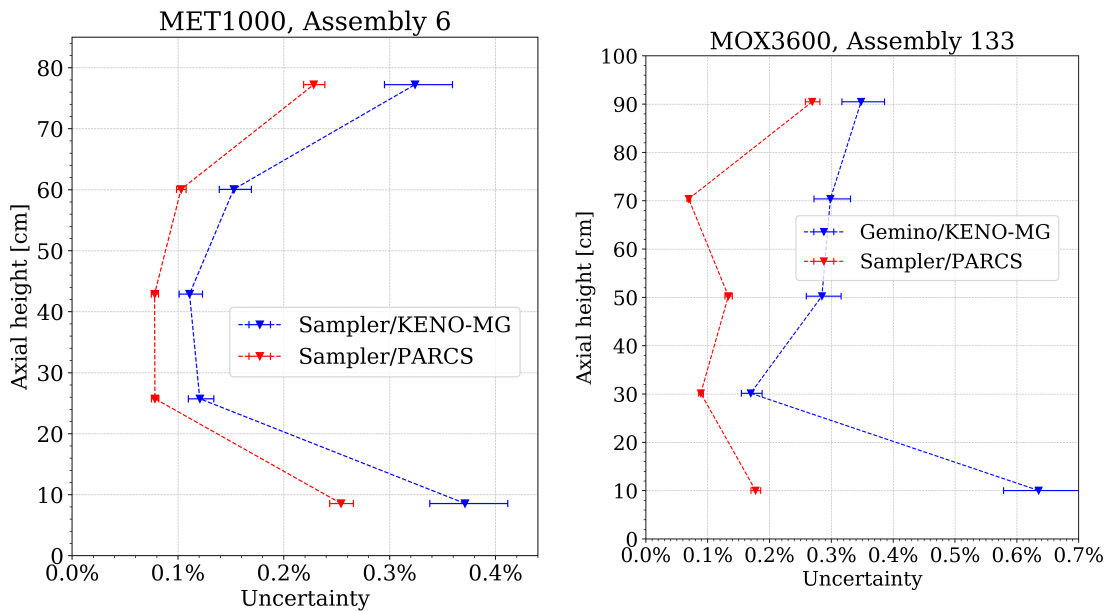
Figure 6.33 – Ex. I-4: Full core—uncertainty of the axial power.
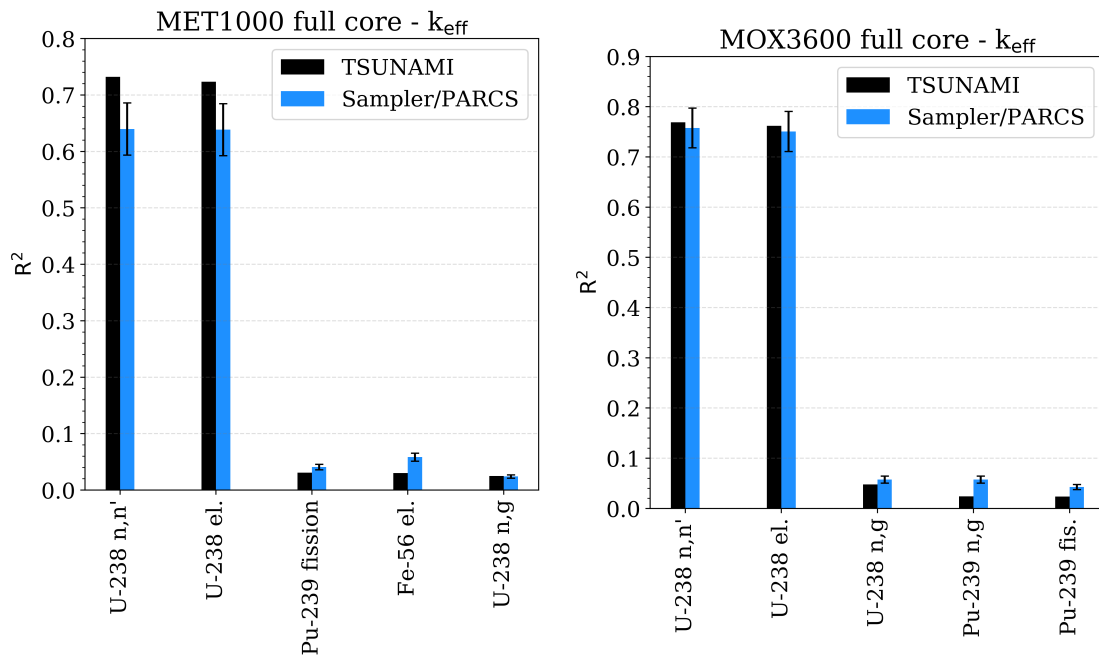
Figure 6.34 – Ex. I-4: Full core eigenvalue sensitivity analysis in terms of R^2.
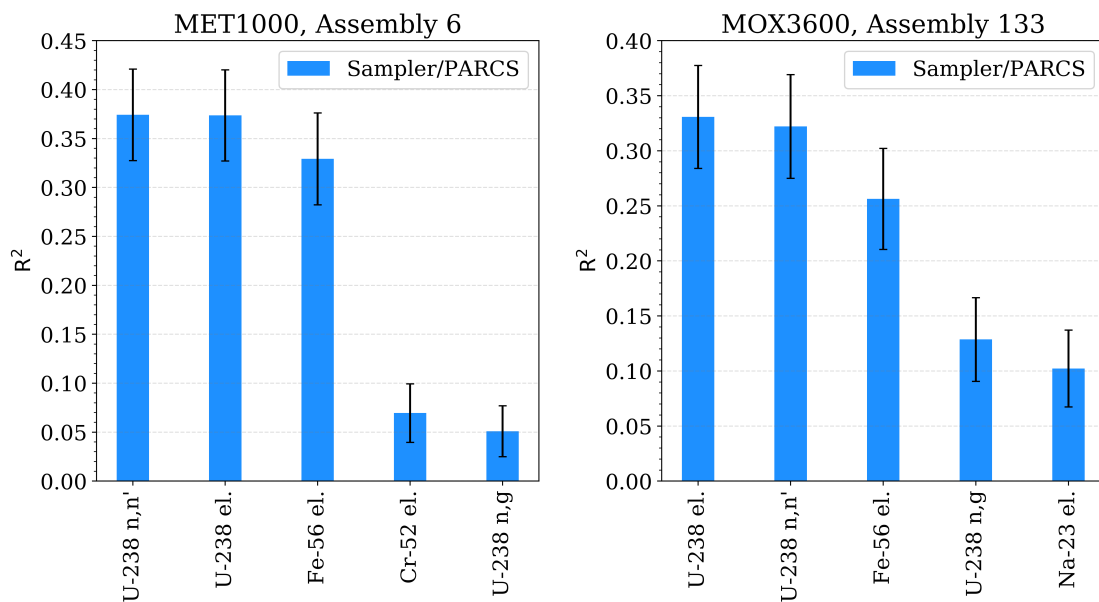
Figure 6.35 – Ex. I-4: Full core assembly power sensitivity analysis in terms of R^2.

6.5   Validation exercises

For the ZPR-6 Assembly 7 and the ZPPR-2 experiment, simplified models, as offered by the benchmark specifications (NEA, 2015b), were developed to determine the eigenvalue. The eigenvalue uncertainties were determined using both TSUNAMI and Gemino with a sample size of 1,000 in combination with KENO-MG as transport solver. The 302-group cross section and 17-group covariance library were applied.

Table 6.7 provides the experimental values with the corresponding experimental uncertainty, as well as the calculated nominal values with the uncertainty due to nuclear data. The Monte Carlo statistical error is below 10 pcm for the nominal KENO-MG eigenvalue results. When considering the nuclear data uncertainty, the calculated eigenvalues are in good agreement with the experiment. It is noted that the uncertainty caused by nuclear data is four to five times higher than the experimental uncertainty.

The top contributors to the eigenvalue uncertainties are presented in Figure 6.36. As in the studies of MET1000 and MOX3600 models, the dominating contribution to the eigenvalue uncertainty comes from inelastic scattering of ^{238}U. While elastic scattering of ^{238}U appears significant because of correlations to inelastic scattering, other relevant contributions come from the (n,γ) reaction in ^{238}U and ^{239}Pu and from ^{239}Pu fission.

Table 6.7 – Validation exercise results: benchmark eigenvalue with experimental uncertainty and TSUNAMI/Gemino results with uncertainty due to nuclear data.

	ZPR-6 Assembly 7 (MCF1)	ZPPR-2 (MCF6)
Experiment	0.9866 ± 0.0023	0.9889 ± 0.0021
TSUNAMI-MG	0.9892 ± 0.0105 (1.06%)	0.9933 ± 0.0099 (1.00%)
Gemino/KENO-MG	0.9892 ± 0.0100 (1.01%)	0.9933 ± 0.0090 (0.90%)
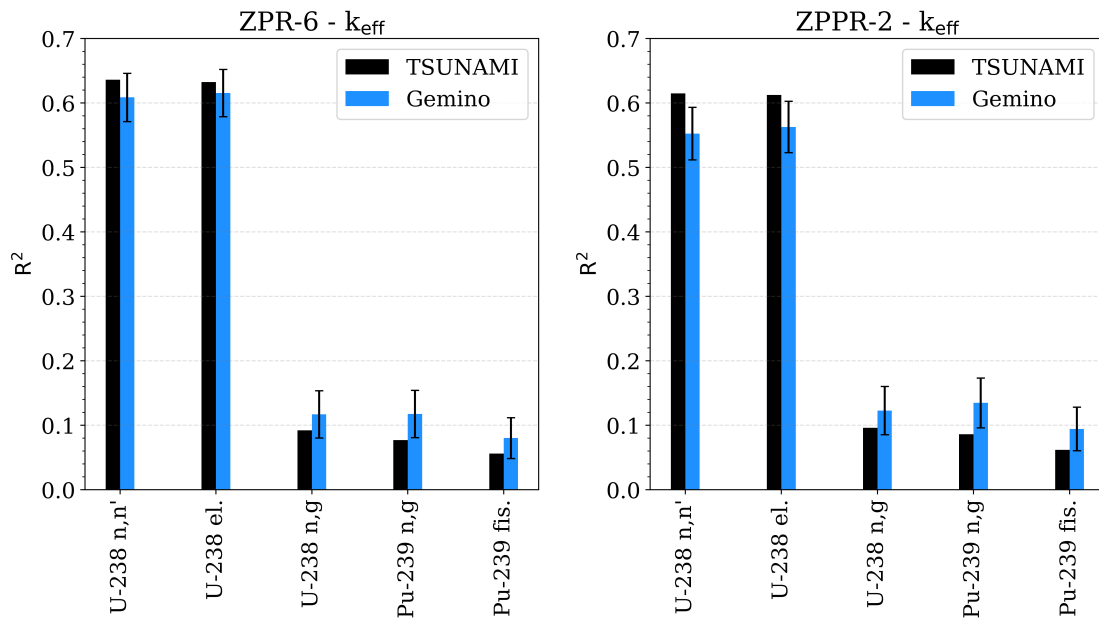
Figure 6.36 – Eigenvalue sensitivity analysis of ZPR-6 and ZPPR-2 in terms of R^2.

7 Summary and future work

The purpose of the doctoral research presented herein was to establish a systematic approach for quantifying nuclear data–induced uncertainties on important system responses in sodium-cooled fast reactor (SFR) systems on all stages of modeling to assess the performance of traditional methods for uncertainty and sensitivity analysis and to determine the major drivers of observed uncertainties. As preparation for analyses with the XSUSA approach using several tools of the SCALE code system, multigroup cross section and covariance libraries were optimized for SFR systems, and the uncertainty and sensitivity analysis capabilities were extended.

The developments and the analysis outcome of this work are summarized in the following section, which is followed by recommendations for further research.

7.1 Thesis summary

The thesis summary is based on the following objectives as specified in Section 1.5 of the Introduction.

Development of sub-exercise benchmark specifications

Specifications for sub-exercises were developed for the UAM SFR benchmark following the guidelines of Phase I of the OECD/NEA UAM LWR benchmark. These sub-exercises cover sensitivity and uncertainty analysis with respect to nuclear data for the pin cell, fuel assembly, and super-cell levels, and they expand the full core exercise of the UAM SFR specification by requesting additional results on the full core neutronics level.

During the development of this thesis, these sub-exercise specifications were included in the full UAM-SFR benchmark specifications.

Generation of multigroup libraries for SFR analysis with SCALE

As a basis for analyses with modules of the SCALE code system, new multigroup cross section libraries were generated with AMPX. The performance of the new libraries was investigated in terms of the eigenvalue, the neutron flux and reaction rates in criticality calculations, as well as for the generation of group constants. A library using 302 energy groups and a fast neutron flux spectrum as the weighting function led to very good agreement with reference CE results. The new library's performance was further demonstrated in calculations of experiments from the International Criticality Safety Benchmark Evaluation Project handbook. The 302-group library will be available to SCALE users with the next rcode elease.

A corresponding 302-group covariance library was generated for uncertainty analyses. Since covariance data in the high energy range is often only given in a coarse energy structure, additional covariance libraries with a reduced number of energy groups were generated. A library with only 17 groups was found to provide a sufficient resolution of the uncertainties relevant for the investigated SFR systems while significantly reducing the computational burden for random sampling–based sensitivity analyses.

Implementation of the XSUSA method in SCALE 6.2

The XSUSA method for random sampling–based uncertainty analyses with respect to nuclear data was implemented in SCALE 6.2 as a child sequence of SCALE's Sampler sequence. This time-efficient approach allows the perturbation of cross sections after the self-shielding calculation: the self-shielding calculation must be performed only once for the nominal case. To consider implicit effects that are neglected with this approach, an approximation was implemented that only requires one additional TSUNAMI-1D calculation per self-shielding cell as part of the pre-processing. Although it was found that implicit effects play a negligible role for the output quantities investigated for SFRs in this work, there might be an impact for other output quantities or other reactor systems.

Extension of the sensitivity analysis

The XSUSA sensitivity analysis allowed for the computation of the squared multiple correlation coefficient R^2 to identify the major contributors to the output uncertainty. This analysis was extended by a second sensitivity index, the semi-partial squared multiple correlation coefficient SPC^2, which offers a different interpretation than R^2. Additionally, the calculation of corresponding variance-based indices similar to Sobol' indices was enabled to allow for sensitivity analysis with consideration of nonlinear effects. To allow comparisons with results from perturbation theory, the calculation of R^2 and SPC^2 was implemented based on sensitivity coefficients from the TSUNAMI code.

R^2 allows for the reliable identification of the top contributors to the investigated output uncertainties. Due to the consideration of the influence of correlated nuclide reactions, R^2 sometimes shows unexpected contributors. The analysis of SPC^2 can be used to identify important correlations since highly correlated nuclide reactions do not appear in the SPC^2 ranking.

The calculation of SPC^2 with the random sampling approach requires a very large sample size, even for simple models. Furthermore, all presented approaches for the SPC^2 calculation involve large matrices that required modifications to allow their inversion; these modifications can introduce unknown biases.

In conclusion, R^2 is the most practical and reliable sensitivity index that allows the identification of the major contributors to the output uncertainty. To identify which of the correlated nuclide reactions is causing the major contribution to the output uncertainty, one at a time perturbations can be performed. Despite large uncertainties of important nuclide reactions in the high-energy range, a linear system behavior was observed for the studied output quantities. The calculation of linearized versions of R^2 is consequently justified and time-consuming calculations with Sobol' indices become unnecessary.

The analysis of R^2 and SPC^2 based on Sampler calculations will be available to SCALE users with the next code release.

Systematic uncertainty and sensitivity analysis of SFR systems

Systematic uncertainty and sensitivity analyses with respect to nuclear data were performed based on the developed specifications. By systematically analyzing every level of modeling, it was found that the main conclusions from full core neutronics analysis can be drawn from simple models. That is, the analysis of simple models is sufficient for first assessments of the impact of nuclear data uncertainties, and it is also sufficient for identifying the major drivers of the uncertainties.

In general, it was found that the uncertainties for eigenvalues and reactivity coefficients were significantly larger than uncertainties for corresponding LWR models. In particular due to the different flux spectra, large uncertainties—sometimes as high as 50%—of various nuclide reactions in the high-energy range play a greater role for SFR analysis. For most output quantities, the main contributor to the uncertainties was identified as inelastic scattering of ^{238}U. Other relevant contributors are the scattering reactions of the coolant ^{23}Na, scattering reactions of ^{56}Fe as part of the structural material, followed by neutron capture reactions of the fuel, coolant, and structure. In contrast, the neutron multiplicity or fission reactions of the fuel that are usually found to be important contributors in LWR calculations do not appear for these systems.

By comparing results based on various methods and models, the analyses that were performed in this work contribute to the development and assessment of calculation methods and models for uncertainty analysis, accompanying best-estimate reactor simulations of SFRs.

7.2   Recommendations for further research

The research presented in this thesis was focused on the analysis of the impact of nuclear data uncertainties on SFR neutronics calculations. In particular, the covered input uncertainties and the extent of the analyses present opportunities for further research, as proposed in the following sections.

Impact of nuclear data uncertainties on coupled neutronics/thermal hydraulics calculations

Safety assessments for licensing of SFRs will involve the analysis of transients such as unprotected loss of flow (ULOF), unprotected loss of heat sink (ULOHS), and un-

protected transient over power (UTOP). Following the *Best Estimate Plus Uncertainty* approach, it is necessary to propagate nuclear data uncertainties in these transient calculations to safety-relevant output quantities. For the consideration of feedback effects (e.g., density, expansion, and Doppler feedback), coupled neutronics/thermal hydraulics calculations must be performed.

In the analysis of LWRs, it has been demonstrated that nuclear data uncertainties can introduce significant uncertainty in transient calculations. For example, A. Aures found 6-9% uncertainty of the reactivity as well as a nonlinear effect on the reactor power uncertainty during a transient calculation of a small LWR core (Aures et al., 2020), indicating a relevant impact on safety-relevant parameters such as the maximum fuel temperature. With respect to SFRs, several analyses have been performed by Argonne National Laboratory (ANL) in their studies of an advanced burner reactor concept. Although N. Stauff and G. Zhang found that nuclear data uncertainties had a significant impact on integral parameters such as reactivity coefficients, they only observed small effects on the reactor's transient behavior (Stauff et al., 2016; Zhang et al., 2017).

Even though ANL's initial analyses suggest that there is only a small influence on transient calculations, it is necessary to thoroughly study the impact of nuclear data uncertainties in coupled neutronics/thermal hydraulics calculations to demonstrate the impact on safety analysis for all relevant SFR concepts. In this way, recommendations for the consideration nuclear data uncertainties in licensing calculations can be made, and safety margins of safety-related quantities can be appropriately defined.

Nuclear data uncertainties

The calculations in this thesis consider nuclear data uncertainties as provided in the ENDF/B-VII.1 nuclear data library release (Chadwick et al., 2011). During the development of this thesis, ENDF/B-VIII.0 (Brown et al., 2018) was released. In addition to changes of the nominal cross sections, the cross section uncertainties were updated for many important nuclides. For example, the change of the ^{238}U inelastic scattering uncertainty is significant: instead of a maximum uncertainty of about 50% in the high energy range, a maximum uncertainty of about 11% is provided. Since this reaction was identified as the most significant contributor to the output uncertainty for most of the investigated output quantities addressed in this thesis, a change in this uncertainty is expected to have a significant impact on the output uncertainties themselves and

on the ranking of top contributing nuclide reactions. It is expected that the ranking is no longer strongly dominated by this single reaction, so it will be possible to identify additional nuclide reactions and to make additional recommendations for further evaluations or measurements.

When analyzing the impact of nuclear data uncertainties in reactor physics calculations, it must be considered that not necessarily all uncertainty information provided by ENDF/B is captured in the applied covariance library. For example, the AMPX covariance library format cannot consider the dependence of the fission spectrum from the incident energy; uncertainties are currently included for mean incident energies (Wiarda et al., 2016). Since the fission spectrum of ^{239}Pu was identified as one significant contributor to the uncertainty, it is possible that even slight changes have a noticeable impact on the results. Another example is uncertainty information on angular distributions that is provided in the ENDF/B releases but cannot be included in the AMPX covariance libraries due to format limitations. Since scattering reactions of several nuclides were identified as top contributors to the observed output uncertainties, it would be interesting to study the impact of these uncertainties. For example, I. Hill reports significant uncertainties caused by angular dependent elastic scattering data (P1 moments) in integral fast spectrum benchmarks (Hill and Jeong, 2017). The extension of the covariance library format should consequently be pursued to consider all available uncertainty information. However, it should also be noted that the computer codes that use the covariance library must be able to use the provided data. For example, SCALE is not able to use the data for both of the provided examples. Modifications of the applied analysis tools are necessary for analysis of all uncertainty information provided.

Even if all the uncertainty data included in an ENDF/B release could be processed, there are uncertainties of nuclear data that are not yet provided. Although it is not significant for SFR analysis, uncertainties of thermal scattering data are not yet included. More importantly for SFRs, angular scattering uncertainty information is only available for a small number of nuclides. Further measurements and evaluations must be performed to provide all the data needed to analyze all sources of uncertainty (Smith, 2015; Kodeli, 2018; Bernstein et al., 2019).

Nuclear data uncertainty intervals are often larger than the experimental error bars for various sets of benchmark experiments (Williams et al., 2015). However, if measurements of the reactor system of interest (or similar systems) are available, then

it is possible to use data adjustment tools such as TSURFER from SCALE to create a library of cross section and uncertainty data adjusted for this system. Uncertainty analyses conducted using this library would result in nominal values close to the measurement and error bars covering the measured uncertainty. Despite the limited operating experience of SFRs and the limited amount of experimental data that are publicly available, a database for SFR systems would help ensure the data adjustment needed to obtain improved predictions of the reactor behavior and more realistic estimates of output uncertainties.

Consideration of additional input uncertainties

The input uncertainties considered in this thesis are not the only nuclear data related uncertainties that can be studied in reactor physics analysis. In case of depletion calculations, uncertainty analyses should include uncertainties of the fission yields and decay data. Significant uncertainties of the eigenvalue, the Doppler reactivity and nuclide densities due to these uncertainties were found for LWR models before (Aures et al., 2017). For example, it would be interesting to investigate if differences found between depletion calculations of an SFR fuel assembly with different nuclear data libraries (Rimpault et al., 2017) can be explained by the corresponding uncertainties.

Nuclear data uncertainties are not the only source of input uncertainties in reactor physics and coupled neutronics/thermal hydraulics analyses. For example, other uncertainties can arise from geometric dimensions, material compositions, operational conditions, and thermal hydraulic parameters. G. Zhang and N. Stauff investigated several sources of uncertainties for neutronics and system analyses of an SFR. They showed that uncertainties of thermal-physical properties of the fuel, cladding, and coolant can have a significant impact on the transient behavior of an SFR (Stauff et al., 2018; Zhang et al., 2018).

All uncertainties in the simulation of SFR systems must be identified to determine reasonable uncertainty ranges and to investigate their impact and importance for safety analyses. A thorough understanding of the uncertainties will improve the understanding of these reactor systems and will inform prioritization to reduce important input uncertainties.

Expansion to other fast reactor systems

The focus of this work was the analysis of SFR systems. However, the industry and several research institutes are also interested in other reactor concepts with fast neutron spectra. For example, Westinghouse is developing a lead-cooled fast reactor system (Westinghouse Electric Company LLC, 2016). In Europe, the lead-bismuth cooled Multi-purpose hYbrid Research Reactor for High-tech Applications (MYRRHA) (Sarotto, 2014) and the Advanced Lead Fast Reactor European Demonstrator (ALFRED) (Alemberti, 2018) are being investigated. Other reactors currently under consideration are gas-cooled fast reactors and molten salt reactor systems with fast neutron spectra (Rearden, 2018).

Although the fast reactors mentioned here share certain similarities with SFR systems, every fast reactor design must be thoroughly investigated in terms of the impact of input uncertainties to neutronics and system analysis calculations. With respect to nuclear data uncertainty analysis, different geometries and materials cause changes in the neutron spectrum, requiring the capabilities of the applied analysis tools for these systems to be thoroughly assessed, and also requiring the same type of systematic analyses that were performed herein for SFRs. For the Westinghouse design, initial nuclear data uncertainty analyses are being performed by North Carolina State University (NCSU) (Trivedi et al., 2019).

A Appendix

A.1 Material and geometry specifications of the SFR sub-exercise models

Table A.1 – Dimensions for fuel pin and fuel assembly of Ex. I-1 and I-2.

	MET1000	MOX3600
Inner fuel radius	-	0.1257 cm
Outer fuel radius	0.3236 cm	0.4742 cm
Inner cladding radius	0.3236 cm	0.4893 cm
Outer cladding radius	0.3857 cm	0.5419 cm
Pin cell pitch	0.8966 cm	1.1897 cm
Number of fuel pins	271	271
Inner subassembly duct flat-to-flat distance	15.0191 cm	19.8418 cm
Outer subassembly duct flat-to-flat distance	15.8123 cm	20.7468 cm
Subassembly pitch	16.2471 cm	21.2205 cm

Table A.2 – Operating conditions.

	MET1000	MOX3600
Coolant temperature	706 K	743 K
Structure temperature (cladding, duct, absorber)	706 K	743 K
Fuel temperature	807 K	1500 K

Table A.3 – Dimensions for primary control rod assembly and supercell of Ex. I-3.

	MET1000	MOX3600
Absorber radius	1.0977 cm	0.9202 cm
Inner cladding radius	1.0977 cm	1.0474 cm
Outer cladding radius	1.1693 cm	1.14765 cm
Pin cell pitch	2.458 cm	2.4438 cm
Number of absorber pins	19	37
Inner interior duct flat-to-flat distance	11.7193 cm	15.2860 cm
Outer interior duct flat-to-flat distance	12.5125 cm	15.6883 cm
Inner subassembly duct flat-to-flat distance	15.0191 cm	19.8418 cm
Outer subassembly duct flat-to-flat distance	15.8123 cm	20.7468 cm
Subassembly pitch	16.2471 cm	21.2205 cm
Super-cell pitch	48.7413 cm	84.882 cm

Table A.4 – Number densities—Structure.

		MET1000	MOX3600	
	Nuclide	Fuel and Absorber Pin Cladding and Duct (HT9)	Fuel Pin Cladding (ODS)	Duct and Absorber Pin Cladding (EM10)
Structure	C	-	3.5740E-04	3.8254E-04
	O	-	3.9924E-04	-
	Si	-	-	4.9089E-04
	Ti	-	5.3824E-04	1.9203E-05
	Cr	1.0366E-02	1.7753E-02	7.5122E-03
	Fe	6.9715E-02	5.3872E-02	7.3230E-02
	Ni	4.2984E-04	3.6588E-04	3.9162E-04
	Mo	4.9007E-04	-	4.7925E-04
	Mn	4.5921E-04	2.3441E-04	4.1817E-04
	P	-	2.7718E-05	-
	Al	-	9.1482E-03	-
	Co	-	2.1852E-04	-
	Cu	-	1.0135E-04	-
	Y	-	2.6616E-04	-

Table A.5 – Number densities—Fuel, coolant and absorber.

	Nuclide	MET1000	MOX3600
	O-16	-	4.2825E-02
	U-234	1.7210E-06	2.1672E-06
	U-235	2.2106E-05	2.1336E-05
	U-236	3.8904E-06	6.3334E-06
	U-238	1.8774E-02	1.7571E-02
	Np-237	4.2264E-05	7.5991E-06
	Np-239	-	5.3141E-06
	Pu-236	7.3569E-10	-
	Pu-238	1.0560E-04	7.4795E-05
	Pu-239	2.1525E-03	1.9750E-03
	Pu-240	1.2570E-03	1.0276E-03
	Pu-241	1.8043E-04	1.8497E-04
Fuel	Pu-242	2.7677E-04	3.0146E-04
	Am-241	8.8828E-05	3.6901E-05
	Am-242g	-	1.7558E-08
	Am-242m	8.9023E-06	1.9169E-06
	Am-243	9.1054E-05	4.0860E-05
	Cm-242	7.4075E-06	3.2303E-06
	Cm-243	7.7307E-07	2.4680E-07
	Cm-244	7.1010E-05	1.1034E-05
	Cm-245	1.5116E-05	9.4349E-07
	Cm-246	9.1659E-06	4.7941E-08
	Cm-247	-	1.6226E-09
	Zr	7.2802E-03	-
	Mo	2.7287E-03	4.5802E-03
Coolant	Na-23	2.2272E-02	2.1924E-02
Absorber (natural B4C)	C	1.9657E-02	2.70E-02
	B-10	1.5018E-02	2.32E-02
	B-11	6.3609E-02	8.49E-02

A.2 Energy group structures of the SCALE/AMPX SFR libraries

Table A.6 – Upper energy boundaries of the 302-group structure.

Group	Upper energy (eV)	Group	Upper energy (eV)	Group	Upper energy (eV)
1	2.00000E+07	102	5.50000E+05	203	4.40506E+04
2	1.38400E+07	103	5.36647E+05	204	4.29630E+04
3	1.34986E+07	104	5.23397E+05	205	4.19022E+04
4	1.31653E+07	105	5.10474E+05	206	4.08677E+04
5	1.28400E+07	106	4.97871E+05	207	3.98586E+04
6	1.25232E+07	107	4.85578E+05	208	3.88745E+04
7	1.22140E+07	108	4.73589E+05	209	3.79147E+04
8	1.19125E+07	109	4.61896E+05	210	3.69786E+04
9	1.16183E+07	110	4.50492E+05	211	3.60656E+04
10	1.13315E+07	111	4.39369E+05	212	3.51751E+04
11	1.10517E+07	112	4.28521E+05	213	3.43067E+04
12	1.07788E+07	113	4.17941E+05	214	3.34596E+04
13	1.05127E+07	114	4.07622E+05	215	3.26335E+04
14	1.02532E+07	115	3.97558E+05	216	3.18278E+04
15	1.00000E+07	116	3.87742E+05	217	3.10419E+04
16	9.75310E+06	117	3.78169E+05	218	3.02755E+04
17	9.51230E+06	118	3.68832E+05	219	2.95280E+04
18	9.27744E+06	119	3.59725E+05	220	2.87990E+04
19	9.04838E+06	120	3.50844E+05	221	2.80879E+04
20	8.82497E+06	121	3.42181E+05	222	2.73944E+04
21	8.60708E+06	122	3.33733E+05	223	2.67181E+04
22	8.39457E+06	123	3.25493E+05	224	2.60584E+04
23	8.18700E+06	124	3.17456E+05	225	2.54150E+04
24	7.98516E+06	125	3.09618E+05	226	2.47875E+04
25	7.78801E+06	126	3.01974E+05	227	2.41755E+04
26	7.59572E+06	127	2.94518E+05	228	2.35786E+04
27	7.40818E+06	128	2.87246E+05	229	2.29964E+04
28	7.22527E+06	129	2.80154E+05	230	2.24287E+04
Continued					

Table A.6 – Upper energy boundaries of the 302-group structure (cont.).

Group	Upper energy (eV)	Group	Upper energy (eV)	Group	Upper energy (eV)
29	7.04688E+06	130	2.73237E+05	231	2.18749E+04
30	6.87289E+06	131	2.66491E+05	232	2.13348E+04
31	6.70320E+06	132	2.59911E+05	233	2.08080E+04
32	6.64757E+06	133	2.53494E+05	234	2.02943E+04
33	6.59241E+06	134	2.47235E+05	235	1.93443E+04
34	6.53770E+06	135	2.41131E+05	236	1.70000E+04
35	6.37628E+06	136	2.35177E+05	237	1.50654E+04
36	6.21885E+06	137	2.29371E+05	238	1.32951E+04
37	6.06531E+06	138	2.23708E+05	239	1.17329E+04
38	5.91555E+06	139	2.18184E+05	240	1.03543E+04
39	5.76950E+06	140	2.12797E+05	241	9.13761E+03
40	5.48812E+06	141	2.07543E+05	242	8.03000E+03
41	5.22046E+06	142	2.02419E+05	243	7.11638E+03
42	4.96585E+06	143	1.97421E+05	244	6.28018E+03
43	4.84325E+06	144	1.92547E+05	245	5.54224E+03
44	4.72367E+06	145	1.87793E+05	246	5.01483E+03
45	4.60704E+06	146	1.83156E+05	247	4.53760E+03
46	4.49329E+06	147	1.78634E+05	248	4.31630E+03
47	4.27415E+06	148	1.74224E+05	249	4.07172E+03
48	4.06570E+06	149	1.69922E+05	250	3.71508E+03
49	3.86741E+06	150	1.65727E+05	251	3.36154E+03
50	3.67880E+06	151	1.61635E+05	252	3.01640E+03
51	3.49938E+06	152	1.57644E+05	253	2.86929E+03
52	3.32871E+06	153	1.53752E+05	254	2.75220E+03
53	3.24653E+06	154	1.49956E+05	255	2.61797E+03
54	3.16637E+06	155	1.46253E+05	256	2.46962E+03
55	3.08819E+06	156	1.42642E+05	257	2.25000E+03
56	3.01194E+06	157	1.39120E+05	258	2.03888E+03
57	2.86505E+06	158	1.35686E+05	259	1.82780E+03
58	2.72532E+06	159	1.32335E+05	260	1.66220E+03
59	2.59240E+06	160	1.29068E+05	261	1.58460E+03
60	2.46597E+06	161	1.25881E+05	262	1.50000E+03
Continued					

Table A.6 – Upper energy boundaries of the 302-group structure (cont.).

Group	Upper energy (eV)	Group	Upper energy (eV)	Group	Upper energy (eV)
61	2.42521E+06	162	1.22773E+05	263	1.36060E+03
62	2.38513E+06	163	1.19742E+05	264	1.23410E+03
63	2.36533E+06	164	1.16786E+05	265	1.17050E+03
64	2.34570E+06	165	1.13902E+05	266	1.11200E+03
65	2.30693E+06	166	1.11090E+05	267	1.06320E+03
66	2.26880E+06	167	1.08347E+05	268	1.01650E+03
67	2.23130E+06	168	1.05672E+05	269	9.61120E+02
68	2.12248E+06	169	1.03063E+05	270	7.48520E+02
69	2.01897E+06	170	1.00518E+05	271	5.82950E+02
70	1.96912E+06	171	9.80365E+04	272	4.54000E+02
71	1.92050E+06	172	9.56160E+04	273	3.53570E+02
72	1.87308E+06	173	9.32552E+04	274	2.75360E+02
73	1.82684E+06	174	9.09527E+04	275	2.14450E+02
74	1.73774E+06	175	8.87071E+04	276	1.67020E+02
75	1.65299E+06	176	8.65169E+04	277	1.30070E+02
76	1.61218E+06	177	8.43808E+04	278	1.00000E+02
77	1.57237E+06	178	8.22974E+04	279	7.88930E+01
78	1.53355E+06	179	8.02655E+04	280	6.14420E+01
79	1.49569E+06	180	7.82837E+04	281	4.78510E+01
80	1.42274E+06	181	7.63509E+04	282	3.72700E+01
81	1.35335E+06	182	7.44658E+04	283	2.90230E+01
82	1.28735E+06	183	7.26272E+04	284	2.25000E+01
83	1.22456E+06	184	7.08340E+04	285	1.76040E+01
84	1.19433E+06	185	6.90851E+04	286	1.37500E+01
85	1.16484E+06	186	6.73794E+04	287	1.06770E+01
86	1.10803E+06	187	6.57158E+04	288	8.31530E+00
87	1.05399E+06	188	6.40933E+04	289	6.50000E+00
88	1.00259E+06	189	6.25108E+04	290	5.04350E+00
89	9.77835E+05	190	6.09674E+04	291	3.92790E+00
90	9.61672E+05	191	5.94621E+04	292	3.05000E+00
91	9.53692E+05	192	5.79940E+04	293	2.38000E+00
92	9.07180E+05	193	5.65621E+04	294	1.86000E+00
Continued					

Table A.6 – Upper energy boundaries of the 302-group structure (cont.).

Group	Upper energy (eV)	Group	Upper energy (eV)	Group	Upper energy (eV)
93	8.62936E+05	194	5.51656E+04	295	1.45000E+00
94	8.20850E+05	195	5.38035E+04	296	1.13000E+00
95	7.80817E+05	196	5.24751E+04	297	8.76430E-01
96	7.42736E+05	197	5.11795E+04	298	8.50000E-01
97	7.06512E+05	198	4.99159E+04	299	6.82560E-01
98	6.72055E+05	199	4.86834E+04	300	6.25000E-01
99	6.39279E+05	200	4.74815E+04	301	5.31580E-01
100	6.08101E+05	201	4.63091E+04	302	4.13990E-01
101	5.78443E+05	202	4.51658E+04		1.00000E-05[*]

[*] Lower energy boundary.

Table A.7 – Upper energy boundaries of selected group structures.

Group	Upper energy (eV)			
	8g	11g	17g	24g
1	2.00000E+07	2.00000E+07	2.00000E+07	2.0000E+07
2	2.23130E+06	3.67880E+06	1.00000E+07	1.00000E+07
3	8.20850E+05	2.23130E+06	3.67880E+06	6.06531E+06
4	3.01974E+05	1.35335E+06	2.01897E+06	3.67880E+06
5	1.11090E+05	1.00259E+06	1.35335E+06	2.23130E+06
6	3.98586E+04	8.20850E+05	1.00259E+06	1.35335E+06
7	1.50654E+04	3.01974E+05	8.20850E+05	8.20850E+05
8	7.48520E+02	1.11090E+05	4.97871E+05	4.97871E+05
9	1.00000E-05*	3.98586E+04	3.01974E+05	3.01974E+05
10		1.50654E+04	1.11090E+05	1.83156E+05
11		7.48520E+02	7.63509E+04	1.11090E+05
12		1.00000E-05*	3.98586E+04	6.73794E+04
13			2.47875E+04	4.08677E+04
14			2.02940E+04	2.47875E+04
15			1.50654E+04	1.50654E+04
16			2.46962E+03	9.13761E+03
17			7.48520E+02	5.54224E+03
18			1.00000E-05*	3.36154E+03
19				2.03888E+03
20				1.23410E+03
21				7.48520E+02
22				4.54000E+02
23				2.75360E+02
24				1.67020E+02
25				1.00000E-05*

* Lower energy boundary.

A.3 Random sampling of cross sections

This section describes the standard approach for correlated sampling of cross sections based on a normal distribution as it is implemented in XSUSA. The general procedure is followed by a few notes on the practical application when using covariance matrices for nuclear data as contained in the evaluated data files. Although this section refers to cross sections, this procedure can be applied on any type nuclear data (e.g. decay data and fission yields) as long as corresponding covariance matrices are provided.

A.3.1 General procedure

The desired output of the random sampling procedure are perturbation factors p_i, which can be used to modify the nominal value of a cross section in energy group i:

$$x_i = p_i \cdot \mu_i, \tag{A.1}$$

with μ_i being the nominal value of the cross section that is considered the mean value of the normal distribution, and x_i being the modified cross section value after the perturbation. In the following, the cross sections in their individual energy groups are called parameters.

We assume that we have a number of k correlated parameters for which their covariances are described in covariance matrix C of size $k \times k$. We are interested in obtaining samples for these parameters for a sample size of N. The following steps must be performed (Thomopoulos, 2013):

1. Modification of the covariance matrix if necessary (see notes in Section A.3.3):

   (a) Remove columns/rows of the covariance matrix corresponding to zero variances. The reduced covariance matrix has now size $k' \times k'$.

   (b) Make the covariance matrix C *positive definite*.

2. Convert the positive definite covariance matrix to a correlation matrix R, size $(k' \times k')$.

3. Perform Cholesky decomposition: $R = D \cdot D'$, with D being the lower triangular matrix, size $(k' \times k')$.

4. For a sample size N, determine $k' \times N$ independently sampled values from a standard normal distribution, i.e. a normal distribution with mean value $\mu = 0$ and standard deviation $\sigma = 1$.

5. Multiply the $(k' \times N)$ matrix of *independent* samples with the lower Cholesky matrix D to obtain a $(k' \times N)$ matrix of *dependent* standard samples y_i.

6. Transform standard samples y_i into non-standard normal random values x_i for each parameter $i \in [1, k']$:

$$x_i = \mu_i + \sigma_i \, y_i, \tag{A.2}$$

$$= \mu_i + \sigma_{i,rel} \, \mu_i \, y_i, \tag{A.3}$$

$$= \mu_i \cdot (1 + \sigma_{i,rel} \, y_i), \tag{A.4}$$

with μ_i being the mean value of parameter i, and $\sigma_{i,rel}$ being the relative standard deviation of the individual parameter from the original covariance matrix. With Eq. A.1, this expression of x_i results in an expression for the desired perturbation factor:

$$p_i = 1 + \sigma_{i,rel} \, y_i. \tag{A.5}$$

7. Expand the matrix of perturbation factors $(k' \times N)$ to the size of original covariance matrix $(k \times N)$ by adding $p_i = 1$ for parameters with zero variance.

A.3.2   Random sampling based on conditional distributions

For the calculation of variance-based sensitivity indices as described in Section 5.1, cross section perturbations of only a group of cross sections need to be generated based on the known perturbations of another group of cross sections.

Let group A include the cross sections for which new perturbations shall be generated based on known cross section perturbations of group B. The vector of mean values of the cross sections $\boldsymbol{\mu}$ and the total covariance matrix $\mathbf{C}$ can then be divided as follows:

$$\boldsymbol{\mu} = \begin{pmatrix} \boldsymbol{\mu}_A \\ \boldsymbol{\mu}_B \end{pmatrix}, \quad \mathbf{C} = \begin{pmatrix} \mathbf{C}_{AA} & \mathbf{C}_{AB} \\ \mathbf{C}_{BA} & \mathbf{C}_{BB} \end{pmatrix}. \tag{A.6}$$

The conditional distribution of the cross sections of group A, $\mathbf{x}_A$, is a multivariate normal distribution with mean values and covariance matrices given known values for group B, $\mathbf{x}_B$:

$$\boldsymbol{\mu}_{A|B} = \boldsymbol{\mu}_A + \mathbf{C}_{AB}\,\mathbf{C}_{BB}^{-1}\left(\mathbf{x}_B - \boldsymbol{\mu}_B\right), \quad \mathbf{C}_{A|B} = \mathbf{C}_{AA} - \mathbf{C}_{AB}\,\mathbf{C}_{BB}^{-1}\,\mathbf{C}_{BA}. \tag{A.7}$$

The conversion of the conditional covariance matrix $\mathbf{C}_{A|B}$ in the corresponding correlation matrix and the subsequent Cholesky decomposition is performed as described in Section A.3.1. For each sample, the corresponding values for $\mathbf{x}_B$ are then used to determine the corresponding new mean values $\boldsymbol{\mu}_{A|B}$ for this sample. Afterwards, the random sampling procedure can be followed as described in Section A.3.1 to obtain cross section perturbations for group A. This procedure is followed for each sample until the desired sample size is reached.

A.3.3 Notes on the application with nuclear data

The covariance matrices provided in the evaluated nuclear data files are often not positive semi-definite, i.e. some of the provided matrices have negative eigenvalues. A Cholesky decomposition cannot be performed on those matrices. It is necessary to slightly modify the matrices in order to make them positive semi-definite. The diagonal elements describe the variances and can therefore not be changed. Instead, the off-diagonal elements of the matrix can be slightly modified to increase the matrix eigenvalues.

The evaluated nuclear data files provide covariance matrices for a large number of nuclide reactions. Additionally, covariance matrices describing the correlations between different nuclide reactions are also available: correlations between different reactions of a particular nuclide as well as correlations between reactions of two different nuclides that are e.g. induced by measurements of cross sections based on cross sections of other nuclides. Correlated nuclide reactions need processed together in the sampling procedure. The total covariance matrix for the sampling is in this case

Appendix A. Appendix

comprised of the covariance matrices of the individual reactions and the covariance matrices between the different reactions.
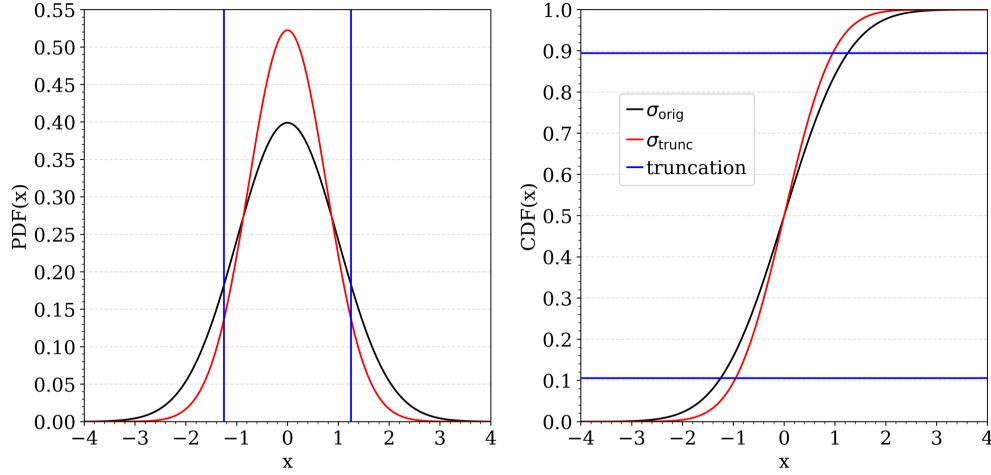
Figure A.1 – Truncation of a standard normal distribution with standard deviation $\sigma_{\mathrm{orig}} = 1$ and resulting truncated distribution with standard deviation $\sigma_{\mathrm{trunc}} < \sigma_{\mathrm{orig}}$.

During the sampling procedure, we need to assure that the resulting perturbed cross section is positive. Therefore the following requirement has to be met:

$$x_i \geq 0 \tag{A.8}$$

$$\Leftrightarrow \qquad \mu_i + \sigma_{i,rel}\, \mu_i\, y_i \geq 0 \tag{A.9}$$

$$\Leftrightarrow \qquad 1 + \sigma_{i,rel}\, y_i \geq 0 \tag{A.10}$$

$$\Leftrightarrow \qquad y_i \geq -\frac{1}{\sigma_{i,rel}} \tag{A.11}$$

This requirement can, for example, be met by truncating the normal distribution from which the independent samples are drawn. In case of XSUSA, the normal distribution is truncated on both sides to preserve the symmetry. Due to this truncation, the standard deviation from which is sampled is smaller than the original standard deviation $\sigma_{i,\mathrm{rel}}$. While the effect is negligible for small uncertainties, the truncation can have an impact for large uncertainties. Figure A.1 shows the probability density function (PDF) and the corresponding cumulative distribution function (CDF) of a standard normal distribution ($\mu = 0$, $\sigma^2 = 1$). If this distribution is truncated (red lines), the standard deviation of the truncated distribution is reduced to σ_{trunc}. The distribution

based on σ_{trunc} is added to clearly show the impact of the truncation.

Other options for avoiding negative cross sections by using a lognormal distribution as basis for the sampling are currently explored by the Dakota team (Swiler et al., 2018).

A.4   Confidence interval of the standard deviation

Uncertainty calculations following the random sampling approach are performed with a limited sample size. When running a few set of calculations with a fixed sample size, but using different nuclear data perturbations in each set, different values for the sample mean and especially the sample standard deviation of the investigated output quantity are obtained. As an example, Figure A.2 presents the development of the eigenvalue uncertainty of the MET1000 pin cell as a function of the sample size for ten different sets of calculations each with a sample size of 1,000. It can be observed that the final standard deviations for 1,000 samples differ significantly between the sets. In this example, the lowest obtained uncertainty is 1.4626% and the largest one is 1.5427%. Within the bandwidth of results is the uncertainty of a calculation with a sample size of 10,000 (1.5169%).

To estimate the statistical error of the output mean value and standard deviation, confidence intervals can be provided as discussed in Section 4.2. Figure A.3 shows the development of the eigenvalue uncertainty from Figure A.2 for only three sets of calculations accompanied with the corresponding 95% confidence intervals. Naturally, the confidence interval is becoming smaller with increasing sample size. When comparing the values at the final sample size of 1,000, their confidence intervals are overlapping.

Figure A.4 shows the development of the confidence interval of the standard deviation as a function of the sample size in case that the output values are normally distributed. Eq. 4.5 in Section 4.2 shows that in this case, the confidence interval is only dependent on the sample size and desired confidence level. Therefore, Figure A.4 shows the upper and lower 95% confidence intervals as relative fractions of the standard deviation. For a sample size of 1,000, the relative confidence interval of the standard deviation σ is $[(1 - 4.199\%) \cdot \sigma, (1 + 4.587\%) \cdot \sigma]$.

The correct interpretation of the confidence interval shall be explained by an example: For 100 random sampling calculations with a fixed sample size N for each calculation (i.e. in total $100 \times N$ individual simulations), 100 sample standard deviations with corresponding 95% confidence intervals are obtained. Approximately 95 of the 100 95% confidence intervals cover the unknown standard deviation. Figure A.5 shows the eigenvalue uncertainty of 100 MET1000 pin cell calculations, each with a sample size of 100, with their corresponding 95% confidence intervals as error bars. Approximately

95 of these error bars cover the unknown eigenvalue uncertainty.
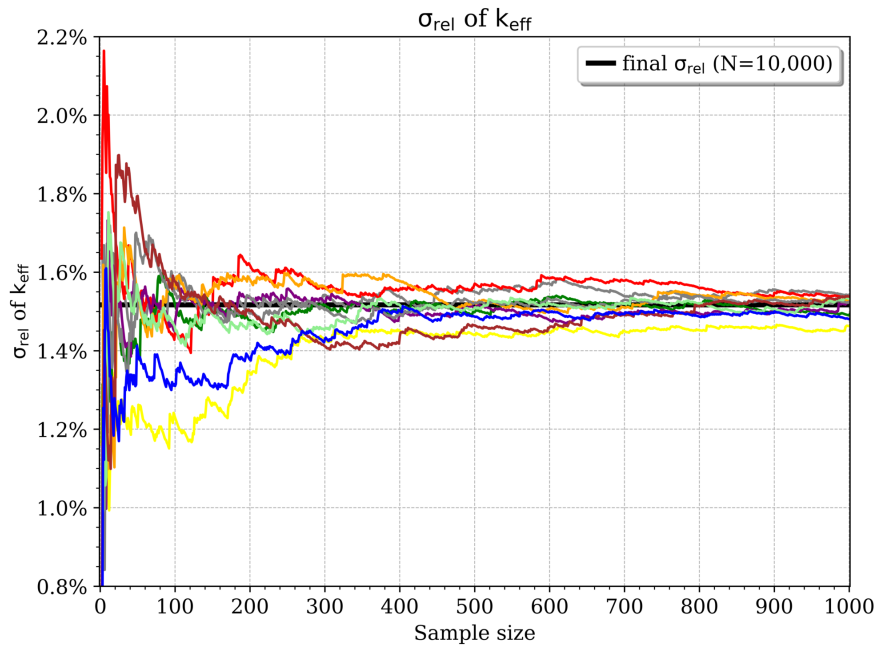
Figure A.2 – Development of the eigenvalue uncertainty over the sample size for ten different random sampling calculations of the MET1000 pin cell.
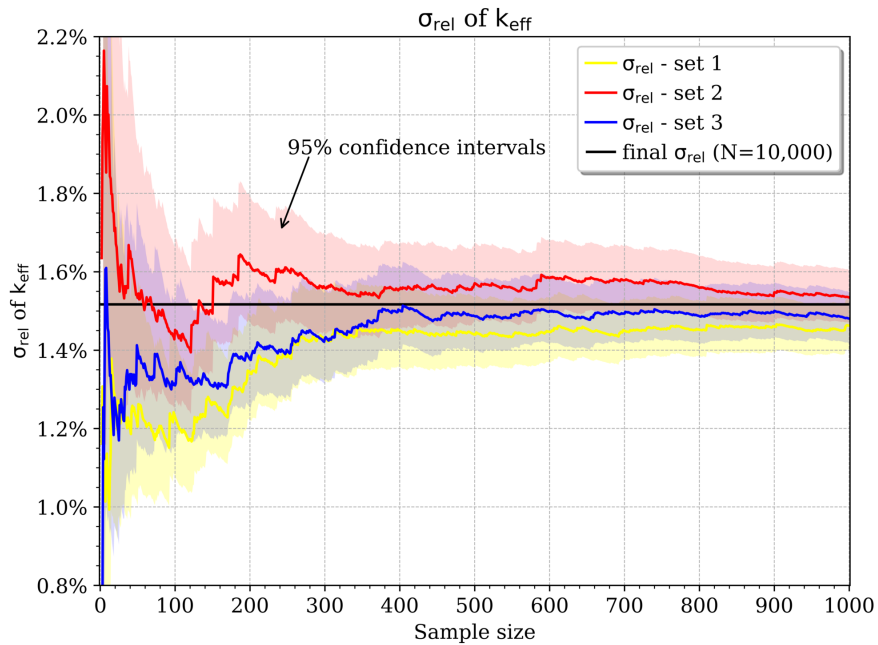
Figure A.3 – Development of eigenvalue uncertainty including their 95% confidence interval over the sample size for three random sampling calculations of the MET1000 pin cell.
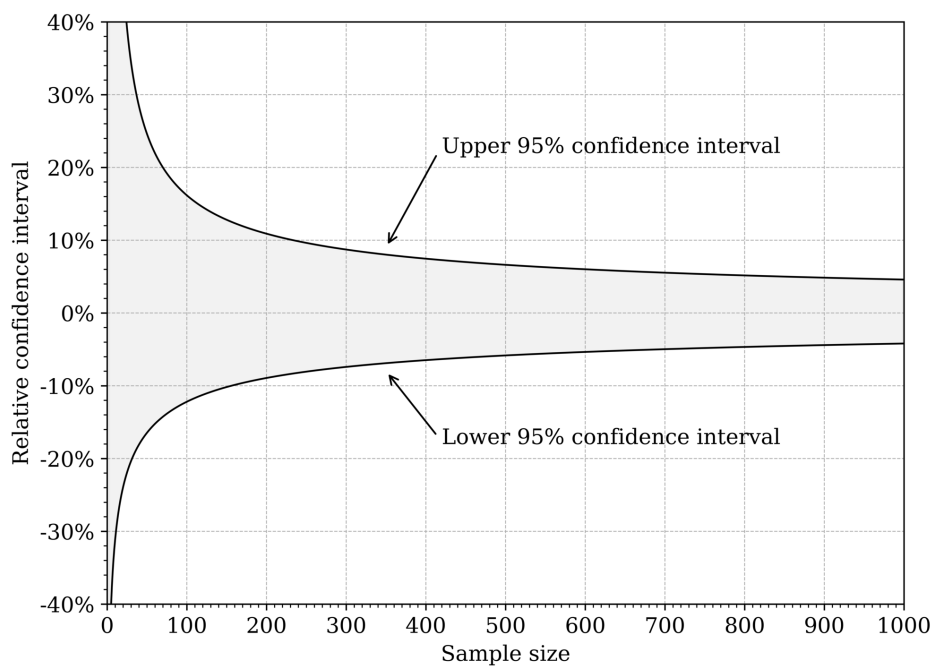
Figure A.4 – Relative confidence interval of the sample standard deviation based on the assumption that the output values are normally distributed.
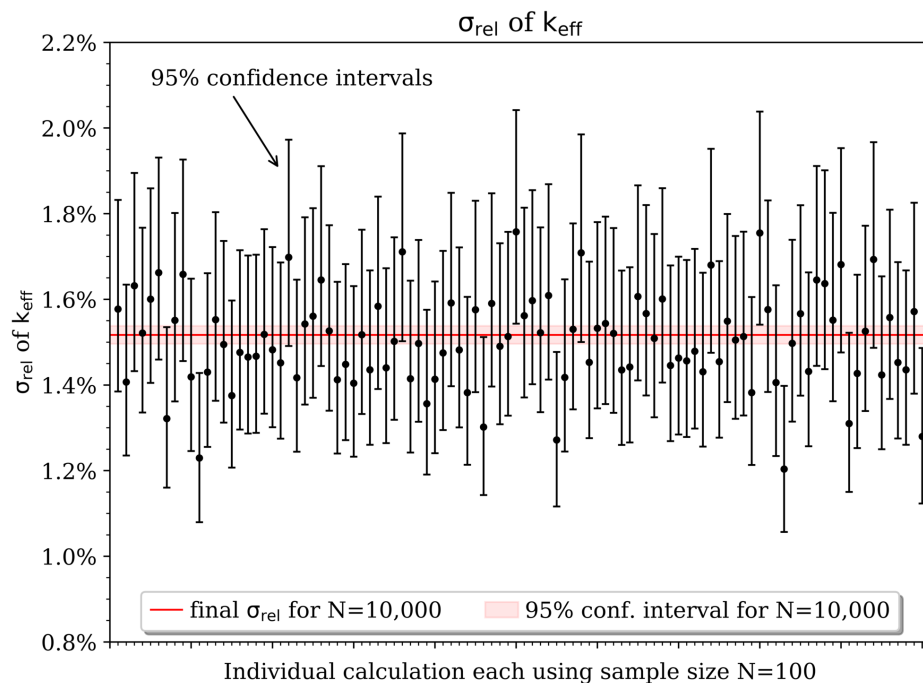
Figure A.5 – Eigenvalue uncertainty for 100 random sampling calculations of the MET1000 pin cell each with a sample size of N=100.

A.5 Uncertainty analysis results

Table A.8 – Ex. I-1: MET1000 pin cell uncertainty analysis results.

Output quantity	TSUNAMI xs302g, cov17g	Sampler xs302g, cov17g	Gemino (expl) xs302g, cov17g	Gemino (tot) xs302g, cov17g	TSUNAMI xs425g, cov19g	Sampler xs425g, cov19g	XSUSA xs425g, cov19g
eigenvalue	1.520%	1.538%	1.543%	1.542%	1.519%	1.555%	1.559%
coolant_mic_el_23Na	5.721%	5.788%	5.789%	5.787%	5.785%	5.842%	5.850%
cladding_mic_el_56Fe	6.348%	6.218%	6.390%	6.390%	6.357%	6.670%	6.826%
fuel_mic_inel_238U	5.588%	5.660%	5.658%	5.656%	5.562%	5.727%	5.725%
fuel_mic_fis_238U	7.691%	7.829%	7.856%	7.859%	7.677%	7.568%	7.594%
fuel_mic_fis_239Pu	0.508%	0.511%	0.511%	0.510%	0.510%	0.509%	0.510%
fuel_mic_fis_240Pu	4.181%	4.264%	4.274%	4.283%	4.159%	4.235%	4.243%
fuel_mic_fis_241Pu	1.034%	1.006%	1.008%	1.007%	1.040%	1.040%	1.043%
fuel_mic_fis_242Pu	5.532%	5.604%	5.616%	5.617%	5.512%	5.575%	5.585%
fuel_mic_n_gam_238U	1.819%	1.816%	1.819%	1.808%	1.816%	1.831%	1.832%
fuel_mic_n_gam_239Pu	6.709%	6.548%	6.552%	6.543%	6.712%	6.682%	6.687%
fuel_mic_n_gam_240Pu	4.270%	3.951%	3.955%	3.942%	4.284%	4.062%	4.065%
fuel_mic_n_gam_241Pu	18.227%	16.401%	16.398%	16.382%	18.197%	16.491%	16.491%
fuel_mic_n_gam_242Pu	4.414%	4.421%	4.427%	4.422%	4.391%	4.416%	4.423%
fuel_mac_fis	1.541%	1.569%	1.573%	1.574%	1.537%	1.528%	1.532%
fuel_mac_abs	0.967%	0.930%	0.931%	0.930%	0.968%	0.933%	0.935%

Table A.9 – Ex. I-1: MOX3600 pin cell uncertainty analysis results.

Output quantity	TSUNAMI xs302g, cov17g	Sampler xs302g, cov17g	Gemino (expl) xs302g, cov17g	Gemino (tot) xs302g, cov17g	TSUNAMI xs425g, cov19g	Sampler xs425g, cov19g	XSUSA xs425g, cov19g
eigenvalue	1.683%	1.705%	1.711%	1.707%	1.682%	1.720%	1.724%
coolant_mic_el_23Na	4.820%	4.916%	4.921%	4.919%	4.893%	4.965%	4.971%
cladding_mic_el_56Fe	5.969%	5.840%	5.932%	5.931%	5.954%	6.214%	6.305%
fuel_mic_inel_238U	6.061%	6.162%	6.157%	6.155%	6.053%	6.245%	6.241%
fuel_mic_fis_238U	7.686%	7.801%	7.838%	7.839%	7.677%	7.575%	7.606%
fuel_mic_fis_239Pu	0.539%	0.552%	0.555%	0.552%	0.540%	0.531%	0.533%
fuel_mic_fis_240Pu	4.267%	4.343%	4.371%	4.370%	4.255%	4.312%	4.323%
fuel_mic_fis_241Pu	1.104%	1.093%	1.096%	1.103%	1.105%	1.092%	1.096%
fuel_mic_fis_242Pu	5.648%	5.689%	5.704%	5.705%	5.648%	5.669%	5.683%
fuel_mic_n_gam_238U	1.752%	1.772%	1.772%	1.740%	1.750%	1.785%	1.785%
fuel_mic_n_gam_239Pu	5.731%	5.711%	5.714%	5.706%	5.723%	5.793%	5.800%
fuel_mic_n_gam_240Pu	3.673%	3.399%	3.402%	3.380%	3.666%	3.462%	3.464%
fuel_mic_n_gam_241Pu	12.762%	11.587%	11.584%	11.561%	12.767%	11.565%	11.565%
fuel_mic_n_gam_242Pu	4.559%	4.399%	4.406%	4.364%	4.551%	4.591%	4.605%
fuel_mac_fis	1.524%	1.556%	1.564%	1.561%	1.520%	1.506%	1.512%
fuel_mac_abs	0.781%	0.763%	0.760%	0.757%	0.780%	0.764%	0.762%

Table A.10 – Ex. I-2: MET1000 fuel assembly uncertainty analysis results.

Output quantity	TSUNAMI xs302g, cov17g	Sampler xs302g, cov17g	Gemino (expl) xs302g, cov17g	TSUNAMI xs425g, cov19g	Sampler xs425g, cov19g	XSUSA xs425g, cov19g
eigenvalue	1.397%	1.416%	1.421%	1.395%	1.427%	1.431%
mac_total_1	1.308%	1.327%	1.343%	1.355%	1.338%	1.345%
mac_total_2	2.030%	2.011%	2.074%	2.009%	2.133%	2.174%
mac_total_3	2.146%	2.197%	2.219%	2.174%	2.172%	2.193%
mac_total_4	1.681%	1.728%	1.695%	1.759%	1.848%	1.818%
mac_abs_1	0.696%	0.647%	0.648%	0.703%	0.665%	0.666%
mac_abs_2	0.937%	0.978%	0.979%	0.957%	0.918%	0.918%
mac_abs_3	0.929%	0.942%	0.949%	0.981%	0.939%	0.943%
mac_abs_4	1.262%	1.337%	1.328%	1.347%	1.324%	1.307%
mac_nu_fis_1	0.941%	0.907%	0.909%	0.944%	0.966%	0.967%
mac_nu_fis_2	0.529%	0.523%	0.524%	0.533%	0.535%	0.536%
mac_nu_fis_3	0.523%	0.544%	0.543%	0.530%	0.523%	0.522%
mac_nu_fis_4	0.940%	0.983%	0.985%	1.021%	0.996%	1.018%
mac_tot_scat_1	1.352%	1.374%	1.390%	1.402%	1.384%	1.391%
mac_tot_scat_2	2.059%	2.039%	2.103%	2.039%	2.164%	2.205%
mac_tot_scat_3	2.183%	2.235%	2.257%	2.212%	2.211%	2.232%
mac_tot_scat_4	1.719%	1.767%	1.735%	1.797%	1.888%	1.859%
doppler	6.341%	6.384%	6.534%	6.507%	7.610%	6.874%
na_void	5.381%	5.460%	5.448%	5.369%	5.205%	5.198%

Table A.11 – Ex. I-2: MOX3600 fuel assembly uncertainty analysis results.

Output quantity	TSUNAMI xs302g, cov17g	Sampler xs302g, cov17g	Gemino (expl) xs302g, cov17g	TSUNAMI xs425g, cov19g	Sampler xs425g, cov19g	XSUSA xs425g, cov19g
eigenvalue	1.499%	1.511%	1.514%	1.502%	1.534%	1.537%
mac_total_1	0.942%	0.989%	0.996%	0.993%	0.996%	1.000%
mac_total_2	1.169%	1.335%	1.362%	1.336%	1.393%	1.410%
mac_total_3	1.461%	1.651%	1.664%	1.644%	1.636%	1.646%
mac_total_4	0.922%	1.197%	1.180%	1.183%	1.208%	1.186%
mac_abs_1	0.764%	0.651%	0.652%	0.797%	0.661%	0.663%
mac_abs_2	0.905%	0.973%	0.973%	0.957%	0.924%	0.925%
mac_abs_3	0.908%	0.937%	0.937%	0.965%	0.936%	0.935%
mac_abs_4	1.123%	1.217%	1.208%	1.175%	1.166%	1.158%
mac_nu_fis_1	0.960%	0.899%	0.901%	0.946%	0.954%	0.955%
mac_nu_fis_2	0.510%	0.501%	0.502%	0.510%	0.516%	0.516%
mac_nu_fis_3	0.515%	0.534%	0.534%	0.522%	0.519%	0.517%
mac_nu_fis_4	0.897%	0.928%	0.941%	0.916%	0.885%	0.905%
mac_tot_scat_1	0.978%	1.023%	1.031%	1.027%	1.030%	1.034%
mac_tot_scat_2	1.184%	1.351%	1.378%	1.353%	1.410%	1.427%
mac_tot_scat_3	1.489%	1.679%	1.692%	1.672%	1.664%	1.675%
mac_tot_scat_4	0.942%	1.226%	1.209%	1.210%	1.236%	1.215%
doppler	4.974%	4.985%	5.134%	4.992%	5.438%	5.172%
na_void	5.176%	5.383%	5.409%	5.454%	5.204%	5.199%

Table A.12 – Ex. I-3: MET1000 supercell uncertainty analysis results.

Output quantity	TSUNAMI (B) xs302g, cov17g	Sampler (B) xs302g, cov17g	Gemino (expl, B) xs302g, cov17g	TSUNAMI (B) xs425g, cov19g	Sampler (B) xs425g, cov19g	XSUSA (B) xs425g, cov19g	XSUSA (A) xs425g, cov19g
eigenvalue	1.486%	1.491%	1.495%	1.479%	1.503%	1.507%	1.503%
mac_total_1	1.623%	1.643%	1.650%	1.644%	1.622%	1.630%	1.630%
mac_total_2	2.009%	2.023%	2.047%	2.037%	2.116%	2.149%	2.154%
mac_total_3	1.920%	1.913%	1.919%	1.952%	1.960%	1.973%	1.978%
mac_total_4	1.453%	1.462%	1.459%	1.595%	1.645%	1.644%	1.642%
mac_abs_1	1.048%	1.043%	1.042%	1.041%	1.037%	1.038%	1.035%
mac_abs_2	0.763%	0.738%	0.737%	0.765%	0.781%	0.781%	0.780%
mac_abs_3	0.260%	0.259%	0.260%	0.276%	0.284%	0.286%	0.284%
mac_abs_4	0.418%	0.413%	0.415%	0.389%	0.386%	0.388%	0.391%
mac_tot_scat_1	1.641%	1.662%	1.669%	1.663%	1.640%	1.647%	1.648%
mac_tot_scat_2	2.063%	2.077%	2.102%	2.091%	2.173%	2.207%	2.212%
mac_tot_scat_3	2.019%	2.012%	2.018%	2.052%	2.061%	2.075%	2.079%
mac_tot_scat_4	1.584%	1.595%	1.592%	1.739%	1.796%	1.794%	1.793%
control_rod_worth	2.790%	2.775%	2.784%	2.711%	2.661%	2.669%	2.651%

193

Table A.13 – Ex. I-3: MOX3600 supercell uncertainty analysis results.

Output quantity	TSUNAMI (B) xs302g, cov17g	Sampler (B) xs302g, cov17g	Gemino (expl, B) xs302g, cov17g	TSUNAMI (B) xs425g, cov19g	Sampler (B) xs425g, cov19g	XSUSA (B) xs425g, cov19g	XSUSA (A) xs425g, cov19g
eigenvalue	1.513%	1.519%	1.523%	1.512%	1.538%	1.541%	1.539%
mac_total_1	1.768%	1.767%	1.772%	1.665%	1.643%	1.648%	1.649%
mac_total_2	2.005%	2.008%	2.026%	1.929%	1.980%	2.004%	2.011%
mac_total_3	1.928%	1.912%	1.917%	1.860%	1.854%	1.864%	1.876%
mac_total_4	1.410%	1.406%	1.403%	1.472%	1.507%	1.505%	1.503%
mac_abs_1	1.001%	0.992%	0.992%	0.986%	0.978%	0.978%	0.976%
mac_abs_2	0.744%	0.726%	0.726%	0.741%	0.761%	0.761%	0.761%
mac_abs_3	0.260%	0.276%	0.276%	0.262%	0.281%	0.281%	0.278%
mac_abs_4	0.325%	0.336%	0.336%	0.315%	0.333%	0.333%	0.333%
mac_tot_scat_1	1.792%	1.791%	1.797%	1.689%	1.666%	1.671%	1.672%
mac_tot_scat_2	2.067%	2.071%	2.090%	1.991%	2.043%	2.068%	2.075%
mac_tot_scat_3	2.045%	2.031%	2.036%	1.976%	1.971%	1.982%	1.994%
mac_tot_scat_4	1.553%	1.553%	1.550%	1.626%	1.671%	1.668%	1.666%
control_rod_worth	2.520%	2.530%	2.535%	2.509%	2.472%	2.478%	2.450%

Bibliography

U.S. NRC Regulatory Guide 1.157 (Task RS 701-4), Best-Estimate Calculations of Emergency Core Cooling System Performance. U.S. NRC, 1989. https://www.nrc.gov/docs/ML0037/ML003739584.pdf.

A Technology Roadmap for Generation IV Nuclear Energy Systems. GIF-002-00, US DOE Office of Nuclear Energy, 2002. https://www.doi.org/10.2172/859029.

RSK-Empfehlung. Anforderungen an die Nachweisführung bei Kühlmittelverluststörfall-Analysen, 2005. http://www.rskonline.de/sites/default/files/reports/epanlagersk385hp.pdf.

IAEA Safety Standards Deterministic Safety Analysis for Nuclear Power Plants for protecting people and the environment No. SSG-2 Specific Safety Guide. IAEA, 2009. https://www-pub.iaea.org/MTCD/publications/PDF/Pub1428_web.pdf.

Status of Fast Reactor Research and Technology Development, IAEA-TECDOC-1691. IAEA, Vienna, Austria, 2012. http://www-pub.iaea.org/MTCD/Publications/PDF/te_1691_web.pdf.

World List of Nuclear Power Plants. *Nuclear News, March 2019*, pages 35–55, 2019.

R. E. Alcouffe et al. User's Guide for TWODANT: A Code Package for Two-Dimensional, Diffusion-Accelerated, Neutral-Particle Transport, LA-10049-M. Los Alamos National Laboratory, Los Alamos, NM, 1990. https://www.osti.gov/biblio/5985401.

A. Alemberti. Advanced Lead Fast Reactor European Demonstrator - ALFRED Project. In *Presentation, Ansaldo Nucleare, Italy, September 26*, 2018. https://www.gen-4.org/gif/upload/docs/application/pdf/2018-11/geniv_alfred_-_alemberti_-final_-_aa.pdf.

Bibliography

J. Algina. Confidence Intervals for the Squared Multiple Semipartial Correlation Coefficient. *Journal of Modern Appl. Stat. Methods*, 7(1):2–10, 2008. https://digitalcommons.wayne.edu/cgi/viewcontent.cgi?article=1417&context=jmasm.

G. Aliberti, and M. Smith. PERSENT: need of a deterministic code for sensitivity analysis in 3D geometry and transport theory. In *PHYSOR 2014, Kyoto, Japan, September 28 – October 3*, 2015.

ANL. ARC 11.0: Code System for Analysis of Nuclear Reactors. Argonne National Laboratory, Argonne, IL, Available from Radiation Safety Information Computational Center as CCC-824., 2014.

M. Aufiero et al. A collision history-based approach to sensitivity/perturbation calculations in the continuous energy Monte Carlo code SERPENT. *Annals of Nuclear Energy*, 85:245–258, 2015. https://www.doi.org/10.1016/j.anucene.2015.05.008.

A. Aures et al. Benchmarking and Application of the State-of-the-Art Uncertainty Analysis Methods XSUSA and SHARK-X. *Annals of Nuclear Energy*, 101:262–269, 2017. http://dx.doi.org/10.1016/j.anucene.2016.11.025.

A. Aures et al. Uncertainty and Sensitivity Analysis of PWR Mini-Core Transients in the Presence of Nuclear Data Uncertainty using Non-Parametric Tolerance Limits. *Annals of Nuclear Energy*, 137:107146, 2020. https://doi.org/10.1016/j.anucene.2019.107146.

A. Aures et al. Depletion Calculation and Uncertainty / Sensitivity Analysis for a Sodium-Cooled Fast Spectrum Fuel Assembly. In *MC2015, Nashville, TN, April 19–23*, 2015.

L. A. Bernstein et al. Our Future Nuclear Data Needs. *Annual Review of Nuclear and Particle Science*, 69, 2019. https://www.doi.org/10.1146/annurev-nucl-101918-023708.

F. Bostelmann et al. Influence of Nuclear Data on Fast Reactor Calculations. In *PHYSOR 2016, Sun Valley, ID, May 1–5*, 2016.

F. Bostelmann et al. Benchmark for Uncertainty Analysis in Modeling (UAM) for Design, Operation and Safety Analysis of SFRs, Definition of Sub-Exercises. OECD/NEA, 2018.

F. Bostelmann et al. Uncertainty and Sensitivity Analysis in Criticality Calculations with Perturbation Theory and Sampling. In *MC2015, Nashville, TN, April 19–23*, 2015a.

F. Bostelmann et al. Sampling-Based Nuclear Data Uncertainty Analysis in Criticality and Depletion Calculations. In *MC2015, Nashville, TN, April 19–23*, 2015b.

F. Bostelmann et al. SCALE/AMPX Multigroup Libraries for Sodium-Cooled Fast Reactor Systems. *Annals of Nuclear Energy*, 2019. https://doi.org/10.1016/j.anucene.2019.107102.

J. Bousquet et al. Macroscopic Cross Section Generation with SCALE 6.2 for the MYRRHA Minimal Critical Core. In *M&C2017, Jeju, Korea, April 16–20*, 2017.

B. Boyack et al. Quantifying reactor safety margins part 1: An overview of the code scaling, applicability, and uncertainty evaluation methodology. *Nuclear Engineering and Design*, 119(1):1–15, 1990. https://www.doi.org/10.1016/0029-5493(90)90071-5.

B. L. Broadhead. Sensitivity- and Uncertainty-Based Criticality Safety Validation Techniques. *Nuclear Science and Engineering*, 146:340–366, 2004. https://doi.org/10.13182/NSE03-2.

I. N. Bronstein et al. *Taschenbuch der Mathematik*. Harri Deutsch GmbH, Frankfurt am Main, 7th edition, 2008.

D. Brown et al. ENDF/B-VIII.0: The 8th Major Release of the Nuclear Reaction Data Library with CIELO-project Cross Sections, New Standards and Thermal Scattering Data. *Nuclear Data Sheets*, 148:1–142, 2018. https://www.doi.org/10.1016/J.NDS.2018.02.001.

L. Buiron et al. Benchmark for Uncertainty Analysis in Modeling (UAM) for Design, Operation and Safety Analysis of SFRs, Core definitions, Version 1.6. OECD/NEA, 2019.

M. Chadwick et al. ENDF/B-VII.1 Nuclear Data for Science and Technology: Cross Sections, Covariances, Fission Product Yields and Decay Data. *Nuclear Data Sheets*, 112(12):2887–2996, 2011. https://www.doi.org/10.1016/j.nds.2011.11.002.

J. Cohen. *Applied Multiple Regression/Correlation Analysis for the Behavioral Sciences*. Lawrence Erlbaum Associates, London, 3rd edition, 2003.

Bibliography

F. D'Auria et al. The Best Estimate Plus Uncertainty (BEPU) approach in licensing of current nuclear reactors. *Nuclear Engineering and Design*, 248:317–328, 2012. https://doi.org/10.1016/J.NUCENGDES.2012.04.002.

K. L. Destine. DIF3D: A Code to Solve One-, Two-, and Three-Dimensional Finite Difference Diffusion Theory Problems. ANL-82-64, Argonne National Laboratory, 1984. https://digital.library.unt.edu/ark:/67531/metadc283553/m2/1/high_res_d/metadc283553.pdf.

T. J. Downar et al. PARCS v3.0, U.S. NRC Core Neutronics Simulator, Theory Manual. University of Michigan, Ann Arbor, MI, USA, 2010. http://pbadupws.nrc.gov/docs/ML1016/ML101610117.pdf.

N. R. Draper, and H. Smith. *Applied Regression Analysis.* Wiley, New York, 3rd edition, 1998.

J. Engel. On teaching Bootstrap Confidence Intervals. In *ICOTS8, Ljubljana, Slovenia, July*, 2010. https://new.censusatschool.org.nz/wp-content/uploads/2012/09/ICOTS8_4B2_ENGEL.pdf.

D. Foligno. *New evaluation of the delayed neutrons data and associated covariances - Applications on the integral kinetics parameters calculation for an improved safety of 3rd and 4th generation reactors.* PhD thesis, Aix-Marseille Université, France, 2019.

H. Glaeser. Methodenentwicklung und exemplarische Anwendungen zur Bestimmung der Aussagesicherheit von Rechenprogrammergebnissen. GRS-A-3443, Gesellschaft für Anlagen- und Reaktorsicherheit, Garching, Germany, 2008. https://www.grs.de/publikation/grs-A-3443.

H. Glaeser. Thermohydraulische Rechenmethoden zu Transienten und Störfällen im Reaktorkühlkreislauf unter besonderer Berücksichtigung mehrdimensionaler Strömungen (ATHLET, FLUBOX, CFX). GRS-A-3644, Gesellschaft für Anlagen- und Reaktorsicherheit, Garching, Germany, 2012. https://www.grs.de/publikation/grs-A-3644.

M. A. Golberg, and H. A. Cho. *Introduction to Regression Analysis.* WIT Press, Southampton, Boston, 2004.

I. Hill, and S. Jeong. Status and Analysis of P1 Angular Scattering Sensitivity Data Available with the Database for ICSBEP (DICE). In *M&C2017, Jeju, Korea, April 16–20*, 2017.

IAEA. Summary of the Plenary Sessions. In *FR17, Yekaterinburg, Russian Federation, June 26-29*, pages 13–16, 2017. https://www-pub.iaea.org/MTCD/Publications/PDF/STIPUB1836web.pdf.

K. Ivanov et al. Benchmark for Uncertainty Analysis in Modelling (UAM) for Design, Operation and Safety Analysis of LWRs, Volume I: Specification and Support Data for the Neutronics Cases (Phase I). OECD/NEA, 2016.

J. E. Kelly. Generation IV International Forum: A decade of progress through international cooperation. *Progress in Nuclear Energy*, 77:240–246, 2014. https://doi.org/10.1016/j.pnucene.2014.02.010.

B. C. Kiedrowski, and F. B. Brown. Adjoint-Based k -Eigenvalue Sensitivity Coefficients to Nuclear Data Using Continuous-Energy Monte Carlo. *Nuclear Science and Engineering*, 174(3):227–244, 2014. https://doi.org/10.13182/nse12-46.

K. S. Kim et al. The SCALE/AMPX multigroup cross section processing for fast reactor analysis. *Annals of Nuclear Energy*, 132:161–171, 2019. https://www.doi.org/10.1016/j.anucene.2019.04.034.

T. Kim et al. Core design studies for a 1000MWth Advanced Burner Reactor. *Annals of Nuclear Energy*, 36(3):331–336, 2009. https://www.doi.org/10.1016/j.anucene.2008.12.021.

I. Kodeli. Multidimensional Deterministic Nuclear Data Sensitivity and Uncertainty Code System: Method and Application. *Nuclear Science and Engineering*, 138(1):45–66, 2001. https://doi.org/10.13182/NSE00-43.

I. Kodeli. Comments on the status of modern covariance data based on different fission and fusion reactor studies. *EPJ Nuclear Sciences & Technologies*, 4, 2018. https://www.doi.org/10.1051/epjn/2018027.

B. Krzykacz-Hausmann. An approximate sensitivity analysis of results from complex computer models in the presence of epistemic and aleatory uncertainties. *Reliability Engineering and System Safety*, 91(10-11):1210–1218, 2006. https://doi.org/10.1016/j.ress.2005.11.019.

A. M. Kshirsagar. *Multivariate Analysis.* Marcel Dekker, Inc., New York, 1st edition, 1972.

Bibliography

C. H. Lee, and W. S. Yang. MC²-3: Multigroup Cross Section Generation Code for Fast Reactor Analysis. ANL/NE-11-41, Rev.2, Argonne National Laboratory, Lemont, IL, 2012. https://publications.anl.gov/anlpubs/2017/12/138005.pdf.

C. Lee, and W. S. Yang. MC2-3: Multigroup cross section generation code for fast reactor analysis. *Nuclear Science and Engineering*, 187(3):268–290, 2017. https://doi.org/10.1080/00295639.2017.1320893.

J. Leppänen. *Development of a New Monte Carlo reactor physics code*. PhD thesis, Helsinki University of Technology, Finland, 2007. http://montecarlo.vtt.fi/download/P640.pdf.

J. Leppänen et al. The Serpent Monte Carlo code: Status, development and applications in 2013. *Annals of Nuclear Energy*, 82:142–150, 2014. https://doi.org/10.1016/j.anucene.2014.08.024.

R. Little et al. Low-fidelity Covariance Project. *Nuclear Data Sheets*, 109(12):2828–2833, dec 2008. https://doi.org/10.1016/j.nds.2008.11.018.

K. Mikityuk et al. FAST: An advanced code system for fast reactor transient analysis. *Annals of Nuclear Energy*, 32(15):1613–1631, 2005. https://doi.org/10.1016/j.anucene.2005.06.002.

P. Müller. *Wahrscheinlichkeitsrechnung und Mathematische Statistik, Lexikon der Statistik*. Akademie-Verlag, Berlin, 3rd edition, 1980.

NEA. International Handbook of Evaluated Criticality Safety Benchmark Experiments. NEA-1486/14, OECD/NEA, 2015a.

NEA. International Handbook of Evaluated Reactor Physics Benchmark Experiments. NEA-1765/11, OECD/NEA, 2015b.

E. Nikitin. *Extension of the nodal code DYN3D to SFR applications*. PhD thesis, École Polytechnique Fédérale de Lausanne, Switzerland, 2019. https://infoscience.epfl.ch/record/264193/files/EPFL_TH7264.pdf.

E. Nikitin et al. On the use of the SPH method in nodal diffusion analyses of SFR cores. *Annals of Nuclear Energy*, 85:544–551, 2015. https://www.doi.org/10.1016/j.anucene.2015.06.007.

G. Palmiotti. Variational nodal transport methods with anistropic scattering. *Nuclear Science and Engineering*, 115:233–243, 1993. https://doi.org/10.13182/NSE92-110.

C. M. Perfetti, and B. T. Rearden. SCALE Continuous-Energy Eigenvalue Sensitivity Coefficient Calculations. *Nuclear Science and Engineering*, 182(2):332–353, 2016. https://doi.org/10.13182/NSE15-12.

R. Rachamin et al. Neutronic analysis of SFR core with HELIOS-2, Serpent, and DYN3D codes. *Annals of Nuclear Energy*, 55:194–204, 2013. https://www.doi.org/10.1016/j. anucene.2012.11.030.

B. T. Rearden et al. Sensitivity and uncertainty analysis capabilities and data in SCALE. *Nuclear Technology*, 174(2):236–288, 2011. https://doi.org/10.13182/NT174-236.

B. T. Rearden. Nuclear Data and Benchmarking Program. In *Presentation at SCALE Users' Group Workshop, Oak Ridge National Laboratory, August 28*, 2018. https: //www.ornl.gov/sites/default/files/2_BradRearden.pdf.

B. T. Rearden, and M. A. Jessee. SCALE Code System, ORNL/TM-2005/39, Version 6.2. Oak Ridge National Laboratory, Oak Ridge, TN. Available from Radiation Safety Information Computational Center as CCC-834, 2016. https://www.ornl.gov/sites/ default/files/SCALE_6.2.3.pdf.

F. Reitsma et al. The IAEA Coordinated Research Program on HTGR Uncertainty Analysis: Phase I Status and Initial Results. In *HTR 2014, Weihai, China, October 27–31*, 2014.

G. Rimpault. The ERANOS Code and Data System for Fast Reactor Neutronic Analyses. In *PHYSOR 2002, Seoul, Korea, October 7–10*, 2002.

G. Rimpault et al. Objectives and Status of the OECD/NEA sub-group on Uncertainty Analysis in Modelling (UAM) for Design, Operation and Safety Analysis of SFRs (SFR-UAM), IAEA-CN245-220. In *FR17, Yekaterinburg, Russian Federation, June 26–29*, 2017.

D. Rochman et al. Efficient Use of Monte Carlo: Uncertainty Propagation. *Nuclear Science and Engineering*, 177(3):337–349, 2014. https://doi.org/10.13182/NSE13-32.

D. Rochman et al. Nuclear Data Uncertainties for Typical LWR Fuel Assemblies and a Simple Reactor Core. *Nuclear Data Sheets*, 139:1–76, 2017. https://doi.org/10.1016/ j.nds.2017.01.001.

Bibliography

U. Rohde et al. The reactor dynamics code DYN3D - Models, validation and applications. *Progress in Nuclear Energy*, 89:170–190, 2016. https://doi.org/10.1016/j.pnucene.2016.02.013.

J. M. Ruggieri et al. ERANOS 2.1: International code system for GEN IV fast reactor analysis. In *ICAPP, Reno, NV, June 4–8*, 2006. http://www.scopus.com/inward/record.url?eid=2-s2.0-33845741151&partnerID=tZOtx3y1.

J.-M. Ruggieri et al. Sodium-cooled fast reactor (SFR) system safety assessment. Rev. 1, Gen IV International Forum, 2017. https://www.gen-4.org/gif/upload/docs/application/pdf/2017-11/gif-sfr-safetyassessment-20170427_final.pdf.

A. Saltelli et al. *Global Sensitivity Analysis: The Primer*. John Wiley & Sons, Ltd, 2008. https://onlinelibrary.wiley.com/doi/book/10.1002/9780470725184.

A. Saltelli et al. Variance based sensitivity analysis of model output. Design and estimator for the total sensitivity index. *Computer Physics Communications*, 181(2): 259–270, 2010. https://www.doi.org/10.1016/j.cpc.2009.09.018.

M. Sarotto. Possible working range of the MYRRHA core and basic neutronic parameters for safety analyses. 2014. http://openarchive.enea.it/handle/10840/5038?show=full.

E. M. Saylor et al. Criticality Safety Validation of SCALE 6.2.2. ORNL/TM-2018/884, Oak Ridge National Laboratory, Oak Ridge, TN, 2018. https://www.osti.gov/servlets/purl/1479759.

K. Shibata et al. JENDL-4.0: A New Library for Nuclear Science and Engineering. *Journal of Nuclear Science and Technology*, 48(1):1–30, 2012. https://doi.org/10.1080/18811248.2011.9711675.

D. L. Smith. Nuclear Data Uncertainty Quantification: Past, Present and Future. *Nuclear Data Sheets*, 123:1–7, 2015. https://www.doi.org/10.1016/j.nds.2014.12.002.

I. M. Sobol. Sensitivity analysis for non-linear mathematical models. *Mathematical Modelling and Computational Experiment*, 1:407–414, 1993. https://doi.org/1061-7590/93/04407-008.

N. Stauff et al. Impact of Nuclear Data Uncertainties on the Performance of the Advanced Burner Reactor. In *PHYSOR 2016, Sun Valley, ID, May 1–5*, 2016.

N. Stauff et al. Uncertainty Quantification of ABR Transient Analysis - Nuclear Data Uncertainties. In *BEPU2018, Real Collegio, Lucca, Italy, May 13–19*, 2018.

G. Strydom, and F. Bostelmann. IAEA Coordinated Research Project on HTGR Physics, Thermal-Hydraulics, and Depletion Uncertainty Analysis. Prismatic HTGR Benchmark Definition: Phase I, INL/EXT-15-34868, Rev. 1. Idaho National Laboratory, Idaho Falls, ID, 2015. https://inldigitallibrary.inl.gov/sites/sti/sti/6799567.pdf.

J.-C. Sublet et al. The JEFF-3.0/A Neutron Activation File – EAF-2003 into ENDF-6 Format. JEFDOC-982, CEA, France, 2003. https://www.researchgate.net/publication/299348047_The_JEFF-30A_Neutron_Activation_File-EAF-2003_into_ENDF-6_format.

L. P. Swiler et al. Sample Generation for Nuclear Data. SAND2018-10554, Sandia National Laboratories, 2018. https://www.osti.gov/servlets/purl/1474254.

N. T. Thomopoulos. Generating Multivariate Random Variates. In *Essentials of Monte Carlo Simulation: Statistical Methods for Building Simulation Models*, pages 57–70. Springer, New York, NY, 2013. https://doi.org/10.1007/978-1-4614-6022-0_6.

I. Trivedi et al. Uncertainty Quantification on Feedback and Safety Parameters of the Lead-Cooled Fast Reactor. In *M&C 2019, Portland, OR, August 25–29*, 2019.

A. E. Waltar et al. Appendix F: 4-Group and 8-Group Cross sections, Fast Spectrum Reactors. In *Fast Spectrum Systems*, page 643. Springer, New York, 2012a.

A. E. Waltar et al. 1.3 Basic Physics of Fast Reactors. In *Fast Spectrum Systems*. Springer, New York, 2012b.

Westinghouse Electric Company LLC. Demonstration Lead-cooled Fast Reactor, RT-TR-15-30, Revision 1. 2016. https://art.inl.gov/ARTDocumentLibrary/AdvancedDemonstrationandTestReactorOptionsStudy/Attachment_4_Westinghouse_LFR_DR.pdf.

D. Wiarda et al. AMPX-6: A Modular Code System for Processing ENDF/B, ORNL/TM-2016/43. Oak Ridge National Laboratory, Oak Ridge, TN. Available from Radiation Safety Information Computational Center as CCC-834, 2016. https://www.ornl.gov/sites/default/files/AMPX-6.pdf.

W. Wieselquist et al. PSI Methodologies for Nuclear Data Uncertainty Propagation with CASMO-5M and MCNPX: Results for OECD/NEA UAM Benchmark Phase I.

Bibliography

Science and Technology of Nuclear Installations, 2013:1–15, 2013. https://doi.org/10.1155/2013/549793.

S. S. Wilks. Determination of Sample Sizes for Setting Tolerance Limits. *The Annals of Mathematical Statistics*, 12:91–96, 1941. https://doi.org/10.1214/aoms/1177731788.

S. S. Wilks. *Mathematical Statistics*. Wiley, New York, 1962. https://science.sciencemag.org/content/136/3522/1114.2.

M. L. Williams. Perturbation Theory for Nuclear Reactor Analysis. In Y. Ronen, editor, *Handbook of Nuclear Reactors Calculations, Volume III*, pages 63–188. CRC Press, 1986.

M. L. Williams. Sensitivity and Uncertainty Analysis for Eigenvalue-Difference Responses. *Nuclear Science and Engineering*, 155:18–36, 2007. https://doi.org/10.13182/NSE06-11.

M. L. Williams et al. Eigenvalue Sensitivity Theory for Resonance-Shielded Cross Sections. *Nuclear Science and Engineering*, 138:177–191, 2001. https://doi.org/10.13182/NSE00-56.

M. L. Williams et al. A statistical sampling method for uncertainty analysis with SCALE and XSUSA. *Nuclear Technology*, 183:515–526, 2013. https://doi.org/10.13182/NT12-112.

M. Williams et al. Covariance Applications in Criticality Safety, Light Water Reactor Analysis, and Spent Fuel Characterization. *Nuclear Data Sheets*, 123:92–96, 2015. https://www.doi.org/10.1016/j.nds.2014.12.016.

W. S. Yang. Fast reactor physics and computational methods. *Nuclear Engineering and Technology*, 44(2):177–198, 2012. https://doi.org/10.5516/NET.01.2012.504.

G. Zhang et al. Uncertainty Quantification of ABR Transient Safety Analysis. In *BEPU2018, Real Collegio, Lucca, Italy, May 13–19*, 2018.

G. Zhang et al. Dakota-SAS4A/SASSYS-1 Coupling for Uncertainty Quantification and Optimization Analysis. In *M&C2017, Jeju, Korea, April 16–20*, 2017.

Y. Zheng et al. SARAX: A new code for fast reactor analysis part I: Methods. *Nuclear Engineering and Design*, 340:421–430, 2018. https://doi.org/10.1016/j.nucengdes.2018.10.008.

T. Zhu et al. NUSS: A tool for propagating multigroup nuclear data covariances in pointwise ACE-formatted nuclear data using stochastic sampling method. *Annals of Nuclear Energy*, 75:713–722, 2015. https://doi.org/10.1016/j.anucene.2014.09.013.

A. Ziegler, and H.-J. Allelein. 12.2 Schneller Natriumgekühlter Reaktor. In *Reaktortechnik*, pages 342–352. Springer, Berlin Heidelberg, 2nd edition, 2013.

W. Zwermann et al. Influence of Nuclear Covariance Data on Reactor Core Calculations. In *WONDER 2009, Saint-Paul-Lez-Durance, France, September 29 – October 2*, pages 99–104, 2009.

Thesis-related Publications

A. Aures et al. Impact of Nuclear Data on Sodium-Cooled Fast Reactor Calculations. In *EPJ Web of Conferences*, volume 111, 2016. https://doi.org/10.1051/epjconf/201611111003.

A. Aures et al. Reactor Simulations with Nuclear Data Uncertainties. *Nuclear Engineering and Design*, 355:110313, 2019. https://www.doi.org/10.1016/j.nucengdes.2019.110313.

F. Bostelmann et al. Influence of Nuclear Data on Fast Reactor Calculations. In *PHYSOR 2016, Sun Valley, ID, May 1–5*, 2016.

F. Bostelmann et al. SCALE Multi-Group Libraries for Sodium-cooled Fast Reactor Systems. In *M&C2017, Jeju, Korea, April 16–20*, 2017a.

F. Bostelmann et al. Sensitivity Indices for Nuclear Data Uncertainty Analysis with XSUSA and TSUNAMI. In *BEPU2018, Real Collegio, Lucca, Italy, May 13–19*, 2018a.

F. Bostelmann et al. Nuclear Data Uncertainty Analyses with XSUSA and MCNP. In *AMNT 2018, Berlin, Germany, May 29–30*, 2018b.

F. Bostelmann et al. Preliminary SCALE/TSUNAMI Results for the Sub-exercises of the OECD/NEA Benchmark for Uncertainty Analysis in Modeling of Sodium-Cooled Fast Reactors. *Transactions of the American Nuclear Society*, 119, 2018c.

F. Bostelmann et al. Benchmark for Uncertainty Analysis in Modeling (UAM) for Design, Operation and Safety Analysis of SFRs, Definition of Sub-Exercises. OECD/NEA, 2018d.

F. Bostelmann et al. Treatment of Implicit Effects with XSUSA. In *Proc. M&C2017, Jeju, Korea, April 16–20*, 2017b.

F. Bostelmann et al. SCALE Covariance Libraries for Sodium-Cooled Fast Reactor Systems. In *PHYSOR 2018, Cancun, Mexico, April 22–26*, 2018e.

F. Bostelmann et al. SCALE/AMPX multigroup libraries for sodium-cooled fast reactor systems. *Annals of Nuclear Energy*, 2019. https://doi.org/10.1016/j.anucene.2019. 107102.

J. Bousquet et al. Macroscopic Cross Section Generation with SCALE 6.2 for the MYRRHA Minimal Critical Core. In *M&C2017, Jeju, Korea, April 16–20*, 2017.

L. Buiron et al. Benchmark for Uncertainty Analysis in Modeling (UAM) for Design, Operation and Safety Analysis of SFRs, Core definitions, Version 1.6. OECD/NEA, 2019.

G. Rimpault et al. Objectives and Status of the OECD/NEA sub-group on Uncertainty Analysis in Modelling (UAM) for Design, Operation and Safety Analysis of SFRs (SFR-UAM), IAEA-CN245-220. In *FR17, Yekaterinburg, Russian Federation, June 26–29*, 2017.

G. Rimpault et al. Current Status and Perspectives of the OECD/NEA Sub-Group on Uncertainty Analysis in Modelling (UAM) for Design, Operation and Safety Analysis of SFRs (SFR-UAM). In *BEPU2018, Real Collegio, Lucca, Italy, May 13–19*, 2018.

N. E. Stauff et al. Evaluation of the OECD/NEA/SFR-UAM Neutronics Reactivity Feedback and Uncertainty Benchmarks. In *FR17, Yekaterinburg, Russian Federation, June 26–29*, pages IAEA–CN245–149, 2017.

Friederike Bostelmann

Experience

since 01/2018 **Oak Ridge National Laboratory**, Oak Ridge, TN, USA
Post Master's Research Associate in the Reactor Physics Group of the Reactor and Nuclear Systems Division:
- Generation and validation of multigroup cross section libraries for light water reactor and advanced reactor systems,
- Uncertainty and sensitivity analysis of various reactor concepts with respect to nuclear data,
- Further development and application of the SAMPLER sequence for random sampling–based uncertainty analysis.

02/2017 – 04/2017 **Oak Ridge National Laboratory**, Oak Ridge, TN, USA
Guest assignment in the Reactor and Nuclear Systems Division:
- Generation of multigroup cross section libraries with AMPX.

01/2015 – 12/2017 **Gesellschaft für Anlagen- und Reaktorsicherheit gGmbH**, Garching, Germany
Scientific staff in the Core Behavior Department of the Reactor Safety Division:
- Uncertainty and sensitivity analysis with respect to nuclear data,
- Further development and application of the random sampling–based XSUSA code,
- Criticality safety and reactor physics calculations for various reactor types,

05/2014 – 12/2014 **Idaho National Laboratory**, Idaho Falls, ID, USA
Intern in the Very High Temperature Methods Group of the Nuclear Science and Engineering Division:
- Monte Carlo reference simulations for Phase I of the IAEA Coordinated Research Program on HTGR Uncertainties (prismatic reactor type),
- Assistance in the development of the corresponding specifications.

05/2013 – 03/2014 **Jülich Research Centre**, Jülich, Germany
Master Thesis with focus on fuel rod behavior modeling.

01/2012 – 03/2013 **Jülich Research Centre**, Jülich, Germany
Student research assistant:
- Criticality safety and burnup studies using the Monte Carlo Code Serpent,
- Modeling of the Chinese pebble bed reactor HTR-10 and simulation of various critical configurations as contribution to an educational book.

Education

2015–2020	**Ecole polytechnique fédérale de Lausanne**, Switzerland Ph.D. in Nuclear Engineering: *Systematic uncertainty and sensitivity analysis of sodium-cooled fast reactor systems.*
2011–2014	**RWTH Aachen University**, Germany Master of Science in Nuclear Safety Engineering, grade: 1.4 (very good) Master Thesis: *Capabilities of the Transuranus code in fuel rod behaviour power transient analysis.*
2008–2011	**Georg-August-Universität Göttingen**, Germany Bachelor of Science in Physics, grade: 1.8 (good) Bachelor Thesis: *Investigation of vacancy concentrations in silicon after aluminium gettering using platinum diffusion.*

Languages

German	mother tongue
English	fluent in speech and writing

Skills

Reactor physics	Monte Carlo Codes SCALE/KENO-VI and Serpent Deterministic Code SCALE/TRITON
Uncertainty analysis	SCALE/TSUNAMI, SCALE/SAMPLER and XSUSA
Nuclear data	Generation of cross section and covariance libraries with AMPX
Fuel performance	Transuranus (ITU, Karlsruhe)
Programming	Python, C++
Version control	GitLab

Miscellaneous

Hobbies	Member of the Knoxville Choral Society
Volunteering	Oak Ridge Computer Science Girls